Development of segmented flow crystallisers for *in situ* X-ray diffraction analysis

Elizabeth Sarah Galtry

10142881

Thesis submitted for the degree of Doctor of Philosophy, Chemical Engineering

University of Nottingham

September 2024

Abstract

The study of crystallisation through *in situ* analysis methods is key to elucidating the crystallisation processes of polymorphic materials. This thesis presents research on the development of *in situ* X-ray diffraction (XRD) techniques for the study of segmented flow crystallisation. This work was carried out as a joint studentship between University of Nottingham and Diamond Light Source, the UK's national synchrotron research facility.

Chapter 5 describes the commissioning of a temperature-cycling segmented flow crystalliser, the KRAIC-T. Temperature-cycling during crystallisation enabled enhanced control over the crystallisation process of succinic acid. Integration of the KRAIC-T as a sample environment on Beamline I11 at Diamond Light Source involved the use of an upgraded data acquisition technique to improve the signal-to-noise of collected *in situ* powder X-ray diffraction data (PXRD). The study of the slurrying crystallisation of the polymorphic crystal system, *ortho*-aminobenzoic acid, was used to verify the improvement of the *in situ* technique. These data were also used for the development of enhanced data processing techniques.

In situ XRD analysis is largely limited to synchrotron facilities due to the high intensity, high energy X-rays required for XRD investigation of complex sample environments. Chapter 4 discusses the development of the KRAIC-Xl, a segmented flow crystalliser for lab-source PXRD analysis at the Flow-Xl facility, University of Leeds. Proof-of-principles studies found the lab-source system was able to achieve time-resolved PXRD studies of glycine (GLY) anti-solvent crystallisation, finding the initial crystallisation of the highly metastable β-GLY and rapid transformation to the more stable α-GLY polymorph.

Chapter 3 details the development of Python-based processing methodologies for PXRD data collected from the KRAIC-T and KRAIC-Xl systems. Existing processing techniques are often labour-intensive and time-consuming for processing of PXRD from complex environments; specialist Python modules were used to develop novel processing workflows in Chapter 3 maximise the diffraction signal extracted, whilst minimising data processing time.

Chapter 6 discusses the development of the KRAIC-S v2 and v3; upgraded crystalliser designs for serial crystallography during segmented flow at Beamline I19, Diamond Light Source. Beamtime with the KRAIC-S v2 on the cooling crystallisation of paracetamol assessed the system, showing an improved ease-of-use, but highlighted limitations of the serial crystallography technique. Chapter 7 uses the final KRAIC-S v3 design for the study of non-photochemical laser induced nucleation of potassium chloride, achieving induced nucleation of a single particle per droplet and accompanying *in situ* XRD.

Acknowledgements

First and foremost, I would like to express my deepest gratitude to my supervisor, Dr Karen Robertson. Your immense support and encouragement during this PhD have been invaluable. It has been a joy working with you these past years and I am grateful for your guidance and expertise - you have taught me so much. Thank you for your patience and for constantly pushing me to grow both as a researcher and an individual. I would also like to thank my supervisors at Diamond Light Source, Dr Mark Warren, Dr Sarah Day, and Dr Dave Allan. Your support has been pivotal in shaping this research and I sincerely appreciate the time and expertise each of you have contributed. Working under your supervision has been a fantastic experience and I am grateful for the opportunities you have encouraged me to take whilst at Diamond.

Thank you to the University of Nottingham and Diamond Light Source for their funding of this research, and to the Research Complex at Harwell and CMAC for access to lab space whilst based at Diamond. I am grateful to the staff at these institutions for providing me with the support and resources necessary to complete my research. Furthermore, I am grateful for the support from researchers and staff at the Flow-Xl facility, University of Leeds, for their part in this work. A further thanks to my collaborators across the various projects that formed part of this PhD. I am grateful for the opportunity to work with such talented individuals and your contributions have greatly enriched this project.

To the fellow PhD students who have lent a hand during beamtimes; Ben Holland, Hamza Ali, Xena Lewis, Raphael Stone, and Carissa Ponan. Thank you for your efforts, I especially appreciate your patience and good humour during the early hours of the morning! Your generous assistance helped make this research possible, but also made these experiences far more enjoyable too.

A huge thanks the friends I made along the way – Dan, Anna, and Harry: you make me laugh every single day and have been a lifeline during the most challenging moments, especially in these last few months of thesis writing. To my housemates when I was based in Oxford – Henry, Meredydd, Charles, and Emily: thank you for making my time at Diamond truly memorable. Those 2 years were such fun and I cannot wait to see what you all achieve in the coming years and beyond.

A special thanks to family friends, Matt and Julie, for hosting me during my frequent visits to Nottingham; your support helped me immeasurably and I cannot thank you enough. I would like to thank my brother Chris, my friends, Kate and Michael, and my extended family and friends for their love and support throughout these past few years. And most importantly, thank you to my Mum and Dad, your encouragement has been a constant source of strength, and I could not have done it without you.

I would like to dedicate this thesis to my wonderful grandparents, whose love, humour, and strength continue to inspire me.

Table of Contents

Abstract i
Acknowledgements ii
Table of Contents iii
List of Abbreviations ix
Chapter 1 – Introduction 1
1.1 – Context of Research 1
1.2 – Crystallisation Theory 1
1.2.1 – Nucleation 1
1.2.2 – Supersaturation 4
1.2.3 – Crystal growth 5
1.2.4 – Polymorphism 6
1.3 – Crystallisation Techniques 9
1.3.1 – Evaporative crystallisation 9
1.3.2 – Cooling crystallisation 10
1.3.3 – Temperature cycling crystallisation 11
1.3.4 – Anti-solvent crystallisation 12
1.3.5 – Slurrying crystallisation 12
1.4 – Continuous Crystallisation 13
1.4.1 – Batch vs Continuous Crystallisation 13
1.4.2 – Continuous Crystallisers 13
1.4.2.1 – KRAIC tri-segmented flow crystalliser 16
1.5 – *In situ* analysis during crystallisation 17
1.6 – Serial Crystallography 20
1.7 – Research Aims and Objectives 20
1.8 – References 22
Chapter 2 – X-ray Techniques 28
2.1 – X-ray Crystallography 28
2.1.1 – The Unit Cell 28
2.1.2 – Space Groups 29
2.1.3 – X-ray Diffraction and Bragg's Law 30
2.1.4 – X-ray Diffraction Techniques 30
2.1.4.1 – Single Crystal X-ray Diffraction 31
2.1.4.2 – Powder X-ray Diffraction 32
2.2 – X-ray Sources and Instrumentation 35

2.2.1 – Lab-source X-rays 35
2.2.1.1 – The Flow-Xl facility 36
2.2.2 – Synchrotron X-rays 36
2.2.2.1 – Beamline I11 38
2.2.2.2 – Beamline I19 39
2.3 - References 41
Chapter 3 – Development of Powder X-ray diffraction data processing methodology development for segmented flow crystallisation 44
3.1 – Introduction and Aims 44
3.2 – PXRD processing development for Beamline I11 48
3.2.1 – Introduction 48
3.2.1.1 – Individual diffraction frame threshold background subtraction processing in MATLAB 50
3.2.2 – Development of diffraction frame sorting and individual diffraction frame processing with threshold background subtraction in Python 52
3.2.2.1 - Introduction 52
3.2.2.2 – Methodology 52
3.2.2.2.1 – Diffraction frame sorting workflow 52
3.2.2.2.2 – Thresholding background subtraction and 1D integration workflow 54
3.2.2.3 – Results and Discussion 57
3.2.2.4 – Conclusions 61
3.2.3 – Diffraction frame processing with morphological baseline correction in Python 61
3.2.3.1 - Introduction 61
3.2.3.2 – Methodology 63
3.2.3.2.1 – Pre-merging baseline correction workflow 63
3.2.3.2.2 – Post-merging baseline correction workflow 64
3.2.3.3 – Results and discussion 65
3.2.3.3.1 – Comparing pre- and post-merging baseline correction methodologies 67
3.2.3.3.2 – Comparing thresholding and baseline correction workflows 69
3.2.3.3 – Conclusions 72
3.2.4 – Multi diffraction frame processing with post-merging baseline correction in Python (pyFAI_multi_pybaselines.py) 73
3.2.4.1 – Introduction 73

3.2.4.2 – Methodology 73
3.2.4.3 – Results and Discussion 76
3.2.4.4 – Conclusions 76
3.2.5 – Rietveld Refinement 77
3.2.6 – Overall Conclusions 78
3.2.7 – Future work 80
3.3 – PXRD processing development for the Flow-Xl facility 82
3.3.1 – Introduction 82
3.3.2 – Methodology development 84
3.3.3 – Results and Discussion 90
3.3.4 – Conclusions 90
3.3.5 – Future Work 91
3.4 – References 92
Chapter 4 – Lab-source *in situ* X-ray diffraction during segmented flow crystallisation at the Flow-Xl facility 94
4.1 – Introduction and Aims 94
4.2 – KRAIC-Xl crystalliser design 99
4.3 – Methodology and Experimental 102
4.3.1 – KRAIC-Xl 102
4.3.2 – L-glutamic acid crystallisation 103
4.3.3 – Glycine crystallisation 104
4.4 – Results and Discussion 109
4.4.1 - KRAIC-Xl 109
4.4.2 – L-glutamic acid crystallisations 111
4.4.3 – Glycine crystallisations 115
4.5 – Conclusions 121
4.6 – Future Work 123
4.7 – References 125
Chapter 5 – Development of the KRAIC-T, a temperature cycling crystalliser coupled with *in situ* PXRD on Beamline I11 127
5.1 – Introduction 127
5.2 – Commissioning of the KRAIC-T crystalliser system 131
5.2.1 – Heated temperature profile studies 131
5.2.1.1 – Introduction 131
5.2.1.2 – Methodology 131
5.2.1.3 – Results and Discussion 132

5.2.2 – Temperature cycling mediated segmented flow crystallisation of succinic acid 136
5.2.2.1 – Introduction 136
5.2.2.2 – Experimental 138
5.2.2.3 – Results and Discussion 139
5.2.3 – Development of a column heat sink for sub-ambient temperature control 142
5.2.3.1 – Introduction 142
5.2.3.2 – Design and Experimental 143
5.2.3.3 – Results and Discussion 144
5.3 – Slug triggering data acquisition adaptation for the KRAIC-T on Beamline I11 145
5.3.1 – Introduction 145
5.3.2 – Methodology 146
5.3.2.1 – Initial analysis shuttle integration 146
5.3.2.2 – KRAIC-T integration 147
5.3.3 – Results and Discussion 149
5.3.3.1 – Initial analysis shuttle integration 149
5.3.3.2 – KRAIC-T integration 150
5.4 – Study of oABA segmented flow crystallisation and slurrying with *in situ* PXRD at Beamline I11 152
5.4.1 – Introduction 152
5.4.2 – Methodology 154
5.4.2.1 – Kapton X-ray analysis window preparation 156
5.4.2.2 – oABA crystallisations 157
5.4.2.3 – oABA slurrying conditions 158
5.4.3 – Results and Discussion 160
5.4.3.1 – Crystallisation results and discussion 160
5.4.3.2 – oABA slurrying results and discussion 162
5.5 – Overall Conclusions 179
5.6 – Future Work 183
5.7 – References 185
Chapter 6 – Design of an integrated segmented flow crystalliser for *in situ* SCXRD on Beamline I19 187
6.1 – Introduction and Aims 187
6.2 – KRAIC-S v2 design 192
6.3 – KRAIC-S v2 commissioning experiments 196

6.3.1 – Experimental 196
6.3.2 – Results and Discussion 201
6.4 – KRAIC-S v3 design 207
6.5 – Conclusions 210
6.6 – Future Work 211
6.7 – References 215
Chapter 7 – Non-photochemical laser-induced nucleation of potassium chloride in segmented flow with *in situ* XRD on Beamline I19 217
7.1 – Introduction 217
7.2 – NPLIN feasibility studies 221
7.2.1 – Batch KCl NPLIN 221
7.2.2 – Laser tubing damage 224
7.2.3 – NPLIN of KCl in FEP tubing 225
7.2.4 – Slug triggering adaptation for NPLIN 226
7.2.5 – Overall NPLIN feasibility study results 228
7.3 – NPLIN in segmented flow with *in situ* XRD 228
7.3.1 – Experimental 228
7.3.2 – Results and Discussion 231
7.4 – Conclusions 236
7.5 – Future Work 237
7.6 – References 240
Chapter 8 – Conclusions and Future Work 242
8.1 – Conclusions 242
8.2 – Future Work 244
Appendix 246
Appendix A3 – Chapter 3 246
A3.1 – Beamline I11 PXRD data processing scripts 246
A3.2 – Flow-Xl PXRD data processing scripts 246
Appendix A4 – Chapter 4 247
A4.1 – Calibrant data file comparison 247
A4.2 – LGA Frame Selector results 247
Appendix A5 – Chapter 5 249
A5.1 - Temperature profiles for KRAIC-T commissioning 249
A5.2 – oABA crystallisation conditions 252
A5.3 - Rietveld refinement unit cell parameters 253
Appendix A6 – Chapter 6 261

A6.1 – PCM processing procedure 261

List of Abbreviations

a.u.	Arbitrary Units
AgBh	Silver Behenate
ATR	Attenuated Total Reflection
BA	Benzoic acid
C	Column
CBZ	Carbamazepine
CeO_2	Cerium oxide
CNT	Classical Nucleation Theory
CSD	Crystal Size Distribution
DI	Deionised
Diamond	Diamond Light Source
EH1	Experimental Hutch 1
EH2	Experimental Hutch 2
EtOH	Ethanol
FBRM	Focused Beam Reflectance Measurement
FEP	Fluorinated ethylene propylene
FTIR	Fourier Transform Infrared spectroscopy
FWHM	Full Width Half Maximum
GDA	Generic Data Acquisition
GLY	Glycine
H_2O	Water
HPC	Hybrid Photon Counting
HZ	Heating Zone
ID	Inner Diameter
IDP	Isotropic Dielectric Polarisation
IPA	Isopropyl alcohol

KCl	Potassium Chloride
KRAIC	Kinetically Regulated Automated Input Crystalliser
KRAIC-D	Kinetically Regulated Automated Input Crystalliser for Diffraction
KRAIC-R	Kinetically Regulated Automated Input Crystalliser for Raman Spectroscopy
KRAIC-S	Kinetically Regulated Automated Input Crystalliser for Single Crystal X-ray Diffraction
KRAIC-T	Kinetically Regulated Automated Input Crystalliser for Temperature cycling
KRAIC-Xl	Kinetically Regulated Automated Input Crystalliser at Flow-Xl
LDE	Long Duration Experiments
LED	Light Emitting Diode
LGA	L-glutamic acid
MSMPR	Mixed-Suspension Mixed-Product Removal crystalliser
MSZW	Metastable Zone Width
NPLIN	Non-photochemical laser induced nucleation
*o*ABA	*ortho*-aminobenzoic acid
OBC	Oscillatory Baffled Crystalliser
OKE	Optical Kerr Effect
PAT	Process Analytical Technology
PCM	Paracetamol
PXRD	Powder X-ray Diffraction
RT	Room Temperature
S	Supersaturation
SCA	Succinic Acid
SCXRD	Single Crystal X-ray Diffraction
SMPT	Solvent-Mediated Phase Transition
SR	Synchrotron Radiation

STR	Stirred Tank Reactor
TSN	Two-step Nucleation theory
UBA	Urea:Barbituric acid co-crystal
UV/vis	Ultra Violet/visible light
v	Velocity
X	X-ray analysis window
XRD	X-ray Diffraction

Chapter 1 – Introduction

1.1 – Context of Research

Crystallisation is a fundamental step in many industries, most notably the production of pharmaceutical materials. Crystalline products are highly dependent on the crystallisation environment, with methodology and solvents influencing the end material in terms of crystal form, crystal size distribution, and morphology. *In situ* analysis techniques aim to understand crystallisation pathways in order to design processes to control the overall crystalline material.

The work presented in this thesis is on the development of *in situ* analysis techniques during segmented flow crystallisation using powder X-ray diffraction and single crystal X-ray diffraction techniques. This work was carried out as part of a joint studentship with the University of Nottingham, and Diamond Light Source: the UK's national synchrotron. Synchrotron facilities offer high intensity light suitable for a range of analytical techniques including for *in situ* X-ray diffraction in complex sample environments, the focus of this research.

1.2 – Crystallisation Theory

Crystalline solids are the arrangement of atoms or molecules in a long range, periodic repeating pattern in three dimensions.[1] Molecules in a crystal are held together by strong intermolecular interactions, with hydrogen bonding having the strongest influence, with halogen bonding and π-stacking of cyclic molecules also in involved for some molecules.[2] Crystallisation is often used as a purification technique with the highly ordered nature of crystals enabling them to be highly effective at separation from non-similar molecular scale growth units.[3,4] Crystallisation is a key area of scientific interest, particularly in the pharmaceutical industry where the majority of pharmaceutical products contain crystalline material.

1.2.1 – Nucleation

The crystallisation process is underpinned by the initial kinetically controlled nucleation of crystals. Nucleation is defined as the process of forming clusters from a supersaturated homogeneous mother solution.[4] The initial stages of crystallisation from solution are key for the final crystal properties such as polymorphic form and crystal size distribution. For nucleation of crystals, there are various processes in which spontaneous nucleation can occur, shown in Figure 1.01; primary nucleation is where nucleation occurs in the absence of crystalline surfaces. This can be separated into two categories; homogeneous nucleation where spontaneous nucleation occurs in the absence of any foreign surfaces, and heterogeneous nucleation in the presence of foreign surfaces,

such as dust or the reactor walls.[5] Secondary nucleation is induced by the presence of already formed crystalline material in solution.

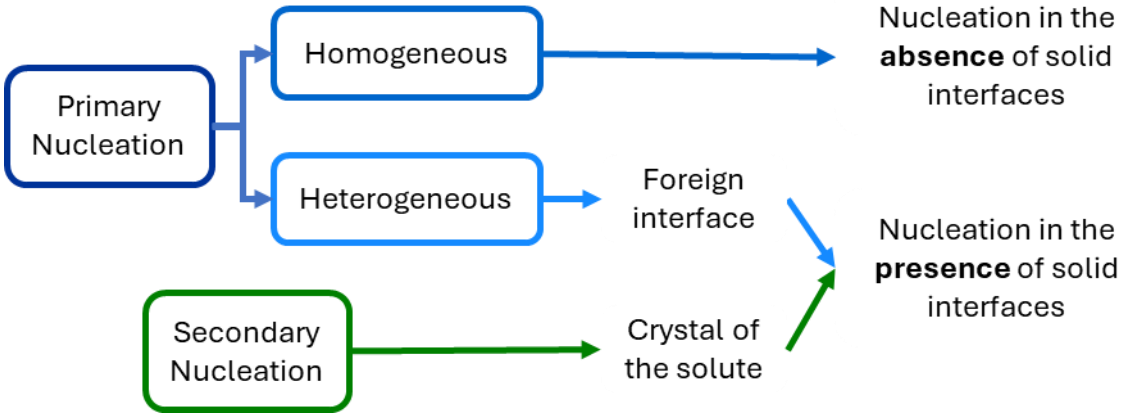

Figure 1.01: Diagram describing the difference classifications of nucleation, with primary spontaneous nucleation in the presence or absence of a foreign surface, and secondary nucleation induced by the presence of crystals. Figure adapted from [5].

The two main theories describing the nucleation process from solution are Classical Nucleation Theory (CNT) and Two-Step Nucleation Theory (TSN), shown in Figure 1.04. CNT is the most widely applied theory to describe the nucleation of small molecule materials. CNT proposes the formation of ordered clusters; small clusters may redissolve in solution, however, larger clusters above a critical size overcome the free energy barrier for the system to become favourable, resulting in formation of nuclei (Figure 1.02). CNT fails to account for observed crystal nucleation rate, often overestimating nucleation rate by several orders of magnitude.[6]

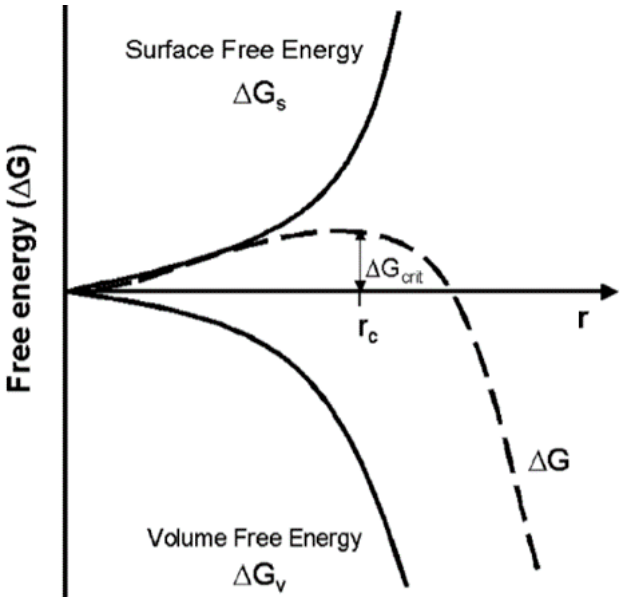

Figure 1.02: Free energy diagram for CNT with free energy change required for cluster formation, ΔG, as a sum of the ΔG(s) free energy change for the formation of a surface and ΔG(v) free energy change for phase transformation. Below the critical cluster size, r(c), the dissolution is favoured and above the energy barrier for nucleation, ΔG(crit), growth is energetically favoured. Figure taken from [7].

The TSN mechanism proposes the formation of an intermediate liquid-like, dense amorphous cluster, followed by the reorganisation into an ordered structure nuclei inside the droplet, beyond a certain critical size (Figure 1.03).

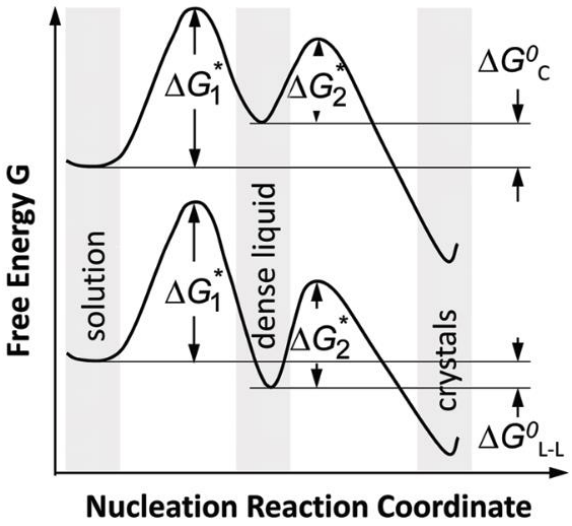

Figure 1.03: Free energy diagram for TSN with ΔG(1) the energy barrier for the formation of the dense-liquid cluster and ΔG(2*) the energy barrier for the formation of a crystalline nucleus in the dense-liquid cluster. The diagram shows two versions of the mechanism with the upper curve describing where the dense liquid is unstable and existing in a metastable state (ΔG(0c)). The lower curve describes a stable liquid-dense clusters compared to the solution (ΔG(0L-L)). Figure taken from [6].*

TSN was initially proposed for macromolecular protein crystallisation with strong experimental evidence for liquid-like clusters from the study of protein systems. However, experimental evidence for the TSN mechanism is limited for ionic or small molecule systems, with some exceptions.[6,8] It has been proposed that the lack of experimental evidence for the TSN in small molecule systems is due to the short lifetimes of the intermediate liquid-dense states that have not been detected.[7] However, the existence of stable, viscous oil phases that prevent nucleation are a well-known phenomenon in the pharmaceutical industry and may provide further evidence for the TSM mechanism.[6]

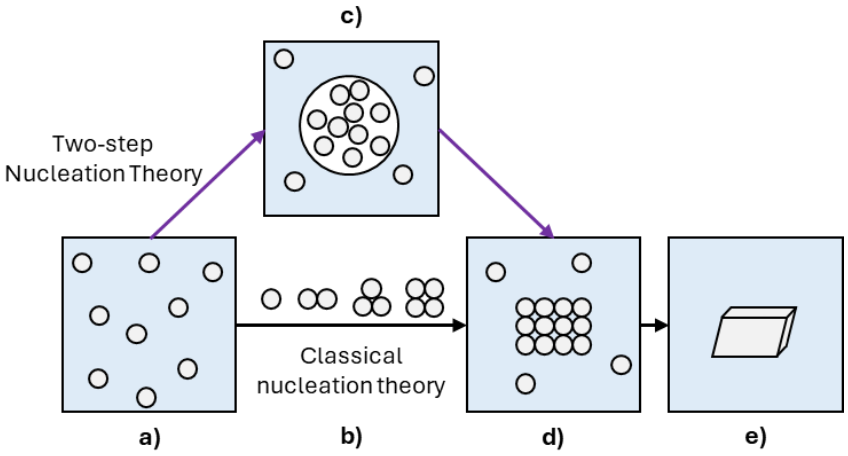

Figure 1.04: Pathways for proposed nucleation mechanisms starting with a) a supersaturated solution, b) CNT proposed ordered sub-critical clusters of solute molecules, c) TSN proposed dense, liquid-like cluster of solute molecules, d) ordered crystalline nuclei, and e) a solid crystal following crystal growth. Diagram adapted from [7].

1.2.2 – Supersaturation

The key factor for crystallisation of a system is the solubility of the solute in a given solvent; the equilibrium solubility is defined as the maximum quantity of solute dissolved at a given temperature. Saturation for a given compound is dependent on both temperature and solvent. As previously stated, nucleation is dependent on supersaturation of solution for spontaneous nucleation to occur; a system is supersaturated when the quantity of dissolved solute is greater than the equilibrium saturation. Conversely, a system is undersaturated when the dissolved solute is less than the equilibrium saturation, and any existing crystals will dissolve. A measure of supersaturation often used in discussing crystallisation is the supersaturation ratio, S; a ratio of the system saturation against the maximum solubility in the conditions present (Equation 1.01). Values >1 indicate supersaturation, with <1 indicating the solution is undersaturated at the current conditions.

Equation 1.01: Calculation of supersaturation ratio, S, using concentration of solution, c, and maximum solubility of solution at the temperature conditions present, c.*

$$S = \frac{c}{c^*}$$

When a critical level of supersaturation is achieved, the solution is “labile” and spontaneous nucleation occurs. Additionally, there are supersaturation conditions wherein the solution is above the equilibrium saturation and supersaturated but not labile, and nucleation does not occur, termed the metastable zone. Graphical depiction of the solubility curve, metastable zone, and metastable boundary shown in Figure 1.05. The interval between the equilibrium solubility and labile zones is termed the metastable zone width (MSZW). As nucleation is a kinetic process, the critical level required to achieve spontaneous nucleation is dependent on experimental factors, including the solid interfaces present such as reactor walls and impurities which lower the energy barrier for nucleation by providing a surface for heterogeneous nucleation. These experimental factors influence the metastable zone width (MSZW) and conditions where the solution is labile.

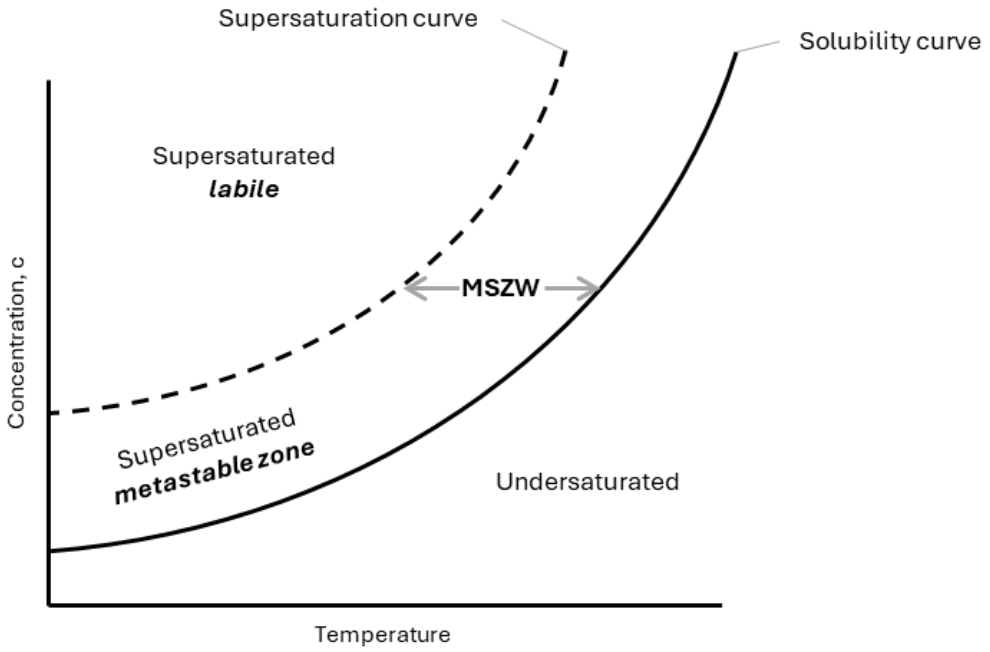

Figure 1.05: Solubility curve for a compound showing metastable boundary, MSZW, and labile regions. Figure adapted from [4].

1.2.3 – Crystal growth

Following nucleation, crystal growth occurs through the transport of solute molecules from the bulk solution via diffusion, migration of growth units to a site on the crystal growth face, and the shedding of solvent molecules from the growth site.[9] The crystal growth is dependent on the crystal structure, and other factors such as the supersaturation of solution, solvent and any impurities present. The difference in growth rates for different crystal faces determines the shape of the crystal particle, named the morphology or habit. Due to differences in crystal structure and preferential growth of crystal faces, different polymorphs can exhibit differences in morphology. Solvents can affect the crystal morphology through preferential adsorption of solvent molecules on specific growth faces, retarding face growth and changing the morphology.[10] Changing solvents may change the intermolecular interactions between crystal molecules and solvent on growth faces, changing face adsorption and therefore the crystal morphology. An example of this is isoniazid, a drug molecule which shows elongated needle-like morphologies grown from water, a plate habit grown in IPA, and a rod habit grown from ethyl acetate (Figure 1.06).[11]

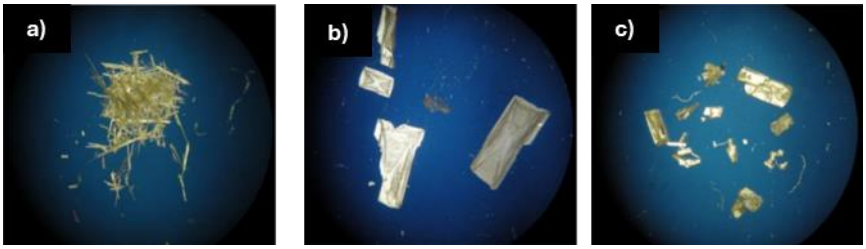

Figure 1.06: Isoniazid crystal grown during cooling crystallisation in a) water, b) IPA, and c) ethyl acetate.[11]

Crystal morphology is important as it affects the manufacturing properties, such as flowability, compressibility, and ease of filtration.[12,13] Deliberate addition of impurities, termed additives, can be used to modify the morphology with the same mechanism as the solvent effect, with interactions with growth faces; additive control has also been shown to inhibit crystal growth.[14–16]

1.2.4 – Polymorphism

Crystalline materials can exhibit multiple solid structures, including polymorphs, co-crystals, hydrates/solvates, and salts, shown in Figure 1.07. Polymorphs show differences in the arrangement of molecules or atoms in the crystal structure. Co-crystals, solvates, and salts are multi-component crystal forms; co-crystals involve the inclusion of one or more, often structurally similar molecule into the crystal structure. Solvates are the inclusion of the solvent molecule into the crystal structure, with hydrates a specific type of solvate with the inclusion of water in the structure. In salt crystal structures there is a proton exchange with the secondary molecule or atom to form ionic structures. Amorphous forms can also be produced that demonstrate no long range order.

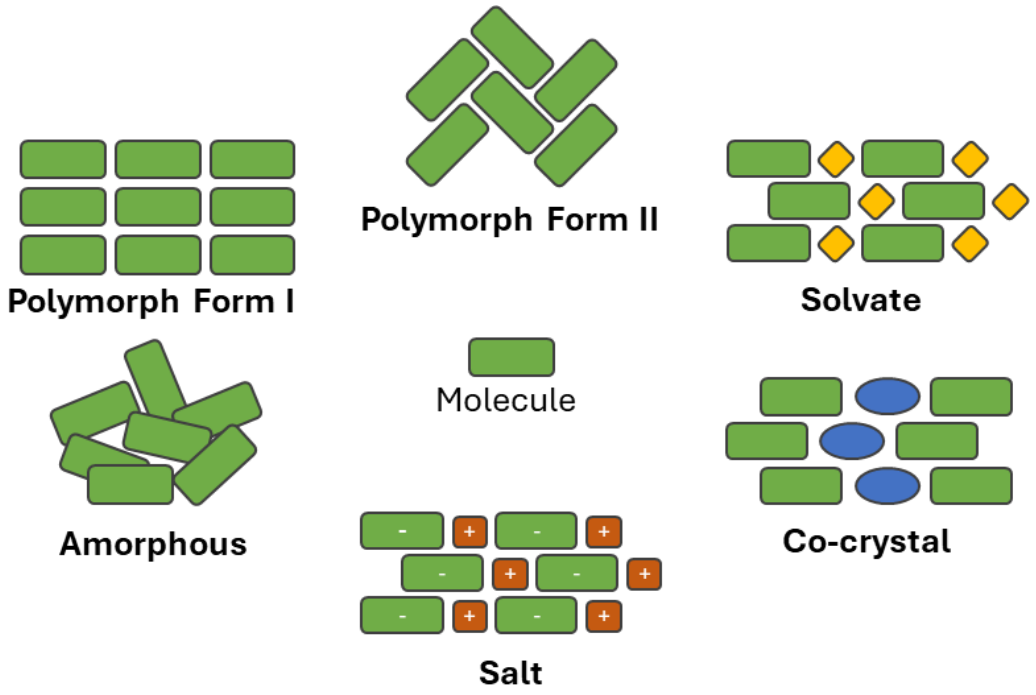

Figure 1.07: Representation of different crystal forms, including polymorphs, solvates, co-crystals, salts, and amorphous forms. Adapted from [17].

For polymorphs, the chemical structure remains unchanged, however, the crystal forms can demonstrate different physical properties, such as melting point, solubility, stability, and bioavailability.[18] Distinguishing between polymorphic forms can be achieved through various analytical techniques including X-ray diffraction (XRD), nuclear magnetic resonance, infrared and Raman spectroscopy, and other thermal analysis techniques such as differential scanning calorimetry and thermogravimetric analysis.[19]

The determination of relative stabilities of polymorphs depends on their free energies; the stable polymorph with the lowest free energy is termed the thermodynamic form.[20] Other polymorphic forms are deemed metastable. During crystallisation often metastable forms initially nucleate rather than the thermodynamically most stable, causing metastable polymorphic forms to be named the kinetic polymorph. This preferential formation of the less stable form is often followed by the crystallisation of more stable forms; this is termed the Ostwald rule of stages.[20]

Thermodynamically, polymorphs can be either monotropically or enantiotropically related. For enantiotropic systems, there is a reversible solid-solid transition that occurs below the melting point, where one form is thermodynamically stable at temperatures below a transition point, and the other polymorph is stable above the transition point.[19] For monotropic systems, the stable form remains thermodynamically stable at all temperatures up to the melting point. Depiction of the free energy plots for monotropic and enantiotropic systems shown below in Figure 1.08.

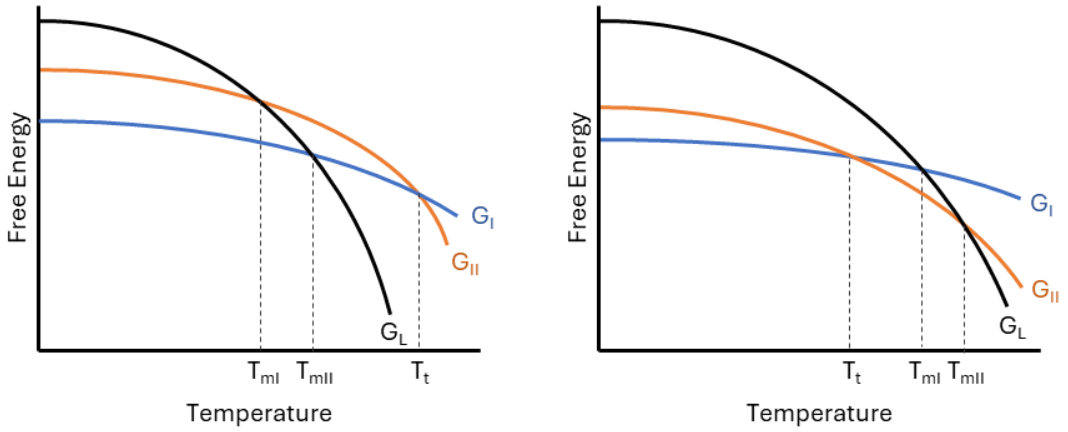

Figure 1.08: Gibbs free energy plots against temperature showing the transitions points for monotropic and enantiotropic polymorphic relationships, left and right respectively. Annotations show free energy, G_L for liquid phase, G_I for polymorphic Form I, G_{II} for Form II. Temperature annotations show T_t transition temperature and T(mI) and T(mII) for melting temperature for polymorphs. Adapted from [21,22].

For crystallisation from solution, enantiotropic polymorphs show an overlap in temperatures above and below the transition point where the different polymorphic forms can be crystallised, whereas monotropic polymorphs do not show an overlap in solubility curves, with the metastable showing higher solubility at all temperatures, shown in Figure 1.09.

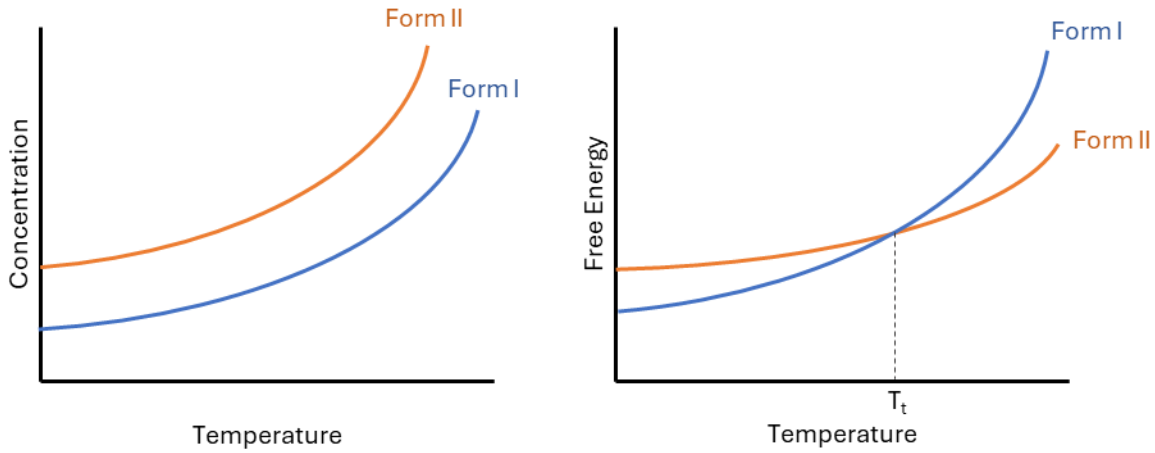

Figure 1.09: Solubility curves for monotropically related and enantiotropically related dimorphic systems, left and right respectively. Monomorphic solubility curves do not cross with the metastable Form II showing a higher solubility. Enantiotropic systems show an overlap of solubility curves with the temperature of transitions, T(t), determining the favoured polymorph. Adapted from [22].

If the relative stabilities of the polymorphic forms are similar in enantiotropic system, multiple polymorphic forms can be crystallised concomitantly.[23] Whilst thermodynamically there is no overlap of solubility curve for monotropic systems, given that nucleation is a kinetic process, there may be an overlap of metastable zones, allowing the concomitant crystal growth of monotropic forms.[22]

Polymorphs can undergo phase transition in solution, termed solvent mediated phase transition (SMPT); this involves the initial crystallisation of the kinetic, metastable polymorph, followed by the dissolution of the metastable form and growth of the stable phase.[24] For monotropic systems, if the metastable form initially nucleates it lowers the supersaturation where the stable form can then nucleate, further lowering the saturation to the point where the metastable form dissolves.[25] SMPT follows Ostwald's rule of stages where the metastable form initially nucleates and transforms to the stable form.

Co-crystal, salt, and solvate forms can exhibit polymorphism themselves, generating a vast potential crystal form landscape for a given system. The drug development process often involves rigorous experimental screenings to discover polymorphs, amorphous forms, and multi-component crystal forms.[26] Computational crystal structure prediction is a growing area of research, aiming to use computational techniques to focus the screening experiments for the discovery of polymorphs, co-crystal, and other crystal forms.[27,28] Computational techniques use energy landscape calculations to identify likely crystal forms, with other screening techniques using hydrogen bond propensity and molecular complementarity to identify potential multi-component crystal forms.[29] Metastable forms are often desired in the pharmaceutical industry due to the higher solubility and enhanced bioavailability compared to stable forms. However, the transformations during the crystallisation process pose difficulty in production of the metastable phase, and solid-solid transitions can cause issues with shelf-life and resulting dosage levels from decreased bioavailability of the stable form.[30] Identification of all possible polymorphs is crucial to

prevent “disappearing polymorph” scenarios where more stable, less bioavailable forms prevent the crystallisation of the drug formulation polymorph. A well-known case of a disappearing polymorph is the HIV drug Ritonavir, where after two years on the market, the crystal form in the drug formulation was unable to be produced; only the stable form with reduced solubility and bioavailability, leading to temporary withdrawal of Ritonavir from the market for reformulation.

1.3 – Crystallisation Techniques

Key characteristics of crystalline products such as overall crystal size, crystal size distribution (CSD), morphology, purity, and polymorphic form are determined by the nucleation and crystal growth stages. A high degree of nucleation leads to smaller overall particles, due to less material for crystal growth. Furthermore, high supersaturation and high levels of nucleation can lead to poorer rejection of impurities.[31] Minimising nucleation and maximising crystal growth can lead to small CSDs. Thus, crystallisation techniques aim to control supersaturation to govern these properties.

1.3.1 – Evaporative crystallisation

Evaporative crystallisation is a commonly used methodology in the screening for new crystal forms. Evaporative crystallisation is a non-steady state batch crystallisation technique that uses evaporation of the solvent to produce nucleation and crystal growth. A solution is kept at a constant temperature allowing evaporation of the solvent; the solvent evaporation causes an increase in saturation of the solution into the labile zone, shown in Figure 1.10. On nucleation, saturation decreases, but continual solvent evaporation increases saturation; this concentration fluctuation moves the solution between labile and metastable zones causing continual nucleation and crystallisation. The evaporative crystallisation process often results in large crystal size distributions due to nucleation and crystal growth occurring throughout the process; a large crystal size distribution is undesirable in the production of chemicals.[32]

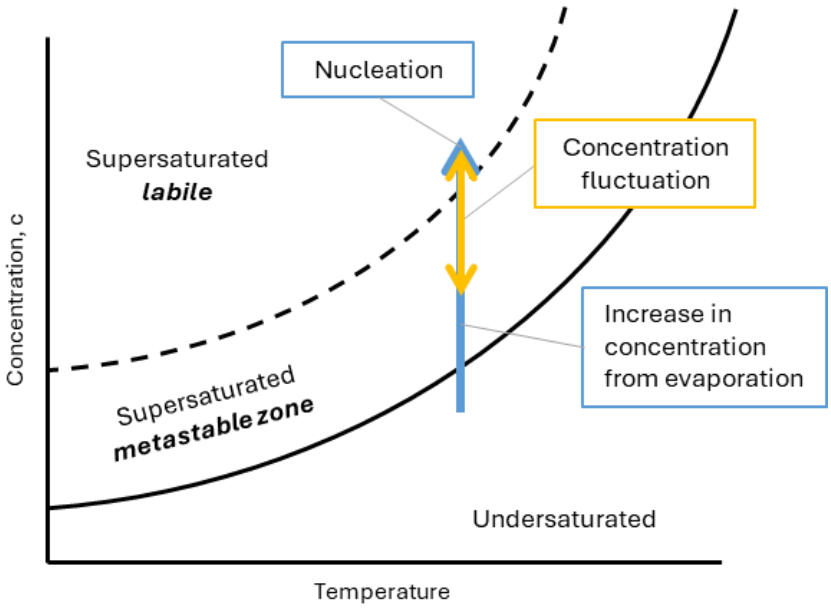

Figure 1.10: Solubility curve and metastable zone diagram depicting evaporative crystallisation; the system is held at a constant temperature, increasing the concentration until nucleation occurs in the labile zone; crystal growth occurs whilst the concentration fluctuations from further evaporation and nucleation cycles. Adapted from [18].

1.3.2 – Cooling crystallisation

Cooling crystallisation controls saturation of the system with temperature decrease to the supersaturated state, shown in Figure 1.11. Nucleation occurs in the labile zone, which decreases solution saturation into the metastable zone where crystal growth occurs. Optimised cooling crystallisation processes maintain supersaturation to within the metastable zone to prevent further nucleation events which ensures a narrow crystal size distribution.[33] Rate of cooling is a key factor in cooling crystallisation; a high rate of cooling can result in high supersaturation and levels of nucleation and crystal growth, impacting CSD and crystal size.

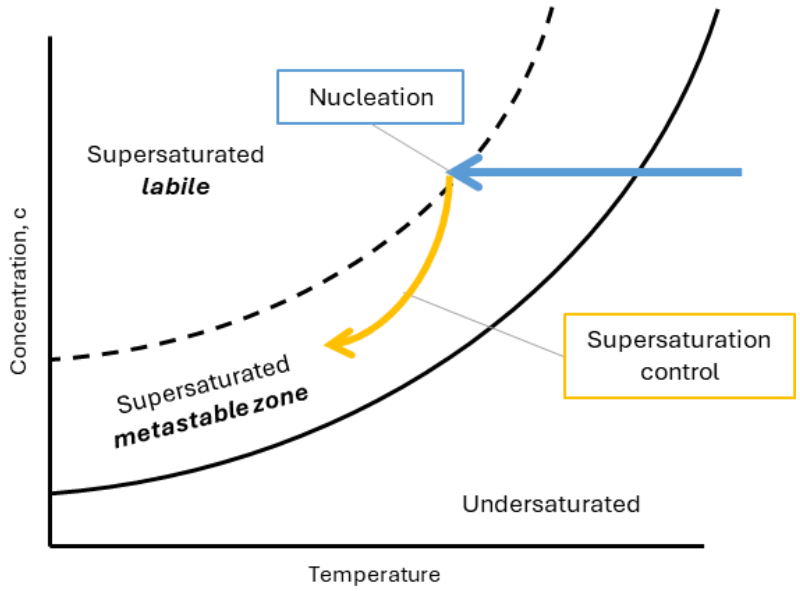

Figure 1.11: Solubility curve for cooling crystallisation; the system is cooled until nucleation occurs in the labile zone. Saturation decreases and crystal growth occurs in the metastable zone. Adapted from [34].

1.3.3 – Temperature cycling crystallisation

Temperature cycling crystallisation is a form of cooling crystallisation, with cooling of solution used to induce supersaturation and nucleation. Temperature cycling uses successive heating and cooling cycles to reduce the saturation to the undersaturated region and redissolve the fine particles, with cooling enabling crystal growth of the remaining particles, illustrated in Figure 1.12. Temperature cycling enables enhanced control over the crystallisation process for improved quality of the crystalline product in terms of crystal size, CSD, morphology and polymorphic form.[35]

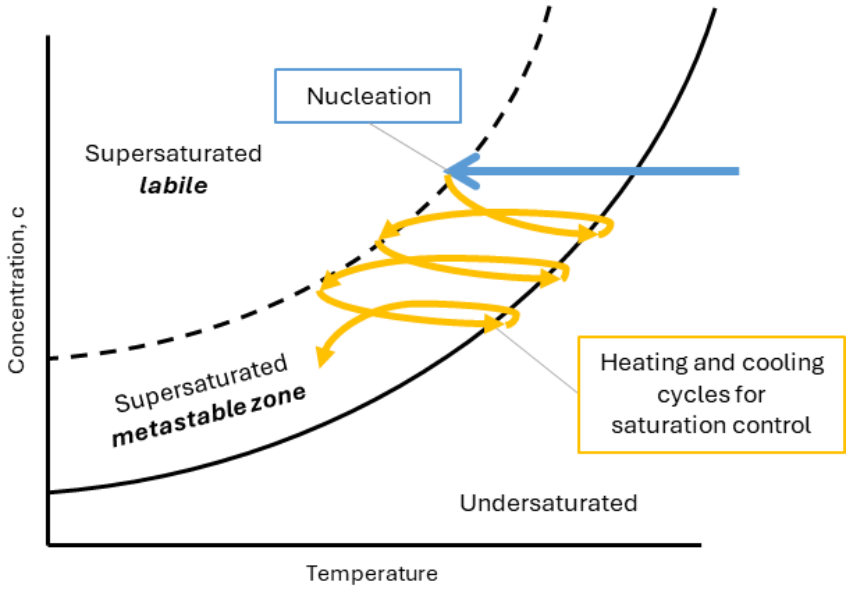

Figure 1.12: Solubility curve depicting temperature-cycling crystallisation with solution cooling to initiate nucleation; successive heating and cooling cycles enable enhanced control of dissolution, recrystallisation and crystal growth. Adapted from [36].

1.3.4 – Anti-solvent crystallisation

Anti-solvent crystallisation involves the addition of a solvent the solute is poorly soluble in, termed an anti-solvent. The addition of the anti-solvent to a saturated solution induces supersaturation, causing nucleation and crystal growth. The difference in solubility between the two solvents creates the supersaturation by lowering the overall solubility curve of the system, shown in Figure 1.13. With slow addition rates, the concentration may remain in the metastable zone during crystallisation for a growth dominated crystallisation process.[37] High addition rates cause a high degree of supersaturation for rapid nucleation and can cause a reduced crystal growth for smaller crystal sizes overall.

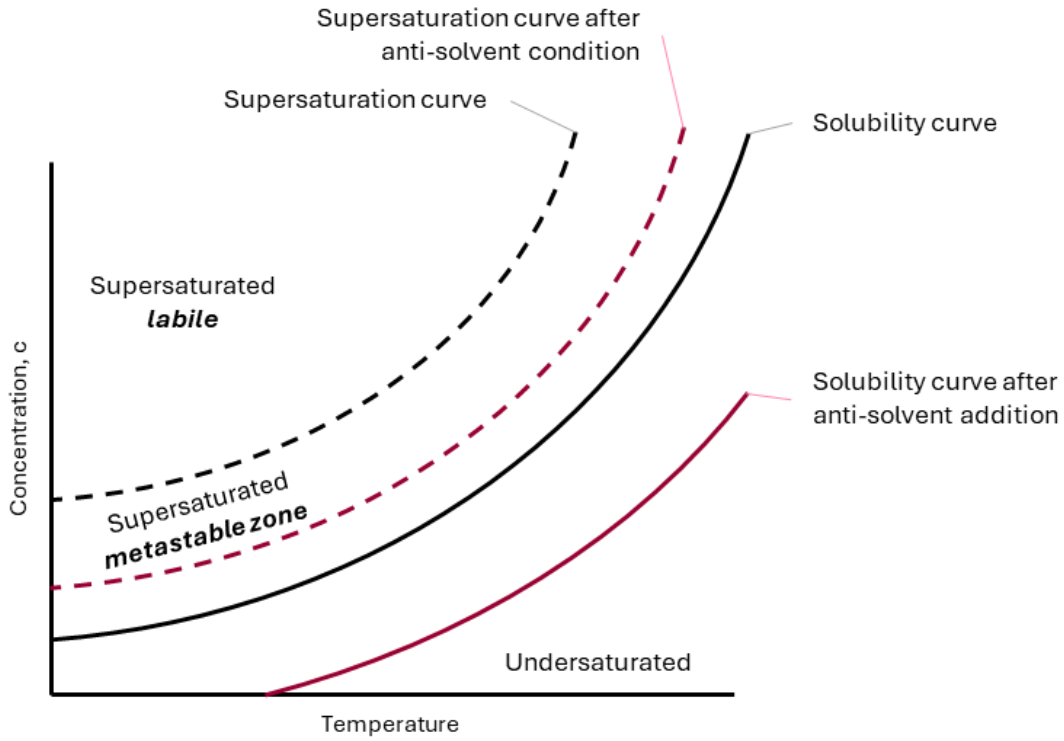

Figure 1.13: Solubility curve depicting the effect of anti-solvent addition for crystallisation; anti-solvent addition lowers the solubility of the system to create supersaturated labile conditions for crystal nucleation and growth.

1.3.5 – Slurrying crystallisation

Slurrying crystallisation involves the oversaturation of solution with excess solid material present in solution: if the metastable polymorph is present solvent-mediated phase transitions transform the metastable polymorph to the stable form. Slurrying crystallisation is often used to investigate the kinetics of transformation of a system in terms of induction times, and whether the system is controlled by growth of the stable polymorph, or dissolution of the metastable form.[38] Furthermore, slurrying crystallisation can be used to establish the relative stability for polymorphs and be used to conduct the for the screening of novel multi-component crystal forms.[39]

1.4 – Continuous Crystallisation

1.4.1 – Batch vs Continuous Crystallisation

Industrial manufacturing processes commonly use batch crystallisation for the production of crystalline products. Batch processes typically use jacketed Stirred Tank Reactors (STRs), with the jacketed temperature control of supersaturation and crystallisation. Scale-up can be challenging for batch crystallisation due to the difference in heat transfer to the bulk from lab scale to industrial scale crystallisers. Furthermore, stirring rate is a critical factor in STR batch crystallisation where it can be challenging to maintain homogeneous mixing, producing more localised areas of supersaturation than smaller scale processes, which influences nucleation and crystal growth.[40] With cooling rates determined by heat transfer from surface to volumes, and issues with bulk mixing in comparison to smaller systems, this can also lead to batch-to-batch variation of crystal product quality.

Continuous crystallisation involves the continual withdrawal of crystalline products, in comparison to batch conditions which removes the product only at the end of the crystallisation run. Generally, continuous processes show more efficient heat transfer to control crystallisation, reducing energy usage, and providing an increased control over the crystallisation process; this provides a greater control over the crystal purity, CSD, morphology, and polymorphic form for the crystalline product, whilst lacking the batch-to-batch variability.[41,42] Furthermore, continuous operation reduces downtime for reactor maintenance, reduces reactor space requirements. Continuous processes can be more easily scaled up, reducing the process development required from lab scale to industrial scale.

1.4.2 – Continuous Crystallisers

In continuous crystallisation, there are two main types of crystallisers, mixed-suspension mixed-product removal (MSMPR) crystallisers, and tubular crystallisers (Figure 1.14). MSMPR crystallisers (Figure 1.14a) are most similar to batch crystallisers with a single or cascade of STRs with a feed solution continuously pumped in whilst product slurry is continuously removed. MSMPRs are generally used in cooling or anti-solvent crystallisations with multi-stage MSMPRs have been shown to produce crystalline product with high yields and high purity.[43] For tubular flow crystallisation processes there are three main categories; plug flow crystallisers, oscillatory baffled crystallisers (OBCs), and segmented flow crystallisers (Figure 1.14b-d).

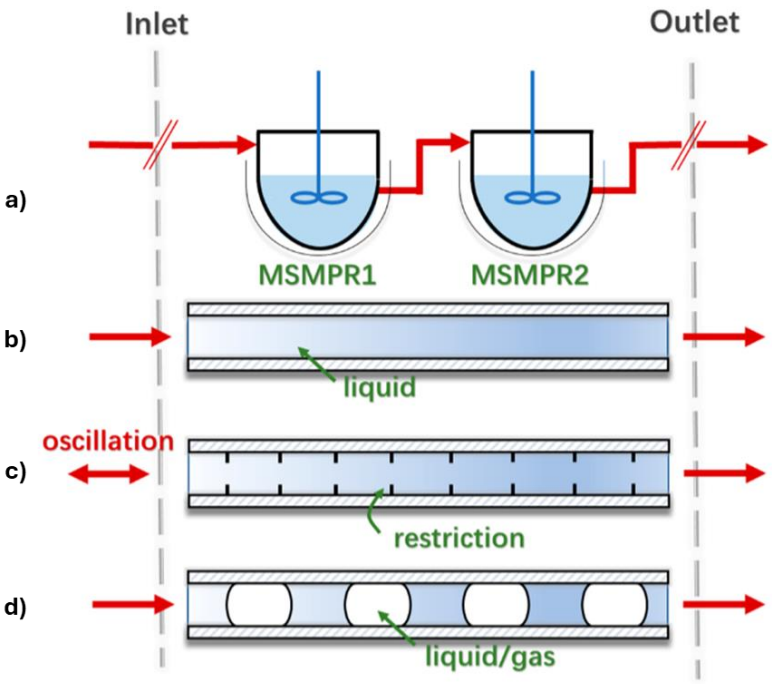

Figure 1.14: Schematic representation of a) MSMPR cascade, b) tubular plug flow crystalliser, c) oscillatory baffled crystalliser, and d) liquid-liquid or gas-liquid segmented flow crystalliser. Figure taken from [44].

Tubular crystallisers generally have a higher complexity compared to STR and MSMPR systems, and therefore higher maintenance costs, however benefit from improved efficiency and simple scale-up.[45] Mechanical mixing in MSMPRs is used to produce the uniform temperature and saturation required, whereas tubular flow crystallisers use techniques such as oscillation, segmentation, and design of tubing components to maximise mixing and avoid crystal fouling and blockages.[46] Thin tubing in tubular flow crystallisers have beneficial effects for heat transfer to solution, providing a greater control over the supersaturation, nucleation and crystal growth. Segmented flow crystallisers divide solution into discrete droplets, termed slugs, which function as microreactors: each slug provides mixing through recirculation and the segmentation prevents back-mixing of the solution, ensuring a consistent residence time for each slug during crystallisation. The lack of back-mixing and slugs with consistent volumes ensures the crystallising solution undergoes equivalent conditions and crystallisation time along the length of the crystalliser and can benefit the crystalline product with a narrower CSD. Segmentation can be achieved with an inert immiscible fluid, termed a carrier fluid, for liquid-liquid segmentation, or with gas for liquid-gas segmentation. Liquid-liquid segmentation is beneficial for preventing blockages; the carrier fluid preferentially wets the tubing walls to prevent encrustation on the walls of the reactor, to prevent blockages in the system. Tri-segmented flow with liquid-liquid-gas segmentation, illustrated below in Figure 1.15, uses the carrier fluid for blockage prevention, with the addition of air segmentation to provide a greater stability of the segments, ensuring no coalescing of slugs to maintain homogeneity.

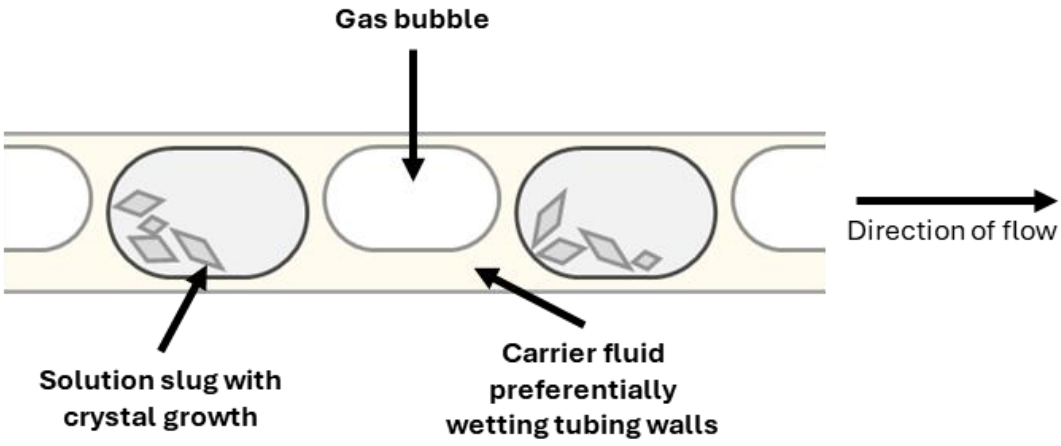

Figure 1.15: Diagram of tri-segmented flow crystallisation with solution slugs, carrier fluid removing solution from the reactor walls and gas segmentation to prevent back mixing.

A key benefit of flow crystallisation is the scope to combine manufacturing stages into one continuous pipeline, such as using flow chemistry stages for synthesis of a compound combined with flow crystallisation for purification and extraction. Some systems combine multiple continuous crystallisation stages, such as MSMPR with a tubular crystalliser, using MSMPR for production of crystal seeds of the desired polymorph, with a subsequent tubular crystalliser section for enhanced supersaturation control for crystal growth ensuring the growth of the desired polymorph.[47]

Flow crystallisation also has applications with small scale microreactor systems in academic research of crystallisation: microfluidic chips with inlaid channels are used to study crystallisation.[48] The microfluidic environment enables observation of crystal nucleation and growth to quantify nucleation, with a high throughput of experimental factors, such as temperature, supersaturation, solvent composition, and anti-solvent addition to name a few.[49,50] A microfluidic study by Bhamidi *et al.* investigated the effect of anti-solvent addition of glycine crystallisation; the study found that through a range of flow rates and anti-solvent concentrations that a higher concentration of IPA anti-solvent to the aqueous glycine flow resulted high supersaturations that favoured the crystallisation of the highly metastable β-glycine.[49]

Microfluidics also have application areas in screening experiments for the discovery of new crystal forms such as polymorph, co-crystals, and salts due to the emphasis of primary nucleation providing conditions to favour the discovery of new forms.[48,51–53] Thorson *et al.* found that an anti-solvent microfluidic chip platform enabled screening of the polymorphic form of indomethacin, using only small volumes (37 nL) to screen 48 unique conditions concurrently.[51] The system identified conditions with a range of solvents for the crystallisation of the stable polymorph, the metastable polymorph, and an amorphous form of indomethacin. Goyal *et al.* demonstrates that microfluidic chips provide a good environment for co-crystal discovery with a microfluidic evaporative crystallisation able to crystallise single crystals for further characterisation, whilst equivalent batch evaporative experiments resulted in microcrystalline or

agglomerates.[52] Furthermore, the microfluidic set up showed promise for anti-solvent screening of polymorphic forms able to identify different polymorphs and morphologies of a known model material whilst batch experiments were not able to distinguish the polymorphic forms.

Microfluidic systems are incompatible with larger solids (> nm), and the large volume reactors (MSMPRs and OBCs) are not feasible for investigating the crystallisation of novel materials in an academic laboratory due to the large volumes of solution required. The need for a mesoscale flow crystalliser capable of handling crystal sizes in the µm – cm range without the need for large volumes of solution (L/h) led to the development of the KRAIC series of segmented flow crystallisers by Robertson *et al*.[54] The KRAIC crystallisers are the basis for the research discussed in this thesis.

1.4.2.1 – KRAIC tri-segmented flow crystalliser

The KRAIC (Kinetically Regulated Automated Input Crystalliser) design is based on flow chemistry apparatus, with a 15 m length of 1/8" internal diameter (ID) FEP tubing for gradual room temperature cooling of hot crystallising solution in flow.[55] Flow crystallisation can suffer from issues with crystal encrustation and blockages; the KRAIC uses tri-segmented flow, shown above in Figure 1.15, with an inert perfluoropolyether carrier fluid, Galden HT135, which preferentially wets the FEP tubing to physically remove the crystallising solution from the reactor walls. Gas segmentation is used to prevent back-mixing to ensure each slug experiences equivalent conditions during crystallisation. The three fluids are immiscible, and segments are produced through combinations of mixer pieces, such as crosspieces, Y-pieces, and T-pieces, depending on the specific requirements of the system. The segmentation takes place in a "segmentation bath", a heated water bath on a hotplate with specially made tubing ports to maintain temperature control of solution pre-segmentation, segmentation bath shown in Figure 1.16b. The solution for the crystallisation is made and maintained at temperature in a stirred round bottom flask on a hotplate, with heated transfer tubes using jacketed tubing connected to a heated water circulator to prevent crystallisation prior to segmentation, shown in Figure 1.16a. A custom designed end piece (Figure 1.16c) recycles carrier fluid and uses neutral solvent flow, typically the chilled solvent used for crystallising solution, to help propel crystals to a vacuum funnel for crystal recovery. Vapourtec SF-10 peristaltic pumps are used to pump the feedstock: the mechanism in peristaltic pumps do not contact the solution to help prevent blockages. However, blockages have been found to occur within the pump tubing, thought to be due to the dwell time of solution in the unheated pump head.[56]

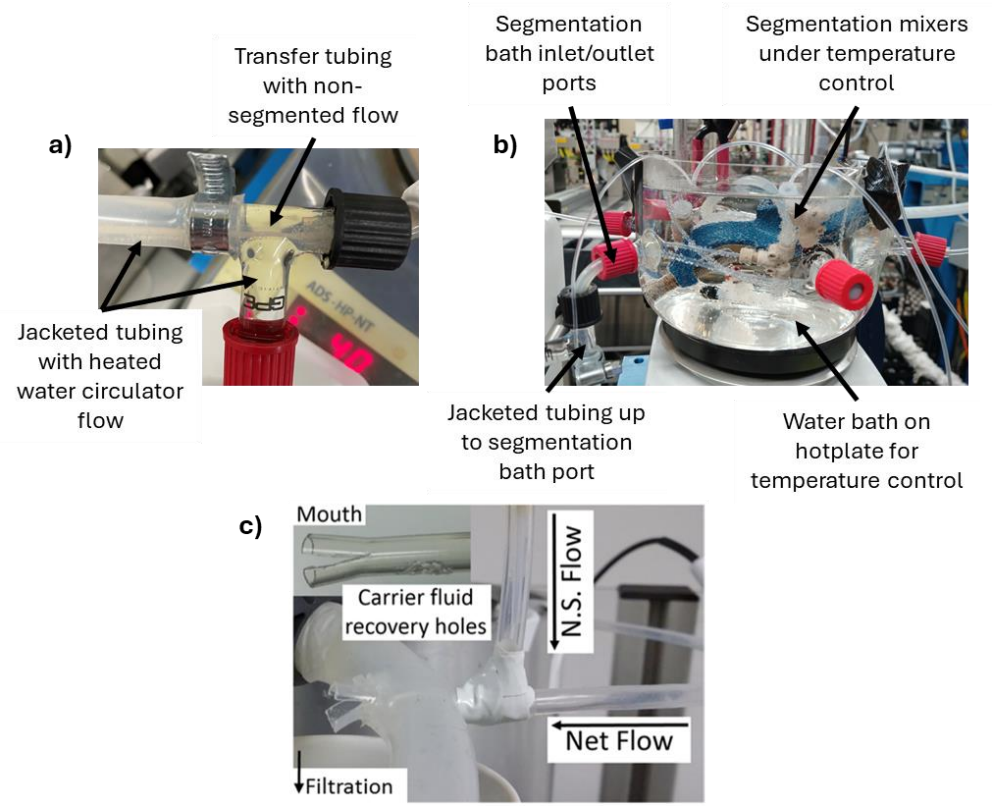

Figure 1.16: Key equipment features of the KRAIC system, with a) heated jacketed tubing pre-segmentation to maintain dissolution, b) heated segmentation bath to maintain dissolution temperature during the segmentation process, and c) endpiece for carrier fluid recovery and neutral solvent (N.S.) flow for crystal collection, taken from [54].

The original KRAIC system showed promise for bridging the gap between microfluidic studies and larger scale industrial continuous crystallisers, with the ability to run for hours with no encrustation.[54] The tri-segmented flow conditions present atypical crystallisation conditions in comparison to batch or other flow processes, with no solid surfaces present for nucleation and crystal growth. The lack of solid interface inhibits primary heterogeneous nucleation from the tubing walls; with only homogeneous nucleation, or heterogeneous nucleation from minor impurity particles and the liquid-liquid interface the only method for nucleation, the metastable zone width in the KRAIC effectively widens, with a larger metastable region but not labile in comparison to other crystallisation methods. Consequently, crystal polymorphic forms not typically seen in solution-based crystallisation have been shown to crystallise in KRAIC segmented flow crystallisation for pyrazinamide and succinic acid.[57,58] This led to the development of *in situ* analysis versions of the KRAIC system, the basis of the research discussed in this thesis.

1.5 – *In situ* analysis during crystallisation

In situ analysis is the direct examination of crystallisation; *in situ* technologies can be used for fundamental studies of nucleation and crystal growth, or for process monitoring to ensure crystal product quality. The main benefit of *in situ* analysis, as opposed to *ex situ* is that *in situ* provides information on the

crystallisation process itself and is not influenced by sample drying or preparation of the crystalline product for analysis.[59]

The first step to gain control of a crystallisation process in regard to the crystallisation of a desired polymorphic form, CSD, and morphology is through observing and understanding the crystallisation process. Process analytical technologies (PATs) are commonly used for the *in situ* study of crystallisation processes in the academic and industry laboratory setting for optimisation of a crystallisation process at the lab scale; PAT currently has applications in commercial manufacturing of pharmaceutical products also.[60] Common PAT methods study the CSD, morphology, particle counts, degree of agglomeration, and chemistry or structure of crystal forms.[61] Focused beam reflectance measurement (FBRM) probes are a commonly used PAT method, used for particle count measurement, nucleation monitoring, and chord length distribution measurement which is an indicator of CSD.[47,62] Inline image analysis probes or external camera systems are an alternative for the FBRM technique, allowing for direct observation of crystals for CSD monitoring, particle counts and morphological analysis for polymorphic identification.[63,64] An external camera system with dual vision, developed by Huo *et al.,* enabled the 3D recreation particle shape of a model L-glutamic acid: the system showed a prismatic morphology for the metastable α-form, and a needle like morphology for the stable β-form.[65] The 3D vision system was able to monitor the crystallisation of L-glutamic acid polymorphs through the identification of the polymorph habits and calculate the CSD for each dimension of the crystals during crystallisation. The computing of CSD, morphology identification and particle counts are currently limited by the computational power required for the complex calculations.

Attenuated Total Refection (ATR) Fourier Transform Infrared spectroscopy (FTIR) or ATR ultraviolet/visible light spectroscopy (UV/vis) probes can be used for accurate measurement of the solute concentration during crystallisation, for *in situ* measurement of supersaturation; together in conjunction with FBRM for nucleation monitoring this can be used for the calculation of the solubility curve and metastable zone width of a system.[44,66] A common technique for chemical and crystal form analysis with *in situ* analysis methods is Raman spectroscopy due to the accessibility of the technology and the ability to monitor polymorphic form.[44] Raman spectroscopy probes are often used in batch and continuous crystallisation processes for crystal form measurement and are often coupled with ATR-UV/vis for solution information for supersaturation and MSZW measurements.[67–69] Raman spectroscopy monitoring during a continuous single stage MSMPR crystallisation of carbamazepine by Acevedo *et al.* showed that production of the stable polymorph polymorphic purity was achieved after 6 residence times of the crystalliser, and was stable for the 4 more residence times of the system.[67]

For tubular flow processes, different lengths along the crystalliser corresponds to different crystallisation times, as such, different points along the crystallisation process can be observed and studied. However, the use of FBRM, imaging, ATR-IR, UV/vis, or Raman probes to investigate different points along

the crystallisation process in tubular crystallisation is challenging due the disruption it can cause to the flow processes, particularly in segmented flow, and issues with fouling of the intrusive probe with high slurry densities.[44] There are examples of probes being used for the study of in continuous crystallisation processes, by inserting the probe at various points in oscillatory baffled systems, or in an MSMPR-OBC system using probes in the MSMPR and at the outlet of the tubular flow.[47,70] The use of a FBRM probes in the MSMPR-OBC system by Gao *et al.* enabled optimisation of the MSMPR seed production process with finely tuned seeds to the desired size, polymorphic form, and density.[47] The following tubular crystallisation process then enabled the growth of the desired polymorphic form to a large crystal size and uniform size distribution compared to a single MSMPR crystallisation, highlighting the benefit of tubular crystallisation. To provide an alternative to PAT probes to eliminate interference or fouling of the probe, external imaging systems are providing a favourable alternative to FBRM probes for monitoring of CSD, morphology, and polymorphic transitions where morphology is related to polymorphic form.

For the investigation of segmented flow with Raman spectroscopy, Pallipurath *et al.* developed a non-invasive Raman spectroscopic analysis version of the KRAIC, named the KRAIC-R.[58] The results from the initial KRAIC paper showed the crystallisation of an unusual polymorph of succinic acid for solution-based techniques, α-SCA, as well as the typical β-SCA. The development of the KRAIC-R enabled the Raman characterisation of succinic acid crystallisation at two time-points of the crystallisation process.[54] The results of the KRAIC-R investigation achieved time-resolved *in situ* analysis showing the concomitant nucleation of α-SCA and β-SCA, with partial transformation of α-SCA to β-SCA over the course of the crystallisation.

X-ray diffraction (XRD) is one of the most powerful methods for *in situ* analysis of crystallisation given the ability of powder XRD (PXRD) to give distinctive peaks that represent the unique crystal structure for a given system and distinguish crystal forms. PXRD is a common technique for post-crystallisation analysis of the crystalline product for the ability to quantify the respective amounts in a mixture of crystal forms. However, PXRD for *in situ* analysis of crystallisation is mainly limited to synchrotron studies due to the high flux required to overcome the high background scattering present from sample container material or solution. The high frequency detectors at synchrotrons also enable the study of processes with short timescales, such as nucleation or polymorphic transitions.[71–75] To achieve PXRD analysis of polymorphic systems in segmented flow, Levenstein *et al.* developed the KRAIC-D (KRAIC for diffraction) in collaboration with Beamline I11, the high resolution PXRD beamline at Diamond Light Source, investigating the nucleation and growth pathways of concomitant.[59] The development of lab-source X-ray instrumentation has recently enabled the *in situ* study of crystallisation at lab-source facilities, such as Flow-Xl at the University of Leeds: a lab source X-ray facility for *in situ* PXRD of crystallisation in Flow.[75] Further information of XRD techniques, including synchrotron and lab source analysis is described in Chapter 2.

1.6 – Serial Crystallography

Serial crystallography is a technique typically used for the structural solution of proteins; proteins typically do not grow large crystals so require synchrotron radiation for the extraction of single crystal XRD (SCXRD) for structure solution.[76] However, the protein micro-crystals suffer from radiation damage and a full single crystal dataset cannot be collected. During serial crystallography data collection, partial datasets are collected from hundreds or, more often, thousands of crystals, usually from a continuous stream of crystal slurry in-beam. The resulting partial datasets are then merged and solved for structure solution of the proteins. There is an emerging need for serial crystallography for structure solution of small molecule chemical systems due to issues with radiation sensitivity, solvent loss, instability, or difficulty to grow large crystals, similar to protein systems.[74] Furthermore, the ongoing advances to fourth-generation synchrotron light sources will increase the brightness of the X-ray beam, likely increasing the occurrence of radiation sensitivity during SCXRD data collection.[77,78] Microfluidic systems are a common method for sample delivery of crystals for serial crystallography, for the ability to precisely control the flow environment for the throughput of crystal slurry and to co-locate the crystals and X-ray beam.[79–82] Segmented flow systems in microfluidics are also aiming to achieve time-resolved study of the crystallisation of protein compounds, with segmented flow beneficial for ensuring repeatable environments.[83]

Research by Dr Lois Wayment and Dr Karen Robertson in collaboration with Beamline I19, the small molecule single crystal diffraction beamline at Diamond Light Source, developed a version of the KRAIC system to investigate if a serial crystallography approach could be achieved with *in situ* SCXRD during crystallisation: the KRAIC-S.[56] This initial KRAIC-S study proved that serial crystallography is achievable in the segmented flow KRAIC system but requires further optimisation to improve structural solution.

1.7 – Research Aims and Objectives

The main aim of this research is the development of *in situ* XRD analysis techniques to study crystallisation processes through the enhancement of existing techniques for PXRD and SCXRD at Diamond Light Source. Furthermore, this research featured a collaboration with the University of Leeds for the development of a lab-source PXRD system at the Flow-Xl facility. The research discussed in this thesis has four main objectives:

1) The improvement of *in situ* PXRD studies through the integration of a temperature cycling segmented flow crystalliser, the KRAIC-T, into Beamline I11. Chapter 5 details the commissioning of the KRAIC-T, through investigation of the effects of temperature cycling on succinic acid crystallisation. The integration of the temperature controlled KRAIC-T aimed to enhance the study of concomitant polymorphic systems during crystallisation through the adaption of a slug triggering data

acquisition from previous KRAIC-S studies. The new data acquisition technique aims to improve the data quality, quantity, and efficiency of *in situ* PXRD studies. The efficacy of the slug triggering adaption is studied through the temperature cycling slurrying crystallisation of a polymorphic material, *ortho*-aminobenzoic acid, during beamtime on Beamline I11.

2) The design and development of a lab-source *in situ* PXRD system for the study of the polymorphic landscape during segmented flow crystallisation (Chapter 4). This research was a collaboration with the Flow-Xl facility, University of Leeds, to develop a lab-source *in situ* PXRD KRAIC system (the KRAIC-Xl). This work investigated if the larger scale KRAIC system could achieve diffraction from a lab-source system where background scattering might limit the detection of diffraction signal. Study of the anti-solvent crystallisation of the polymorphic compounds, L-glutamic acid and glycine were used as the proof-of-principle for the KRAIC-Xl. The research aims to widen the accessibility of X-ray *in situ* techniques from purely a synchrotron-based methodology to be more widely available with lab-source systems.

3) The improvement of data processing techniques for *in situ* PXRD for the segmented flow systems. Data processing for *in situ* PXRD experiments with complex sample environments can be time-consuming and are not able to provide real-time data during limited beamtime. Chapter 3 discusses the development of flexible Python-based data processing workflows with minimal computational processing time for the maximum extraction of diffraction signal from segmented flow environments at Beamline I11 and the Flow-Xl facility. The rapid processing aims to allow researchers to process data during crucial beamtime to feedback into their experiments to maximise data quality and results collected.

4) To expand capabilities for *in situ* SCXRD studies at Beamline I19 through the optimisation of apparatus to enable further studies during crystallisation. The KRAIC-S system required further optimisation and a greater understanding of the parameters for serial crystallography in the system. Chapter 6 discusses the progression of the KRAIC-S design for enhanced ease-of-use of the system, tested through the cooling crystallisation of paracetamol. The optimised KRAIC-S crystalliser was then used for the study of the non-photochemical laser nucleation phenomenon through experiments with potassium chloride, discussed in Chapter 7.

1.8 – References

1. Myerson, A. S. & Ginde, R. Chapter 2. Crystals, Crystal Growth, and Nucleation. in *Handbook of Industrial Crystallization* 33–66 (2002).
2. Aakeröy, C. B., Champness, N. R. & Janiak, C. Recent advances in crystal engineering. *CrystEngComm* **12**, 22–43 (2009).
3. Schwartz, A. M. & Myerson, A. S. Chapter 1. Solutions and Solution Properties. in *Handbook of Industrial Crystallization* (ed. Myerson, A. S.) 1–32 (Elsevier Science & Technology, 2002).
4. Davey, R. & Garside, J. *From Molecules to Crystallizers*. (Oxford University Press, 2000).
5. Beckmann, W. Chapter 2. Mechanisms of Crystallization. in *Crystallization: Basic Concepts and Industrial Applications* (ed. Beckmann, W.) 7–34 (2013).
6. Vekilov, P. G. Nucleation. *Cryst Growth Des* **10**, 5007–5019 (2010).
7. Erdemir, D., Lee, A. Y. & Myerson, A. S. Nucleation of crystals from solution: Classical and two-step models. *Acc Chem Res* **42**, 621–629 (2009).
8. Gebauer, D., Völkel, A. & Cölfen, H. Stable Prenucleation Calcium Carbonate Clusters. *Science (1979)* **322**, 1819–1822 (2008).
9. Sangwal, K. Chapter 3. Kinetics and Mechanism of Crystallization. in *Nucleation and Crystal Growth: Metastability of Solutions and Melts* 105–144 (John Wiley & Sons, Inc, 2018).
10. Berkovitch-Yellin, Z. Toward an ab Initio Derivation of Crystal Morphology. *J. Am. Chem. Soc* **107**, 8239–8253 (1985).
11. Payne, P. Control of solid form and particle morphology using additives and crystallisation conditions. (University of Bath, 2020).
12. Pudasaini, N. *et al.* Downstream Processability of Crystal Habit-Modified Active Pharmaceutical Ingredient. *Org Process Res Dev* **21**, 571–577 (2017).
13. Lovette, M. A. & Doherty, M. F. Needle-Shaped Crystals: Causality and Solvent Selection Guidance Based on Periodic Bond Chains. *Cryst Growth Des* **13**, 3341–3352 (2013).
14. Thompson, C., Davies, M. C., Roberts, C. J., Tendler, S. J. B. & Wilkinson, M. J. The effects of additives on the growth and morphology of paracetamol (acetaminophen) crystals. *Int J Pharm* **280**, 137–150 (2004).
15. Xie, S., Poornachary, S. K., Shan Chow, P. & H Tan, R. B. Direct Precipitation of Micron-Size Salbutamol Sulfate: New Insights into the Action of Surfactants and Polymeric Additives. *Cryst Growth Des* **10**, 3363–3371 (2010).

16. Berkovitch-Yellin, Z. *et al.* Crystal Morphology Engineering by 'Tailor-Made' Inhibitors: A New Probe to Fine Intermolecular Interactions. *J. Am. Chem. Soc* **107**, 3111–3122 (1985).

17. Sharma, A., Mishra, R. & Tandon, P. Polymorphism in Pharmaceutical Compounds. *Conference: Advancements and FuturisticTrends in Material Science* (2011).

18. Beckmann, W. Seeding the Desired Polymorph: Background, Possibilities, Limitations, and Case Studies. *Org Process Res Dev* **4**, 372–383 (2000).

19. Tung, H.-H., Paul, E. L., Midler, M. & McCauley, J. A. Chapter 3. Polymorphism. in *Crystallization of Organic Compounds: An Industrial Perspective* 49–76 (John Wiley & Sons, Inc, 2009).

20. Sangwal, K. Chapter 4. Phase Transformation and Isothermal Crystallization Kinetics. in *Nucleation and Crystal Growth: Metastability of Solutions and Melts* 145–188 (John Wiley & Sons, Inc, 2018).

21. Mao, C., Pinal, R. & Morris, K. R. A quantitative model to evaluate solubility relationship of polymorphs from their thermal properties. *Pharm Res* **22**, 1149–1157 (2005).

22. Reutzel-Edens, S. M. Achieving polymorph selectivity in the crystallization of pharmaceutical solids: Basic considerations and recent advances. *Curr Opin Drug Discov Devel* **9**, 806–815 (2006).

23. Bernstein, J., Davey, R. J. & Henck, J.-O. Concomitant Polymorphs. *Angew. Chem. Int. Ed.* **38**, 3440–3461 (1999).

24. Cardew, P. T. & Davey, R. J. The kinetics of solvent-mediated phase transformations. *Proc. R. Soc. Lond. A* **398**, 415–428 (1985).

25. Takiyama, H. Supersaturation operation for quality control of crystalline particles in solution crystallization. *Advanced Powder Technology* vol. 23 273–278 Preprint at https://doi.org/10.1016/j.apt.2012.04.009 (2012).

26. Newman, A. Specialized Solid Form Screening Techniques. *Org. Process Res. Dev* 457–471 (2013) doi:10.1021/op300241f.

27. Day, G. M. *et al.* Significant progress in predicting the crystal structures of small organic molecules - A report on the fourth blind test. *Acta Crystallogr B* **65**, 107–125 (2009).

28. Habgood, M., Sugden, I. J., Kazantsev, A. V., Adjiman, C. S. & Pantelides, C. C. Efficient handling of molecular flexibility in ab initio generation of crystal structures. *J Chem Theory Comput* **11**, 1957–1969 (2015).

29. Sarkar, N., Gonnella, N. C., Krawiec, M., Xin, D. & Aakeröy, C. B. Evaluating the Predictive Abilities of Protocols Based on Hydrogen-Bond Propensity, Molecular Complementarity, and Hydrogen-Bond Energy for Cocrystal Screening. *Cryst. Growth Des.* **20**, 7320–7327 (2020).

30. Sangwal, K. Chapter 8. Ostwald Ripening, Crystal Size Distribution, and Polymorph Selection. in *Nucleation and Crystal Growth: Metastability of Solutions and Melts* 361–422 (John Wiley & Sons, Inc, 2018).

31. Tung, H.-H. Industrial perspectives of pharmaceutical crystallization. *Org Process Res Dev* **17**, 445–454 (2013).

32. Tung, H.-H., Paul, E. L., Midler, M. & McCauley, J. A. Chapter 8. Evaporative Crystallization. in *Crystallization of Organic Compounds: An Industrial Perspective* 167–178 (John Wiley & Sons, Inc, 2009).

33. Tung, H.-H., Paul, E. L., Midler, M. & McCauley, J. A. Chapter 7. Cooling Crystallization. in *Crystallization of Organic Compounds: An Industrial Perspective* 137–166 (John Wiley & Sons, Inc, 2009).

34. Lawton, S. *et al.* Continuous crystallization of pharmaceuticals using a continuous oscillatory baffled crystallizer. *Org Process Res Dev* **13**, 1357–1363 (2009).

35. Wu, Z., Yang, S. & Wu, W. Application of temperature cycling for crystal quality control during crystallization. *CrystEngComm* **18**, 2222–2238 (2016).

36. Bakar, M. R. A., Nagy, Z. K. & Rielly, C. D. Seeded batch cooling crystallization with temperature cycling for the control of size uniformity and polymorphic purity of sulfathiazole crystals. *Org Process Res Dev* **13**, 1343–1356 (2009).

37. Tung, H.-H., Paul, E. L., Midler, M. & McCauley, J. A. Chapter 9. Antisolvent Crystallization. in *Crystallization of Organic Compounds: An Industrial Perspective* 179–205 (John Wiley & Sons, Inc, 2009).

38. O'Mahony, M. A., Maher, A., Croker, D. M., Rasmuson, Å. C. & Hodnett, B. K. Examining solution and solid state composition for the solution-mediated polymorphic transformation of carbamazepine and piracetam. *Cryst Growth Des* **12**, 1925–1932 (2012).

39. Ter Horst, J. H. & Cains, P. W. Co-crystal polymorphs from a solvent-mediated transformation. *Cryst Growth Des* **8**, 2537–2542 (2008).

40. Wieckhusen, D. Chapter 10. Development of Batch Crystallizations. in *Crystallization: Basic Concepts and Industrial Applications* (ed. Beckmann, W.) 187–202 (2013).

41. McGlone, T. *et al.* Oscillatory Flow Reactors (OFRs) for Continuous Manufacturing and Crystallization. *Org Process Res Dev* **19**, 1186–1202 (2015).

42. Chen, J., Sarma, B., Evans, J. M. B. & Myerson, A. S. Pharmaceutical crystallization. *Cryst Growth Des* **11**, 887–895 (2011).

43. Jiang, M. & Braatz, R. D. Designs of continuous-flow pharmaceutical crystallizers: developments and practice. *CrystEngComm* **21**, 3551 (2019).

44. Ma, Y. *et al.* Recent Progress in Continuous Crystallization of Pharmaceutical Products: Precise Preparation and Control. *Org. Process Re. Dev.* **24**, 1785–1801 (2020).

45. Zhang, D., Xu, S., Du, S., Wang, J. & Gong, J. Progress of Pharmaceutical Continuous Crystallization. *Engineering* **3**, 354–364 (2017).

46. Porta, R., Benaglia, M. & Puglisi, A. Flow Chemistry: Recent Developments in the Synthesis of Pharmaceutical Products. *Org Process Res Dev* **20**, 2–25 (2016).

47. Gao, Z., Wu, Y., Gong, J., Wang, J. & Rohani, S. Continuous crystallization of α-form L-glutamic acid in an MSMPR-Tubular crystallizer system. *J Cryst Growth* **507**, 344–351 (2019).

48. Shi, H. H. *et al.* Progress of crystallization in microfluidic devices. *Lab on a Chip* vol. 17 2167–2185 (2017).

49. Bhamidi, V. *et al.* Antisolvent Crystallization and Polymorph Screening of Glycine in Microfluidic Channels Using Hydrodynamic Focusing. *Cryst Growth Des* **15**, 3299–3306 (2015).

50. Shim, J. U. *et al.* Control and measurement of the phase behavior of aqueous solutions using microfluidics. *J Am Chem Soc* **129**, 8825–8835 (2007).

51. Thorson, M. R., Goyal, S., Gong, Y., Zhang, G. G. Z. & Kenis, P. J. A. Microfluidic approach to polymorph screening through antisolvent crystallization. *CrystEngComm* **14**, 2404–2412 (2012).

52. Goyal, S. *et al.* Solvent compatible microfluidic platforms for pharmaceutical solid form screening. *RSC Adv* **6**, 13286–13296 (2016).

53. Goyal, S. *et al.* A microfluidic platform for evaporation-based salt screening of pharmaceutical parent compounds. *Lab Chip* **13**, 1708–1723 (2013).

54. Robertson, K., Flandrin, P.-B., Klapwijk, A. R. & Wilson, C. C. Design and Evaluation of a Mesoscale Segmented Flow Reactor (KRAIC). *Cryst. Growth Des.* **16**, 4759–4764 (2016).

55. Plutschack, M. B., Pieber, B., Gilmore, K. & Seeberger, P. H. The Hitchhiker's Guide to Flow Chemistry. *Chem. Rev.* **117**, 11796–11893 (2017).

56. Wayment, L. E. Continuous flow for materials synthesis, assembly and crystallisation at Diamond: discovery and delivery of high value materials. (University of Bath, Bath, 2020).

57. Scott, C. D. *et al.* Integrated plug flow synthesis and crystallisation of pyrazinamide. *React. Chem. Eng.* **3**, 631–634 (2018).

58. Pallipurath, A. R., Flandrin, P.-B., Wayment, L. E., Wilson, C. C. & Robertson, K. In situ non-invasive Raman spectroscopic characterisation of succinic acid polymorphism during segmented flow crystallisation. *Mol. Syst. Des. Eng* **5**, 294–303 (2020).

59. Levenstein, M. A. *et al.* Dynamic Crystallization Pathways of Polymorphic Pharmaceuticals Revealed in Segmented Flow with Inline Powder X-ray Diffraction. *Anal. Chem.* **92**, 7754–7761 (2020).

60. Simon, L. L. *et al.* Assessment of recent process analytical technology (PAT) trends: A multiauthor review. *Org Process Res Dev* **19**, 3–62 (2015).

61. Ulrich, J. & Frohberg, P. Problems, potentials and future of industrial crystallization. *Front Chem Sci Eng* **7**, 1–8 (2013).

62. Acevedo, D. *et al.* Evaluation of focused beam reflectance measurement (FBRM) for monitoring and predicting the crystal size of carbamazepine in crystallization processes. *CrystEngComm* **23**, 972–985 (2021).

63. Galata, D. L. *et al.* Applications of machine vision in pharmaceutical technology: A review. *European Journal of Pharmaceutical Sciences* **159**, 105717 (2021).

64. Gao, Z. *et al.* Image Analysis for In-line Measurement of Multidimensional Size, Shape, and Polymorphic Transformation of L-Glutamic Acid Using Deep Learning-Based Image Segmentation and Classification. *Cryst. Growth Des* **18**, 4275–4281 (2018).

65. Huo, Y. *et al.* In Situ Measurement of 3D Crystal Size Distribution by Double-View Image Analysis with Case Study on L-Glutamic Acid Crystallization. *Ind. Eng. Chem. Res.* **59**, 4646–4658 (2020).

66. Dunuwila, D. D. & Berglund, K. A. ATR FTIR spectroscopy for in situ measurement of supersaturation. *J Cryst Growth* **179**, 185–193 (1997).

67. Acevedo, D. *et al.* Raman Spectroscopy for Monitoring the Continuous Crystallization of Carbamazepine. *Org. Process Res. Dev.* **22**, 156–165 (2018).

68. Tacsi, K. *et al.* Polymorphic Concentration Control for Crystallization Using Raman and Attenuated Total Reflectance Ultraviolet Visible Spectroscopy. *Cryst. Growth Des.* **20**, 73–86 (2020).

69. Lin, M., Wu, Y. & Rohani, S. Simultaneous Measurement of Solution Concentration and Slurry Density by Raman Spectroscopy with Artificial Neural Network. *Cryst. Growth Des* **20**, 1752–1759 (2020).

70. Kacker, R., Maaß, S., Emmerich, J. & Kramer, H. Application of inline imaging for monitoring crystallization process in a continuous oscillatory baffled crystallizer. *AIChE Journal* **64**, 2450–2461 (2018).

71. Nguyen, T. Y., Roessler, E. A., Rademann, K. & Emmerling, F. Control of organic polymorph formation: Crystallization pathways in acoustically levitated droplets. *Z Kristallogr Cryst Mater* **232**, 15–24 (2017).

72. Gnutzmann, T., Nguyen Thi, Y., Rademann, K. & Emmerling, F. Solvent-triggered crystallization of polymorphs studied in situ. *Cryst Growth Des* **14**, 6445–6450 (2014).

73. Levenstein, M. A. *et al.* Evaluation of microflow configurations for scale inhibition and serial X-ray diffraction analysis of crystallization processes. *Lab Chip* **20**, 2954–2964 (2020).

74. Schriber, E. A. *et al.* Chemical crystallography by serial femtosecond X-ray diffraction. *Nature* **601**, 360–365 (2022).

75. Turner, T. D. *et al.* Flow-Xl: a new facility for the analysis of crystallization in flow systems. *J. Appl. Cryst* 57 (2024) doi:10.1107/S1600576724006113.

76. Zhao, F. Z. *et al.* A guide to sample delivery systems for serial crystallography. *FEBS Journal* **286**, 4402–4417 (2019).

77. Christensen, J. *et al.* Radiation damage in small-molecule crystallography: Fact not fiction. *IUCrJ* **6**, 703–713 (2019).

78. Chapman, H. N. Fourth-generation light sources. *IUCrJ* vol. 10 246–247 Preprint at https://doi.org/10.1107/S2052252523003585 (2023).

79. Beyerlein, K. R. *et al.* Mix-and-diffuse serial synchrotron crystallography. *IUCrJ* **4**, 769–777 (2017).

80. Calvey, G. D., Katz, A. M. & Pollack, L. Microfluidic Mixing Injector Holder Enables Routine Structural Enzymology Measurements with Mix-and-Inject Serial Crystallography Using X-ray Free Electron Lasers. *Anal Chem* **91**, 7139–7144 (2019).

81. Pinker, F. *et al.* ChipX: A novel microfluidic chip for counter-diffusion crystallization of biomolecules and in situ crystal analysis at room temperature. *Cryst Growth Des* **13**, 3333–3340 (2013).

82. Stellato, F. *et al.* Room-temperature macromolecular serial crystallography using synchrotron radiation. *IUCrJ* **1**, 204–212 (2014).

83. Stubbs, J. *et al.* Droplet microfluidics for time-resolved serial crystallography. *IUCrJ* **11**, 237–248 (2024).

Chapter 2 – X-ray Techniques

2.1 – X-ray Crystallography

Crystallography is the study of crystal structure, with small-molecule crystallography the identification and structural confirmation of organic, inorganic, and organometallic systems with molecular sizes of a few atoms to several hundred.[1] Macromolecular crystallography is the structural study of large biological structures and proteins. This chapter discusses X-ray crystallographic theory and methods at lab-source and synchrotron X-ray sources. This chapter provides an overview of the concepts in crystallography and diffraction relevant to the work presented in this thesis.

2.1.1 – The Unit Cell

A crystalline solid is made from the regular arrangement of atoms or molecules repeated in three dimensions to form a highly ordered structure. The unit cell is the simplest repeating unit in a crystal lattice, defined by single points in space known as lattice points, unit cell is shown below in Figure 2.01i.[2] The shape and size of the unit cell is defined by the unit cell parameters: the a, b, c axes and α, β, γ angles between them. The lattice points give rise to lattice planes that intersect the lattice periodically and can be described by Miller Indices: Miller indices (hkl) are reciprocals of the fractional intercepts the planes make with the crystallographic axes, shown in Figure 2.01ii.

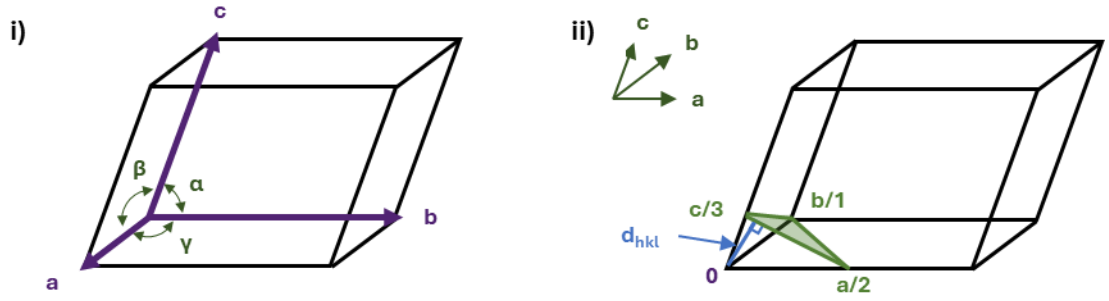

Figure 2.01: i) Representation of the unit cell and unit cell parameters, and ii) unit cell will plane described by 2 1 3 hkl Miller Indices, with d(213) plane spacing, adapted from [3].

There are four lattice types that exist for three-dimensional structures, shown below in Figure 2.02. The different structures are defined by the location of the lattice points in the unit cell: primitive (P) with the simplest arrangement of lattice points, body-centred (I), centred (C), and face-centred (F).

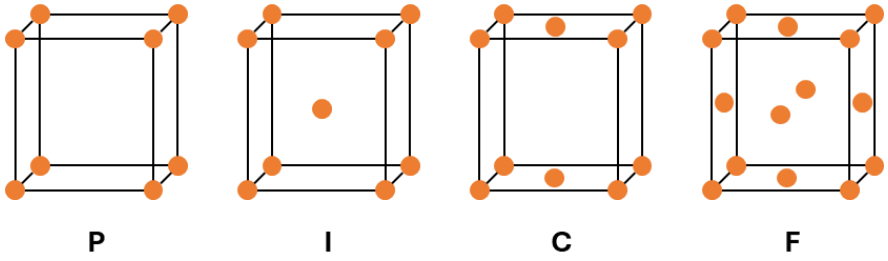

Figure 2.02: Diagram of the four lattice types with different lattice point locations. Adapted from [3].

All possible symmetries for the unit cell result in seven possible lattice shapes, the seven crystal systems. Combining this with the possible lattice types results in 14 possible lattices that all crystal structures can form with: the Bravais lattices, summarised below in Table 2.01.

Table 2.01: The seven crystal systems and 14 Bravais lattices, adapted from [3].

Crystal Systems	Unit cell parameters	Lattices
Cubic	$a = b = c$ $\alpha = \beta = \gamma = 90°$	P, I, F
Hexagonal	$a = b \neq c$ $\gamma = 120°$ $\alpha = \beta = 90°$	P
Tetragonal	$a = b \neq c$ $\alpha = \beta = \gamma = 90°$	P, I
Trigonal	$a = b = c$ $\alpha = \beta = \gamma \neq 90°$	P
Orthorhombic	$a \neq b \neq c$ $\alpha = \beta = \gamma = 90°$	P, I, C, F
Monoclinic	$a \neq b \neq c$ $\alpha = \gamma = 90°$ $\beta \neq 90°$	P, C
Triclinic	$a \neq b \neq c$ $\alpha \neq \beta \neq \gamma \neq 90°$	P

2.1.2 – Space Groups

Symmetry within the unit cell can reduce the unit cell to asymmetric units – the smallest structural unit that can generate the complete crystal structure through symmetry operations.[4] The symmetry operations can be either non-translational (inversion centre, rotation, reflection, rotation-inversion) or translational (screw axis; translation and rotation, and glide planes; translation and reflection). The symmetry elements acting upon the Bravais lattices gives the space group of a crystal: in total 230 unique space groups are possible given the combination of the lattice types and allowed symmetry elements.[5]

2.1.3 – X-ray Diffraction and Bragg's Law

In a crystallographic experiment, X-rays are scattered elastically by electrons in atoms, the wavelength of X-rays are comparable to the interatomic distances in crystal structures (0.8 – 3.0 Å) allowing X-rays to diffract from the planes of atoms in the crystal structure. Bragg's Law describes how X-rays are diffracted by planes of atoms in a crystal, shown below in Figure 2.03.[6]

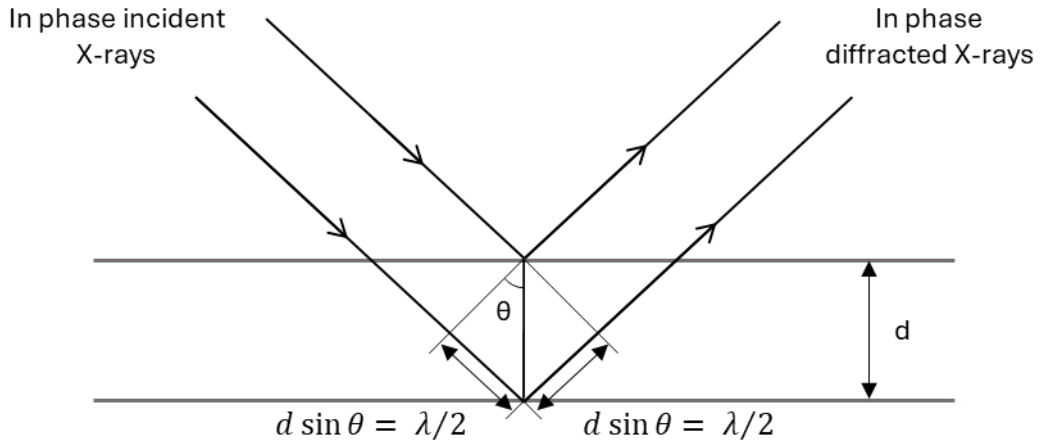

Figure 2.03: Derivation of the Bragg Law with X-rays interacting with planes in a crystal, with the d spacing in between the places, and angle of incident X-rays, ϑ, with path difference of the X-rays. Adapted from [7].

Bragg's Law is derived from treating layers of atoms in a crystal structure as planes for diffraction to occur, separated by a distance, d. Constructive interference occurs when the path difference between X-rays is an integer multiple of the wavelength, resulting in a diffraction peak. The angle at which constructive interference occurs, θ, for X-rays of a particular wavelength λ is given by the Bragg equation (Equation 2.01). Bragg's Law shows that X-rays on a crystalline compound will produce diffraction maxima, called reflections.

Equation 2.01: Bragg's Law relating X-ray diffraction angle, ϑ, to the crystal plane spacing, d, and wavelength of incident X-rays, λ. Bragg's Law simplifies diffraction as a reflection (Figure 2.03) so n = 1.

$$2d \sin\theta = n\lambda$$

X-rays are diffracted by the electron clouds around atomic nuclei, with the intensity of diffraction dependent on both the number of electrons in the atom and the angle of incidence. The positions of diffraction peaks provide the dimensions of the crystal unit cell, while the intensities provide information on the electron density distribution within the repeating unit.[7]

2.1.4 – X-ray Diffraction Techniques

There are two main X-ray diffraction techniques: powder X-ray diffraction (PXRD), where microcrystalline samples are studied, and single crystal X-ray diffraction (SCXRD), where the sample is a single crystal. SCXRD using lab source instruments are generally limited to the study of crystals with dimensions in the 50 μm or larger range.

2.1.4.1 – Single Crystal X-ray Diffraction

SCXRD involves the collection of diffraction data from a single crystal: the crystal is rotated around the diffractometer axes to vary the diffraction planes relative to the X-ray beam (d); the X-ray wavelength (λ) is constant, and the diffraction reflections are measured as a function of the diffraction angle, 2θ.[7,8] The diffraction patterns observed relate to the electron density crystal structure through Fourier transformation: the diffraction pattern exists in reciprocal space, an inversely proportional representation of the crystal lattice. Data collection on a detector measures the locations and intensity of reflections (Figure 2.04). Ideally, the single crystal experiment aims to collect diffraction data at a large enough total rotation range to measure all reflections to a desired resolution in the reciprocal lattice to produce a complete dataset for structure determination.[9]

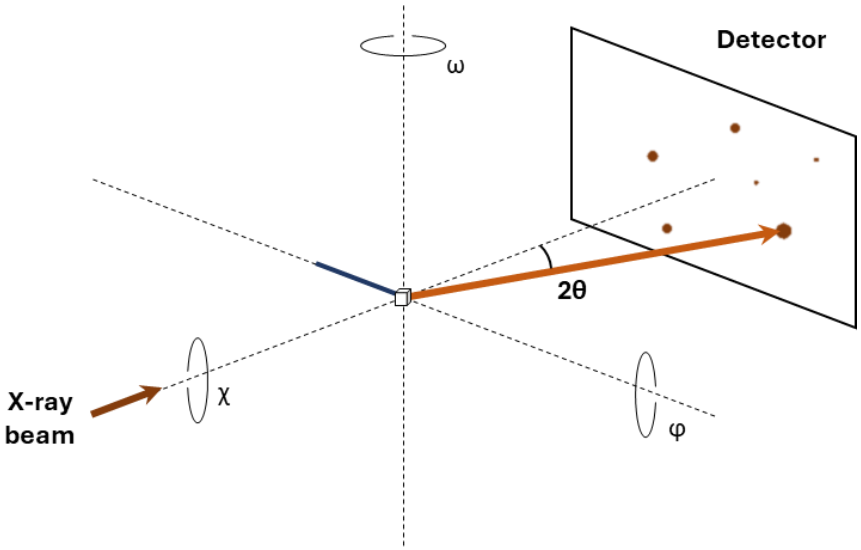

Figure 2.04: Layout of a diffractometer with goniometer rotations of crystal to vary d-spacing in beam. Diffraction pattern 2ϑ and intensity recorded on an area detector. Figure adapted from [7].

The intensity of X-ray in the diffraction pattern is dependent on the crystal structure, however, the electron density cannot be directly derived from the experimental measurements.[10] An SCXRD experiment measures the amplitude of diffracted X-ray beams but does not account for the relative phase, termed the "phase problem". The phases are obtained for structure determination from further means such as Direct methods and Patterson methods. Direct methods is often used for small molecule systems in scenarios with no prior knowledge of the crystal structure; it estimates the phase relationships between several strong reflections to help improve the understanding of electron density. The Patterson method is often used for crystal systems where a few heavy atoms are present and uses inputs of the positions of a few known atoms in the structure to provide information on the approximate positions of atoms for structure solution.[11] Using SCXRD data, the faces of crystal can be assigned

Miller indices in a process called Face Indexing, a helpful tool for understanding crystal growth and morphology.[12]

The data processing for single crystal data usually proceeds as follows:[13]

1. **Spot finding**: identifies the location of reflections on detector images
2. **Indexing**: from the spot finding routine, indexing aims to identify a suitable reciprocal space lattice and assign Miller indices to the reflections, and **refinement** of the lattice based on the assigned reflections.
3. **Integration**: the integrated intensity is obtained for reflections.
4. **Scaling**: data is corrected based on factors, such as beam intensity, volume of crystal, sample absorption, beam polarisation, and detector sensitivity.
5. **Structure solution**: processed data is used to solve the structure with software like Olex2 and using specialist computer programs like SHELX.[14,15]

A complete dataset cannot always be obtained from a single crystal due to factors such as radiation damage, or the instability of delicate crystals. To address this, serial crystallography techniques (discussed further in the Chapter 1) are used to collect partial "wedges" of data from multiple crystals. By merging the partial datasets from thousands of crystals, a high data completeness required for structural determination can be achieved.

2.1.4.2 – Powder X-ray Diffraction

In PXRD, the sample should be microcrystalline, containing a large number (millions) of small, < 10 μm, randomly oriented crystallites. The random orientation of the crystallites ensures that every set of lattice planes will, in certain crystallites, be in the correct orientation to diffract the incident beam. For powder diffraction, multiple reflection from sets of lattice planes with the same d-spacing merge into rings with the same 2θ angle (Figure 2.05). The diffracted signal is recorded by a detector, example of an area detector is shown in Figure 2.05a+b. Point detectors, shown in Figure 2.05c, by comparison, measure a small scale slice through the rings. The data collected on a 2D area detector is integrated to produce a 1D diffraction pattern of 2θ angle vs peak intensity (counts).[16] The loss of angular information in comparison to SCXRD makes structure solution from powder data far more challenging.

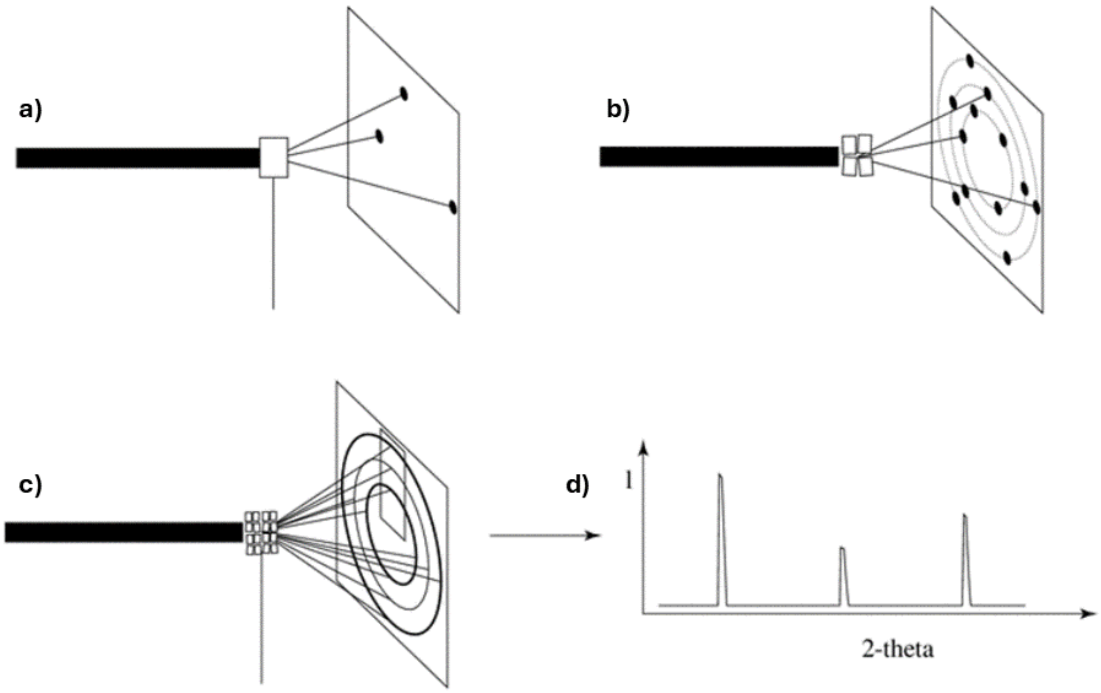

Figure 2.05: Representations of a) diffraction spots from a single oriented crystal, b) diffraction spots from 4 crystals at different orientations with respect to the beam, c) diffraction from a polycrystalline material with the resulting powder rings, and d) the resulting powder pattern obtained by scanning the outlined rectangle in c). Figure taken from [16].

Structural information about a sample can be extracted from a powder pattern through analysis of peak positions, intensities, and shape. Peak positions are primarily determined by size, shape, and symmetry of the unit cell; peak intensities are determined by the scattering density (atomic co-ordinates) in the unit cell. The peak shape can reveal important information about the microstructure, such as lattice strain and crystallite size.[16] However, peak shape can be dependent on instrument parameters, such as X-ray source, optics and detector. As such, it is necessary to distinguish the instrument effects from the microstructure information through calibration of the instrument with a calibration standard. Unlike SCXRD, PXRD provides information about a bulk sample for phase identification of a mixture of crystal forms; identification of forms present can be done via comparison with the patterns of known forms taken from a database.[17] The relative intensities of the peaks can give quantitative information about the amount of each phase present.

For the collection of high-quality structural data, single crystal diffraction is the method of choice, however, there are conditions where SCXRD is not possible due to poor quality or too small crystals.[18] Structural refinement of a crystal system from powder data can be achieved through the Rietveld refinement method. To achieve sufficient data quality for Rietveld refinement, typically high intensity synchrotron sources are required. The Rietveld method uses refinement of a complete structure model where atomic positions and lattice parameters are adjusted to best fit an experimental diffraction pattern.[18] The method is dependent on an initial structural model, with iterative refinement to minimize the difference between the calculated and observed pattern. If the

crystal structure is not closely related to a known compound it can be difficult to refine a structure using this trial and error technique. Multi-phase Rietveld refinement through fitting of multiple phases to each dataset can be used to obtain quantitative information on the phases present in the powder sample (Figure 2.06).[16] The calculated model is based on the sum of two or more models, each with their own parameters and scale factor used for the quantitative analysis of phases.[19] The quality of refinement can be assessed through the agreement factors (R-factors), however, the R-factors can be influenced by a number of factors, including high background noise and so the best indication of quality of refinement is visual inspection of the calculated and observed pattern: the "residual plot", shown in Figure 2.06d.

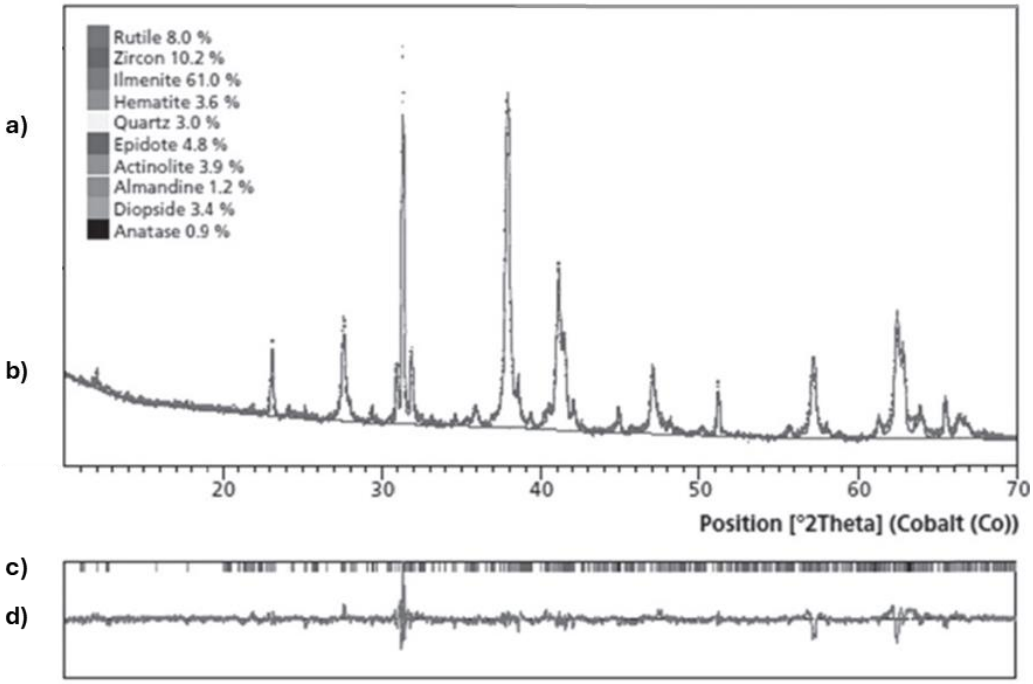

Figure 2.06: Multi-phase Rietveld refinement plot showing a) qualitative percentage balance of each phase present, b) overlaid PXRD pattern, calculated PXRD pattern, and baseline fitting, c) tick marks indicating the location of fitted peaks, and d) the difference between calculated and observed plot: the "residual plot". Figure adapted from [20].

PXRD patterns are interpreted assuming random orientation of crystallites; if the micro-crystals have shapes like flat plates or needles, they can pack in non-randomly, preferentially exposing some planes in the crystal to the X-ray beam: this is termed "preferred orientation".[18] Preferred orientation causes a poor powder averaging effect that can lead to certain diffraction peaks to be more intense relative to others.[21] Preferred orientation must be considered when quantifying phases present in the powder mixture during refinement as it can cause errors in the calculations.[18]

PXRD has applications in non-ambient studies such as for temperature-dependent polymorphism, high pressure experiments, dehydration/rehydration, and real-time observation of synthesis processes, however these often require the high energy, highly penetrating X-ray beams and the high speed detectors often used at synchrotrons.

2.2 – X-ray Sources and Instrumentation

When discussing X-ray generation, there are a few key characteristics of the X-ray beam to consider; the flux, the integrated intensity of the X-ray beam in terms of photons per second; the flux density, the intensity of the flux for a given area; the brightness, the flux within the beam divergence of the radiation cone; the brilliance, the brightness per area, essentially the intensity in the cross section of the beam.[22] The brilliance is the best descriptor for comparing X-ray sources, as the brilliance cannot be improved by optical techniques, only by increasing the brilliance of the X-ray source.

2.2.1 – Lab-source X-rays

Lab-source X-ray instruments are routinely used for diffraction analysis with in-house systems available in many research institutions. Lab-source X-ray instruments typically use X-ray cathode tubes for X-ray generation: hot filament generates electrons at the cathode and the target is positively charged (anode), when the electrons strike the target X-rays are generated.[23] Higher currents produce more X-rays for a "brighter" X-ray beam, with higher voltages generating higher energy X-rays. However, the current is limited as the target will melt at currents that are too high. Higher energies can be achieved for lab source systems through a rotating anode X-ray source: this uses the rotation of the anode to cool the target before re-entry into the electron beam, overall enabling higher currents and X-ray energies. Microfocus X-ray sources use improved focussing of the electron beam; this smaller focal point of the electron beam allows improved cooling of the anode, enabling significantly higher brilliance than conventional X-ray sources.[22] However, microfocus sources are considerably more expensive than typical X-ray anode tubes.

The two most common choices for X-ray tube anode materials are copper and molybdenum; they produce different wavelengths of X-rays at 1.5418 Å and 0.7107 Å respectively. The copper radiation is of higher flux and are diffracted more efficiently than molybdenum so is useful for small or weakly diffracting crystals.[24] Copper is also used for crystals with large unit cells as it provides a greater spread of diffraction ensuring no overlap of diffraction peaks. Molybdenum is useful for systems with heavier elements as it is less absorbed by heavier atoms; molybdenum is also able to collect to a higher resolution than copper.

The most widely available form of detector used in X-ray instruments are charge-coupled devices area detectors, benefitting from the simultaneous measurement of many reflections.[24] However, Hybrid Photon Counting (HPC) detectors are the next generation of area detectors, commonplace in synchrotron facilities for the low noise enabling data collection of much weaker diffraction crystals, especially important for macromolecular studies.[25] HPC detectors also have higher frame rates and higher count rates enabling enhanced time resolutions for *in situ* studies.

2.2.1.1 – The Flow-Xl facility

The Flow-Xl facility at the University of Leeds was developed to collect *in situ* XRD data during flow crystallisation processes (Figure 2.07). As such, Flow-Xl uses a Copper microfocus rotating anode X-ray source (MM007-HF) and X-ray optics (VariMax Very High Flux X-ray optics) to achieve an ultra-high brightness at the sample position.[26] The HPC area detector has 100 µm pixel size and fast speed (up to 100 Hz) to monitor processes with short timescales. The Flow-Xl facility additionally has a HORIBA Jobin Yvon Labram HR Evolution Raman Spectrometer for simultaneous measurements of X-ray and Raman *in situ* data.

Collaboration with the Flow-Xl facility, discussed in Chapter 4 with data processing development in Chapter 3, aimed to investigate the feasibility of lab-source systems for *in situ* XRD in a complex, mesoscale flow system.

Figure 2.07: The X-ray enclosure of the Flow-Xl lab-source X-ray instrument for in situ studies during crystallisation.

2.2.2 – Synchrotron X-rays

Synchrotron sources are large particle accelerators, often national or internationally run facilities, able to produce synchrotron radiation (SR) billions of times brighter than radiation from X-ray tubes.[23] In synchrotrons, electrons are generated and accelerated to high speeds with a linear accelerator and then further accelerated through a series of bending magnets and straight sections under vacuum in a booster ring. On reaching nearly the speed of light, the electrons are injected into the storage ring where at insertion devices, such as wigglers and undulators, the electrons are oscillated to produce SR. SR is used at experimental end stations called beamlines to conduct experiments (Figure 2.08).

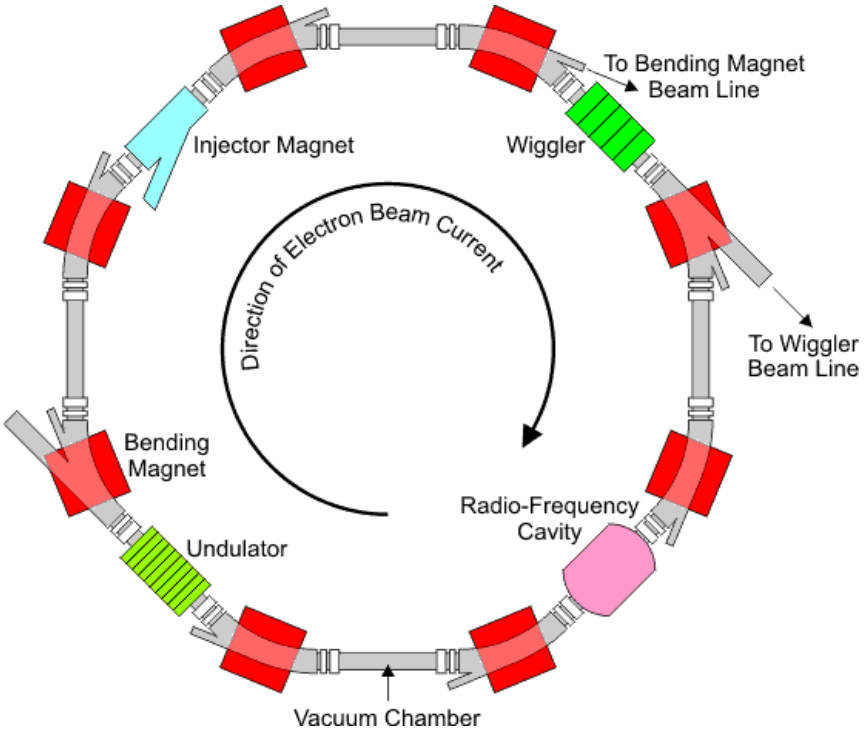

Figure 2.08: Diagram showing a synchrotron with key features such as straight sections and bending magnets for curving electron beam, wiggler and undulator insertion devices for creation of synchrotron radiation for use at beamlines. Image taken from [27].

At synchrotron sources, the radiation produced covers a large spectrum, from infrared to hard X-rays, with some beamlines allowing the tuneability of X-ray wavelength through use of monochromators. The very high intensities are the desirable feature of SR, able to achieve diffraction patterns from crystals in the sub-50 µm dimensions typically limited by lab-source experiments, or crystals with weak diffraction. The high penetrating power of the hard X-rays are also ideal for *in situ* analysis to overcome the high background scattering often present in complex sample environments.

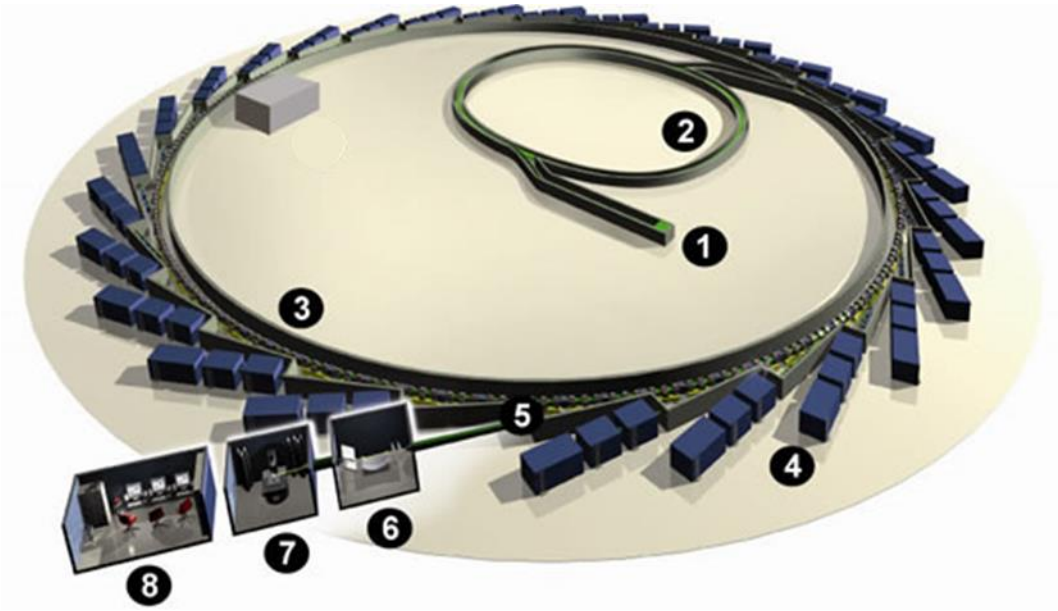

Figure 2.09: Schematic diagram of a synchrotron with key features labelled and discussed below. Figure taken from [28].

Figure 2.09 shows key components of a synchrotron research facility including (1) the initial electron gun for electron generation and linear accelerator for initial acceleration. (2) the booster ring where a series of bending magnets and straight sections are used to accelerate electrons to nearly the speed of light. (3) the storage ring where the beam is passed through bending magnets, straight sections, and radio frequency voltage sources utilised to maintain the electron speed. (4) Beamlines where X-rays are generated at insertion devices for use in experiments. At beamlines, the electrons process through the front end, (5), to an optics hutch (6) to filter and focus the beam. Experiments take place at the experimental hutches (7) and are controlled by researchers in control hutches (8).

Diamond Light Source (Diamond) is the UK's national synchrotron, with 32 beamlines used for different analytical techniques with research focusses of ranging from macromolecular crystallography, small molecule crystallography, to surfaces and interfaces. This research project was jointly funded by the University of Nottingham and Diamond, in collaboration with Beamlines I11 and I19.

2.2.2.1 – Beamline I11

Beamline I11 is the high resolution powder diffraction beamline at Diamond, with an undulator source for X-rays used to produce a highly collimated, low divergence beam of X-rays in the range of 7 – 25 keV. The beam is optimised for data collection at 0.8266 Å (15 keV).[29] I11 has two experimental hutches, the upstream experimental hutch 1 (EH1) for high-resolution, high throughput of powder samples, and downstream experimental hutch 2 (EH2) the long duration experiments (LDE).[30]

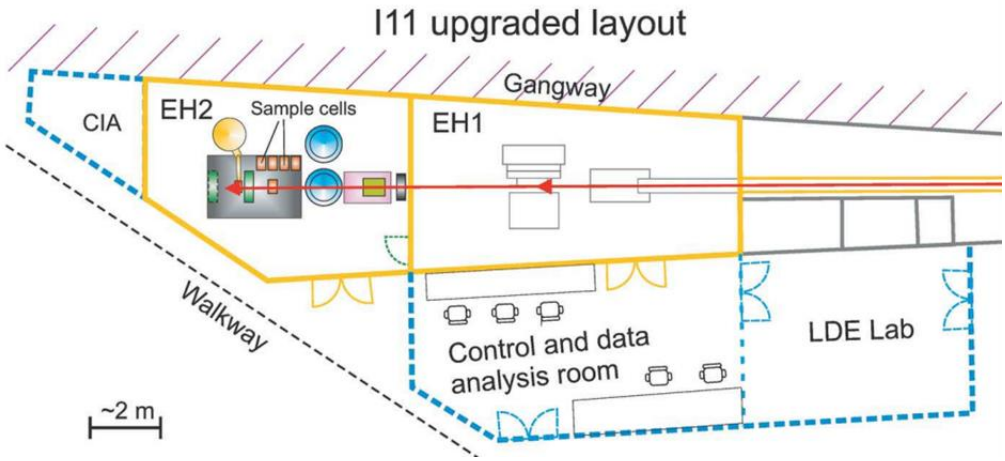

Figure 2.10: Schematic of Beamline I11 layout with initial optics hutch, upstream EH1, downstream EH2 for LDE experiments and control room. Image taken from [30].

EH1 features more typical PXRD experiments with spinning quartz or borosilicate capillaries to achieve good powder averaging and a liquid nitrogen cryostream and hot gas blower for variable temperature PXRD measurements. EH1 features a robot arm and carousel hosting prepared powder capillaries, enabling an automated, fast 30 s changeover of powder experiment for a high throughput of experiments with high resolution powder patterns.[31]

The LDE experimental hutch (EH2) has a large pixellated area detector at a lower resolution than EH1 but with fast detection rates for monitoring of *in situ* processes. EH2 houses multiple long duration experiments with sample measurements every week over month to year timeframes to monitor slow kinetic systems or processes, including the structural stability of gas storage materials, battery materials, and *in situ* monitoring of slow mineral formations recreating planetary environments. EH2 is also set up with a large sample stage for larger or bespoke sample environment requirements. The layout of Beamline I11 (Figure 2.10) enables experimental set up in EH2 whilst experiments are ongoing in EH1, allowing for more complex experimental set ups in EH2 whilst maintaining beam usage. The KRAIC segmented flow crystallisers with *in situ* PXRD, the development of which is discussed in Chapter 5 with data processing development in Chapter 3, uses the large sample stage in EH2, making use of the extra space in EH2 for more complex sample environments and large, fast detection rate detector for studying *in situ* processes.

2.2.2.2 – *Beamline I19*

Beamline I19 is the small molecule single crystal diffraction beamline at Diamond, with an undulator X-ray source and tuneable wavelength range of 0.5 – 2.5 Å (25 – 5 keV).[32] Like I11, Beamline I19 has two experimental hutches, the upstream EH1 for high throughput chemical crystallography studies, and EH2 for complex, bulky sample environment studies, such as time-resolved light activation studies, high-pressure studies, gas cell studies and cryostat temperature studies.[33] Layout of Beamline I19 shown in Figure 2.11.

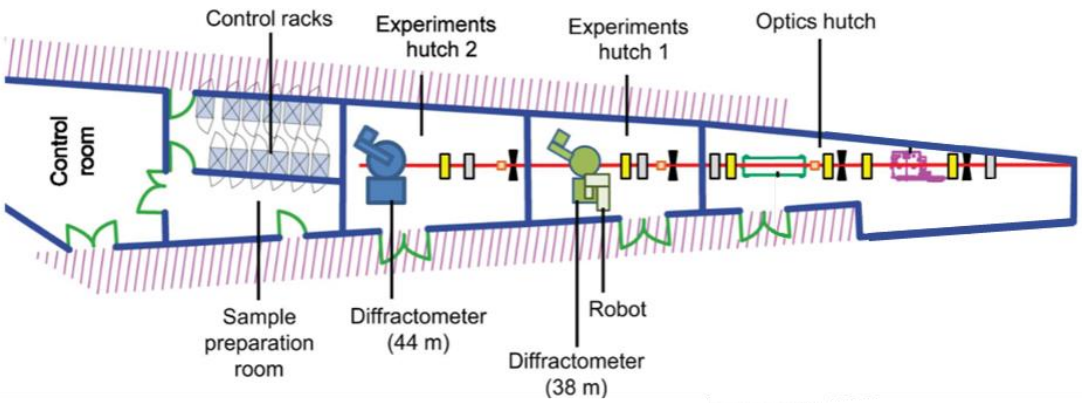

Figure 2.11: Schematic of layout of Beamline I19, with optics hutch, upstream EH1 with robot for high throughput studies, EH2 for complex sample environments, and control room. Image taken from [32].

EH1 for I19 has a robot arm similar to I11 EH1, enabling high-throughput SCXRD experiments, often used with mail-in samples and remote user operation. SCXRD at Beamline I19 EH1 enables the study of micron-sized crystals too small for typical lab based systems. EH2 featured a photon counting pixel area detector with rapid, shutterless operation for time-resolved *in situ* studies. Also like I11, the layout of I19 enables beamtime to be conducted in EH1 whilst complex experiments are set up in EH2, ensuring maximum beam usage. Studies of segmented flow crystallisation with *in situ* SCXRD at Beamline I19 EH2 are discussed in this thesis in Chapter 6 and 7.

2.3 - References

1. Ooi, L. Chapter 1. An Introduction to the Method. in *Principles of X-ray Crystallography* 3–22 (Oxford University Press Inc., 2010).
2. Clegg, W. *Crystal Structure Determination*. (Oxford University Press Inc., 1998).
3. He, B. B. Chapter 1. Introduction. in *Two-Dimensional X-Ray Diffraction* 1–27 (John Wiley & Sons, Inc, 2009).
4. Ooi, L. Chapter 4. Spaces Groups. in *Principles of X-ray Crystallography* 48–65 (Oxford University Press Inc., 2010).
5. Clegg, W. Chapter 1. Fundamentals of X-ray crystallography. in *X-ray Crystallography* 1–32 (2015).
6. Atkins, P. ., de Paula, J. & Smith, D. Chapter 17. Metallic, ionic, and covalent solids. in *Elements of Physical Chemistry* 420–448 (Oxford University Press Inc., 2013).
7. Weller, M., Overton, T., Rourke, J. & Armstrong, F. Chapter 8. Physical techniques in inorganic chemistry. in *Inorganic Chemistry* 234–270 (Oxford University Press Inc., 2014).
8. Cole, J. Chapter 5. Background theory for data collection. in *Crystal Structure Analysis - Principles and Practice* (ed. Clegg, W.) 53–72 (Oxford University Press Inc., 2009).
9. Rajashankar, K. & Dauter, Z. Chapter 17. Data collection for crystallographic structure determination. in *Structural Genomics and Drug Discovery. Methods in Molecular Biology* (ed. Anderson, W. F.) vol. 1140 211–237 (Humana Press Inc., 2014).
10. Main, P. Chapter 1. Introduction to diffraction. in *Crystal Structure Analysis - Principles and Practice* (ed. Clegg, W.) 1–8 (Oxford University Press Inc., 2009).
11. Clegg, W. Chapter 9. Patterson syntheses for structure determination. in *Crystal Structure Analysis - Principles and Practice* (ed. Clegg, W.) 117–132 (Oxford University Press Inc., 2009).
12. Girolami, G. S. Chapter 21. Bragg's Law, Scattering Planes, and d-Spacings. in *X-ray Crystallography* (ed. Murdzek, J.) 225–234 (University Science Books, 2016).
13. Winter, G. *et al.* DIALS: Implementation and evaluation of a new integration package. *Acta Crystallogr* **D74**, 85–97 (2018).
14. Sheldrick, G. M. A short history of SHELX. *Acta Crystallogr* **A64**, 112–122 (2008).

15. Dolomanov, O. V., Bourhis, L. J., Gildea, R. J., Howard, J. A. K. & Puschmann, H. OLEX2: A complete structure solution, refinement and analysis program. *J Appl Crystallogr* **42**, 339–341 (2009).

16. Evans, J. S. O. Chapter 17. Powder Diffraction. in *Crystal Structure Analysis - Principles and Practice* (ed. Clegg, W.) 251–270 (Oxford University Press Inc., 2009).

17. He, B. B. Chapter 7. Phase Identification. in *Two-Dimensional X-Ray Diffraction* 191–217 (John Wiley & Sons, Inc, 2009).

18. Girolami, G. S. Chapter 41. Powder X-ray Diffraction. in *X-ray Crystallography* (ed. Murdzek, J.) 439–450 (University Science Books, 2016).

19. School of Crystallography Birkbeck College University of London. Multiphase Refinements. *Advanced Certificate in Powder Diffraction on the Web* Preprint at http://pd.chem.ucl.ac.uk/pdnn/refine2/multi.htm (2006).

20. Rietveld, H. M. The Rietveld method. *Phys. Scr.* **89**, 098002 (2014).

21. Nelmes, R. J. & McMahon, M. I. High-Pressure Powder Diffraction on Synchrotron Sources. *J. Synchrotron Rad.* **1**, 69–73 (1994).

22. Kern, A. Chapter 2.1. Instrumentation for laboratory X-ray scattering techniques. in *International Tables for Crystallography* (eds. Gilmore, C. J., Kaduk, J. A. & Schenk, H.) vol. Volume H 26–50 (International Union of Crystallography, 2019).

23. Girolami, G. S. Chapter 13. Generation of X-rays. in *X-ray Crystallography* (ed. Murdzek, J.) 145–156 (University Science Books, 2016).

24. Clegg, W. Chapter 6. Practical aspects of data collection. in *Crystal Structure Analysis - Principles and Practice* (ed. Clegg, W.) 73–92 (Oxford University Press Inc., 2009).

25. Förster, A., Brandstetter, S. & Schulze-Briese, C. Transforming X-ray detection with hybrid photon counting detectors. *Phil. Trans. R. Soc. A* **377**, 20180241 (2019).

26. Turner, T. D. *et al.* Flow-Xl: a new facility for the analysis of crystallization in flow systems. *J. Appl. Cryst* 57 (2024) doi:10.1107/S1600576724006113.

27. School of Crystallography Birkbeck College University of London. How do Synchrotrons Work? . *Advanced Certificate in Powder Diffraction on the Web* http://pd.chem.ucl.ac.uk/pdnn/inst2/work.htm (2006).

28. Diamond Light Source. The Diamond Machine. *Bird's eye view of the synchrotron* https://www.diamond.ac.uk/Science/Machine/Components.html (2024).

29. Thompson, S. P. *et al.* Beamline I11 at Diamond: A new instrument for high resolution powder diffraction. *Review of Scientific Instruments* **80**, 075107 (2009).

30. Murray, C. A. *et al.* New synchrotron powder diffraction facility for long-duration experiments. *J Appl Crystallogr* **50**, 172–183 (2017).

31. Thompson, S. P. *et al.* Fast X-ray powder diffraction on I11 at Diamond. *J Synchrotron Radiat* **18**, 637–648 (2011).

32. Nowell, H., Barnett, S. A., Christensen, K. E., Teat, S. J. & Allan, D. R. I19, the small-molecule single-crystal diffraction beamline at Diamond Light Source. *J Synchrotron Radiat* **19**, 435–441 (2012).

33. Allan, D. R. *et al.* A Novel Dual Air-Bearing Fixed-χ Diffractometer for Small-Molecule Single-Crystal X-ray Diffraction on Beamline I19 at Diamond Light Source. *Crystals (Basel)* **7**, 336 (2017).

Chapter 3 – Development of Powder X-ray diffraction data processing methodology development for segmented flow crystallisation

This chapter features the development of processing scripts for powder X-ray diffraction data. The work is building on the MATLAB scripts used for processing of the original KRAIC-D data, developed by Dr Mark Levenstein and Dr Lois Wayment. The scripts for the processing of Beamline I11 data discussed in this chapter were developed with input from Dr Sarah Day, Beamline Scientist at I11, and Dr Dean Keeble, Data Analysis Scientist at Diamond Light Source. The processing workflow for Flow-Xl data was developed using CrysAlisPro functions (frame selector and powder extraction tools) developed by Rigaku for the Flow-Xl facility.

3.1 – Introduction and Aims

Segmented flow crystallisation with *in situ* PXRD presents challenges for data processing due to the atypical conditions present: due to the segmented flow the multi-crystalline slugs are not present in-beam during all data acquisitions. As a result, poor powder averaging and high levels of background scattering from solution, air, and carrier fluid causes poor signal-to-noise for diffraction data. Previous data collected with the KRAIC-D on Beamline I11, discussed further in Chapter 5, was acquired with continuous pulsed 100 ms detector acquisitions resulting in diffraction frames with few spots and low signal-to-noise. The majority of frames featured background scattering only; a typical diffraction frame from the flow crystallisation of carbamazepine in the KRAIC-D on Beamline I11 is shown below in Figure 3.01a.[1]

To improve data quality from the next generation KRAIC-T flow crystalliser for diffraction on Beamline I11, a data collection technique termed the slug triggering mechanism was adapted from previous work on Beamline I19 (for more details see Chapter 6 + 7). The introduction of the slug triggering mechanism as the data acquisition method for the KRAIC-T on Beamline I11 has improved the data quality of diffraction frames by locating and then following multi-crystalline slugs in-beam for a prolonged period of time (1.7 s). This resulted in greater power averaging, leading to more detector frames having powder rings and high signal-to-noise, discussed further in Chapter 5 and shown below in Figure 3.01b. Furthermore, the slug triggering mechanism improved the hit-rate of crystals, minimising the collection of background frames with no diffraction.

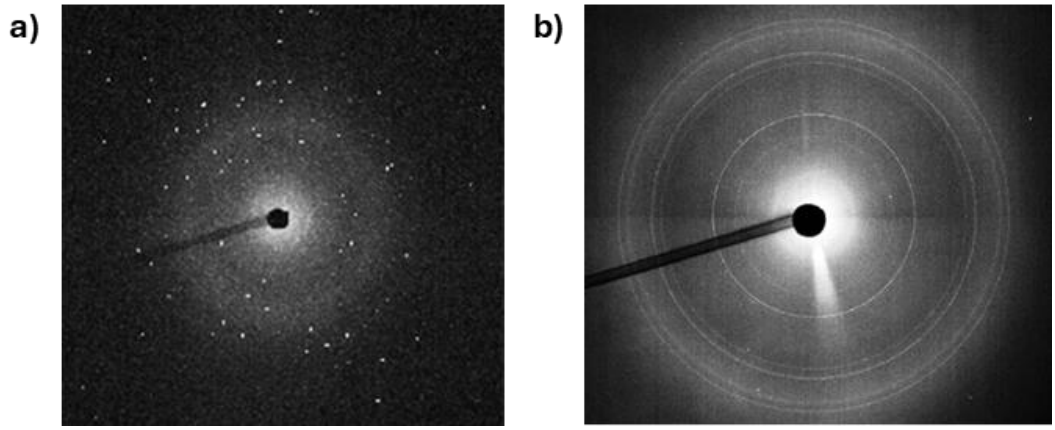

Figure 3.01: PXRD frames acquired on Beamline I11 EH2 of a) carbamazepine collected from the KRAIC-D with a 100 ms static acquisition,[1] b) ortho-aminobenzoic acid collected from the KRAIC-T with a 1.7 s slug triggering acquisition. N.B. Slug triggering acquisitions featured complete powder diffraction rings in comparison to single crystal-like spots acquired with short 100 ms acquisitions.

The original processing methodology, developed by Dr Mark Levenstein, and used by Dr Lois Wayment for the KRAIC-D data used MATLAB scripts for processing from a 2D detector frame to the 1D integrated diffraction pattern. The MATLAB methodology, discussed further in Section 3.2.1.1, used subtraction of a background frame to remove the majority of background scattering, thresholding to remove any remaining background noise, and azimuthal 1D integration of the 2D frame to produce the final PXRD pattern. This processing methodology suffered from poor processing speeds due to the inherent slow speeds of the MATLAB programming language. Section 3.2.2 of this chapter discusses the development of a Python-based processing procedure with the background subtraction and thresholding technique and is assessed with the slug triggering acquired data. Given the significant differences in data attributes due to the slug triggering data acquisition, considerable changes were required to the processing methodology compared to the previous MATLAB processing technique developed for the KRAIC-D data processing, discussed in Sections 3.2.3 – 3.2.4. Key foci for the method development are using Python and Python compatible libraries to enhance the data processing efficiency and resultant data quality.

Also discussed in Section 3.3 is the development of a data processing procedure for the *in situ* PXRD experiments with a lab source X-ray instrument for the KRAIC-Xl crystalliser at the Flow-Xl Facility, University of Leeds. The development of the KRAIC-Xl is discussed in Chapter 4. Due to the early stages of development of the KRAIC-Xl system, the slug triggering mechanism has not yet been adapted, resulting in a low hit-rate of crystal slugs and a high number of frames containing background scattering only. Therefore, the KRAIC-Xl diffraction data is comparable to KRAIC-D data, with pulsed 100 ms shutterless, continuous detector acquisitions resulting in low signal-to-noise for diffraction data. Furthermore, the lab source X-ray system results in diffraction frames with poorer signal-to-noise and broad peaks, providing further challenges for

processing of *in situ* PXRD of segmented flow. Section 3.3 discusses the use of the Rigaku CrysAlisPro software for the extraction of diffraction frames, and the adaptation of the developed Python scripts in Section 3.2 to KRAIC-Xl data.

Typical PXRD experiments do not often require post-processing of the data due to the X-ray transparent powder containers, such as borosilicate or quartz capillaries, which produce minimal background scattering. Furthermore, amorphous scattering in the XRD pattern can be analysed to characterise the amorphous material in the sample, so baseline correction is not used.[2] However, *in situ* experiments can have increased noise due to background scattering from the sample environment or increased material for background scattering, such as the carrier fluid, solution, and air present in the KRAIC system. There is no routine data processing procedure for *in situ* PXRD experiments, with the processing requirements often highly dependent on the sample environment and synchrotron facility; an *in situ* experiment on laser powder bed diffusion at the High Energy Materials P07 beamline at the PETRA III synchrotron at DESY used a single background frame collection to subtract from all subsequent diffraction patterns to correct for background noise.[3] The use of a single background frame indicates consistency in the background scattering present, unlike the KRAIC XRD systems, where the continuously moving segmented flow fluids in-beam caused inconsistency in the background scattering. Finding a good-fit background frame for KRAIC-D data processing was a time-consuming process as a result. The laser powder bed experiment subsequently used FIT2D, a data analysis program developed by the European Synchrotron Research Facility, for the 1D integration from the 2D data.[4] FIT2D has been a widely used software since its creation in 1997 for powder data handling, however, suffers from slow data processing speeds and limitations from poor detector geometry calibration capabilities.[5]

An *in situ* PXRD plug-flow fixed-bed cell experiment at DESY, the German synchrotron, used Dioptas, a commonly used Python-based program for the processing of 2D X-ray diffraction data.[5,6] Dioptas benefits from a Python codebase for increased processing speeds, including the use of pyFAI, a Python library for calibration and integration of PXRD data collected on 2D detector systems.[5,7] Dioptas also offers a range of background subtraction capabilities, with a user-defined background option or an automatic background subtraction algorithm.

DAWN is a software package for the calibration and processing of PXRD data created at Diamond Light Source.[8] DAWN benefits from fast integration times for 100 ms per diffraction frame. DAWN was used in the original data processing methodology for the KRAIC-D for the calibration of the detector using a collected calibrant file at the sample position. However, DAWN could not handle the background correction and data processing of the high signal-to-noise 100 ms diffraction frames.

The aims of the data processing methodology development for the KRAIC XRD systems are to streamline the processing workflow with Python libraries to increase the speed of processing and improve the extracted data quality.

Furthermore, the processing methodology must be robust and applicable to both the KRAIC-T and KRAIC-Xl systems, with minimal adjustment required. For this reason, DAWN is not a suitable program to develop the processing methodology around due some limitations with data formats accessible in the software. Dioptas, whilst having improved processing speeds due to the Python codebase and options for background subtraction methods, is tailored to high pressure and high temperature environments which may hinder processing of the specific features of the KRAIC PXRD data. The pyFAI library used by Dioptas for image integration and detector calibration is open source and accessible using Jupyter workbooks providing flexibility for calibration of different detector types required for KRAIC PXRD processing development.[9] In this Chapter, the pyFAI module is assessed for KRAIC-T PXRD data and applied for the KRAIC-Xl data also.

3.2 – PXRD processing development for Beamline I11

3.2.1 – Introduction

For the development of the PXRD data processing procedure, diffraction data from an awarded I11 beamtime was used; CY30306-1: temperature cycling segmented flow slurrying of *ortho*-aminobenzoic acid (*o*ABA). The slurrying study in the KRAIC-T temperature cycling crystalliser aimed to investigate the solvent-mediated phase transitions of the polymorphic *o*ABA system. *o*ABA has three distinctive polymorphs: the stable Form I, and the metastable Forms II and III, shown below in Figure 3.02.[10] *o*ABA is a well-studied material during solution-based crystallisation processes, and has a clear distinction between powder patterns, shown in Figure 3.03. The full description of *o*ABA characteristics such as molecular structure, crystal structures, and crystallographic information, such as unit cell parameters, is detailed further in Section 5.4.1 in Chapter 5. For full details of the KRAIC-T experimental conditions and beamtime results, see Section 5.4.

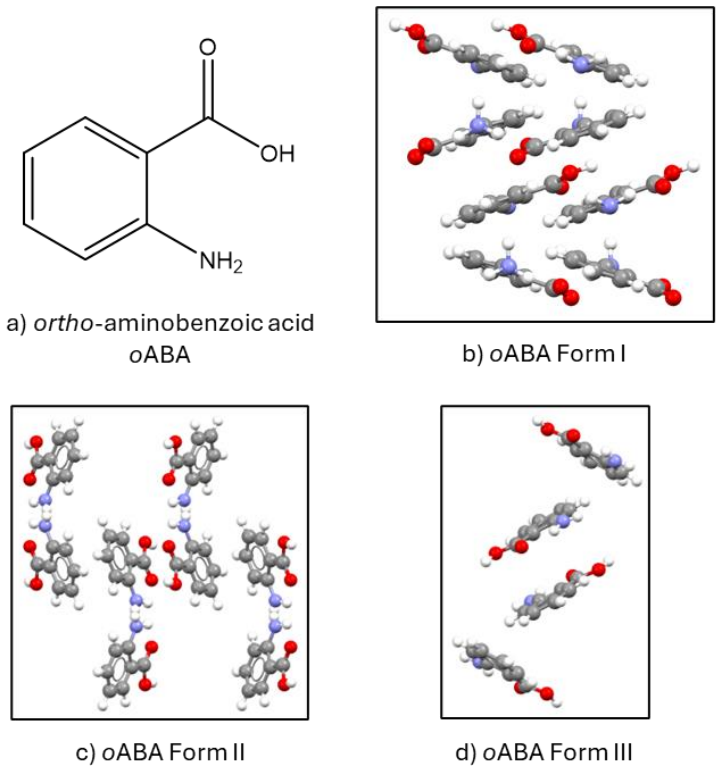

Figure 3.02: a) molecular structure of oABA with the crystal structures of the three polymorphs extracted from the Cambridge Structural Database; b) orthorhombic $P2_1cn$ Form I, refcode AMBACO01, viewed down the a-axis, c) orthorhombic Pbca Form II, refcode AMBACO03, viewed down the c-axis, d) monoclinic $P2_1/a$ Form III, refcode AMBACO06, viewed down the c-axis.[11–13]

*o*ABA was chosen as the material for this experiment due to the distinct powder patterns and the close relative stability of the polymorphs making it a model compound for *in situ* PXRD studies of crystallisation, with the aim to assess the efficacy of slug triggering data collection and function of the KRAIC-T crystalliser. The *o*ABA material purchased for the experiments contained Form II and Form III, resulting in polymorphic diffraction data to assess the efficacy of the new data processing procedure in comparison to the original methodology. The PXRD pattern of the material is shown in comparison to the polymorphic form references in Figure 3.03.

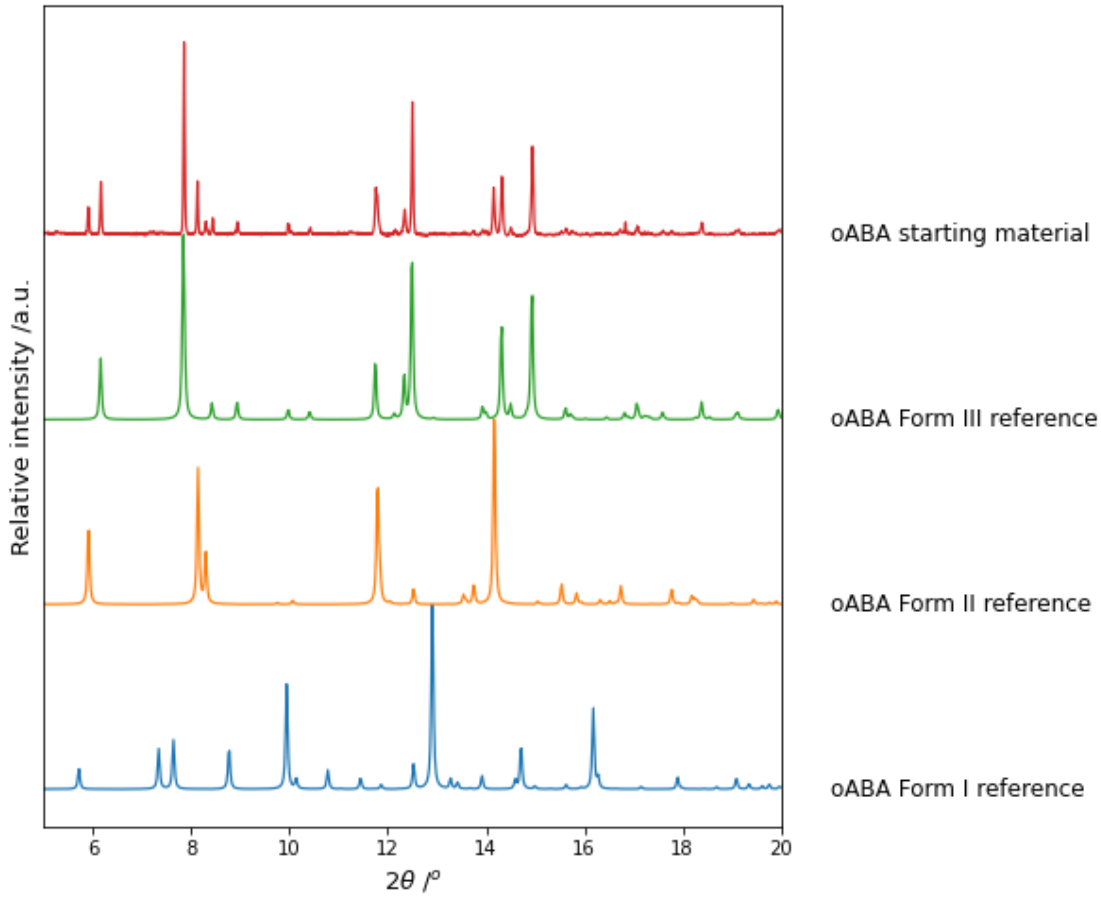

Figure 3.03: PXRD plot of Mercury generated reference oABA polymorphic forms AMBACO01, AMBACO03, and AMBACO06 for Forms I-III respectively, against oABA starting material.[11–13] *Starting material data analysed by capillary data collection on I11 at 0.824 Å in Experimental Hutch 1 (EH1). Data plotted at 0.824 Å. N.B. starting material shows presence of Form II and III of oABA.*

*o*ABA slurrying was conducted in a 90:10 volume/volume H_2O:IPA solvent mixture in the KRAIC-T, the different slurrying conditions are defined in the slurrying run name, for example "1_*o*ABA_45:60_1" features the slurrying of *o*ABA with temperature cycling between KRAIC-T column settings of 45 °C and 60 °C for Column 1 (C1) and Column 2 (C2) respectively. "1_" describes the first slurrying run, with the final "_1" describing the first repeat of the conditions. The overall segmented flow rate used was 6.2 mL/min for *o*ABA slurries of 26 g/L; a supersaturation ratio of 1.6 (calculated using Equation 1.01) for the 40 °C starting material slurry. Data was collected at three X-ray analysis windows on

the KRAIC-T at crystalliser lengths of 4.3 m, 7.0 m, and 9.6 m and flow slurrying times of 05:35 min, 08:50 min and 12:25 min. A “collection set” is defined as multiple slug triggering collections acquired at the same window in succession. In total, the *o*ABA example data has 21 collection sets, with 293 individual datasets total: an average of 14 datasets per collection set. The descriptor of “X1_01” describes a collection set at X-ray analysis window 1 (X1), the first repeat at X1 for the given conditions. See Chapter 5 Section 5.4 for further *o*ABA experimental details.

For the PXRD data processing methods discussed in this chapter, the Workflow Key in Figure 3.04 has been used to graphically illustrate the workflows distinguishing functions (process, input, output, and decision), with contrast for a user function or script function.

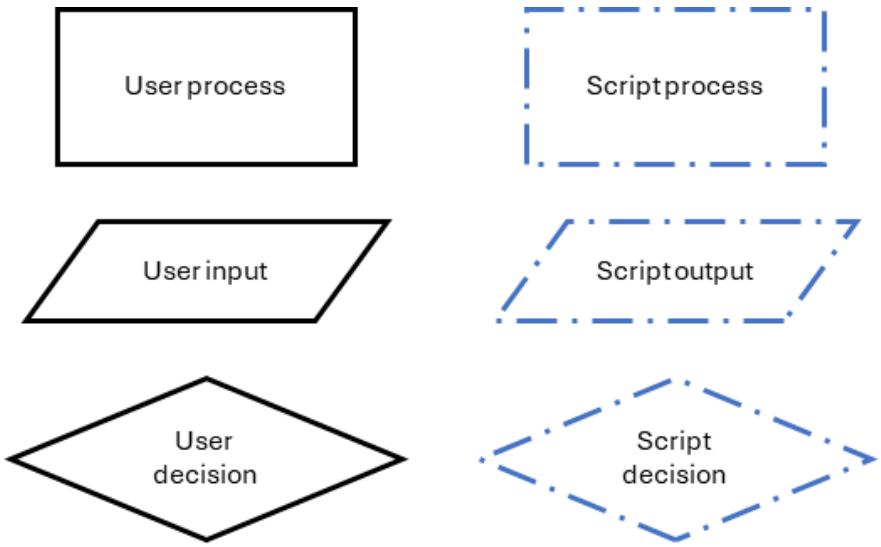

Figure 3.04: Key for data processing workflows, with different outline styles illustrating user or script functions.

3.2.1.1 – Individual diffraction frame threshold background subtraction processing in MATLAB

The previous MATLAB methodology for data processing of KRAIC-D data is summarised in Figure 3.05.

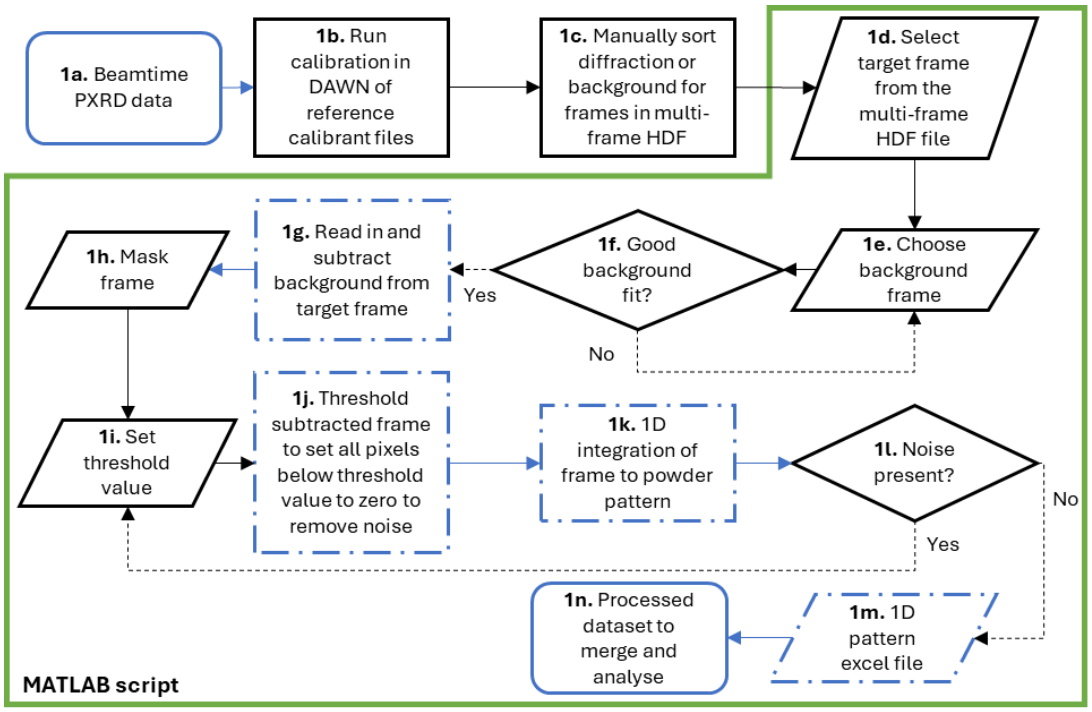

Figure 3.05: Workflow for MATLAB PXRD data processing procedure. The exported pattern is merged with other processed patterns and analysed to identify polymorphic forms.

The MATLAB processing procedure is a user intensive process with four user input steps, two user decisions, and two pre-MATLAB user processes. Pre-MATLAB detector calibration (Step 1b) uses calibrant diffraction frames collected at the sample positions and calibration settings generated in DAWN manually input into the script. Detector masking (Step 1h) is manually input by pixel using pixel values masked by the user in DAWN.

For extraction of the diffraction intensity, the MATLAB processing technique uses subtraction of a background frame (Steps 1e-g) and intensity value thresholding to remove any residual noise (Steps 1i-l); these processes are iterative until a suitable match of background frame is found and a suitable threshold intensity value is found to remove residual noise. The background frame subtraction is necessitated by the variability of the background scattering for the diffraction frames, thus this technique is reliant on a good-fit background frame to achieve maximum extraction of the diffraction intensity.

Alongside the time consuming manual steps, the azimuthal 1D integration calculations (Step 1k) also take significant computational processing time, with 27.3 s total processing time for a single dataset. Following this processing procedure, the outputted 1D data is merged with others in the same experimental conditions and analysed by eye against reference patterns to assess crystal forms present.

For a single dataset, the total computational processing time 41.0 s. The iterative process for defining the thresholding value includes the lengthy 1D integration step, increasing the total processing time significantly. Together with the user requirement for background selection, the total processing time for a single dataset can be in the range of 4 – 8 min.

The key aims of developing an updated PXRD processing technique are to improve the efficiency of the methodology; to reduce computational processing time, reduce user processing time, and to improve data quality and overall diffraction signal-to-noise. In order to decrease the processing time, the scripts were developed using Python, which offers access open source Python libraries for improved processing speed and data quality. The Python scripts were developed in Jupyter Notebook, an open source program designed to support scientific workflows with interactive cells with for the visualisation of scientific data through graphics and plots.[9]

3.2.2 – Development of diffraction frame sorting and individual diffraction frame processing with threshold background subtraction in Python

3.2.2.1 - Introduction

The processing workflow discussed in this section uses a diffraction frame sorting Python script (diffraction_sorting.py) to efficiently sort frames with diffraction from frames with background scattering only. The individual diffraction frame processing methodology (pyFAI_thresholding.py) uses the same background subtraction and thresholding technique as the MATLAB script. The processing workflow is enhanced by an automatic good-fit background selection stage and an open source Python module, pyFAI, for calibration, masking, and 1D integration.[7]

3.2.2.2 – Methodology

3.2.2.2.1 – Diffraction frame sorting workflow

A diffraction frame sorting workflow was developed in Python (diffraction_sorting.py) to sort background frames efficiently from diffraction frames, shown in Figure 3.06. This replaces the manual sorting by eye in the MATLAB workflow (Step 1c). It functions by assessing the intensity of the 5th most intense pixel and separating the low intensity frames as background scattering only.

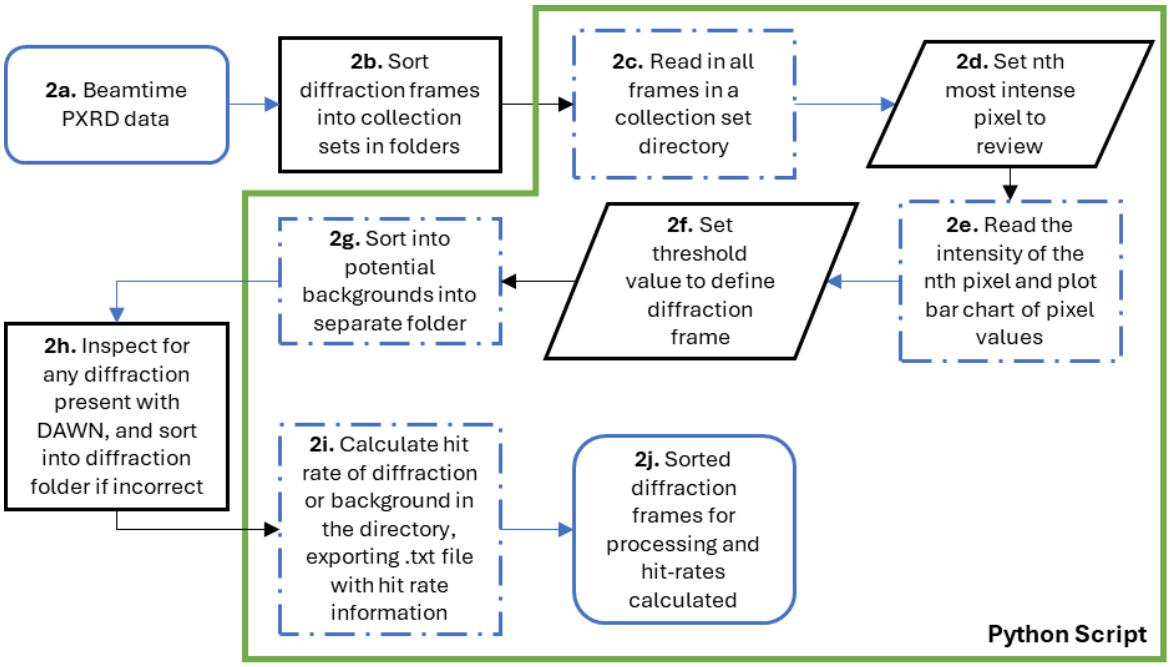

Figure 3.06: Workflow for the Python diffraction frame sorting process (diffraction_sorting.py).

The workflow requires user input for choosing a pixel intensity to review (Step 2d): the 5th most intense pixel was chosen because it generally showed a good distinction between high and low levels of diffraction. From this, the script produces a pixel intensity against diffraction frame bar chart for a collection set (Step 2e), example shown below in Figure 3.07.

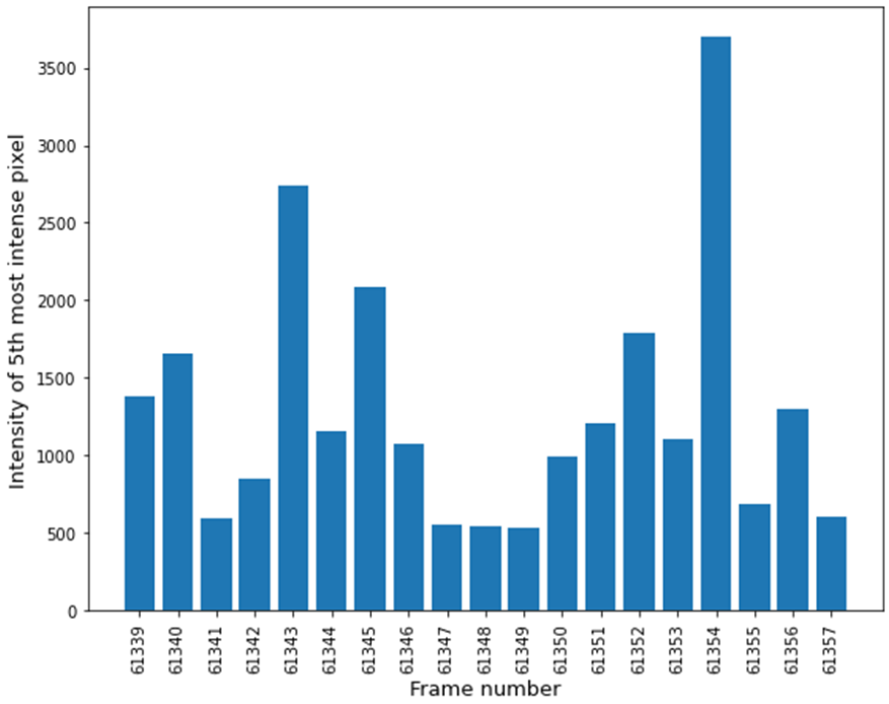

Figure 3.07: Bar chart showing 5th most intense pixel intensity for 2_oABA_45:65_1 Collection set X2_01 frames produced from diffraction_sorting.py script.

The pixel intensity chart shows frames with high intensity, and likely high levels of diffraction. From this, the user inputs a pixel intensity cutoff value to sort high

intensity and low intensity frames into separate folders (Step 2f). User input is required to visually inspect the low intensity frames for diffraction in DAWN and sort into appropriate diffraction and background folders. From this, the script then calculates hit-rate statistics for a collection set, shown in Figure 3.08.

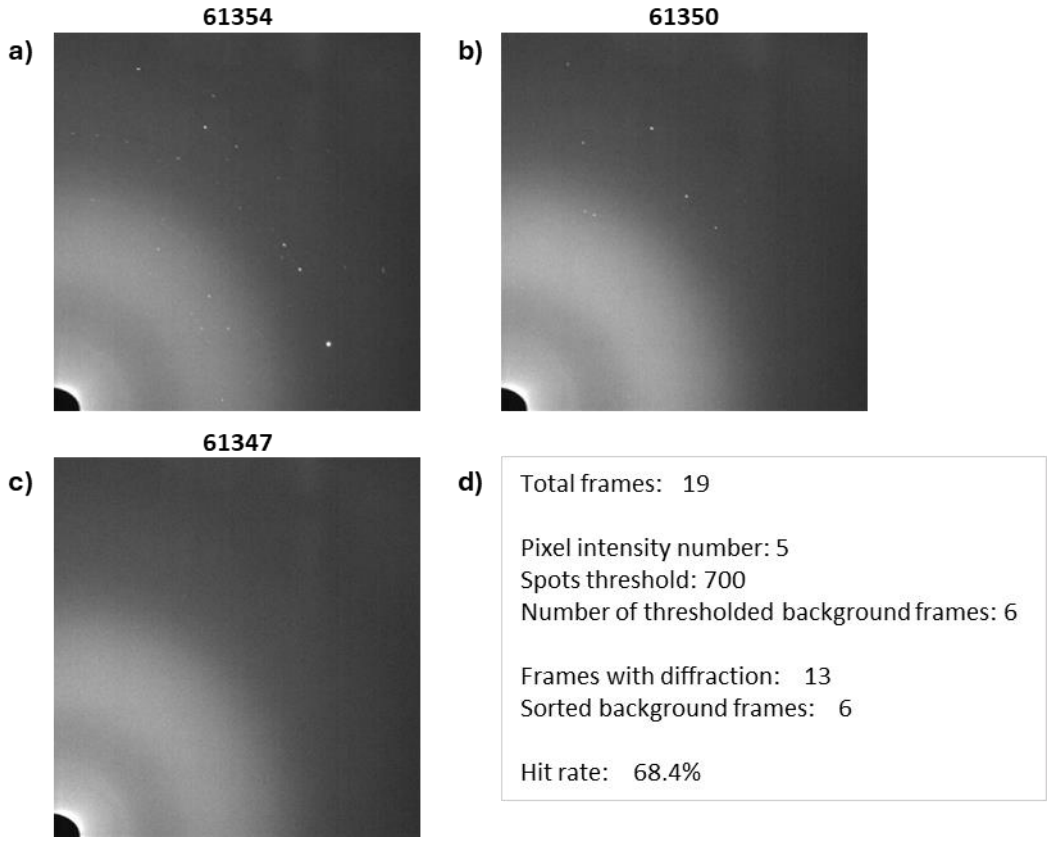

Figure 3.08: From 2_oABA_45:65_1 X2_01 collection set, a) scan 61354, a diffraction frame with higher levels of diffraction, b) 61350, a diffraction frame with low levels of diffraction, c) 61347, a frame with no diffraction - background scattering only d) output hit-rate statistics produced from diffraction_sorting.py script.

3.2.2.2.2 – Thresholding background subtraction and 1D integration workflow

Following the separation of diffraction frames from background frames, the Python thresholding workflow processes diffraction frames individually. The script (pyFAI_thresholding.py) uses a Python library for increased processing speed: pyFAI – Fast Azimuthal Integration for Python.[7] PyFAI was developed for the integration of X-ray data collected using an area detector, with additional tools for calibration, pyFAI-calib2. PyFAI-calib2 is a tool for calibration of the diffraction setup, in regards to beam energy and position, sample to detector distance, and detector geometry using a well known reference material (such as CeO_2) , generating a reference geometry file (.poni).

The Python pyFAI thresholding PXRD processing workflow is described below in Figure 3.09.

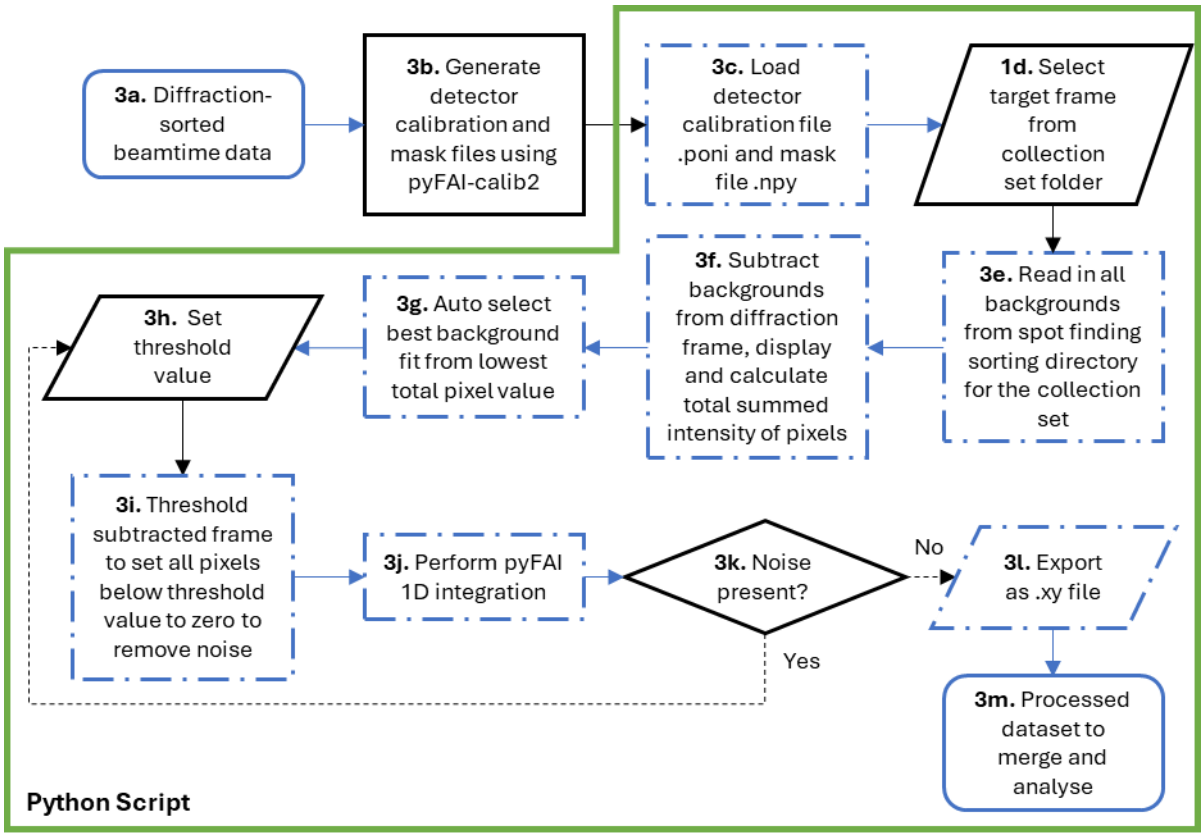

Figure 3.09: Workflow for Python pyFAI thresholding processing procedure (pyFAI_thresholding.py).

The initial calibration (Step 3b) is generated from inputting a calibrant file into pyFAI-calib2 with the detector information and calibrant specified, user generation of a mask for hot pixels and beamstop (Figure 3.10a), and calibration with user input for the calibrant powder rings locations (Figure 3.10b). From the pyFAI-calib2 calibration, a mask file and .poni file are generated relevant to diffraction frames containing beam centre, sample to detector distance, wavelength, pixel size and further detector positional information.

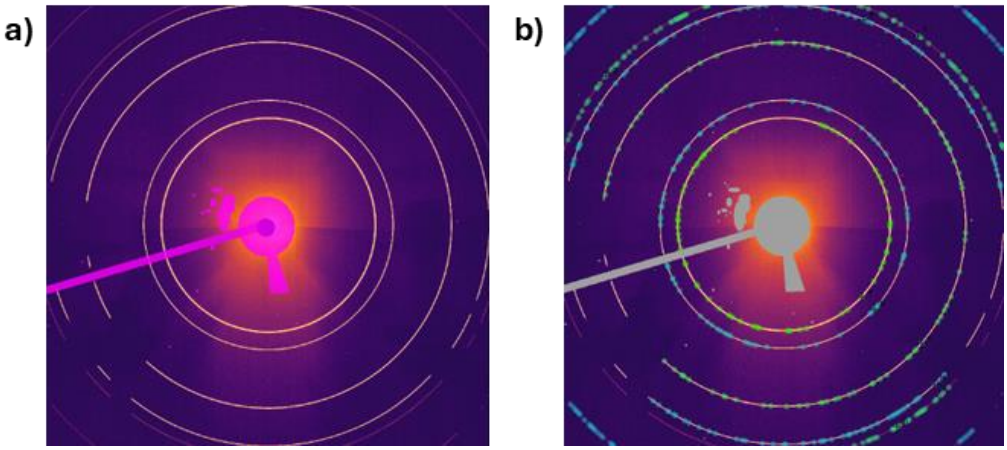

Figure 3.10: pyFAI-calib2 calibration images of cerium oxide (CeO_2) calibration of Kapton union sample position for oABA example beamtime data showing a) the mask generation step, masking beam stop and hot pixel areas, and b) user selected calibrant CeO_2 rings.

The automatic best-fit background selection process (Steps 3e-g, Figure 3.09) performs background subtraction of the diffraction frame with all background frames for the collection set output by the diffraction sorting workflow. The best-fit background is then selected by choosing the background subtraction frame with the lowest total pixel intensity. This is under the assumption that the lowest total pixel intensity represents the best overall removal of background scattering intensity leaving only diffraction intensity. The background selection is shown below in Figure 3.11.

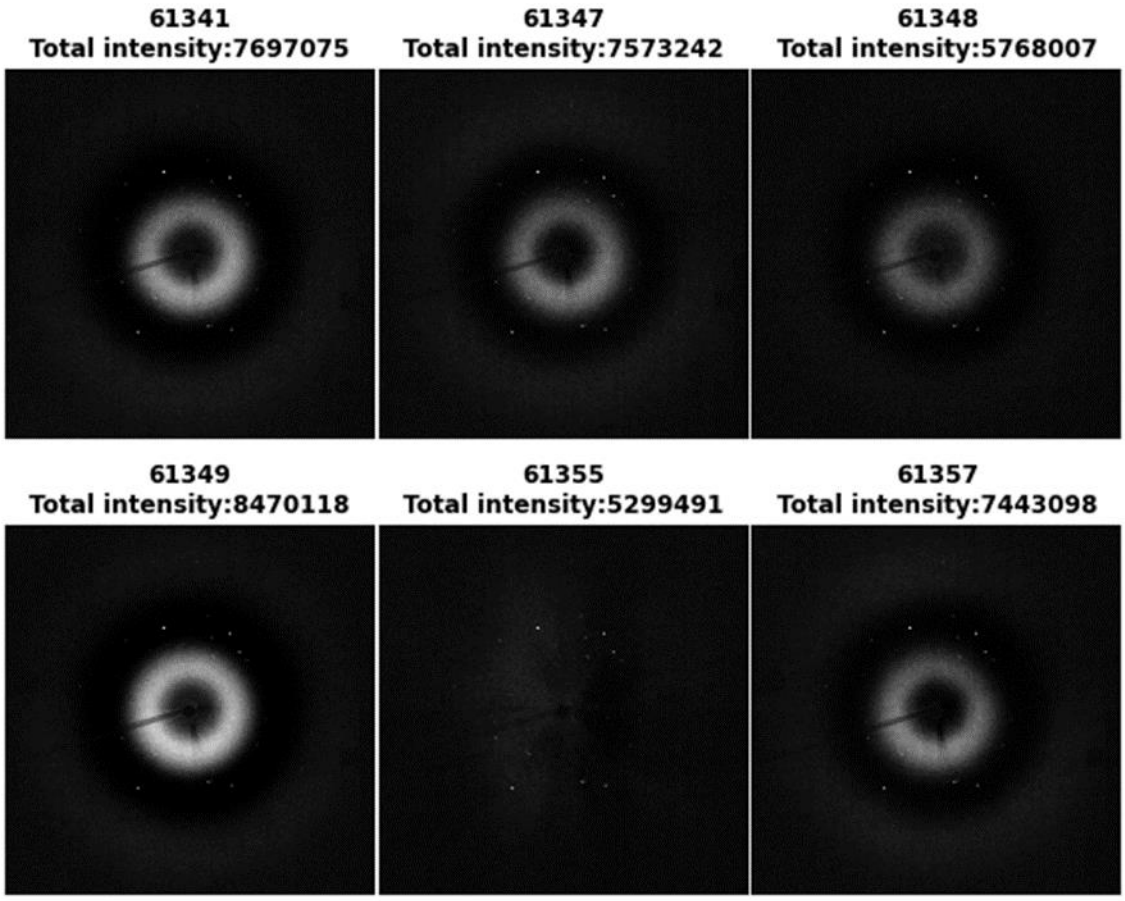

Figure 3.11: Background selection (Steps 3e-g) for diffraction frame processing with Python pyFAI thresholding workflow. Background frame 61355 displays the removal of the most background scattering with lowest total intensity, providing the best-fit background.

Following background selection, the diffraction frame is background subtracted with the best-fit selection and requires user input for thresholding value, the intensity value under which all pixels are set to zero (Step 3h, Figure 3.09). This is iterative based on the output of pyFAI 1D integration step: if noise is still present further thresholding is required, shown below in Figure 3.12.

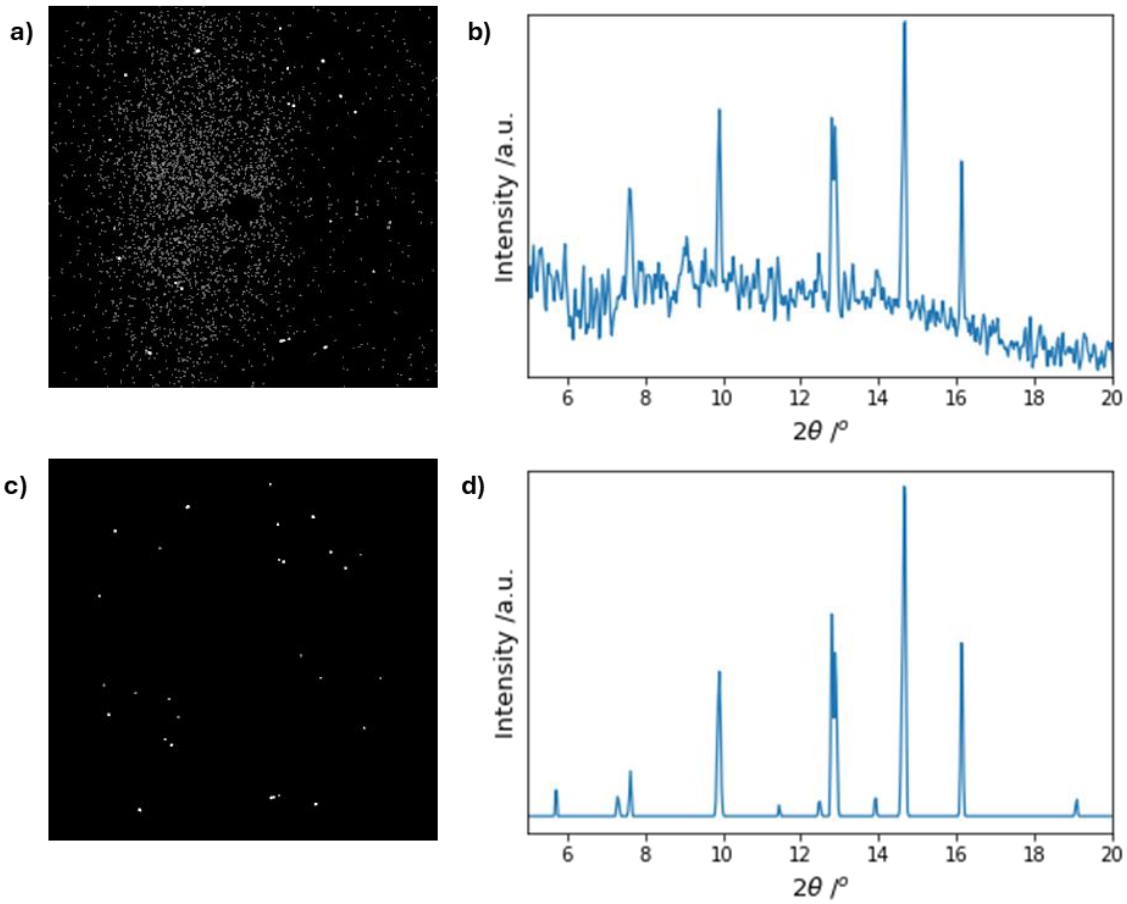

Figure 3.12: a) poorly thresholded diffraction frame with remaining noise, shown corresponding plot b) with noise in 1D diffraction plot, c) well thresholded diffraction frame with no remaining noise, shown in d) with corresponding 1D diffraction plot.

Following the iterative thresholding process (Steps 3h-k, Figure 3.09), the resultant 1D diffraction plot is exported as an .xy file and compared against reference patterns to identify polymorphic forms. The 1D patterns are summed together with other patterns in the same collection set for better statistics and improved powder averaging, which gives more reliable relative peak intensities.

3.2.2.3 – Results and Discussion

The previous MATLAB script has three script processes with a total of four user inputs, two user processes, and two user decisions. The user process to separate diffraction frames from background scattering alone is time consuming, requiring inspection of each frame individually. The workflow is a user intensive process with several iterative loops, exacerbated by the 1D integration calculation (Step 1k) which takes a total computational processing time of 27.3 s. The total MATLAB script computational processing time is 41.0 s; with user input time included for background selection and determination of the threshold value, a diffraction frame takes an estimated 4 – 8 min to process. With 293 diffraction frames from the *o*ABA beamtime, this would take an estimated 19 – 40 hr to process all of the frames, not including diffraction frame sorting or collection set merging.

The Python diffraction sorting workflow has several user requirements for two user inputs and user processes for inspection of low intensity frames per collection. The previous MATLAB workflow required visual inspection of every frame, a significantly more user-intensive, time consuming process. The total Python script computational processing time is 1.6 s; including the 5 min of user inspection per collection set this gives a total of 1 hr 45 min to separate the diffraction data for all 21 collection sets for the *o*ABA example data. This is significantly less that the total time for manual individual inspection and separation of diffraction data. The diffraction sorting workflow also incorporates automatic calculation of collection set hit-rates for crystalliser efficiency calculations and slug triggering mechanism appraisal required in Chapter 5.

The Python pyFAI thresholding workflow has two user inputs, one user process and one user decision creating one iterative loop only, with six script processes. The equivalent steps with the MATLAB workflow have four user inputs, one user process, and two user decisions creating two iterative loops, with three script processes. This is a reduction of user steps from seven to four; the transfer of steps from user to script-defined decreases the user processing time for an overall less user-intensive process. A comparison of computational and estimated total processing time for the MATLAB and Python thresholding scripts is shown below in Table 3.01.

*Table 3.01: Comparison of processing times for MATLAB and Python thresholding processing scripts. *MATLAB technique used manual diffraction frame sorting so no equivalent processing script step – estimated several additional hours for manual sorting.*

	Processing times for Workflow	
	MATLAB - thresholding technique	**Python - thresholding technique (diffraction_sorting.py and pyFAI_thresholding.py)**
Diffraction and background frame sorting	n/a *	1 hr 45 min
Computational processing time for 1D integration step	27.3 s	2.4 s
Total computational processing time per frame	41.0 s	5.2 s
Estimated total processing time with user input per frame	4 - 8 min	2 min
Estimated total processing time for all 293 *o*ABA frames	19 - 40 hr	9 hr 45 min

The pyFAI 1D integration (Step 3i) takes a total computational processing time of 2.4 s for loading calibration, loading the mask, and performing the 1D integration step, a considerable decrease from the 27.3 s for the 1D calculation in MATLAB. This is due to the MATLAB script using unoptimized calculations in a slower processing language, compared to the optimised pyFAI calculations and faster inherent processing time in Python. The Python pyFAI thresholding workflow computational processing time is a total of 5.2 s, a decrease from the 41.0 s total for the MATLAB script. With user input time considered for the

thresholding iterative loop and frame input, a diffraction frame takes an estimated 2 min to process: the total processing time for the 293 diffraction frames from the *o*ABA beamtime would be 9 hr 45 min total, with an additional 1 hr 45 min for diffraction frame separation. Overall, the diffraction sorting and pyFAI thresholding PXRD processing workflow estimated to be 11 hr 30 min total, 7.5 – 28.5 hr faster than the predicted MATLAB processing time for 293 *o*ABA beamtime frames, without considering the additional time for diffraction frame sorting. The Python workflow used Python to enable increased processing speeds with pyFAI for 1D integration and incorporated an auto background fitting step to reduce user input time. Furthermore, the pyFAI-calib2 user interface improved the ease-of-use of the masking step to remove hot pixels compared to the MATLAB script in which manual pixel inputs were required directly into the script. The incorporation of the calibration step into the pyFAI framework further improved ease-of-use and streamlined the processing workflow.

The main drawback of the thresholding technique is the requirement of a good-fit background to maximise signal-to-noise extraction. However, due to the improved crystal hit-rates with the addition of the slug triggering mechanism for data acquisition, the number of total background frames has considerably decreased and there is often not a good-fit background suitable for the diffraction frames.

Different slug triggering collection sets often used slightly different motor speeds for slug flow rate matching and X-ray window targeting heights to target the bulk of *o*ABA slurry density. As a result, the quantity of background noise collected varied between collection sets due to differing collection times, and quantity of scattering material (solvent, air, and carrier fluid) in-beam depending on the width of tubing in area targeted. This variation in background scattering necessitates background subtraction using background frames from the same collection. This further reduces the total background frames available.

The 1_*o*ABA_45:60_1 collection set X2_01 had a hit rate of 90% with only three background frames available for background subtraction. The background frames collected likely due to the slug triggering not acquiring from the correct position in the slug. The low number of background frames and the background scattering not representing the typical background scattering for the crystal sample positions caused the background subtracted frames in 1_*o*ABA_45:60_1 collection set X2_01 to have poor background matching, example shown below in Figure 3.13.

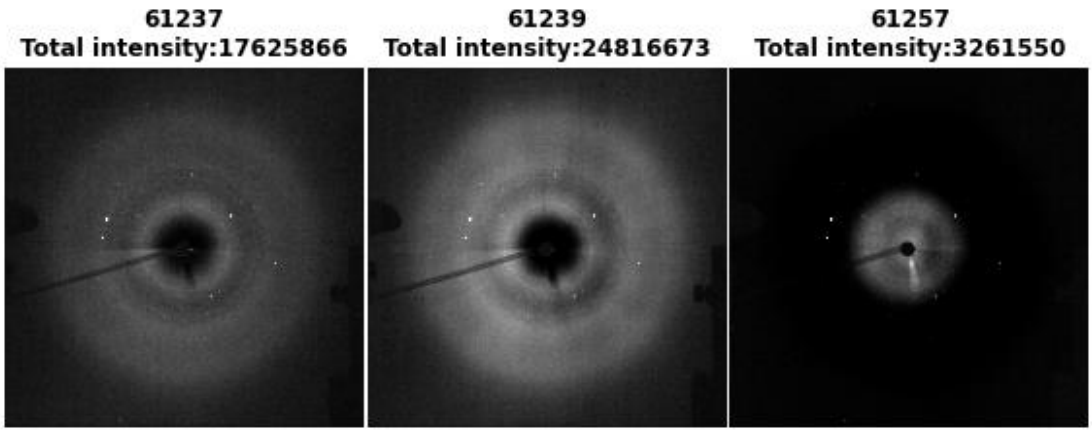

Figure 3.13: Background matching for a diffraction frame 61250 from oABA_run10_45_60 collection set X2_01, high levels of background scattering remain present after background subtraction.

Consequently, high threshold values were required to eliminate noise from poor background fits, therefore cutting off significant portions of diffraction intensity and effectively lowering the overall signal-to-noise. Example diffraction frame 61250 from 1_*o*ABA_45:60_1 collection set X2_01 is shown below in Figure 3.14 against the *o*ABA references. It shows the presence of *o*ABA Form I, however, there are few overall peaks, with the 12.90° peak clipped due to over-thresholding to eliminate residual noise.

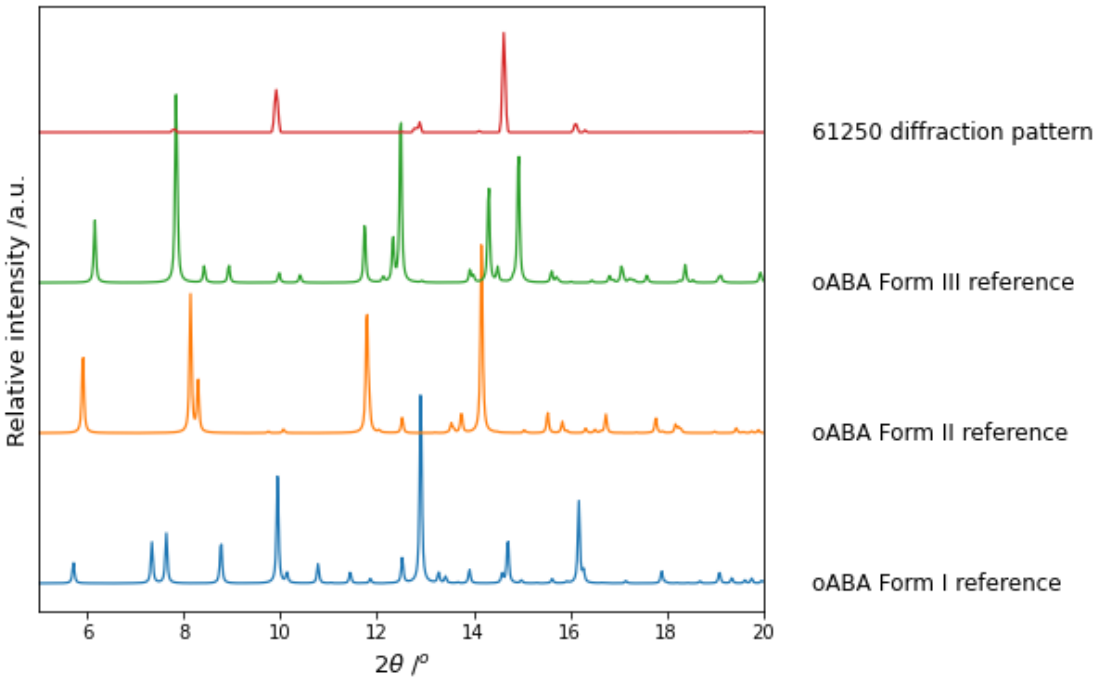

Figure 3.14: Integrated 1D powder pattern for 61250 diffraction frame against oABA Mercury generated reference patterns.

3.2.2.4 – Conclusions

Overall, the use of Python, introduction of pyFAI 1D integration, and auto-background fitting has significantly decreased the computational processing time of a single diffraction frame from 41.0 s to 5.2 s, with a reduction in processing time for the 1D integration step alone by 89%. However, the thresholding technique is not well suited to the slug triggering acquired data due to the low overall availability of background frames: the small range of background frames available often do not match the background scattering in diffraction frames, requiring over-thresholding and loss of diffraction signal. Further changes were required to the processing methodology to extract the highest amount of diffraction signal from the variable background scattering: the further developments are discussed in the following sections with the development of a baseline correction technique.

3.2.3 – Diffraction frame processing with morphological baseline correction in Python

3.2.3.1 - Introduction

The Python scripts discussed in this section use a morphological baseline correction technique for removal of background scattering from raw 1D integrated diffraction patterns. The script uses the same pyFAI library for calibration, masking, and 1D integration of diffraction frames, shown in previous workflows to significantly decrease the processing time compared to the MATLAB workflow and improve ease-of-use of the processing technique. Baseline correction is a feature of a number of PXRD processing programs, including Dioptas and DAWN,[5,8] however, to remain within a streamlined Python workbook workflow, the processing methodology discussed here uses pybaselines: a Python library for baseline correction of experimental data with a range of techniques including polynomial, smoothing, and morphological methods.[14]

Raw 1D integrated diffraction data from the example *o*ABA *in situ* PXRD of segmented flow is shown in Figure 3.15. The air, carrier fluid, and solution in segmented flow causes background scattering variations across slug triggering data collections.

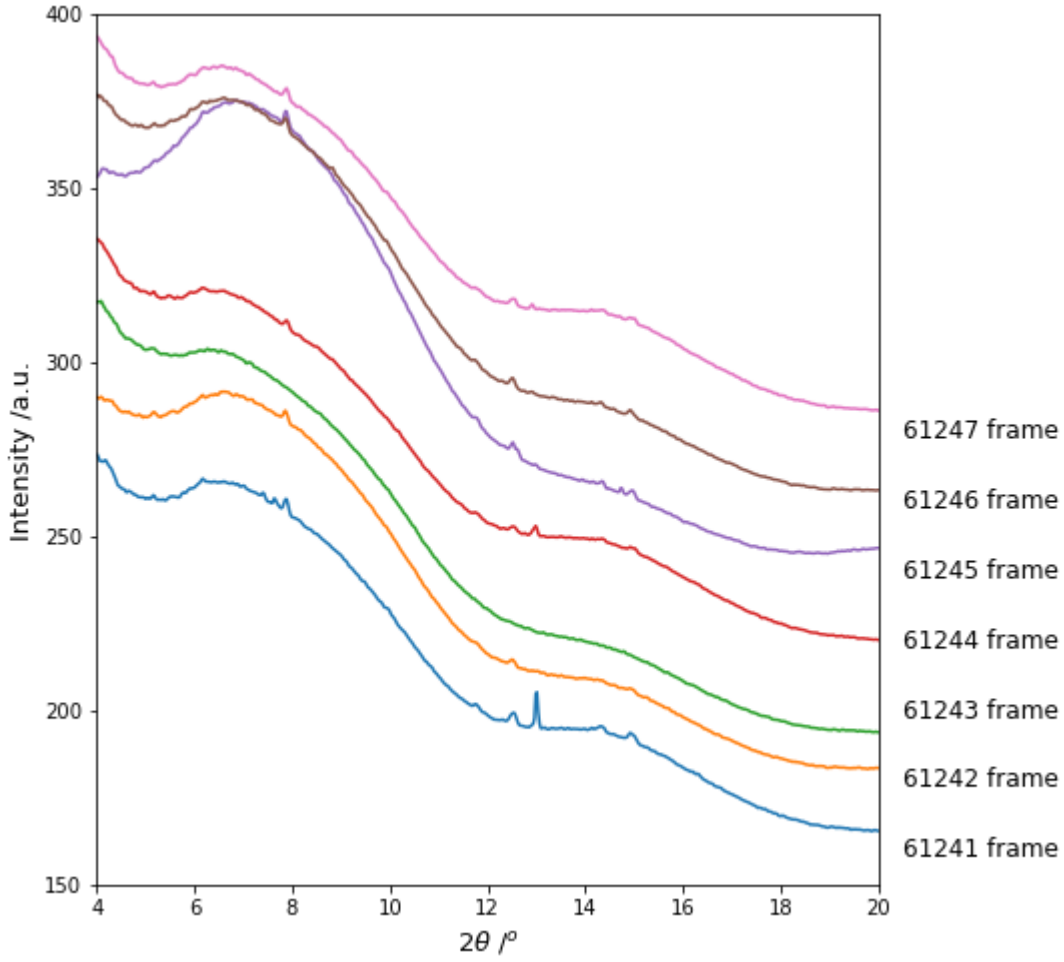

Figure 3.15: Offset PXRD plot of raw 1D integrated frames from 1_oABA_45:60_1 collection set X2_01.

There is significant variation in baseline for two humped regions: a large hump in the 6 – 12° 2θ range and a smaller second hump in the 12 – 18° 2θ range. Diffraction signal-to-noise is varied, with the 61241 frame featuring strong diffraction, 61243 showing poor diffraction with only a single small peak in the 5.7 – 6.2° 2θ area. Generally, the diffraction data contains two large background scattering humped regions with small diffraction peaks throughout: this makes it a good candidate for morphological baseline correction. Morphological baseline correction is a non-linear signal processing technique used to separate "special structures" from the overall background shape.[15] For the extraction of diffraction signal from I11 beamtime data, the special structuring element used with this technique is approximate to the full width half maximum of the diffraction peaks, termed the "half width"; features broader than the half width are removed, resulting in the retention of narrow diffraction peaks and removal of the wider background scattering humps.

The processing workflows presented in these sections use the basic morphological baseline correction (mor()) from the pybaselines Python library.[14,15] To assess the best procedure for extracting the maximum signal-to-noise, two baseline correction workflows were assessed: the first performing baseline correction on each 1D diffraction pattern, then merging the collection

set for analysis termed “pre-merging baseline correction” (pybaselineCorrected_merged.py), the second procedure merges all raw 1D patterns in a collection set, then performs a single baseline correction step on the merged pattern, termed “post-merging baseline correction” (rawMerged_pybaselineCorrected.py).

The pybaseline correction techniques are then compared to the thresholding technique in Section 3.2.3.3.2 to assess improvements to processing efficiency and overall data quality.

3.2.3.2 – Methodology

3.2.3.2.1 – Pre-merging baseline correction workflow

As with the previous processing workflow, the initial step of sorting diffraction frames from background scattering only is required. This is achieved by the same script, diffraction_sorting.py. The pre-merging baseline correction workflow is described below in Figure 3.16.

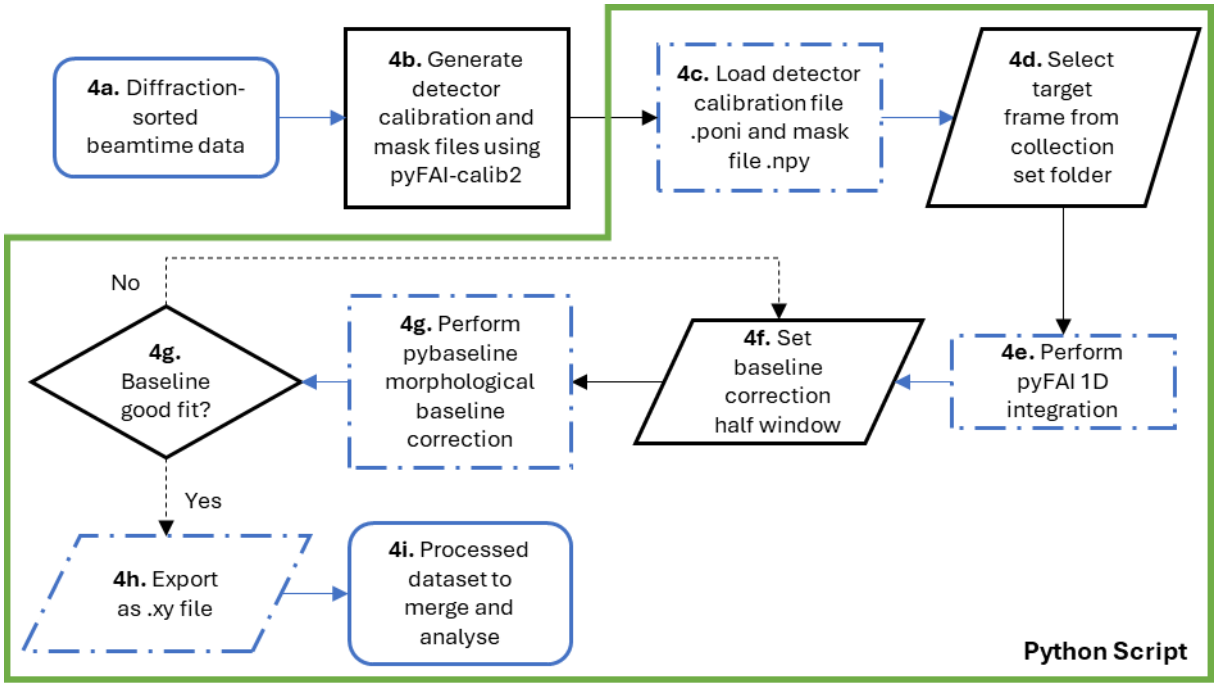

Figure 3.16: Workflow for pre-merging baseline correction methodology PXRD data processing (pyFAI_pybaseline_correction.py).

The initial pyFAI-calib2 calibration, masking and frame loading steps (4b-d) are unchanged from the Python thresholding script. The pyFAI 1D integration step (4e) is performed on the unaltered diffraction frame to produce a raw 1D pattern as shown in Figure 3.15. Using the raw pattern as reference, the user sets a half window numeric value approximate to the full width half maximum of the diffraction signal data points and inspects the produced baseline for a good fit.

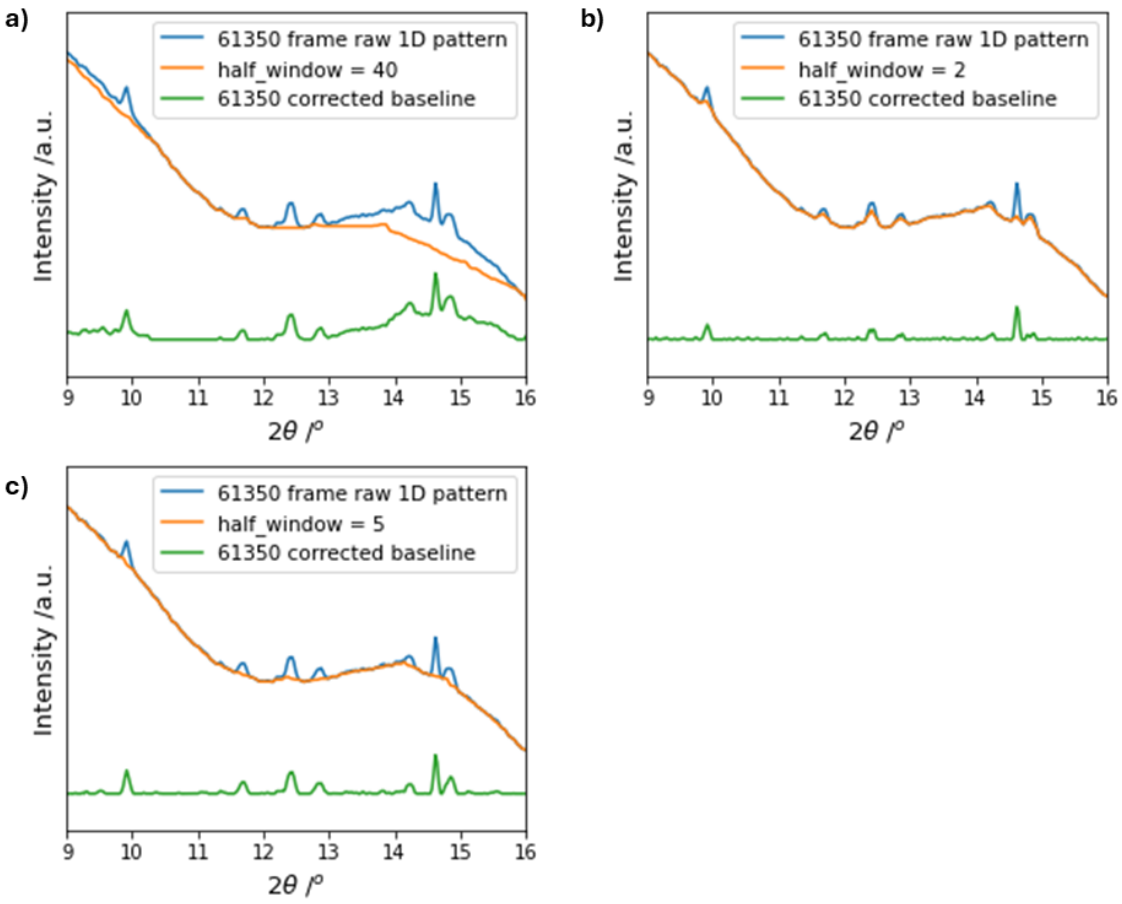

Figure 3.17: PXRD plots of 61350 raw 1D integrated pattern with pybaselines morphological baseline and resultant baseline corrected PXRD pattern for a) high half window of 40, b) low half window of 2, c) good-fit half window of 5.

User input is required to select an appropriate half window to maximise diffraction signal extraction; too high a half window value fails to fully remove the background scattering (Figure 3.17a), too low a half window value clips and removes diffraction signal (Figure 3.17b), a good-fit half window value removes background signal leaving generally only diffraction peaks (Figure 3.17c). Following the processing for all diffraction frames in a collection set, the resulting patterns are merged to improve powder averaging and analysed against reference materials.

3.2.3.2.2 – Post-merging baseline correction workflow

For the post-merging baseline correction workflow, the preliminary diffraction sorting workflow is used (diffraction_sorting.py) to separate diffraction frames from background signal only. This post-merging baseline correction workflow merges raw 1D patterns in a collection set, then performs the baseline correction on the merged datasets. The workflow is shown below in Figure 3.18.

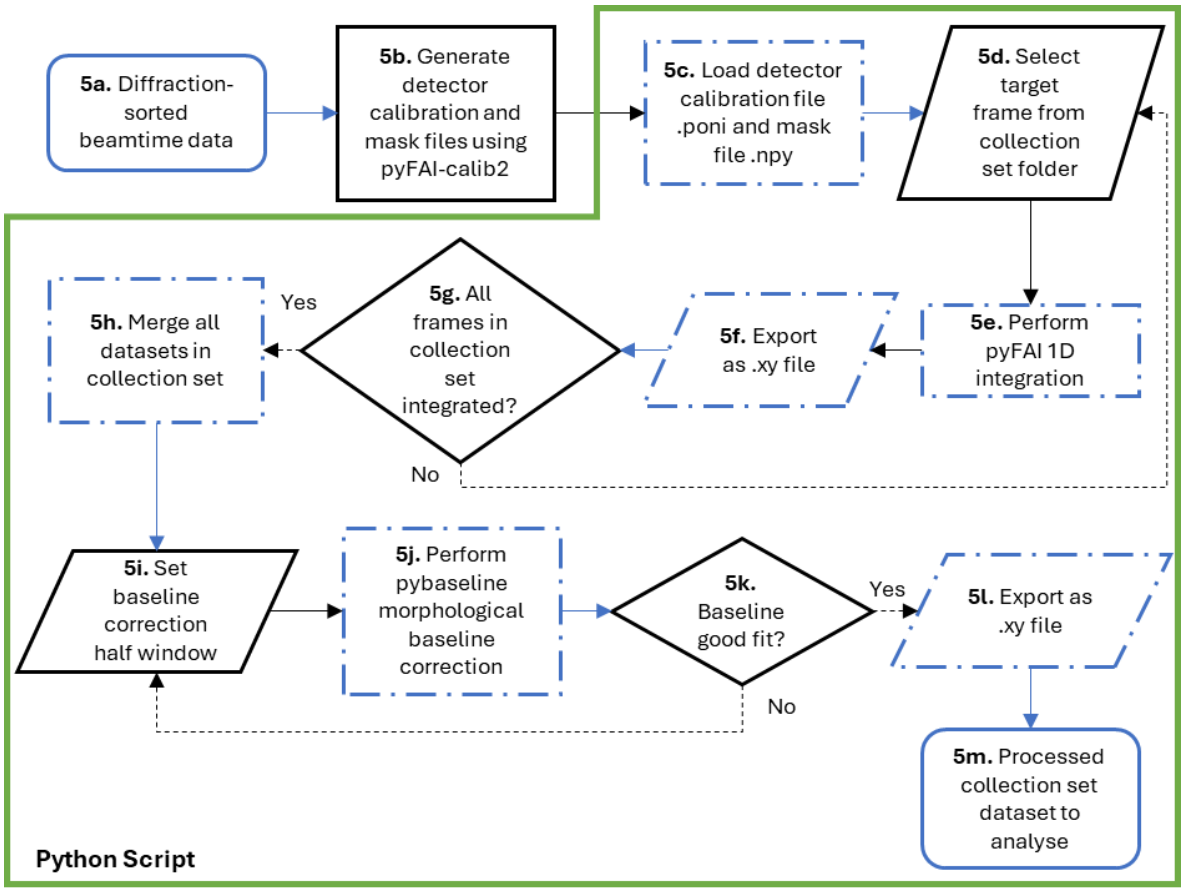

Figure 3.18: Workflow for post-merging baseline correction processing methodology with pyFAI integration, merging of raw datasets in a collection set and pybaselines morphological baseline correction (rawMerged_pybaselineCorrected.py).

The workflow follows the same general steps as the pre-merging baseline correction workflow with initial pyFAI-calib2 calibration and masking. The main change is the processing order, with first 1D integration on all datasets in a collection set (Steps 5d-g), merging the raw datasets, and then performing pybaseline morphological baseline correction once per collection set, exporting a single merged PXRD pattern for the collection set.

3.2.3.3 – Results and discussion

As with the thresholding processing regime, merging individual datasets for a collection set is necessary to achieve improved powder averaging and therefore the overall data quality in terms of relative peak intensities for extracting polymorphic ratios in data refinement stages. The comparison of a single dataset solved using the pre-merging baseline correction processing workflow and the merged 1_*o*ABA_45:60_1 X1_01 collection set pattern processed with the same technique are shown in Figure 3.19.

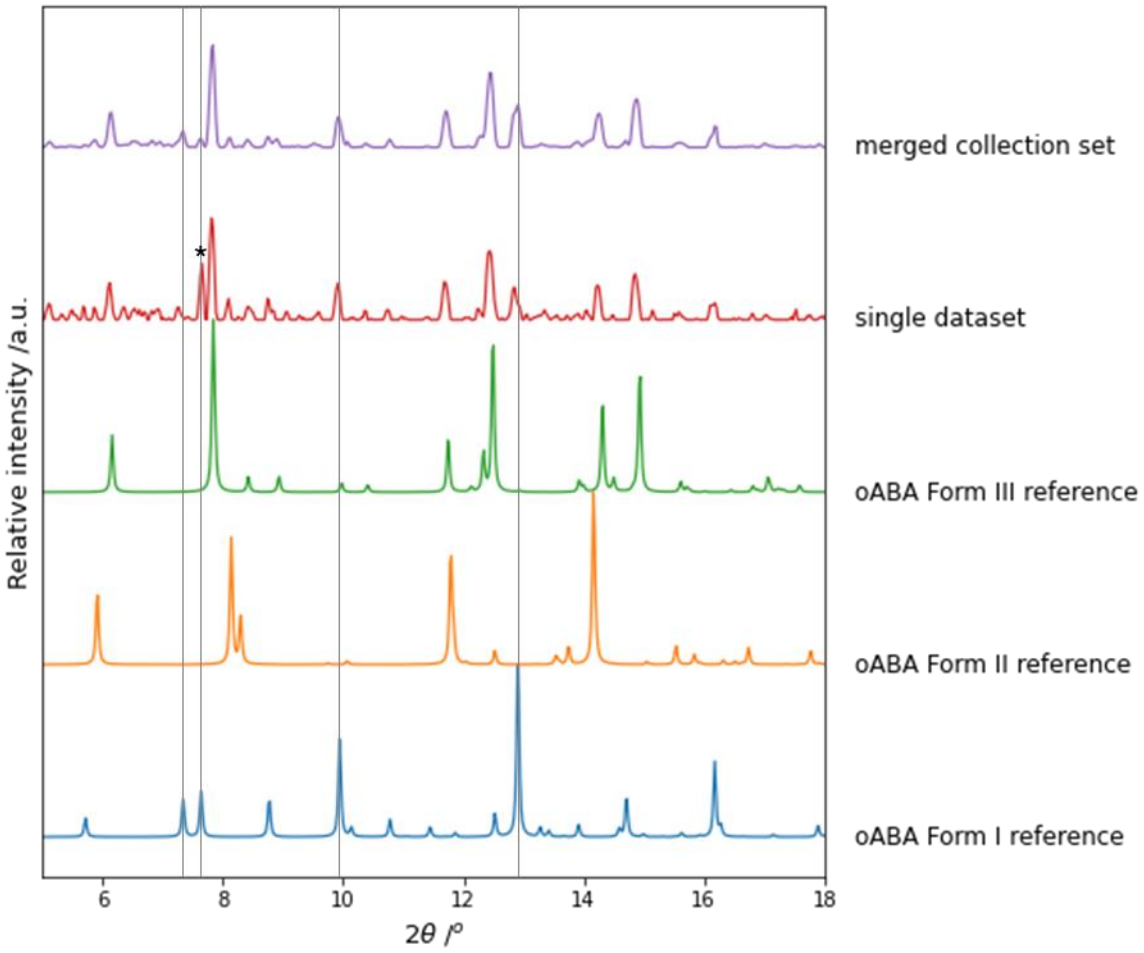

Figure 3.19: PXRD plot comparing reference oABA patterns against single dataset processed with pre-merging baseline correction workflow shown in Figure 3.16, and merged collection set for 1_oABA_45:60_1 X1_01 collection set. Marked peak (*) shows intense oABA Form I peak due to poor powder averaging.

A single dataset can show detailed polymorphic information with the example single dataset showing the presence of all three *o*ABA polymorphic forms, shown in Figure 3.19. However, the single acquisition does not achieve good powder averaging with the relative peak heights indicating a preferred orientation of crystals captured in beam: the Form I marked (*) peak at 7.64° 2θ shows significant intensity relative to the other main Form I peaks at 9.94° and 12.92° 2θ.

The merged 1_*o*ABA_45:60_1 X1_01 collection set, shown in Figure 3.19 consisting of seven merged datasets, shows more consistent relative peak heights for Form I, however, there remains some discrepancies; the 7.35° 2θ Form I peak more intense than the 7.64° 2θ peak. High background scattering noise in this region can account for some small discrepancies in peak heights in this region. Furthermore, merging patterns in a collection set improves the overall signal-to-noise, with the reduction in noise seen particularly in the high background scattering region 5 – 9° 2θ and the 13 – 14° 2θ region for the merged dataset.

3.2.3.3.1 – Comparing pre- and post-merging baseline correction methodologies

A comparison of the computational processing time for pre- and post-merging baseline correction processing workflows is shown below in Table 3.02.

Table 3.02: Comparison of processing times for pre- and post-merging Python pyFAI and pybaselines baseline correction workflows.

	Processing times for Workflow	
	Pre-merging baseline correction	**Post-merging baseline correction**
Total computational processing time per frame	3.02 s	2.42 s
Estimated total processing time with user input per frame	1 min	20 s
Estimated time for merging frames for a collection set	30 s	1 min
Estimated total processing time for all frames	4 hr 53 min	1 hr 38 min

The pre-merging baseline correction workflow (pyFAI_pybaseline_correction.py) takes a total of 3.02 s computational processing time per dataset for calibration, 1D integration, morphological baseline correction and exporting. Including user input time for the two user inputs and user decision for half width baseline correction, a single diffraction frame can be processed in a maximum of 1 min. For merging the baseline corrected datasets, it takes 0.17 s computational processing time to merge a collection set; including user input time for collection set folder location it takes a maximum of 30 s to merge a collection set. Therefore, the total processing time for the 293 individual *o*ABA diffraction frames was 4 hr 53 min, with the merging of 21 collection sets taking a total of 10:30 min, and diffraction frame sorting of 1 hr 45 min giving an overall total time of 6 hr 49 min for full processing of the *o*ABA beamtime data.

The post-merging baseline correction workflow (rawMerged_pybaselineCorrected.py) takes a total of 2.42 s computational processing time for the 1D integration Steps 5c-f per dataset, requiring only user input for frame selection. This gives an approximate total processing time per frame of 20 s. The average computational processing time for collection set merging and pybaseline correction (Steps 5h-l) is 0.93 s: with the addition of user input time for baseline correction half width giving a total processing time of 1 min per collection set. Overall, the post-merging baseline correction workflow would have a total processing time of 1 hr 38 min for the 293 *o*ABA diffraction frames dataset 1D integration, with 21 min for collection set merging and baseline correction and 1 hr 45 min for the initial diffraction frame sorting. This results in a total processing time of 3 hr 34 min for *o*ABA beamtime data

processing. The processing steps for the two workflows with pyFAI-calib2 calibration, pyFAI 1D integration, and morphological baseline correction with pybaselines mor() remain unchanged: modifying the order in which these processes occur to require one user input for baseline correction of merged datasets, rather than each individual dataset, significantly reduces the total processing time. Diffraction patterns output using the two workflows are compared in Figure 3.20.

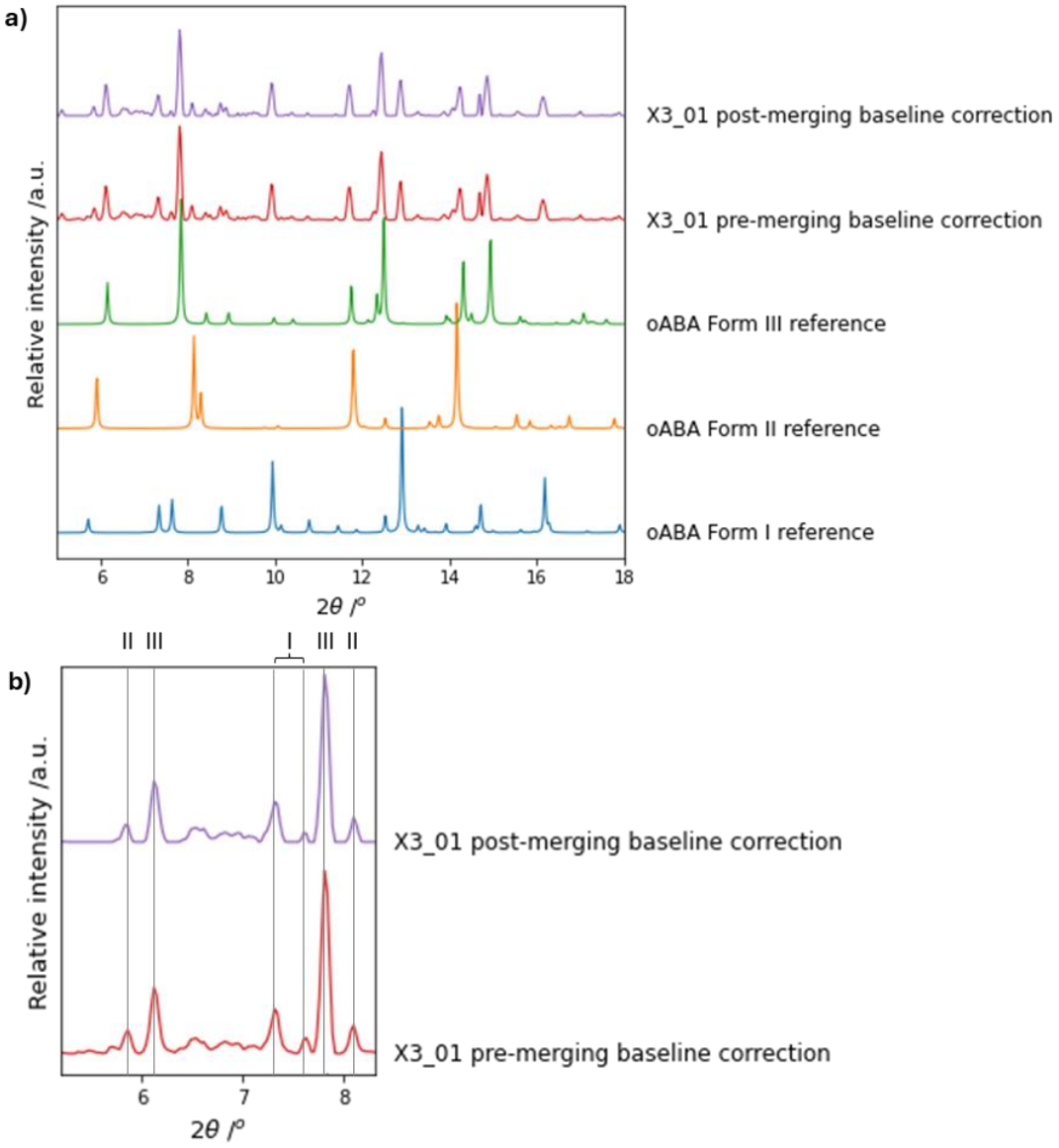

Figure 3.20: Diffraction patterns of 1_oABA_45:60_1 X3_01 collection set processed with the two processing workflows with pre- and post-merging baseline correction against oABA references. a) shows full diffraction patterns, b) showing the of 5 – 8° 2θ region. Key oABA Form I-III peaks marked on 5 – 8° 2θ plot.

As shown in Figure 3.20, both diffraction patterns shown some remaining noise in the 5 – 8° 2θ region: the region with high background scattering intensity, as shown previously in Figure 3.15. However, there is not a considerable difference between the two patterns for the different processing regimes (Figure 3.20b),

with a slight reduction in noise for this dataset with the post-merging baseline correction technique.

Given the increased processing speed for the post-merging baseline correction technique and no significant changes in processing outcome in terms of residual noise or signal-to-noise, it is the preferred workflow for baseline correction data processing.

3.2.3.3.2 – Comparing thresholding and baseline correction workflows

To validate that the post-merging baseline correction technique was the preferred processing workflow for I11 *in situ* diffraction of segmented flow, the processed collection set patterns were compared against the equivalent patterns processed with the thresholding technique. Comparison is shown below in Figure 3.21.

The PXRD patterns produced using the baseline correction technique show higher noise than the thresholding, predominantly in the 5 – 8° 2θ region. Collection set X2_02 shows a lower signal-to-noise due to the low crystal density in-beam at this point in the temperature cycling process due to dissolution of the hot column on the KRAIC-T; this results in high noise in the 5 – 8° 2θ region.

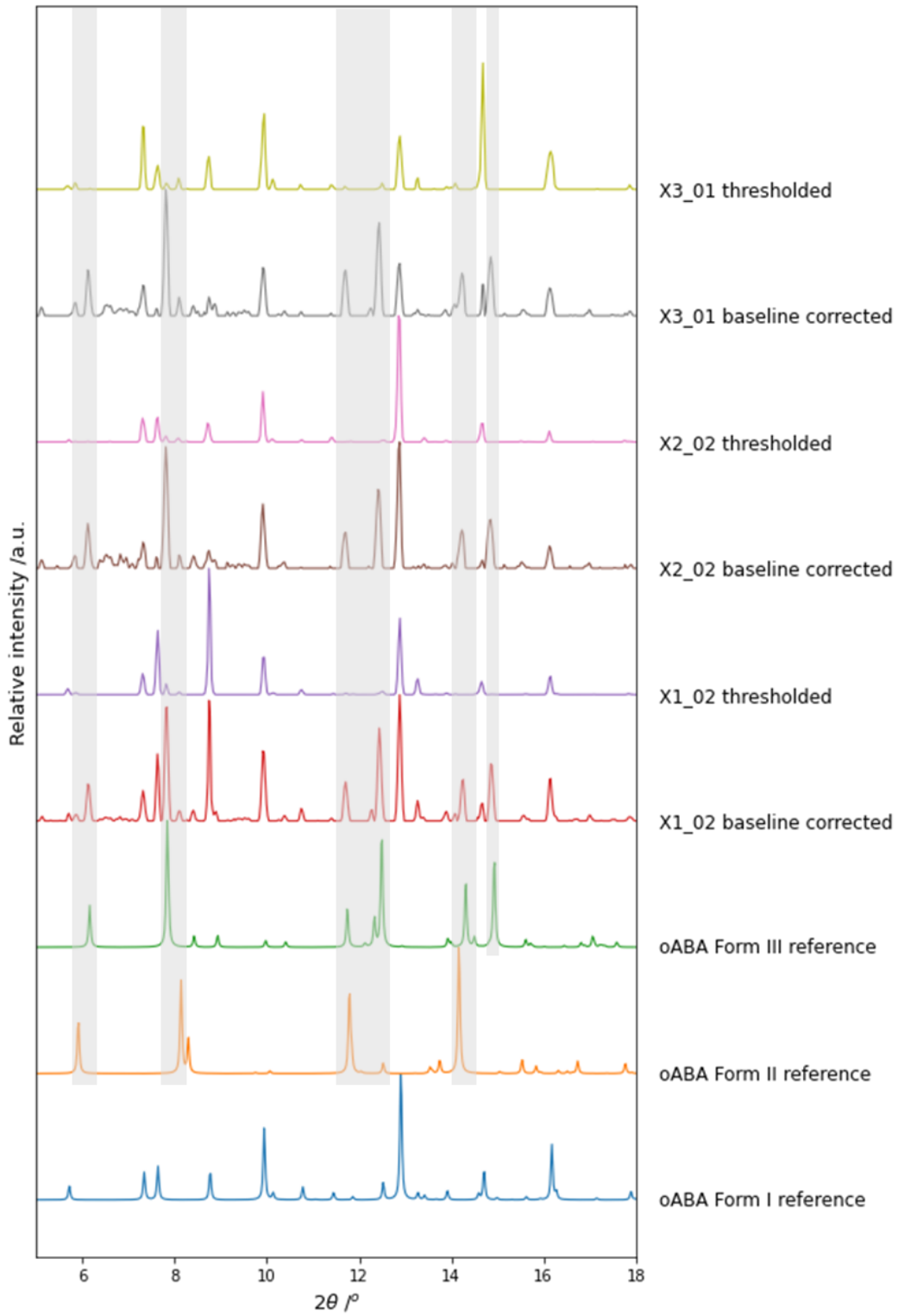

Figure 3.21: PXRD plots of reference oABA patterns against 1_oABA_45:60_1 collection sets processed using the thresholding technique and morphological baseline correction technique. Highlighted key oABA Form II and III peaks which lose intensity with the thresholding technique.

With the thresholding technique, the majority of powder patterns show predominant *o*ABA polymorphic Form I with trace Form II and III. However, for the baseline corrected patterns, the dominant diffraction peaks are Form III with Form I and trace Form II. This is likely due to poor availability of good-fit

backgrounds with the thresholding technique causing the over-subtraction of signal in the 5 – 8° 2θ region, or under-subtraction requiring over-thresholding. This results in the loss of key Form III diffraction peaks at 6.16° and 7.84° 2θ. Visual inspection of the baseline fit with the baseline correction technique prevents over- or under- correction (shown in Figure 3.17), resulting in a truer representation of polymorphic presence in term of relative peak heights.

For an example where strong Form III presence was found with the thresholding technique is compared against the equivalent baseline corrected pattern in Figure 3.22.

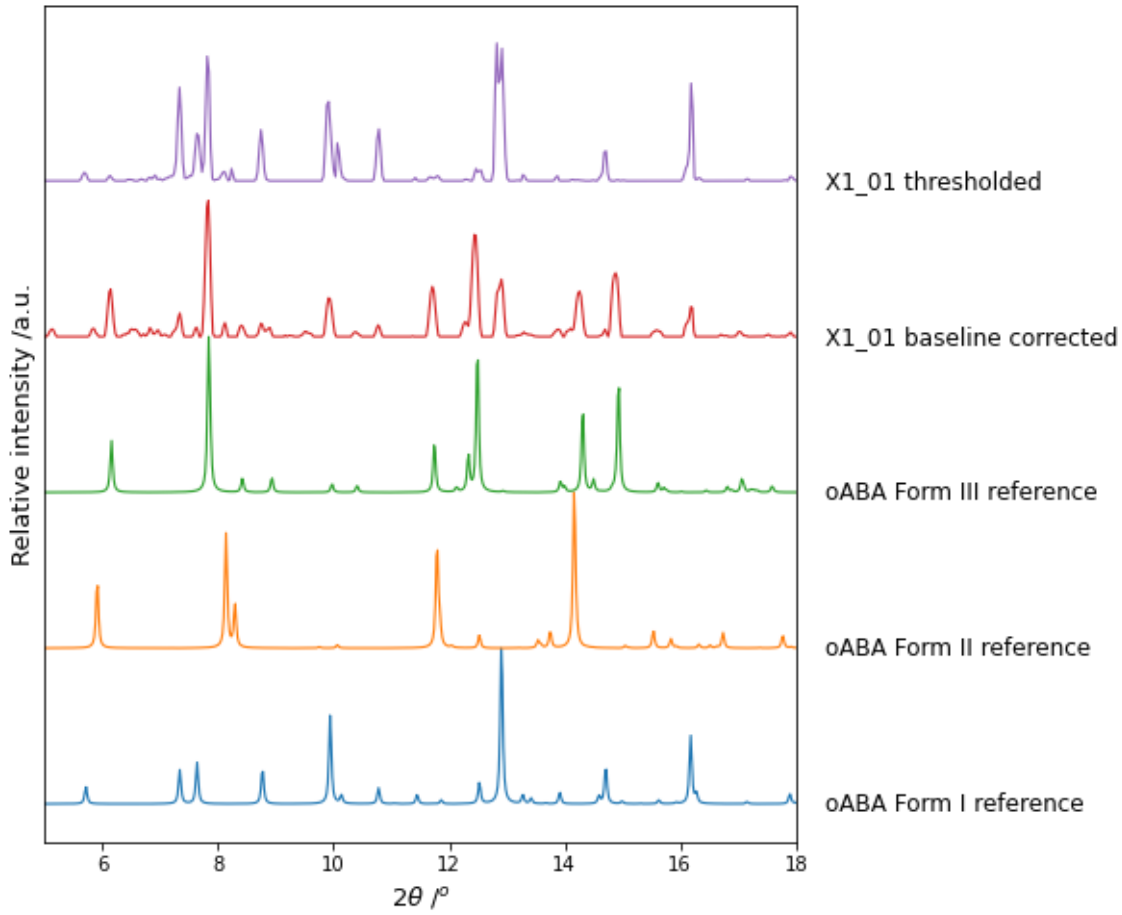

Figure 3.22: PXRD plot of reference oABA patterns against 1_oABA_45:60_1 X1_01 collection set processed using the thresholding technique and morphological baseline correction technique.

The resultant thresholding pattern shows strong Form III presence at 7.84° 2θ but has inconsistent relative Form III peak heights with minimal signal intensity for what should be a strong Form III peak at 12.50° 2θ. The overall polymorphic presence remains predominantly Form I but shows issues with peak splitting at 12.90° 2θ caused by potential over-thresholding required to remove the bulk of noise.

As discussed previously in Section 3.2.3.3.1, the post-merging baseline correction technique has a total estimated processing time of 3 hr 34 min for

*o*ABA beamtime data: 1 hr 45 min for diffraction frame sorting, 1 hr 38 min for *o*ABA diffraction frame processing and 21 min for baseline correction of collection sets. Conversely, the thresholding technique (discussed in Section 3.2.2.3) has a total estimated processing time of 11 hr 30 min for *o*ABA diffraction frame processing due to the increased processing time for the background auto selection and the thresholding iterative loop requiring reintegration for each threshold iteration. Also, the post-merging baseline correction is significantly quicker due to only performing the baseline correction per collection set rather than per diffraction frame, significantly reducing the overall processing time.

Given the significant reduction in processing time, non-reliance on collection of background frames and improvements in data quality in terms of relative peak heights and more uniform extraction of diffraction signal with a truer representation of polymorphic balance, the post-merging baseline correction is the preferred processing method for I11 segmented flow data collected via the slug triggering data acquisition technique. The post-merging technique visualises all 1D raw integrated diffraction patterns (as shown in Figure 3.15) to ensure the user can inspect the patterns for unique peaks on a single diffraction pattern. If these peaks are lost on the final pattern, processing with the post-merged technique would be preferred.

3.2.3.3 – Conclusions

The development of a morphological baseline correction technique has shown significant improvement for the processing workflow of I11 *in situ* PXRD of segmented flow collected with the slug triggering mechanism. For the comparison of different baseline correction workflows (pre-merging and post-merging baseline correction), an efficient workflow with merging of raw 1D pyFAI integrated datasets and performing pybaselines morphological baselines correction on the merged collection sets (post-merging baseline correction) was found to reduce the total processing time of example *o*ABA beamtime data to 3 hr 34 min compared to 6 hr 49 min for the pre-merging workflow. A comparison of the resultant collection set data with the pre- and post-merging technique showed minimal differences in output PXRD patterns in terms of signal-to-noise, relative peak heights, and polymorphic forms present.

Comparison of the post-merging baseline correction technique and the thresholding technique showed considerable differences in the resultant PXRD patterns: whilst the baseline correction datasets showed more apparent noise, the extracted diffraction peaks showed a truer representation of polymorphic presence and improved relative peak heights. Furthermore, the thresholding technique relies on a high number of background frames to achieve good-fit background subtraction to extract the highest signal-to-noise is unsuited to data collected with the slug triggering technique due to the high hit-rate of crystalline slugs minimising background collection.

In conclusion, the preferred processing method for I11 *in situ* PXRD of segmented flow collected with the slug triggering mechanism is the post-merging baseline correction technique. This technique shows efficient processing speeds and improvement in data quality with extraction of high signal-to-noise improving the identification of polymorphic forms of *o*ABA example data. The main inefficiency of this data processing workflow is the user input required for 1D integration of individual frames, which is addressed by the development of a multi-frame collection set processing technique below in Section 3.2.4.

3.2.4 – Multi diffraction frame processing with post-merging baseline correction in Python (pyFAI_multi_pybaselines.py)

3.2.4.1 – Introduction

Discussed in the Section 3.2.3 is the development of a post-merging baseline correction processing workflow: it showed improvements in total processing time and resultant data quality compared to the previous thresholding processing technique. Performing 1D integration with pyFAI on individual diffraction frames, merging a collection set, and then performing a single pybaselines morphological baseline correction was shown to be the most efficient method at 1 hr 59 min estimated processing time for the *o*ABA beamtime data example. Furthermore, this technique did not compromise on data quality, with high signal-to-noise and a more accurate polymorphic resolution than previous thresholding techniques.

The majority of processing time for the post-merging baseline correction technique was Step 5d where the user input required to change between individual diffraction frames and the repetitive loop to complete the 1D integration for all diffraction frames. Given that user input time accounts for the inefficiency of the post-merging baseline correction processing methodology, a streamlined processing workflow was developed to perform the technique on every diffraction frame in a specified folder (collection set). This workflow, the multi-frame baseline correction technique is discussed in this section.

3.2.4.2 – Methodology

Similar to previous methodologies, the initial stages of the workflow, for diffraction frame sorting, pyFAI-calib2 integration and masking is required. The multi-frame baseline correction workflow is summarised in Figure 3.23.

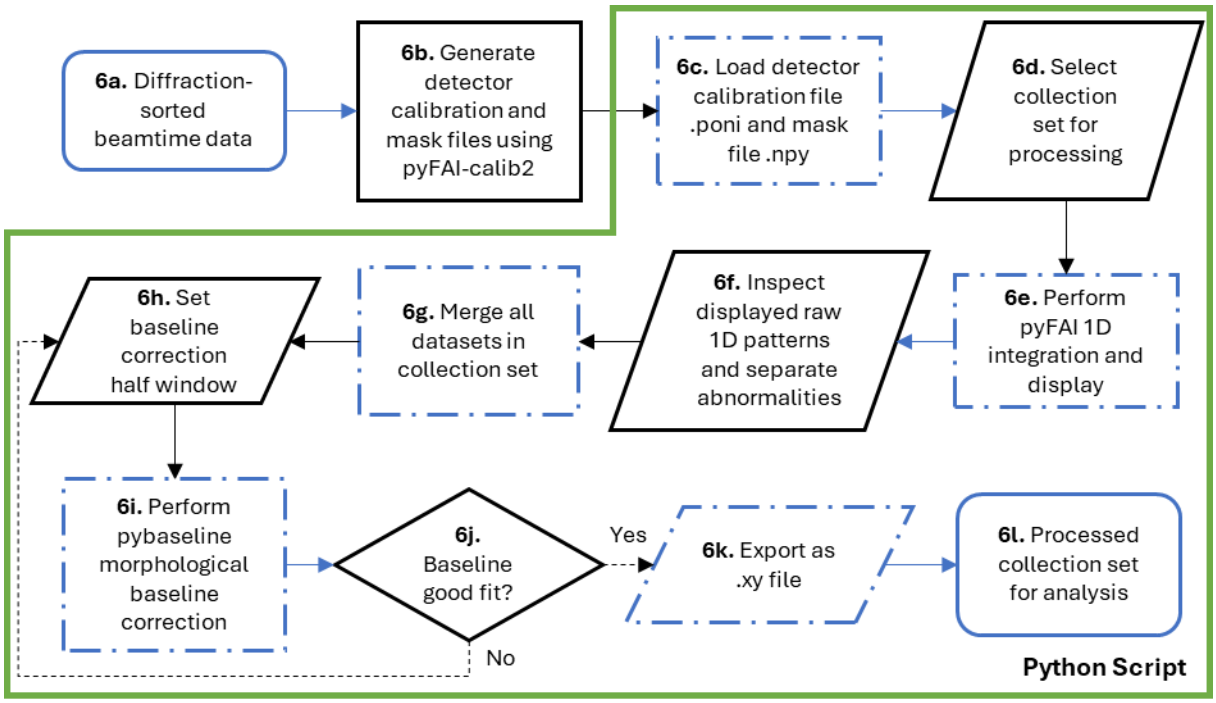

Figure 3.23: Workflow for multi-frame baseline correction PXRD processing procedure.

The workflow 1D integrates every diffraction frame from a specified collection set folder using pyFAI calibration, masking, and 1D integration (Steps 6b-e). This workflow includes a step for user inspection of the raw 1D patterns for outlier identification – for example, the occurrence of a blockage where diffraction intensity increases rapidly with successive frames, or removal of diffraction frames with low diffraction. Example of raw 1D pattern inspection shown below in Figure 3.24.

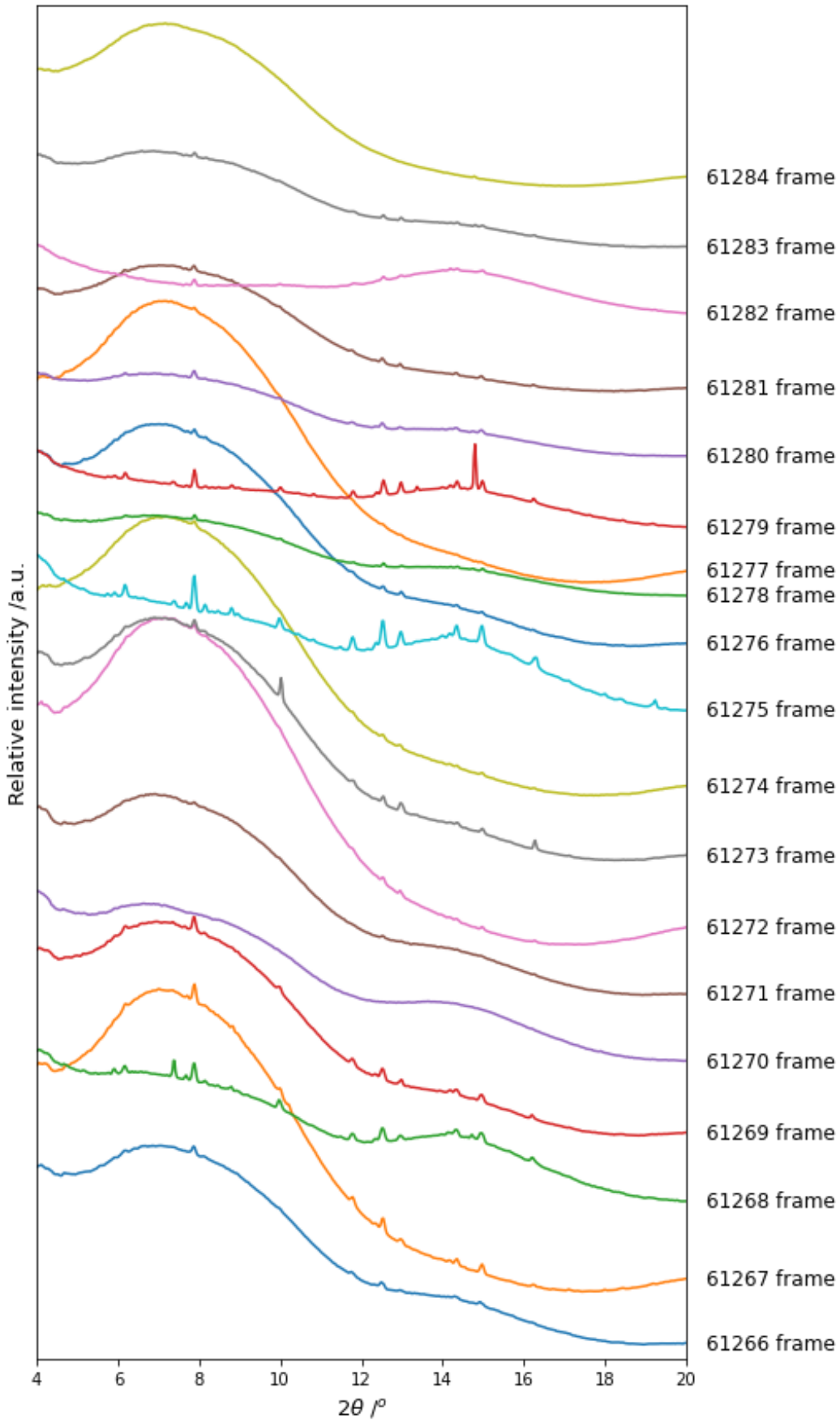

Figure 3.24: Raw 1D diffraction plot for diffraction frames in 1_oABA_45:60_1 X3_01 collection set.

In the Figure 3.24 example, no blockage build up is found, however, low signal-to-noise diffraction patterns the 61270 patterns would be removed due to no visible peaks in the 1D plot. In previous workflows, individual patterns would be inspected in this manner during the baseline correction or thresholding steps; this multi-frame workflow specifies this as Step 6f to ensure nothing is missed in this more automated process.

The morphological baseline correction iterative loop (Steps 6h-j) is carried out on the merged collection set pattern, as per the previous methodologies with half width baseline correction modification described in Figure 3.17 previously. The baseline corrected pattern for the collection set is exported as an .xy file for further analysis and polymorph identification.

3.2.4.3 – Results and Discussion

The visualisation of the raw 1D patterns, shown in Figure 3.15 and Figure 3.24, ensures the user can inspect the patterns for any unique peaks, such as polymorph present on a single pattern; should this occur, individual pybaseline correction with the pre-merging technique can be used to investigate in further detail.

The multi-frame baseline correction technique takes a computational processing time of 4.91 s for a collection set with 19 diffraction frames (1_*o*ABA_45:60_1 X3_01); the average collection set contains 14 diffraction frames. Accounting for user input time for the collection set folder location, inspection of 1D patterns and separation of outliers, and baseline correction iterative loop, the estimated processing time per collection set is 3 min. For the 21 collection sets for the example *o*ABA beamtime data this gives an estimated total processing time of 2 hr 48 min including the diffraction frame sorting process. This more streamlined process removes the manual diffraction frame input loop from the post-merging baseline correction, replacing it with an automatic collection set folder processing: this overall reduces the estimated processing time from 3 hr 34 min to 2 hr 48 min.

3.2.4.4 – Conclusions

Overall, coupling the diffraction frame sorting script with the fast processing script creates an efficient data processing pipeline for separating diffraction frames and processing collection set powder pattern for analysis. This efficient processing workflow takes an estimated 2 hr 48 min processing time for the example *o*ABA beamtime data; faster than the individual post-merging baseline correction workflow 3 hr 34 min estimated processing time for the same produced diffraction pattern.

3.2.5 – Rietveld Refinement

To confirm the quality of the final processed datasets using standard powder diffraction analysis techniques, the KRAIC-T datasets were profile fitted with the Rietveld refinement method in the TOPAS software.[16,17] Rietveld refinement, as introduced in Chapter 2, refines a structural model to best fit an experimental diffraction pattern. The Rietveld method can be particularly useful to identify different crystal forms in a powder sample, providing a relative weight percentage balance of the different phases present.

The patterns processed with the background subtraction and thresholding technique could not be solved for phase analysis with the Rietveld method: this is likely due the combination of the low signal and poorer powder averaging seen for the thresholded patterns (Figure 3.22). For the baseline corrected processed patterns, the Rietveld refinement could identify the presence or absence of *o*ABA polymorphs when fitted against the *o*ABA reference data. However, the Rietveld fitting was slightly improved by preferred orientation corrections (Figure 3.25); the powder averaging in the summed datasets is not equivalent to typical powder averaging where data is collected from millions of crystallites in random orientations.

From the refinement, the polymorphic percentage of each phase was extracted and used to compare the crystallisation runs of *o*ABA. These values are not definitive, especially from *in situ* systems with limited powder averaging, but give an idea on the presence of polymorphic forms and whether they are present to a major or minor degree. The baseline corrected patterns show an improvement in powder averaging compared to the thresholded technique and provide a more realistic insight into the quantities of polymorphs present.

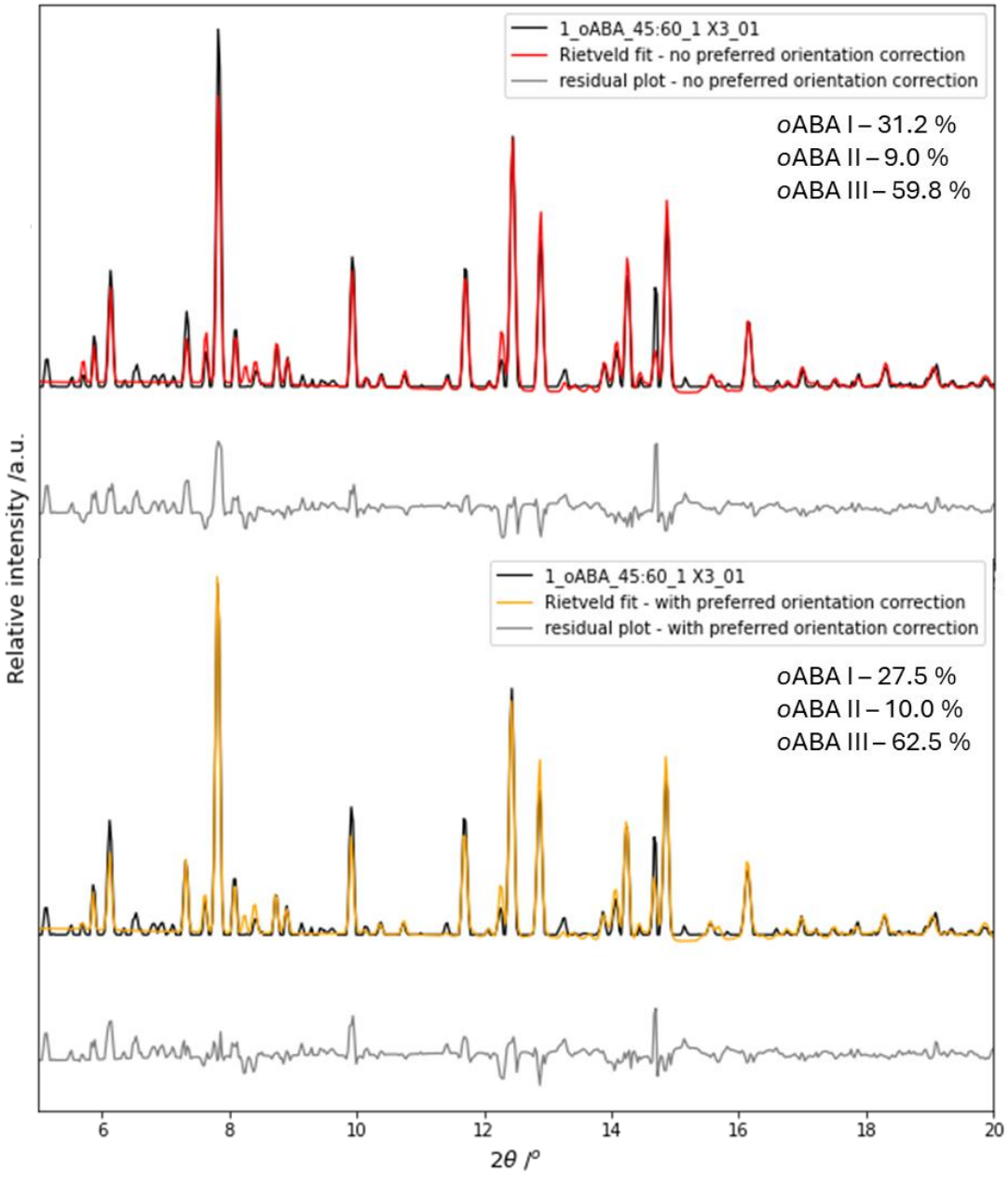

Figure 3.25: Rietveld refinement plots for oABA data with and without preferred orientation correction. Preferred orientation correction results in a slightly improved residual plot by accounting for the oABA Form III peak at 7.8 ° 2ϑ. Resulting oABA polymorphic percentages annotated.

3.2.6 – Overall Conclusions

Development of I11 PXRD processing scripts in Python gives open access to the processing techniques with open source Jupyter notebook used for the developments presented here. Example data from the KRAIC-T *o*ABA temperature cycling segmented slurrying beamtime (CY30306-1) was used to assess and quantify improvements to the processing technique. The *o*ABA data differs from previous I11 KRAIC-D data acquired with continual 100 ms acquisitions by using a newly developed data acquisition technique, discussed

further in Chapter 5. The slug triggering data methodology acquires PXRD from multi-crystalline slugs in flow for an elongated 1.7 s, resulting in datasets with higher signal-to-noise and a higher hit-rate of diffraction frames with minimal frames containing background scattering only.

The first script developed (diffraction_sorting.py) is a tool to assist sorting diffraction frames from background scattering only, reducing the total time spent sorting frames and producing hit-rate statistics required for assessment of the slug triggering technique, discussed further in Chapter 5.

Several data processing workflows were developed, the first focussing on transfer and improvement of the thresholding background subtraction technique from MATLAB to Python. A developed background frame selector automatically selects the best-fit background to extract the best signal-to-noise from the thresholding process, reducing the user input required per dataset. Python library pyFAI, a specialist XRD module for azimuthal integration of area detector data, enabled streamlined calibration, masking, and 1D integration for a total 2.4 s computational processing time per dataset – a significant decrease from the 27.3 s computational processing time for the equivalent steps in MATLAB. Through the combination of an auto background fit step and pyFAI 1D integration, total processing time was significantly reduced from an estimated 19 – 40 hr for the MATLAB script to 11 hr 30 min for the Python thresholding process. However, the reliance of this technique on a range of background frames for well-matched background scattering subtraction proved to be unsuitable for slug triggering data collections: slug triggering improves crystal high hit-rates compared to the previous KRAIC-D data collections, which does not provide a suitable range of background scattering to achieve high signal-to-noise.

Due to the issues with the reliance of the thresholding technique on the number of background frames, an alternative background correction methodology was trialled using morphological baseline correction. The raw 1D integrated patterns show broad background scattering features with narrow diffraction signal, making it a candidate for morphological extraction of diffraction features. Using pybaselines: a Python library for baseline correction of experimental data, multiple processing workflows were developed using the morphological baseline correction technique to assess the most effective and efficient process. The preferred technique was found to be 1D integration of the diffraction frames in a collection set with pyFAI, merging the collection set raw patterns, and finally baseline correction on the merged pattern. The converse method of baseline correction on every 1D pattern, then merging was found to take significantly longer; an estimated 6 hr 49 min compared to 3 hr 34 min for the post-merging technique. The two methods showed no significant difference in output PXRD patterns in terms of signal-to-noise and overall noise. The preferred post-merging technique was compared against the thresholding results to assess the efficacy; morphological baseline correction showed improved extraction of diffraction signal in the sample *o*ABA datasets, particularly in the high background scattering regions (5 – 9° 2θ). The thresholding technique likely over-background subtracts or under-subtracts in

this region from poor background matching. This causes uneven loss of diffraction signal in this region and a misrepresentation of polymorphic forms. This problem was unlikely to be an issue for previous KRAIC-D data acquired with 100 ms acquisitions due to the high number of background frames collected, allowing for a better background match: it is a more prevalent issue with the slug triggering data collection with higher hit-rate of crystalline slugs, and low background only collection. The post-merging baseline correction technique was modified further for multi-frame collection set processing to provide a more efficient process: processing the *o*ABA example data with an estimated 2 hr 48 min total.

Overall, several processing workflows have been developed for processing of *in situ* PXRD data for segmented flow. With the example *o*ABA beamtime data, morphological baseline correction was shown to be the best background scattering correction technique due to the quality of the data produced, and overall processing speed. Processing in Python and use of pyFAI and pybaselines Python libraries has significantly decreased computational processing time – with pyFAI 1D integration taking 2.4 s as opposed to the 27.3 s for the equivalent MATLAB process.

3.2.7 – Future work

All developed scripts will be made available for future users of Beamline I11 for processing of *in situ* PXRD data during segmented flow; the open source Python scripts should be more accessible for users than the licensed MATLAB software. Given the speed of processing, this now allows for data processing during beamtimes to inform experimental decisions, rather than performing experiments without knowing the results. This could maximise scientifically relevant beam usage, a benefit to Diamond and the users themselves.

Given the current speed of processing with the Python workflows and individual processing workflow developed, there is scope to include auto-processing into the General Data Acquisition (GDA) software as part of the data acquisition process. This would require collaboration with Diamond data scientists to adapt GDA's current Python auto-processing to be tailored to the segmented flow technique with pyFAI and pybaseline morphological baseline correction, coupled with the slug triggering data acquisition. Users would need to input pyFAI-calib2 calibration and an initial detector mask at the beginning of beamtime with an initial half width for morphological baseline correction. The automated processing could provide near instant results improving the ease-of-use for non-expert users and improve beamtime output. The patterns could be reprocessed at a later stage to improve output PXRD patterns, should the initial half width or masking inputs be non-ideal.

Alongside the basic morphological baseline correction used here, the pybaselines library also contains various versions of morphological baseline correction and smoothing effects that could potentially improve the data quality extracted or reduce the overall noise. A future investigation to further refine the

baseline correction methodology would be beneficial to potentially improve the processing technique and resultant data output further.

The processing methodologies have been developed using *o*ABA beamtime data during slurrying, meaning generally a high crystal density in beam: future processing methodology development would be advisable with a range of crystal densities to assess overall efficacy. These scripts have been adapted and tested with lab source PXRD data of segmented flow crystallisation from the Flow-Xl facility, discussed in Section 3.3 of this Chapter.

3.3 – PXRD processing development for the Flow-Xl facility

3.3.1 – Introduction

The KRAIC-Xl crystalliser at the Flow-Xl facility is a tri-segmented flow crystalliser for lab source *in situ* X-ray diffraction analysis, shown below in Figure 3.26. The Flow-Xl facility is designed for the time resolved, *in situ* study of crystallisation processes with X-ray diffraction and Raman spectroscopy, housing a custom Rigaku XtaLab Synergy Custom X-Ray Diffractometer with Horiba Labram HR Evolution Raman Microscope w/ External Raman Probe. Prior to the Flow-Xl facility, *in situ* XRD flow studies required a synchrotron X-ray source due to the high background scattering environments and resultant attenuation of the beam requiring higher energies and a high brightness of the beam. The state-of-the-art X-ray diffractometer has shown the capability to study and provide phase information during micro and milli fluidic flow crystallisation processes.[18] The Flow-Xl facility aims to reduce the demand for synchrotron time, providing an alternative method for X-ray studies, or to give users with feasibility experiments and preliminary data for beamtime to provide a basis for beamtime applications. The CrysAlisPro software developed by Rigaku typically is used for the processing of single crystal XRD data, however, the collaboration between the Flow-Xl facility and Rigaku has enabled development of the software for Frame Selection for flow reactor powder experiments and PXRD pattern extraction.[19]

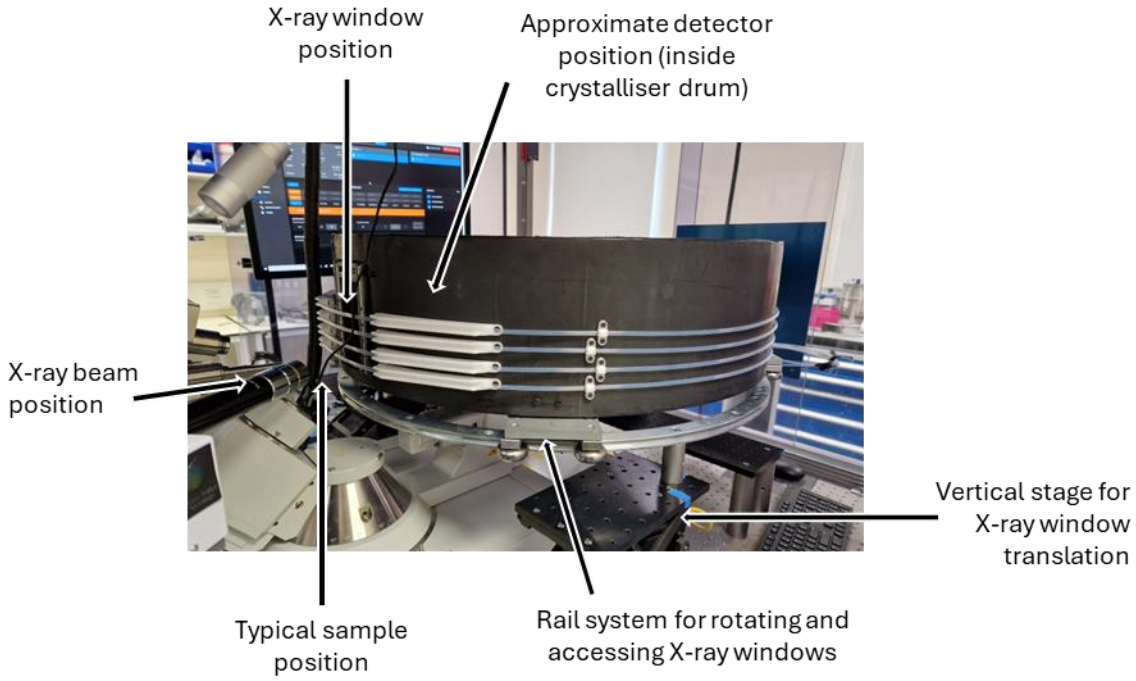

Figure 3.26: Image of the KRAIC-Xl in the Flow-Xl X-ray enclosure with annotations to show positions of beam, X-ray windows, detector, typical sample positions, and movement rail and vertical translation stage.

The KRAIC environment provides challenges for lab-source study due to the increased material in beam (compared to smaller, microfluidic devices) which may cause attenuation, reducing the possible diffraction signal. As such, the

KRAIC-Xl was developed as a proof-of-principle crystalliser to assess if lab-source *in situ* XRD is possible in a larger, meso-scale crystallisation system. The development of the KRAIC-Xl is discussed further in Chapter 4, alongside the proof-of-principle crystallisation studies. The crystallisation studies investigated the ethanol anti-solvent crystallisation of model compounds L-glutamic acid (LGA) and glycine (GLY) from aqueous solution.

LGA is a polymorphic material with two polymorphs, a metastable α-LGA and the stable β-LGA.[20] The LGA crystallisations used a 20.00 g/L aqueous feedstock dissolved at 60 °C, with "nucleation promoter" jacketed tubing at 14 °C after anti-solvent addition and segmentation to promote further crystal nucleation and growth. The crystallisation and crystal growth post-nucleation promoter on the main body of the crystalliser was at ~25 °C. For a total flow rate of 6.00 mL/min, the anti-solvent fractions for ethanol addition to LGA solution was varied by modifying the ratio of solution and ethanol flow rates, for ethanol fractions varying between 0.300 – 0.500. GLY is another model polymorphic compound with three polymorphic forms: the stable γ-GLY, and the metastable α-GLY and β-GLY forms.[21] The GLY anti-solvent crystallisations in the KRAIC-Xl were conducted with GLY aqueous feedstocks of ~62.5 g/L dissolved at 24 °C. Anti-solvent addition took place in a slightly increased temperatures of 28 – 33 °C, with the remainder of the crystal growth taking place at the Flow-Xl enclosure temperature of ~25 °C. The majority of conditions studied used a total flow rate of 8.20 mL/min, similarly, varying the ratio of solution and ethanol flow rates to vary the anti-solvent fractions to between 0.400 – 0.520. For both LGA and GLY crystallisations, increased anti-solvent fractions increased the crystal density produced, and was discovered to be a key factor for *in situ* PXRD data collection with the lab source system with KRAIC-Xl. For more details on the LGA and GLY crystal structures, crystallisation conditions, and crystallisation results in terms of the polymorphic forms grown, see Chapter 4.

The KRAIC-Xl uses three X-ray windows with the Aquapel-coated, Kapton PTFE union design to enable time-resolved crystallisation studies in segmented flow. Due to the compact X-ray enclosure, the KRAIC-Xl was mounted on a rotating rail system to move the crystalliser to access and replace the windows in the event of a blockage. During crystallisation trials of L-glutamic acid (LGA) and glycine (GLY), the X-ray instrument used Copper K-α X-ray energy at 1.5406 Å with HyPix-6000HE detector of 800 x 775 px with 100 µm pixel size with continuous, pulsed 100 ms frame acquisitions. The detector acquisition is equivalent to the original KRAIC-D data collection at Beamline I11. The GLY anti-solvent crystallisation proof-of-principle experiments were successful, with diffraction data captured during several conditions and X-ray windows. LGA anti-solvent crystallisation showed reduced crystalline material and minimal diffraction noted. The resultant diffraction frames were similar to the original KRAIC-D frames, with similar background scattering levels, and diffraction spots or smeared spots, not forming powder rings forming as with KRAIC-T slug triggering acquired data. The diffraction spots are considerably larger and diffuse in comparison to the synchrotron data. The comparison of KRAIC-D and KRAIC-Xl data frame is shown below in Figure 3.27. GLY data was used to

develop the processing methodology, see Chapter 4 for further experimental details.

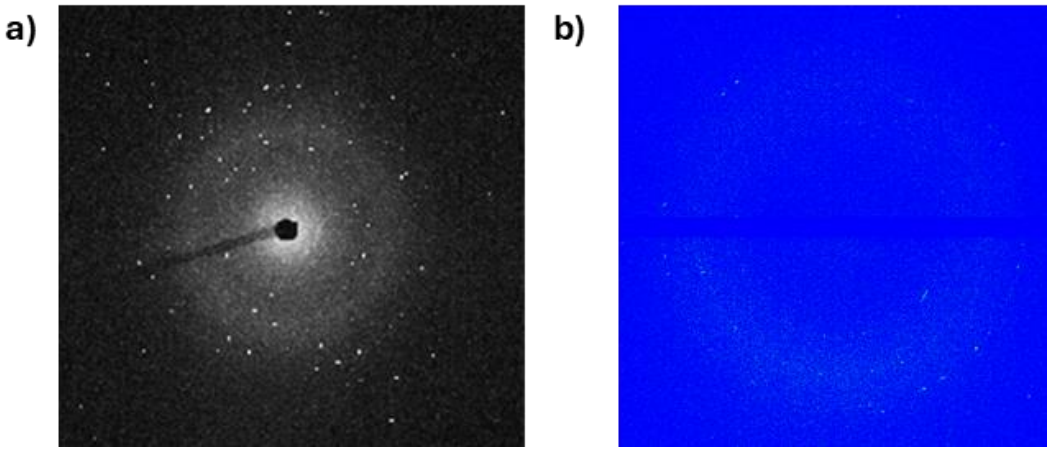

Figure 3.27: Diffraction frames of 100 ms acquisition for a) carbamazepine collected with the KRAIC-D on Beamline I11 EH2, and b) glycine collected with the KRAIC-Xl at the lab-source Flow-Xl facility.

3.3.2 – Methodology development

The processing workflow for KRAIC-Xl data is shown below in Figure 3.28. The workflow uses the key defined previously in Figure 3.04, with “Script” outline also used for CrysAlisPro elements for the Flow-Xl workflow.

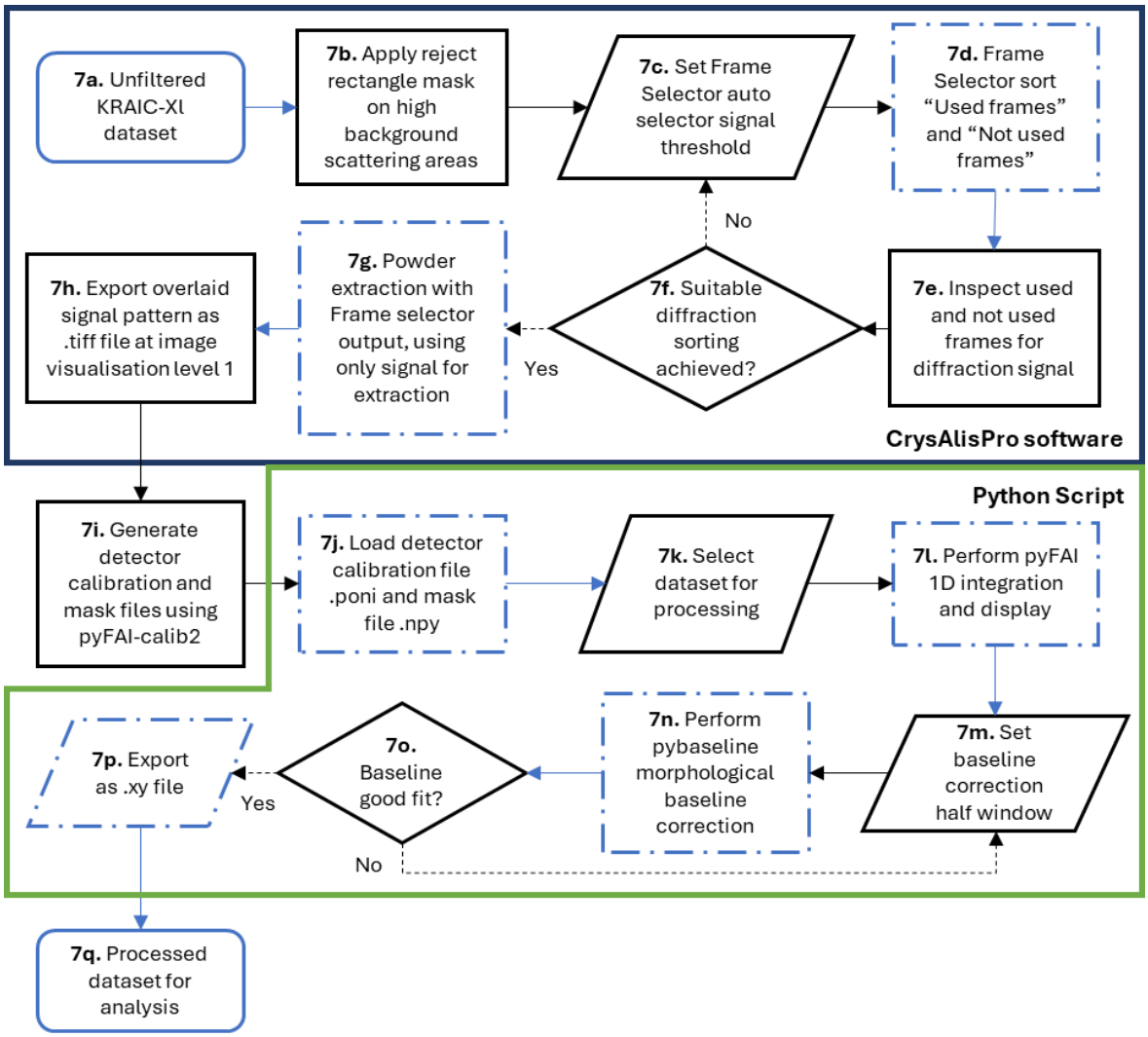

Figure 3.28: Workflow for the processing of KRAIC-Xl data collected at the Flow-Xl facility, using CrysAlisPro and Python scripts in Jupyter notebook.

The workflow uses the Frame Selector functionality in the CrysAlisPro software to filter diffraction frames from background scattering only frames (Steps c – f).[19] The Frame Selector was developed by Rigaku for the Flow-Xl facility for the purpose of flow reactor powder data extraction and uses a diffraction signal threshold level to set the status of a diffraction frame to "Used" or "Not used". Visual inspection by the user of the Frame Selector output is required to check the sorting of diffraction and background frames, with the Data Collection Movie mode in the software enabling quick judgement of the diffraction frame sorting.

The Frame Selector tool outputs the frame status into the Powder Extraction tool in CrysAlisPro, which creates an overlaid diffraction pattern with the option to use all signal or diffraction signal only, the comparison of the diffraction frames options and resultant PXRD pattern is shown below in Figure 3.29.

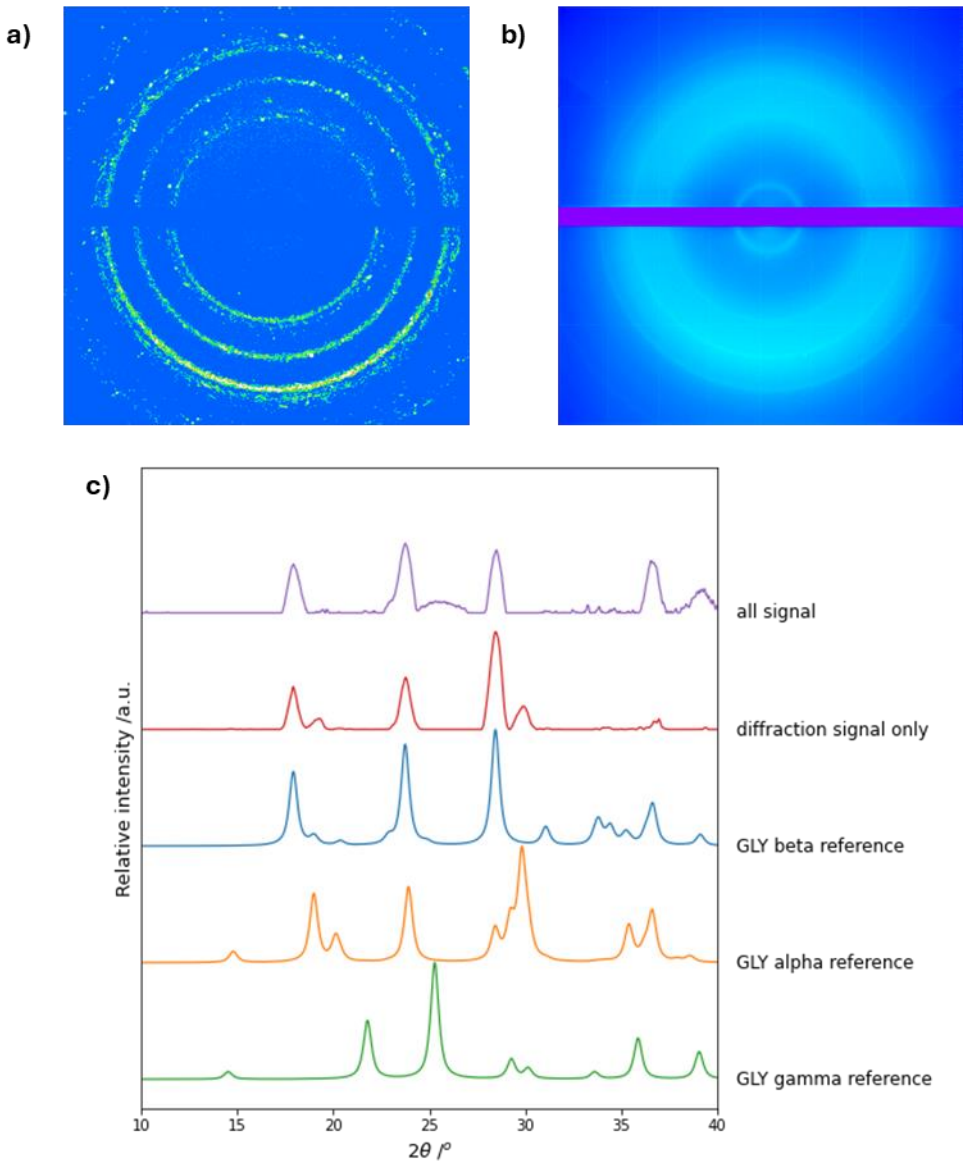

Figure 3.29: Overlaid diffraction frames from the Powder Extraction tool for a) diffraction signal only, b) all signal, and c) resultant processed PXRD patterns against GLY references generated from Mercury (GLYCIN, GLYCIN01, and GLYCIN02 for β-, γ-, and α-GLY forms respectively.[22–24]

Using all signal for the overlaid diffraction pattern results in better resolution at higher angles with the peak at 36.6 ° 2θ but results in loss of key α-GLY polymorphic peaks at 19.0 ° and 29.8 ° 2θ, therefore the diffraction signal only methodology is preferred.

The KRAIC-Xl was not centred on the typical X-ray sample position and external detector calibration was required; positions shown in Figure 3.26. Calibration frames were collected with a similar methodology as synchrotron KRAIC experiments, using a calibrant (Silver Behenate, AgBh) ground into a fine powder, mixed with microscope fluid, affixed between Kapton sheet, and attached to the Kapton tubing in the sample collection position. PXRD diffraction frames of the calibrant were then collected in the sample position. The AgBh calibrant files were processed in the pyFAI calibration tool (pyFAI-calib2). The detector calibration files collected were sub-optimal, with broad

AgBh rings and poor distinction of ring numbers 7 – 12, resulting in sub-optimal detector calibration. Similar to the KRAIC-T processing methodology, the Jupyter notebook Python script used pyFAI for 1D azimuthal integration of the overlaid dataset frame, and pybaselines morphological baseline correction for removal of remaining background noise to produce a single PXRD pattern for a dataset.

Based on the sub-optimal detector calibration with a detector distance of 57.6 mm, the produced GLY patterns featured peaks in the incorrect locations, not aligning with the reference patterns, shown below in Figure 3.30.

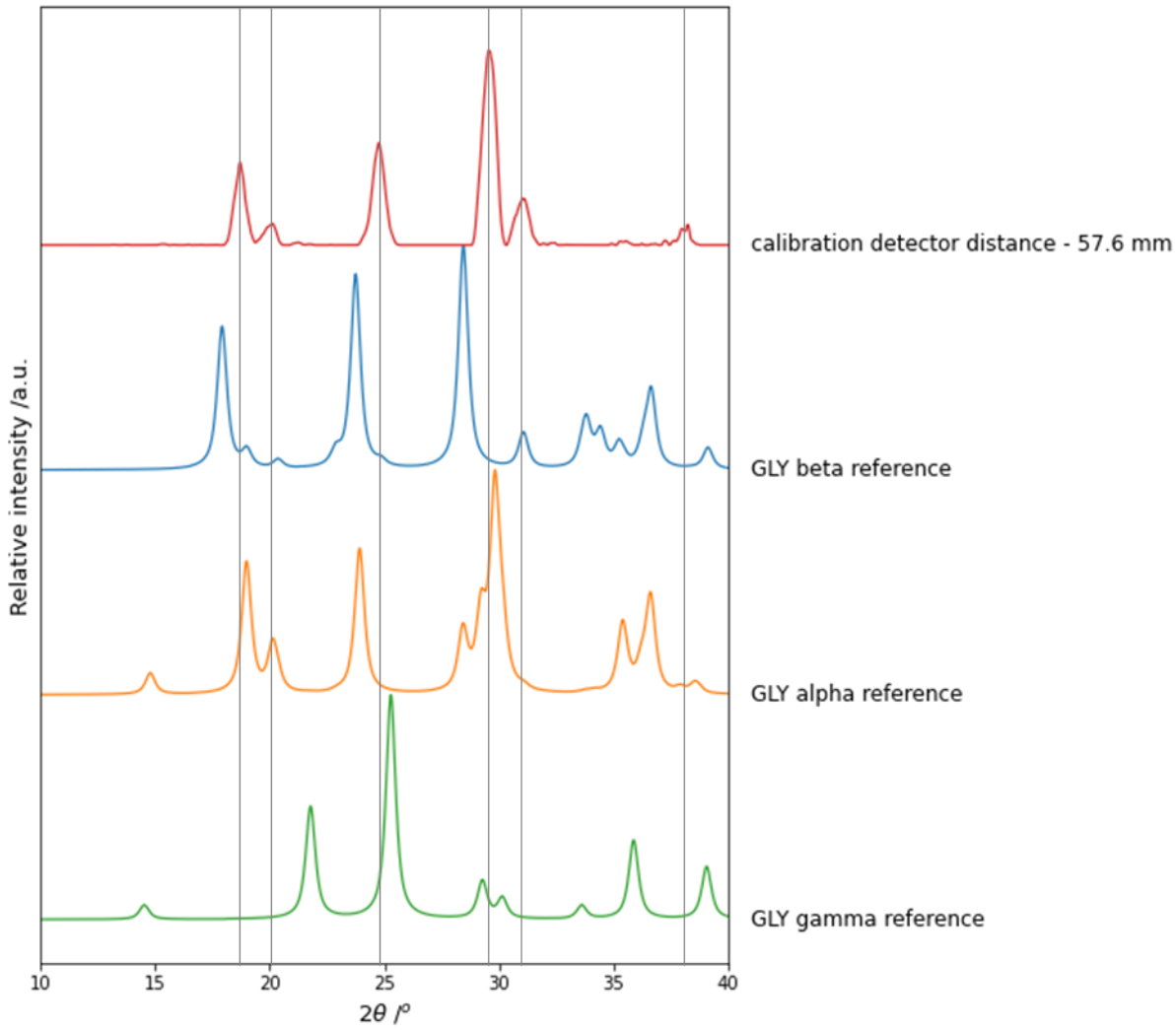

Figure 3.30: PXRD pattern of GLY collected at Flow-Xl in the KRAIC-Xl with the incorrect calibrated detector distance of 57.6 mm, again GLY references.[22–24]

Based on the three main peaks on the incorrect detector distance pattern, and the anti-solvent crystallisation, it is likely that the GLY pattern shows β- or α-GLY. Comparing the peak positions for against the reference patterns, there is a correlation between the β-GLY peaks and the KRAIC-Xl pattern, with a consistent offset position; the α-GLY peaks do not show a consistent offset to the KRAIC-Xl pattern.

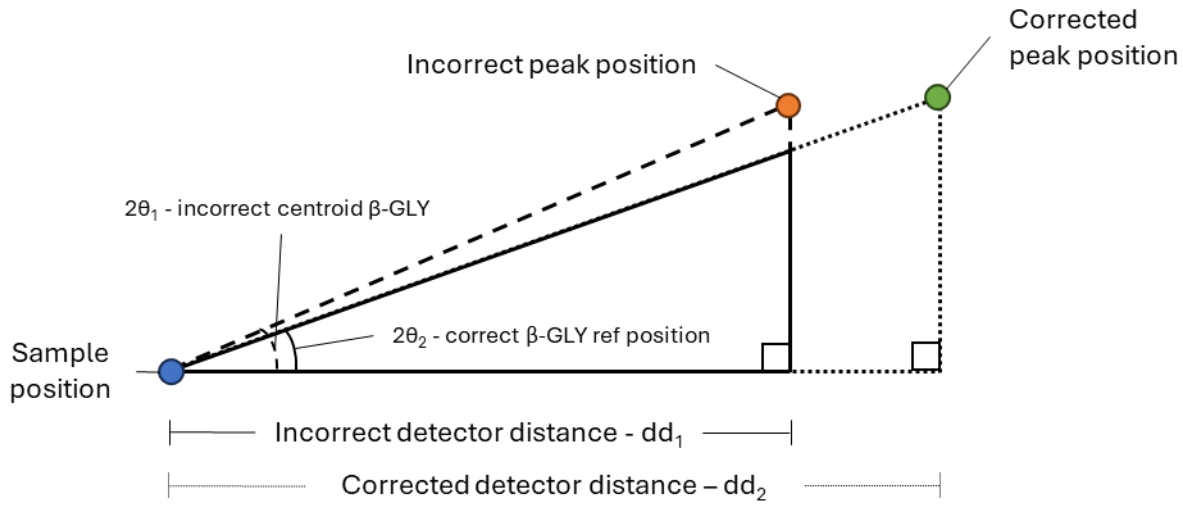

Figure 3.31: Diagram depicting detector distance geometry based on reference 2θ β-GLY values, $2\theta_2$. correct reference β-GLY 2θ position, $2\theta_2$. corrected detector distance, dd_2, and incorrect detector distance, dd_1.

By calculating the centroid 2θ position of the three main peaks in the KRAIC-Xl GLY pattern, and based on the geometry shown in Figure 3.31, showing the relationship between the incorrect and reference 2θ values and the detector distance values, Equation 3.01 can be established to calculate the correct detector distance.

Equation 3.01: Calculation of corrected detector distance, dd_2, using incorrect detector distance, dd_1, and incorrect centroid β-GLY 2θ position, $2\theta_1$, and correct reference β-GLY 2θ position, $2\theta_2$.

$$dd_2 = \frac{dd_1 \tan 2\theta_1}{\tan 2\theta_2}$$

The calculated corrected detector distance for each of the three main β-GLY peaks for a collection is averaged and re-input into the calibration .poni file used to reintegrate the diffraction pattern, repeating Steps7j – q for the workflow shown in Figure 3.28. In order to assess the consistency of the corrected detector distance, the calculation was performed for each GLY dataset and included in the processing script. The comparison of corrected and non-corrected detector distance for the resultant PXRD patterns are shown in Figure 3.32. With the corrected detector distance, the PXRD pattern clearly shows dominant β-GLY form with presence of α-GLY also.

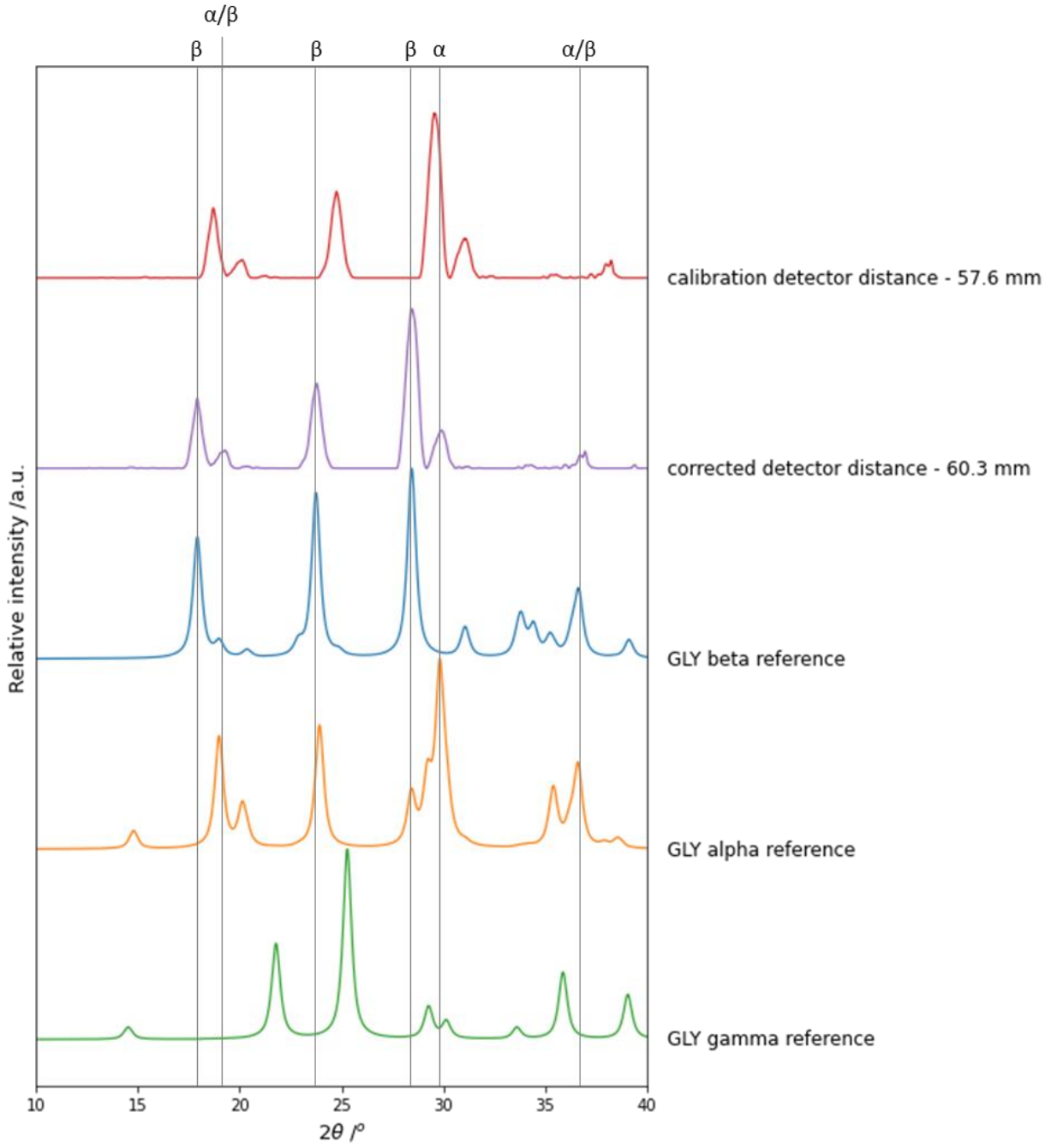

Figure 3.32: PXRD patterns of incorrect and corrected detector distances for GLY patterns from KRAIC-Xl crystallisation, against GLY reference patterns. Key peak positions for α-GLY and β-GLY annotated.

3.3.3 – Results and Discussion

The diffraction sorting workflow for the KRAIC-T data (Figure 3.06) took approximately 1.6 s computation processing time for collection sets in the range of 5 – 35 frames. The datasets for the KRAIC-Xl data contain in the range of 1231 - 14400 frames which would take an estimated ~ 11 mins computational processing time for the largest dataset, also requiring inspection of the frames themselves. The Python script for diffraction sorting and processing with multi-dataset integration and baseline correction (Figure 3.06 and Figure 3.23) are limited by computational memory and are currently unable to process the large 14400 datasets using the computer accessible for processing. But as a result, alternative methods were developed using the CrysAlisPro software and functions developed for the Flow-Xl facility. Whilst not ideal to use two programs for the processing of data, it is necessary due to the format of data acquired. In future work, processing of the large datasets could be conducted with the Python technique on a high performance computing cluster, however this may detract from the accessibility of the workflow making data processing during experiments unfeasible.

The Frame Selector tool in CrysAlisPro for a dataset of 14400 frames takes approximately 20 min computational processing time, however the benefit of this method is that it reads directly into the Powder Extraction tool in CrysAlisPro which generates the overlaid diffraction frame and PXRD pattern. Using the signal only Processing the individual frames in Python would take considerable time and are unfeasible for this reason.

The initial calibrated detector distance of 57.6 mm was found to be incorrect, with the average corrected detector distance of 60.4 mm, an increase of on the calibrated detector distance by 2.8 mm. The incorrect detector distance is due to the poor calibrant diffraction frames with wide powder rings and a loss of intensity in the main area of the diffraction frames. The systematic error in corrected detector distance was found to be consistent, with an average corrected detector distance of 60.4 mm ± 0.4 mm, the error can be attributed to the movement of the KRAIC-Xl on the rail system to access and replace the X-ray windows: the return of the KRAIC-Xl to the measurement position was not returned to the exact same position, causing some variation in the measurement. The correction of the detector position relies on knowing what the shifted diffraction pattern is, which was possible with the basic glycine diffraction patterns, however, may not be possible in more complex examples. Furthermore, if the level of diffraction is lower, the correction may not be possible to identify peak positions due to incorrectly integrated patterns.

3.3.4 – Conclusions

The development of the processing methodology for *in situ* PXRD data from segmented flow crystallisation in the KRAIC-Xl at the Flow-Xl facility, has required the use of two processing programs: CrysAlisPro, and Jupyter notebooks with Python scripting. The 100 ms acquired detector frames required

a different processing methodology to slug triggering acquired data on I11 due to the different format of the data; data collected with the KRAIC-Xl often had 14400 frames in one dataset, an increase by a factor of 1000. The Python KRAIC-T processing methodologies cannot handle the quantities of data based on the current set up, necessitating the use of CrysAlisPro. The Frame Selector tool in CrysAlisPro was time consuming for separating diffraction frames from background frames (~20 min for a dataset of 14400 frames), however enabled easy addition of frames to form an overlaid diffraction pattern, suitable for exporting into Python. Further processing could not be completed in CrysAlisPro due to the sample position requiring calibration.

The overlaid PXRD frame was processed with a Python method, using pyFAI for calibration and 1D integration, and pybaselines for morphological baseline correction, as with the KRAIC-T processing technique. The resultant PXRD patterns required correction due to poor calibrant files and incorrect detector distance (57.6 mm). The corrected detector distance was an average of 60.4 mm ± 0.4 mm and produced PXRD patterns with the expected peak positions, showing distinction between different glycine polymorphs.

3.3.5 – Future Work

For the future KRAIC-Xl design developments, ensuring the X-ray window position is on the typical sample position for data acquisition may negate the need for external calibration, and allow for the full processing methodology to be conducted in CrysAlisPro to streamline the workflow.

Now that the proof-of-principle has been achieved and the initial KRAIC-Xl design has shown *in situ* XRD is achievable in the mesoscale reactor, future work may include adding the slug triggering mechanism to the system to improve signal-to-noise. This would require significant modification to the processing methodology, as seen with the changes made to the KRAIC-T workflow with the changes made since the original KRAIC-D. These modifications may allow for processing in Python to reduce the overall processing time.

Future calibration of the KRAIC-Xl should prioritise collecting high-quality calibrant detector files, testing the calibration in pyFAI-calib2 prior to proceeding with the full experiment to ensure good calibration is achieved. An alternative calibrant, such as the commonly used cerium oxide and lanthanum hexaboride may show improved signal in key regions of the detector frame and should be tested for this purpose. Furthermore, loading the calibrant into the Kapton X-ray window tube may ensure an improved calibration, rather than affixing the calibrant sample above the tube.

3.4 – References

1. Levenstein, M. A. *et al.* Dynamic Crystallization Pathways of Polymorphic Pharmaceuticals Revealed in Segmented Flow with Inline Powder X-ray Diffraction. *Anal Chem* **92**, 7754–7761 (2020).

2. Rowe, M. C. & Brewer, B. J. AMORPH: A statistical program for characterizing amorphous materials by X-ray diffraction. *Comput Geosci* **120**, 21–31 (2018).

3. Uhlmann, E., Krohmer, E., Schmeiser, F., Schell, N. & Reimers, W. A laser powder bed fusion system for in situ x-ray diffraction with high-energy synchrotron radiation. *Review of Scientific Instruments* **91**, (2020).

4. Hammersley, A. P. FIT2D: An Introduction and Overview. *https://www.esrf.fr/computing/scientific/FIT2D/FIT2D_INTRO/fit2d.html* (1997).

5. Prescher, C. & Prakapenka, V. B. DIOPTAS: A program for reduction of two-dimensional X-ray diffraction data and data exploration. *High Press Res* **35**, 223–230 (2015).

6. Bischoff, B. *et al.* In situ/operando plug-flow fixed-bed cell for synchrotron PXRD and XAFS investigations at high temperature, pressure, controlled gas atmosphere and ultra-fast heating. *J Synchrotron Radiat* **31**, 77–84 (2024).

7. Kieffer, J., Valls, V., Blanc, N. & Hennig, C. New tools for calibrating diffraction setups. *J Synchrotron Radiat* **27**, 558–566 (2020).

8. Filik, J. *et al.* Processing two-dimensional X-ray diffraction and small-angle scattering data in DAWN 2. *J Appl Crystallogr* **50**, 959–966 (2017).

9. Kluyver, T. *et al.* Jupyter Notebooks—a publishing format for reproducible computational workflows. in *Positioning and Power in Academic Publishing: Players, Agents and Agendas - Proceedings of the 20th International Conference on Electronic Publishing, ELPUB 2016* 87–90 (2016). doi:10.3233/978-1-61499-649-1-87.

10. Simone, E., Steele, G. & Nagy, Z. K. Tailoring crystal shape and polymorphism using combinations of solvents and a structurally related additive. *CrystEngComm* **17**, 9370–9379 (2015).

11. Brown, C. J. The crystal structure of anthranilic acid. *Proc. Roy. Soc. A.* **302**, 185–199 (1968).

12. Boone, C. D. G., Derissen, J. L. & Schoone, J. C. Anthranilic acid II (o-aminobenzoic acid). *Acta Cryst.* **B33**, 3205–3206 (1977).

13. Hardy, G. E., Kaska, W. C., Chandra, B. P. & Zink, J. I. Triboluminescence-structure relationships in polymorphs of hexaphenylcarbodiphosphorane and anthranilic acid, molecular crystals, and salts. *J. Am. Chem. Soc.* **103**, 1074 (1981).

14. Erb, D. pybaselines: A Python library of algorithms for the baseline correction of experimental data (v1.1.0). Preprint at https://doi.org/10.5281/zenodo.10676584 (2024).

15. Perez-Pueyo, R., Soneira, M. J. & Ruiz-Moreno, S. Morphology-Based Automated Baseline Removal for Raman Spectra of Artistic Pigments. *Appl Spectrosc* **64**, 595–600 (2010).

16. Coelho, A. A. TOPAS and TOPAS-Academic: An optimization program integrating computer algebra and crystallographic objects written in C++: An. *J Appl Crystallogr* **51**, 210–218 (2018).

17. Bruker AXS. TOPAS. *Version 4.2* (2009).

18. Turner, T. D. *et al.* Flow-Xl: a new facility for the analysis of crystallization in flow systems. *J. Appl. Cryst* 57 (2024) doi:10.1107/S1600576724006113.

19. Rigaku Oxford Diffraction. CrysAlisPro. *Version 171.43.109a* (2024).

20. Srinivasan, K. & Dhanasekaran, P. Nucleation control and crystallization of l-glutamic acid polymorphs by swift cooling process and their characterization. *J Cryst Growth* **318**, 1080–1084 (2011).

21. Alieva, A., Boyes, M., Vetter, T. & Casiraghi, C. Selective polymorphism of α-glycine by acoustic levitation. *CrystEngComm* **22**, 7075–7081 (2020).

22. Iitaka, Y. The crystal structure of β-glycine. *Acta Crystallogr* **13**, 35–45 (1960).

23. Iitaka, Y. The crystal structure of γ-glycine. *Acta Crystallogr* **14**, 1–10 (1961).

24. Marsh, R. E. A refinement of the crystal structure of glycine. *Acta Crystallogr* **11**, 654–663 (1958).

Chapter 4 – Lab-source *in situ* X-ray diffraction during segmented flow crystallisation at the Flow-Xl facility

The work in this chapter was undertaken in collaboration with the Flow-Xl facility, University of Leeds. The crystalliser was designed in collaboration with Dr Karen Robertson, and researchers at Flow-Xl; Prof. Nikil Kapur, Prof. Fiona Meldrum, and Dr Tom Turner.

4.1 – Introduction and Aims

In situ analysis to study the crystallisation of materials is a key area of research due to nucleation and crystal growth underpinning main crystal properties such as polymorphic form, morphology, crystal size, and crystal size distribution.[1] Gaining an understanding of the crystallisation behaviours enables the control and optimisation of the crystallisation process to tune the properties of the crystalline product. Synchrotron light source facilities offer the beam capabilities for *in situ* crystallisation studies with X-ray diffraction due to the high flux, brilliance, penetration depth, and temporal resolution compared to lab-source X-ray instruments.[2] In particular, the short acquisition times achievable at synchrotron sources enable time-resolution of kinetic processes, an area of keen interest for mechanistic understanding of synthesis and crystallisation processes.[1] *In situ* XRD to analyse the crystallisation of polymorphic forms is frequently studied at synchrotron facilities, however, access to synchrotron beamtime is highly limited with a time-consuming application route and lengthy peer-review process for awarding beamtime proposals.[2,3]

Recent improvements in lab-source X-ray instrumentation in terms of beam flux achievable and hybrid photon counting detectors have made lab-source *in situ* studies feasible, prompting the development of the Flow-Xl facility; a lab-source X-ray instrument for the *in situ* study of flow crystallisation processes with X-ray diffraction and Raman spectroscopy.[3] The Flow-Xl facility features a custom Rigaku XtaLab Synergy Custom X-Ray Diffractometer with micro-focus Cu K-α X-ray source and 2D hybrid photon-counting detector. The facility also features a Horiba Labram HR Evolution Raman Microscope w/ External Raman Probe for *in situ* Raman studies. Commissioning experiments at Flow-Xl have studied the crystallisation of model organic and inorganic compounds in a range of complex flow sample environments, including microfluidic flow environments. The largest size of flow system studied was crystallisation of Na_2SO_4 in the 2 mm ID borosilicate capillary system. The time-resolved *in situ* analysis showed the nucleation and crystal growth of the metastable Na_2SO_4 phase of the material during cooling crystallisation.[3]

This work proposed the development of a tri-segmented flow KRAIC system for *in situ* XRD for the lab-source X-ray instrument, the Flow-Xl facility. The tri-segmented flow poses greater challenge the lab-source system due to the addition of carrier fluid which increases background scattering. Furthermore, the meso-scale system also contains a larger quantity of solution material in-beam than previously used: the 1/8" (3.175 mm) ID tubing increases the proportion of material in beam by 1.6 times compared to the 2 mm ID microfluidic system studied previously at Flow-Xl. The increased solution and addition of carrier fluid has the potential to attenuate the beam too much and result in no diffraction achievable at the lab-source system. As such, the proposed experiments were the crystallisation of model materials to achieve proof-of-principle for lab-source *in situ* XRD in a meso-scale system during tri-segmented flow crystallisation.

The model compounds chosen for crystallisation trials are L-glutamic acid (LGA) and Glycine (GLY). Both are polymorphic amino acids with extensively studied crystallisation behaviours. LGA has two polymorphs: the metastable α-LGA and stable β-LGA; the molecular structure and crystal structures of LGA are shown below in Figure 4.01 with crystallographic information summarised in Table 4.01.[4,5]

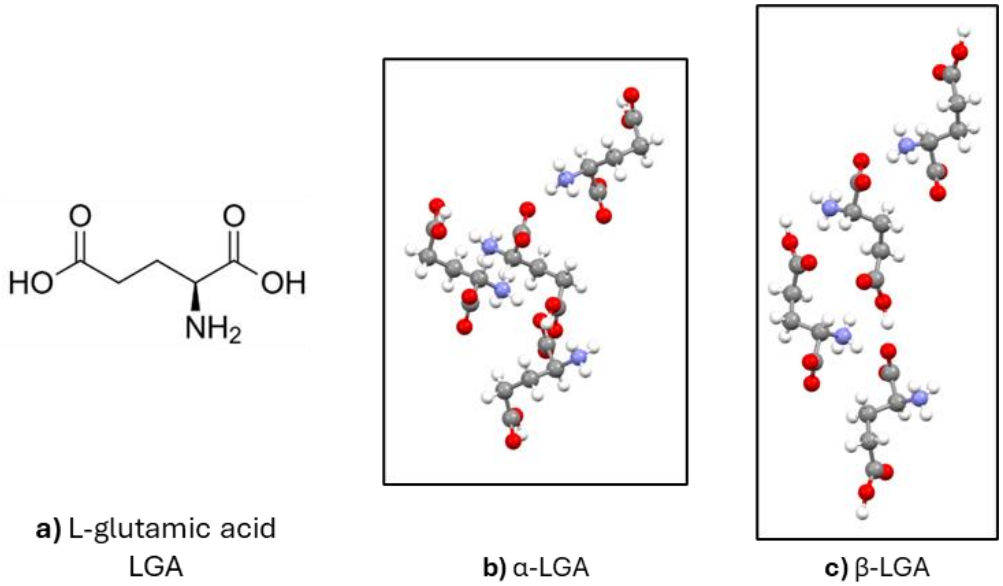

Figure 4.01: a) molecular structure of LGA, and the crystal structures of LGA taken from the Cambridge Structural Database for b) α-LGA, refcode LGLUAC02, viewed down the c-axis, and c) β-LGA, refcode LGLUAC01, viewed down the a-axis.[4,5]

Table 4.01: Summary of crystallographic information for LGA polymorphs, taken from the Cambridge structural database.[4,5]

LGA polymorph	α-LGA	β-LGA
Refcode	LGLUAC02	LGLUAC01
Space Group	P 2_1 2_1 2_1	P 2_1 2_1 2_1
Lattice Type	Orthorhombic	Orthorhombic
a /Å	7.068	5.154
b /Å	10.277	6.942
c /Å	8.755	17.274
α /°	90	90
β /°	90	90
γ /°	90	90
Cell Volume /Å^3	635.944	618.048

Different crystallisation methods, including seeding crystallisation, cooling crystallisation, and additive controlled crystallisation have been shown to achieve polymorphic control during LGA crystallisation.[6–9] Literature batch swift cooling crystallisation experiments of LGA from pure aqueous solution at 40 °C saturation obtained polymorphically pure α-LGA and β-LGA based on held nucleation temperature: high nucleation temperatures (27 – 34 °C) caused lower supersaturations promoted the crystallisation of the stable β-LGA, whilst low nucleation temperatures (1 – 9 °C) with high supersaturations promoted the metastable α-LGA.[9] The solubility curve for LGA in water is shown below in Figure 4.02.

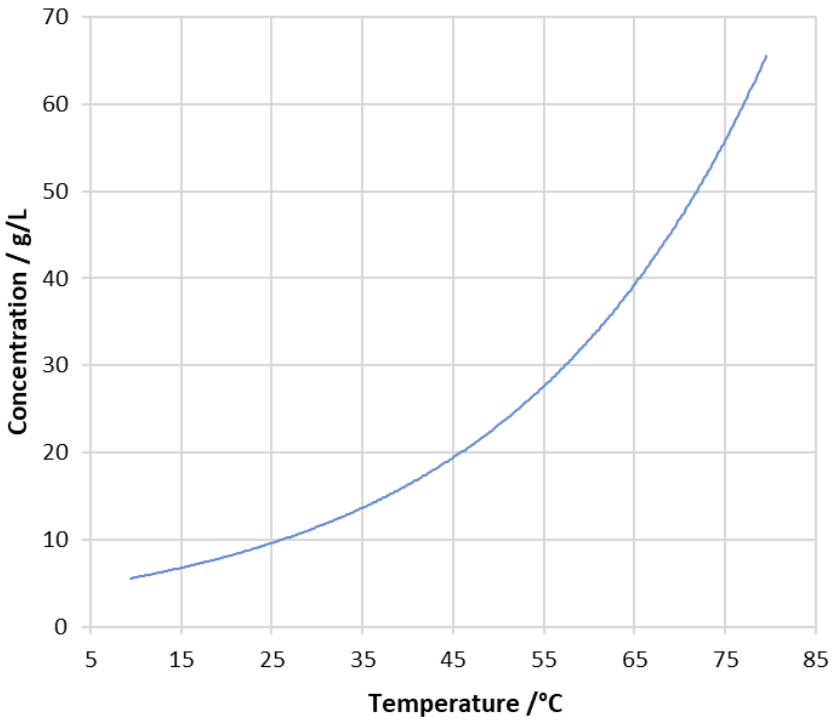

Figure 4.02: Solubility curve for LGA in aqueous solution adapted from [9].

Literature batch cooling crystallisations studied the crystallisation of 10 g/kg LGA solution (~10 g/L) with varied water to ethanol anti-solvent binary solvent mixtures from 60 °C to 10 °C at a cooling rate of -1 °C/min.[10] With no ethanol present, the system crystallised polymorphically pure β-LGA. Increasing the ethanol content increased the presence of α-LGA to polymorphically pure at high ethanol mole fractions of 0.8. High anti-solvent content generates high supersaturation levels, promoting the crystallisation of kinetically favoured metastable form, whilst lower supersaturations promote the crystallisation of the thermodynamically favoured, stable β-LGA polymorph. However, for ethanol anti-solvent crystallisation for aqueous LGA solution in a microfluidic device, polymorphic selectivity is largely controlled by flow rates of solution and anti-solvent, with a non-linear relationship of flow rates influencing local supersaturation and resultant crystal form produced.[10]

Glycine has three known polymorphs: the stable γ-GLY typically crystallised from aqueous acidic or basic solutions, a metastable α-GLY typically crystallised from neutral aqueous solutions, and the least stable β-GLY, commonly crystallised from alcohol anti-solvent addition to aqueous solutions.[11] The molecular structure, and crystal structures of glycine are shown in Figure 4.03 with crystallographic information summarised in Table 4.02.

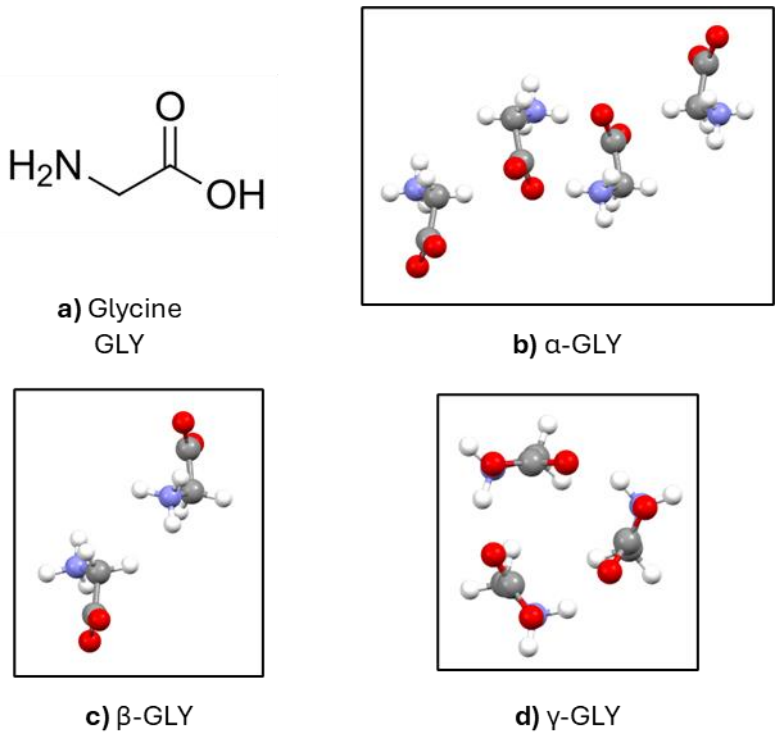

Figure 4.03: a) the molecular structure of glycine with the crystal structures of the three polymorphic forms taken from the Cambridge Structural Database; b) α-GLY form, refcode GLYCIN02, viewed down the a-axis, c) β-GLY, refcode GLYCIN, viewed down the a-axis, and d) γ-GLY, refcode GLYCIN01, viewed down the c-axis.[12–14]

Table 4.02 Summary of crystallographic information for GLY polymorphs, taken from the Cambridge structural database.[12–14]

GLY polymorph	α-GLY	β-GLY	γ-GLY
Refcode	**GLYCIN02**	**GLYCIN**	**GLYCIN01**
Space Group	P 2_1/n	P 2_1	P 3_2
Lattice Type	Monoclinic	Monoclinic	Hexagonal
a /Å	5.1020	5.077	7.037
b /Å	11.9709	6.268	7.037
c /Å	5.4575	5.380	5.483
α /°	90	90	90
β /°	111.70	113.20	90
γ /°	90	90	120
Cell Volume /Å^3	309.698	157.361	235.139

In the presence of water, β-GLY has been shown to rapidly recrystallise with solvent-mediated phase transition into α-GLY with the induction time for recrystallisation in the order of minutes; increasing ethanol content increases the induction times from minutes to hour timescales. Glycine aqueous solubility is shown below in Figure 4.04.[15,16] The solubility of α-GLY and β-GLY in water and ethanol binary solvent mixtures at 36.85 °C (310 K) is shown in Figure 4.05.

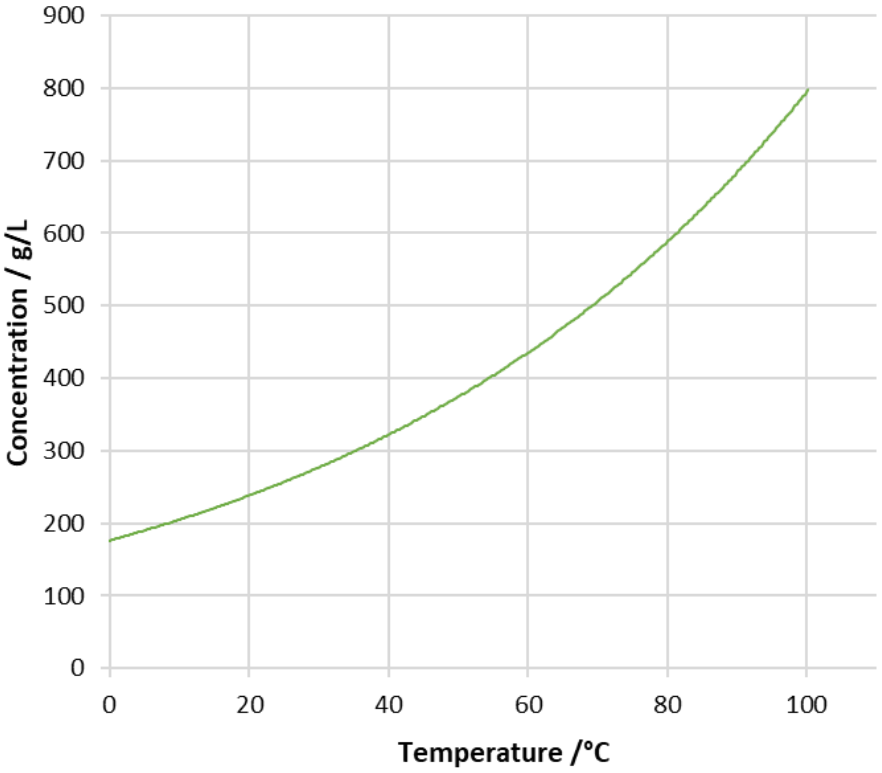

Figure 4.04 : Solubility curve for aqueous glycine, adapted from [15].

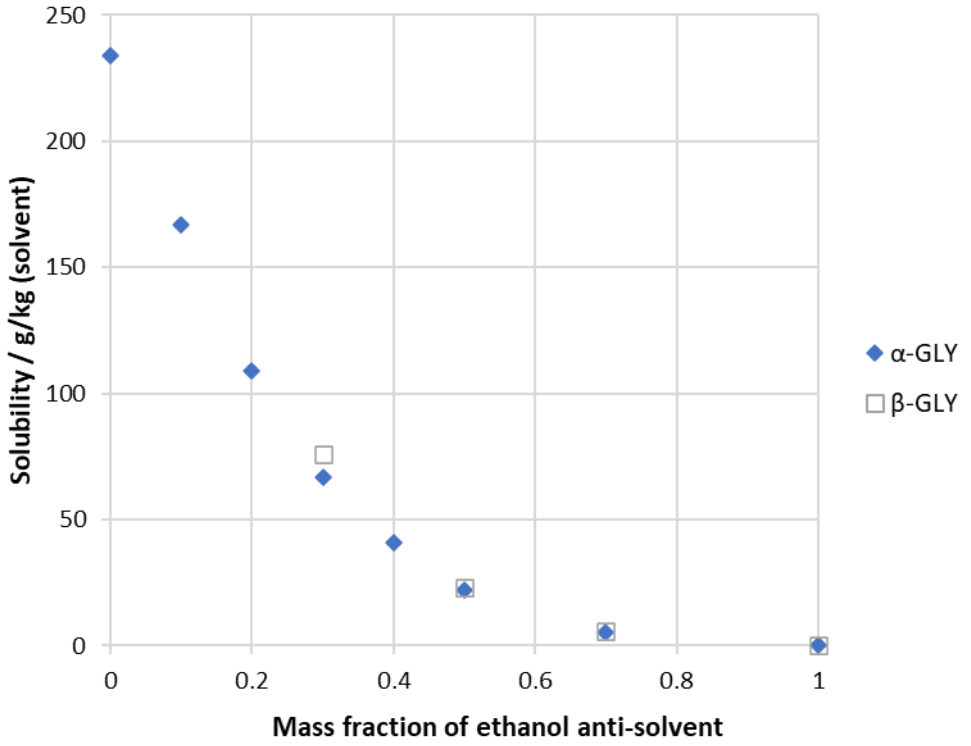

Figure 4.05: Solubility for α- and β-GLY polymorphs a 36.85 °C (310 K) in a range of water-ethanol binary solvent mixtures, adapted from [17] .

4.2 – KRAIC-Xl crystalliser design

The design aims for the *in situ* PXRD system, named the KRAIC-Xl (KRAIC at Flow-Xl) are:

- To have a meso-scale KRAIC crystalliser with ~15 m of 1/8" ID FEP tubing, equivalent to other KRAIC designs
- To have multiple X-ray analysis windows (Xs) for time resolved analysis.
- To be able to easily and safely replace the Kapton X-ray windows.

The X-ray enclosure at the Flow-Xl facility has limited space for the crystalliser sample environment with approximately 120 mm between the X-ray beam out position and detector data collection position, illustrated below in Figure 4.06. As such, the two-column KRAIC designs as used for the original KRAIC-D, KRAIC-T (Chapter 5), and KRAIC-S v2 (Chapter 6) would be unsuitable as the limited space in the hutch prevents crystalliser movement to install and replace the necessary Kapton tubing X-ray analysis windows.

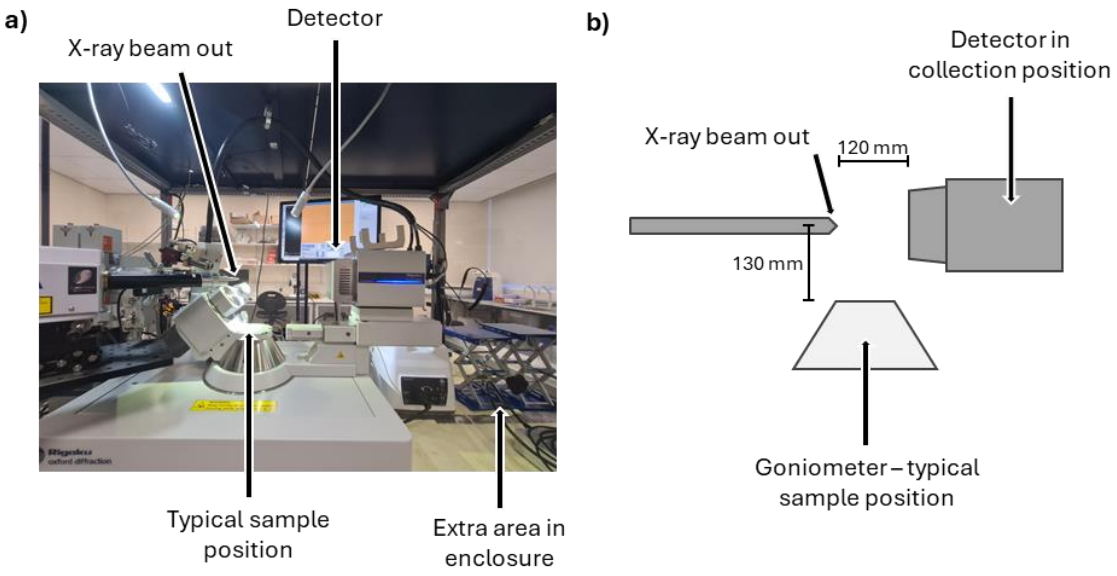

Figure 4.06: a) image of X-ray enclosure at the Flow-Xl facility with key areas annotated, and b) to-scale illustration of the side on view of the Flow-Xl X-ray instrument with the 120 mm distance available for the sample environment.

An alternative KRAIC layout was proposed to adjust to these limitations: using a large 70 cm diameter cylindrical plastic drum as the crystalliser main body to fit over the detector, with a small section removed for the X-ray windows, diagram shown below in Figure 4.07a in the sample collection position. Mounting the KRAIC-Xl drum body on a circular rail system would enable the rotation of the crystalliser out of the sample collection position to install and replace X-ray windows in the event of a blockage. The design would also benefit from protecting the detector from any potential spray during the unblocking process by the drum shielding the detector area, Figure 4.07b.

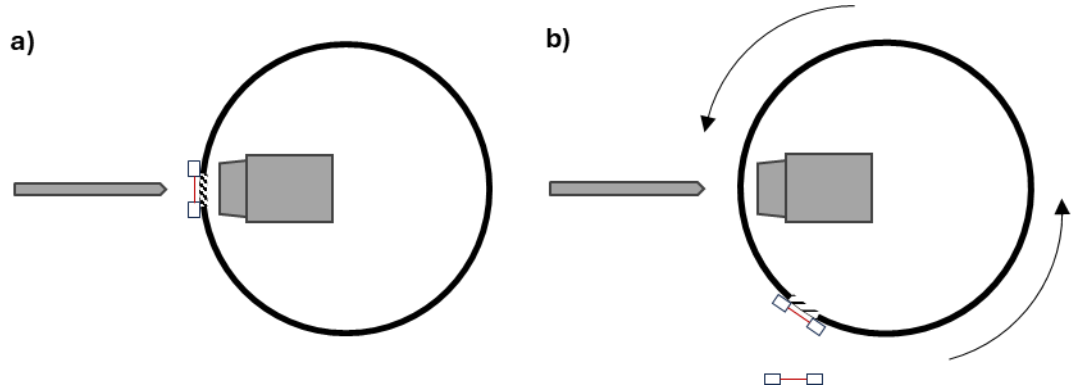

Figure 4.07: Illustration of the top-down view of the proposed KRAIC-Xl design with large 70 cm diameter main body in a) data collection mode with the X-ray window in front of the detector, and b) unblocking mode to change the X-ray window – the crystalliser body shields the detector face from potential spray during the unblocking process.

The proposed crystalliser design was drawn in CAD, shown below in Figure 4.08a. The X-ray window section uses an affixed 20 x 20 mm extruded aluminium frame for the attachment of the Kapton window PTFE union pieces. The crystalliser body allows for four tubing loops of length 2.2 m between each

X-ray window at lengths of 3.1 m, 5.3 m, 7.5 m, and 9.7 m for X1-4 respectively, achieving a 12 m total crystalliser length.

The proposed crystalliser was built using a 70 cm diameter drum piece with tubing guiding pieces with tubing guiding and holder pieces designed for the alignment of the FEP tubing. The tubing guiding pieces were designed in CAD and manufactured with machined PTFE to ensure the tubing is correctly aligned to the X-ray window union pieces, shown in Figure 4.08c. Further tubing holder pieces were designed in CAD and 3D printed to hold the tubing to the KRAIC-Xl body with a gradual incline, shown in Figure 4.08b. The tubing guiding and holder pieces were screwed to the KRAIC-Xl body; the tubing can be threaded through the holder pieces to change the tubing, if necessary.

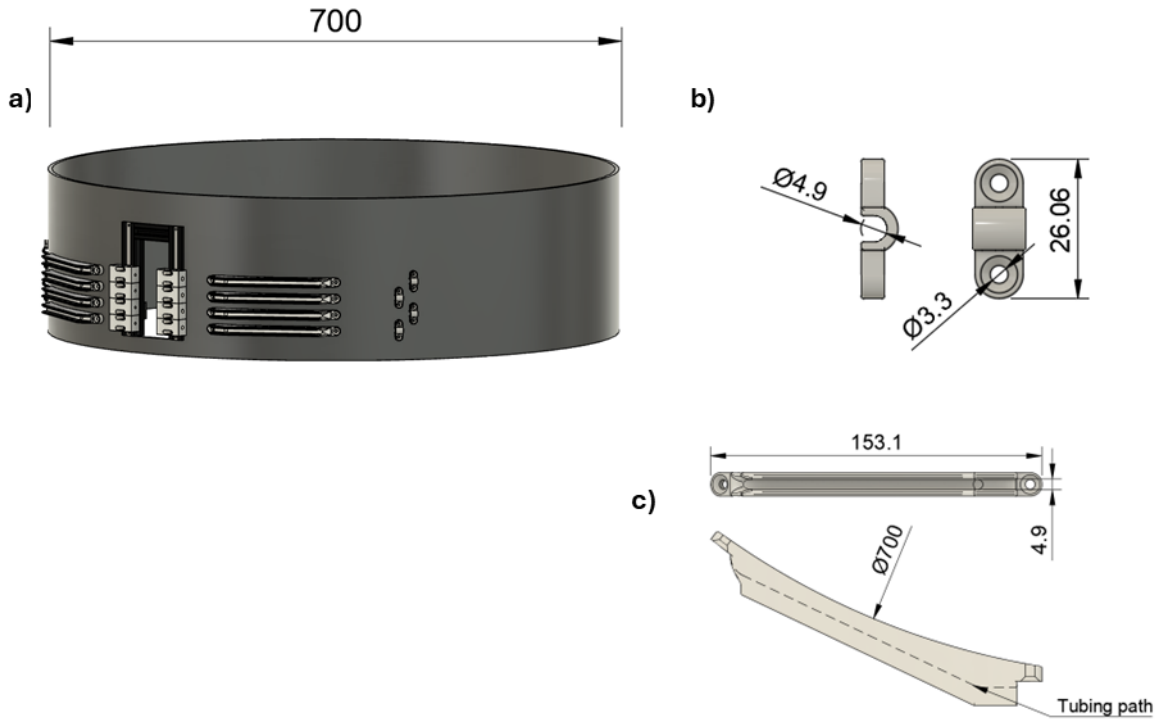

Figure 4.08: CAD drawings with measurements in mm for a) assembled KRAIC-Xl design with drum body, X-ray window frame with Kapton unions, and tubing guiding and holder pieces, b) tubing holder piece design, and c) tubing guiding piece.

The circular rail system acquired for the KRAIC-Xl used size 23 Automotion Curviline sliders, with a custom 70 cm diameter constant radius circular rail with the KRAIC-Xl main body connecting to the four sliders with a 3D printed connector piece. Three motorised Standa vertical translation stages (8MVT188-20) , were used to provide translation of the crystalliser in-beam between X-ray analysis windows. The vertical stages have a travel range of 95 mm with a 200 step motor for translation. The stacked design of the X-ray window unions allows for four X-ray window tubes accessible in beam by the 95 mm travel range. The vertical stages were set up with computer control to adjust between windows during data acquisition The circular rail system is shown constructed in the Flow-Xl enclosure in Figure 4.09a with the 3D printed connector pieces; the full KRAIC-Xl system in position in the Flow-Xl enclosure is shown below in Figure 4.09b.

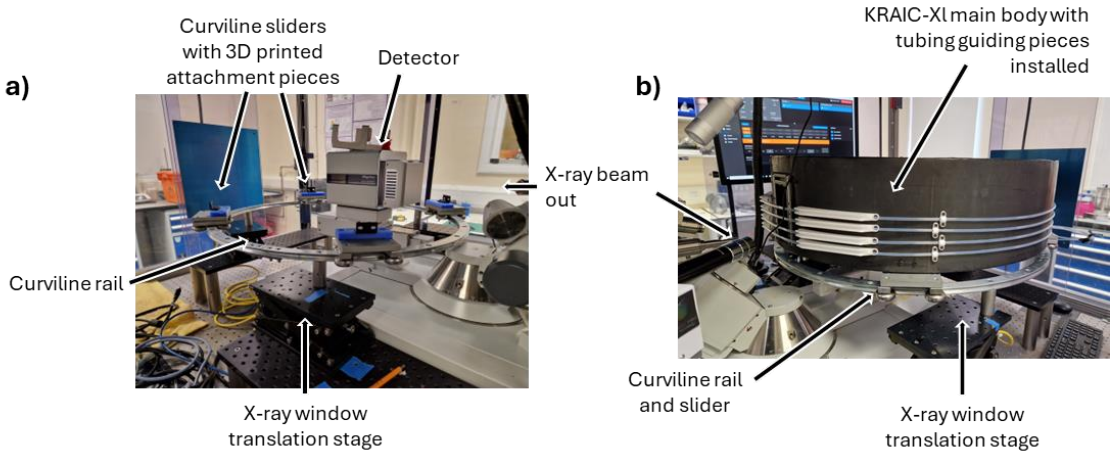

Figure 4.09: Annotated images of a) the rail system in the Flow-Xl X-ray enclosure with an X-ray window translation stage marked, and b) the full KRAIC-Xl system installed on the rail system in the enclosure.

Due to the limited space inside the X-ray enclosure, all the peripheral KRAIC equipment; pumps, hot water circulator, cold water circulator, segmentation bath, endpiece collection vessel, round bottom flasks and hot plates would not fit inside the enclosure. The X-ray enclosure has a junction for cables and other equipment tubing, so flow can be pumped into the enclosure, however, flow would not maintain segmentation through a vertical junction: the segmentation bath and endpiece were set up in the enclosure. Therefore, the majority of the peripheral equipment was designed to be set up outside of the enclosure, with jacketed transfer tubing into the enclosure. The X-ray equipment in the enclosure is humidity-sensitive so covers were made for the segmentation bath and endpiece collection vessel to minimise increases in humidity from the flow equipment.

4.3 – Methodology and Experimental

4.3.1 – KRAIC-Xl

The KRAIC-Xl was set-up in the Flow-Xl X-ray enclosure with 13 m of 1/8” FEP tubing on the KRAIC-Xl body design, as described in the previous Section 4.2, shown in Figure 4.09b. The X-ray analysis windows for the KRAIC-Xl experiments were prepared using the methodology described in the original KRAIC-D paper with an Aquapel hydrophobic coating.[18,19] Due to issues with positioning the vertical translation stages, only X1-3 were accessible in beam. Initially only one window was installed in the X3 position for LGA and the majority of GLY crystallisation conditions to test if X-ray diffraction could be achieved at the maximum crystallisation time available for X-ray analysis in the crystalliser. The final GLY crystallisation condition collected X-ray data at the X1 and X2 positions, investigating time-resolved analysis. The X-ray window position was offset from the typical sample collection position for the Flow-Xl instrument due to KRAIC-Xl mounting limitations on the base breadboard, so a detector distance setting in the CrysAlisPro control software is not equivalent to the sample-to-detector distance. Calibrant data frames were collected for silver

behenate powder mixed with fomblin microscope fluid and affixed between two Kapton sheets and attached to the X-ray window sample position.

The pump used for LGA and GLY solutions was a prototype heated Vapourtec SF-10+ peristaltic pump, with heating elements installed into the pump head for temperature setting options of 40, 60, and 80 °C.

4.3.2 – L-glutamic acid crystallisation

The crystallisation of LGA used a 20.00 g/L aqueous feedstock, dissolved at 60 °C. The increased temperature of the feedstock from the saturation point at 45 °C (Figure 4.02) ensured no crystallisation in transfer tubing prior to ethanol mixing. The crystallisation was driven through ethanol (EtOH) anti-solvent addition and cooling crystallisation from 60 °C to the ~25 °C X-ray enclosure temperature, with a 14 °C nucleation promoter jacketed tubing post-segmentation to further encourage nucleation. The KRAIC-Xl configuration for LGA crystallisations and temperature settings are summarised below in Figure 4.10.

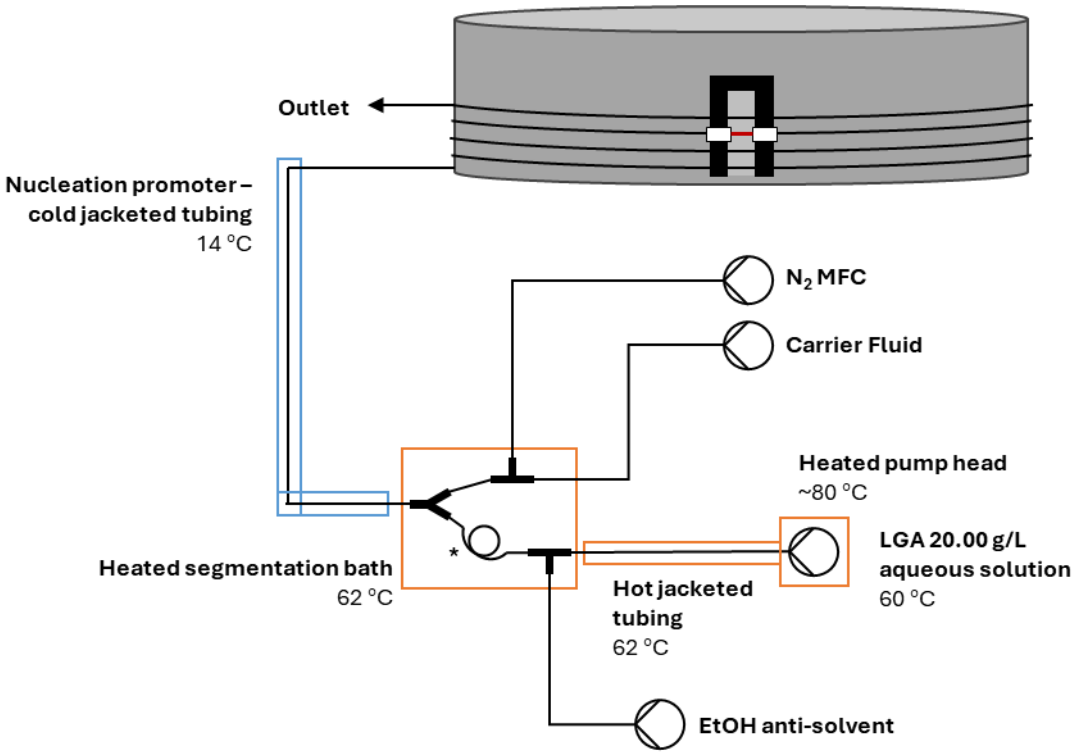

*Figure 4.10: Schematic of the KRAIC-Xl set up for the crystallisation of LGA with X3 window in place. * Tubing of 1/16" ID tubing with ~40cm length.*

Initial testing found the heated SF-10+ pump head did not maintain solution temperature when set to 60 °C for a flow rate of 2.1 mL/min, so the pump heater setting was 80 °C pump setting to maintain solution temperature. The segmentation set up for LGA crystallisations pre-segmented nitrogen flow and carrier fluid with the solution and ethanol anti-solvent mixing at a 1.5 mm through hole T-piece. A ~40 cm length of 1/16" ID FEP tubing between the anti-

solvent mixing and segmentation Y-piece (3.2 mm through hole) aimed to provide greater mixing of anti-solvent and solution prior to segmentation. Flow rates for the LGA segmented flow used Galden carrier fluid flow of 0.7 mL/min and an N_2 MFC setting of 65, which was measured to be an average of 2.3 mL/min. Flow rates for LGA crystallisations are summarised in Table 4.03.

Table 4.03: Summary of flow rates for the LGA anti-solvent crystallisations with the KRAIC-XI.

	Flow rates / mL/min			
Condition identifier	**Solution**	**Ethanol**	**Total**	**Ethanol fraction**
LGA1 - LGA3	2.10	0.90	6.00	0.300
LGA4	2.05	0.95	6.00	0.320
LGA5	1.95	1.05	6.00	0.350
LGA6	1.50	1.50	6.00	0.500

For the resultant 6 mL/min total flow rate, a residence time of 13:14 min was recorded with and X3 crystallisation time of 8:08 min. All conditions produced LGA crystallisation and X-ray data were collected at X3 for all six LGA conditions using instrument settings of X-ray wavelength of 1.5406 Å Cu K-α radiation with the HyPix-6000HE detector of 800 x 775 px with 100 µm pixel size with continuous, pulsed 100 ms frame acquisitions. The LGA datasets for LGA1-4 used a detector setting of 70 mm with unknown beam divergence and aperture settings. LGA5-6 used a detector setting of 70 mm with 10 mR beam divergence with 0 mm aperture. The levels of crystallisation at X3 for various LGA crystallisation runs are shown in Figure 4.11.

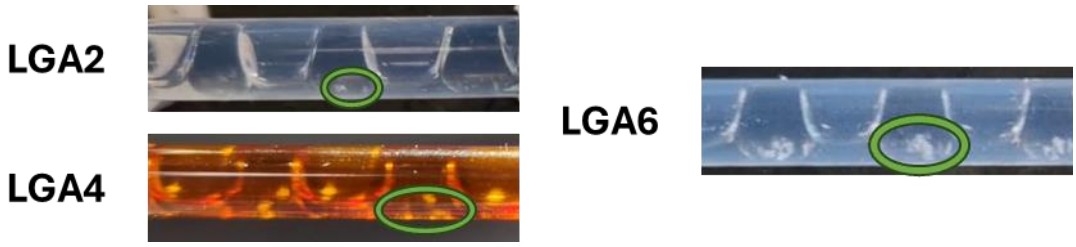

Figure 4.11: Images of the levels of crystallisation around the X3 region for LGA2, LGA4, and LGA6. Note: LGA4 showing the Kapton window tubing section.

4.3.3 – Glycine crystallisation

The GLY crystallisations used two ~62.5 g/L GLY feedstocks, the first at 62.56 g/L aqueous solution, the second at 62.50 g/L. The GLY solutions dissolved at the 23 °C room temperature and were maintained at 24 °C on a hotplate. The chosen ~62.5 g/L concentration was undersaturated from the ~275 g/L solubility at 25 °C (Figure 4.04). The flow rates for GLY crystallisation conditions are shown below in Table 4.04. All GLY crystallisations used an N_2 MFC setting of 65, measured at an average of 2.3 mL/min.

*Table 4.04: Summary of flow rates and resulting ethanol anti-solvent fractions used for GLY crystallisations in the KRAIC-Xl. Set-up 1 + 2 of the KRAIC-Xl described in Figure 4.12, with set-up 1 using a ~40 cm tubing length post-anti-solvent addition. Set-up 2 modified to a ~5 cm tubing length post-anti-solvent addition to minimise blockages. Set-up 3, described in Figure 4.14, modified the segmentation pieces for air segmentation post-anti-solvent addition to mitigate encrustation. *GLY6 ended due to blockage, with GLY7 using the same crystallisation settings with a cyclical wash routine, described further below.*

		Flow rates / mL/min				
Condition identifier	**Set-up**	**Carrier fluid**	**Solution**	**Ethanol**	**Total**	**Ethanol fraction**
GLY1	1	0.70	1.71	1.29	6.00	0.430
GLY2	2	0.90	3.00	2.00	8.20	0.400
GLY3		0.90	2.86	2.14	8.20	0.428
GLY4		0.90	2.78	2.22	8.20	0.444
GLY5		0.90	2.50	2.50	8.20	0.500
GLY6*		0.90	2.40	2.60	8.20	0.520
GLY7*		0.90	2.40	2.60	8.20	0.520
GLY8	3	0.90	2.40	2.60	8.20	0.520
GLY9		0.90	2.50	2.50	8.20	0.500

The ethanol anti-solvent additions result in ethanol fractions ranging between 0.400 – 0.520. The solubility of GLY in water-ethanol binary solvents shown in Figure 4.05, this shows the ~62.5 g/L should be well within the labile zone for GLY to produce spontaneous nucleation and crystal growth.

GLY1-7 used the schematic shown in Figure 4.12. Conditions GLY8+9 used a third segmentation set up shown in Figure 4.14. The temperature settings for GLY conditions are summarised in Table 4.05. The nucleation promoter jacketed tubing installed for LGA crystallisations was filled with air and not used with the water circulator for GLY crystallisations.

Table 4.05: Summary of temperature conditions for GLY crystallisations with the KRAIC-Xl.

	Temperatures / °C			
Condition identifier	**Solution hotplate**	**Hot water circulator - jacketed tubing**	**Segmentation bath**	**Heated pump**
GLY1	24	28	28	40
GLY2-9	24	28	33	60

GLY1 ended before a full residence time was completed due to encrustation in the segmentation bath, as a result the total flow rate was increased for subsequent runs to reduce the dwell time in the segmentation bath. After GLY1, an increased temperature in the segmentation bath was used to attempt to reduce crystal encrustation prior to segmentation. The crystallisation level of GLY was dependent on ethanol fraction and was minimally affected by the difference in temperature settings. The residence time for GLY runs with a total

flow rate of 8.2 mL/min was recorded at 10 min with times of 2:40 min, 4:25 min, 6:21 min, and 8:21 min for X1-4 positions respectively.

All GLY conditions produced GLY crystals however, several segmentation configurations were trialled during GLY crystallisations to attempt to optimise the segmentation and minimising stoppages due to crystal encrustation in the segmentation bath. The KRAIC-Xl schematic used for GLY1-7 is shown below in Figure 4.12. GLY1 used the same segmentation set up as used with LGA crystallisations, with the increased 1/16" tubing length to attempt to achieve good mixing of solution with anti-solvent. However, the immediate crystallisation of GLY on mixing with EtOH pre-segmentation caused crystal build-up and non-uniform pumping causing irregularity in the quantity of crystals in slugs. The segmentation set up was changed for GLY2-7 conditions, reducing the tubing length to ~5cm to minimise time spent by the crystal flow prior to segmentation.

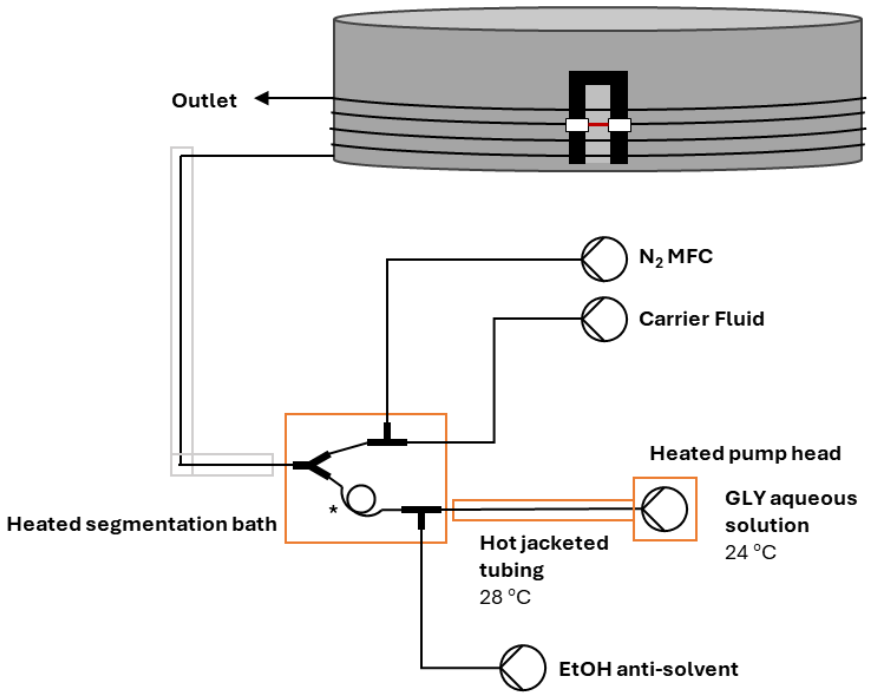

*Figure 4.12: Schematic diagram of the KRAIC-Xl during anti-solvent crystallisation of GLY crystallisation runs 1-7. * GLY1 used a ~40 cm 1/16" ID tubing length post-ethanol addition prior to segmentation. GLY2-7 used a ~5 cm tubing length here to minimise time in segmentation bath.*

GLY2 conditions after two residence times (20 min) was changed to GLY3 conditions then rapidly changed (every ~5 min) to GLY4 and GLY5 conditions due to low crystal densities produced. No X-ray data were collected at GLY2-4 due to the low crystal densities in slugs produced. GLY5 produced a higher crystal density and data were acquired but collection ended due to a full blockage after 15 min. The reduced tubing length for GLY2-7 decreased the speed of encrustation but did not eliminate it, with encrustation forming after 9 minutes. However, the reduced tubing length impaired the mixing with ethanol, producing periodicity in the slugs with different ethanol dosing, as shown below in Figure 4.13.

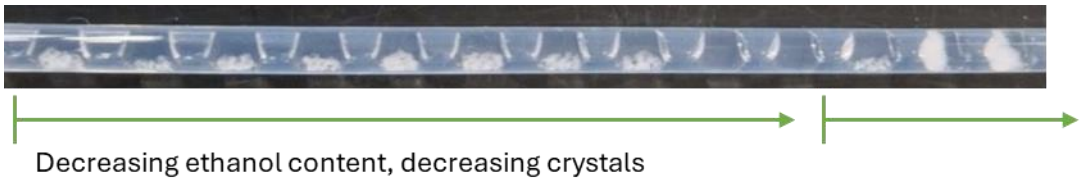

Figure 4.13: Image of rung 1 of KRAIC-Xl during GLY7 conditions showing periodicity in the quantity of crystals in successive slugs due to poor ethanol mixing in the segmentation bath.

For GLY7-9 conditions a method to prevent full blockages was used by flowing with anti-solvent addition for 9 min, then switching to pure GLY solution flow for 2 mins at the total solution flow of 5 mL/min to dissolve GLY encrustation Running with this cyclical flow method maximised X-ray data collection time with minimal down time and caused no issues with crystal flow elsewhere in the crystalliser. The cyclical flow method enabled continual flow for over 1 hour crystallisation runs for GLY7 with no full blockages. A further segmentation set up was trialled for GLY8+9, shown in Figure 4.14. The third segmentation set up used gas segmentation to push the rapidly formed crystals through the tubing prior to carrier fluid introduction. This method did not eliminate encrustation but reduced the frequency of clearing required, with encrustation forming after 12 minutes for the cyclical crystallisation regime. This segmentation method also produced a more even distribution of crystal density in successive slugs, eliminating the periodicity seen for previous conditions.

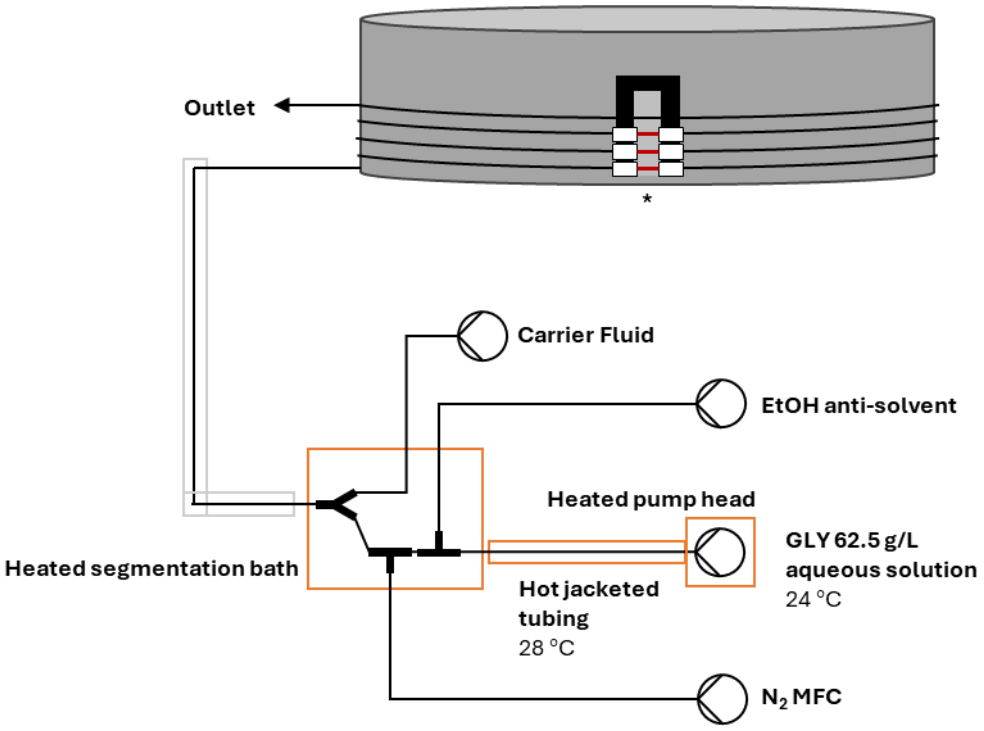

Figure 4.14: Schematic of the KRAIC-Xl during anti-solvent segmented flow crystallisation of glycine, for GLY8+9 conditions. Tubing length between anti-solvent mixing and gas inlet ~ 5 cm. X-ray windows 1+2 were introduced during GLY9 for data collection at different time points.*

GLY1-4 on visual inspection had higher levels of crystallisation compared to LGA6, Figure 4.11. GLY5-9 showed significantly higher levels of crystallisation at the X3 collection position, with comparable levels of crystallisation at X1, shown below for GLY9 in Figure 4.15.

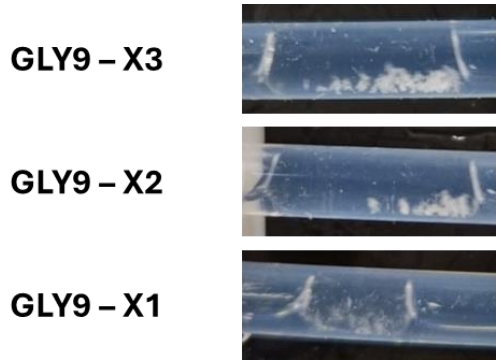

Figure 4.15: Image of crystallisation levels at X1-3 positions for GLY9. Crystallisation levels increase with increasing crystallisation times.

Data were collected for GLY1 and GLY5-9 conditions, with X3 analyses only for GLY1 and GLY5-8. GLY9 studied all three X-ray windows for time-resolved *in situ* analyses but different flow rate and reduced ethanol loading (0.500) . Data collections used the Cu K-α radiation at a wavelength of 1.5406 Å, with HyPix-6000HE detector settings of 800 x 775 px with 100 µm pixel size with continuous, pulsed 100 ms frame acquisitions. Other dataset specific settings are summarised below in Table 4.06. Two collections were completed with a lower beam divergence (4 mR) to test if it decreased background noise and improved clarity of diffraction spots. Two detector distance settings were trialled to test the effect on diffraction also. A dataset identifier of "GLY1_1_variable" describes GLY1 conditions with varying vertical stage heights to better target crystals: the absence of "variable" indicates a single stage height used. GLY9 conditions looked at several X-ray windows and has an "X" identifier also.

Table 4.06: Summary of X-ray instrument settings for GLY data collections during anti-solvent crystallisation in the KRAIC-Xl.

Dataset identifier	X-ray window	Detector position /mm	Beam divergence /mR	Aperture displacement /mm	Stage heights
GLY1_1_variable	3	70	10	0	6.00 - 7.50
GLY5_1	3	70	10	0	7.50
GLY6_1_variable	3	70	10	0	7.00 - 9.00
GLY6_2_variable	3	80	10	0	7.50 - 8.00
GLY7_1_variable	3	80	10	0	7.25 - 7.75
GLY7_2	3	80	10	0	7.50
GLY7_3	3	80	4	1.45	7.50
GLY8_1	3	80	4	1.45	7.50
GLY8_2	3	80	10	0	7.50
GLY9_1_X3	3	80	10	0	7.50
GLY9_2_X2_variable	2	80	10	0	30.00 - 36.00
GLY9_3_X2	2	80	10	0	35.25
GLY9_4_X1_variable	1	80	10	0	71.00 - 77.00
GLY9_5_X1_variable	1	80	10	0	76.50, 76.25

4.4 – Results and Discussion

4.4.1 - KRAIC-Xl

The KRAIC-Xl system was able to achieve *in situ* XRD analysis of crystallisation with a lab-source X-ray instrument at Flow-Xl. Diffraction was achieved for both LGA and GLY crystallisations. The LGA and GLY X-ray data are discussed in further detail in the following sections. In comparison to equivalent studies at synchrotron facilities, the Flow-Xl facility allows for immediate access to the X-ray enclosure in the event of a blockage, rather than the time-consuming synchrotron hutch access safety protocols required. Furthermore, the 360 ° view of the large KRAIC-Xl main body at all times enabled easy monitoring of the crystallisations for blockages. As such, any encrustation that did occur was not able to reach hazardous levels and were easily remedied through changing the Kapton window or running a cleaning solution through the system. Consequently, downtime during experiments at Flow-Xl were minimal, maximising beam usage. Furthermore, the peripheral equipment located outside of the enclosure allowed for monitoring of pump pressure and modification to flow rates without stopping the X-ray data capture. A drawback of the X-ray enclosure is the lack of temperature control, causing the enclosure temperature to reach 25 °C during KRAIC-Xl operation: this limits the scope of cooling crystallisations feasible in the KRAIC-Xl due to the lack of crystalliser or enclosure temperature control. Issues with positioning the vertical translation stages caused the bottom of the crystalliser to be higher than calculated,

resulting in only X1-3 positions to be accessible in-beam for this beamtime, despite the vertical travel range covering the distance between X1 and X4 positions. The vertical stage positioning issues were due to incorrect mounting post heights and should be adjusted for any future work.

The processing methodology was developed using the GLY data and is discussed further in Chapter 3. The processing methodology uses CrysAlisPro for the Frame Selector tool, developed by Rigaku for the Flow-Xl facility, to separate out diffraction signal frames termed "Used Frames" from background scattering only frames.[20] The Used Frames are used to form an overlaid diffraction frame and exported into a Jupyter Notebook Python script that uses pyFAI calibration and 1D integration tools, and pybaselines for morphological baseline correction of diffraction signal.[21–24] As discussed in Chapter 3 during the PXRD data processing development, the initial PXRD data processed using the silver behenate calibrant files collected showed peaks for GLY which did not correlate with reference GLY polymorph patterns, shown previously in Figure 3.29. The three most intense peaks for the processed GLY patterns did not directly match to the reference peak positions, however the relative peak positions correlated with the β-GLY polymorph reference peaks, indicating that the beta form was present, but peaks were shifted due to poor calibration. Using Equation 3.01, the corrected detector distance was calculated based on the offset peak centroids and used to re-calibrate and re-process the GLY X-ray data. The incorrect calibrated and adjusted calculated detector distances for detector settings of 70 mm (d70) and 80 mm (d80) are shown below in Table 4.07.

Table 4.07: Detector distance settings for the incorrect calibrated detector distances and adjusted averaged calculated detector distances, calculated from the GLY data.

Detector distance setting /mm	**Calibrated detector distance /mm**	**Average calculated detector distance /mm**
70	49.59	50.42 ± 0.12
80	57.57	60.40 ± 0.39

The detector distance settings do not match the sample-to-detector distances due to the KRAIC-Xl sample position being offset from the typical sample goniometer position. The silver behenate calibrant files were of poor quality, with large ring thicknesses and loss of intensity for key rings (Appendix A4.1). The poor calibration is shown by the difference in d70 and d80 calibrated detector distances of 7.98 mm, when the offset should be 10 mm. The 10.02 mm difference in corrected detector distances of 50.42 mm and 60.40 mm demonstrates the improvement in calibration. The increased error in the calculated detector distance for the d80 setting is due to several X-ray window positions being used for d80 GLY collections, contributing to the increased error due to slight differences with sample to detector distances for different windows. The corrected detector distance of 50.42 mm was used for processing the LGA data, collected at d70 detector settings. The two calculated detector distances for d70 and d80 were used for processing the GLY data.

The Mercury generated GLY and LGA reference patterns were generated with a 0.5 ° 2θ Full Width Half Maximum (FWHM) to more easily compare against the KRAIC-Xl data with calculated FWHM of the GLY data at ~0.6 ° 2θ, GLY example shown below with Figure 4.16.[4,5,12–14]

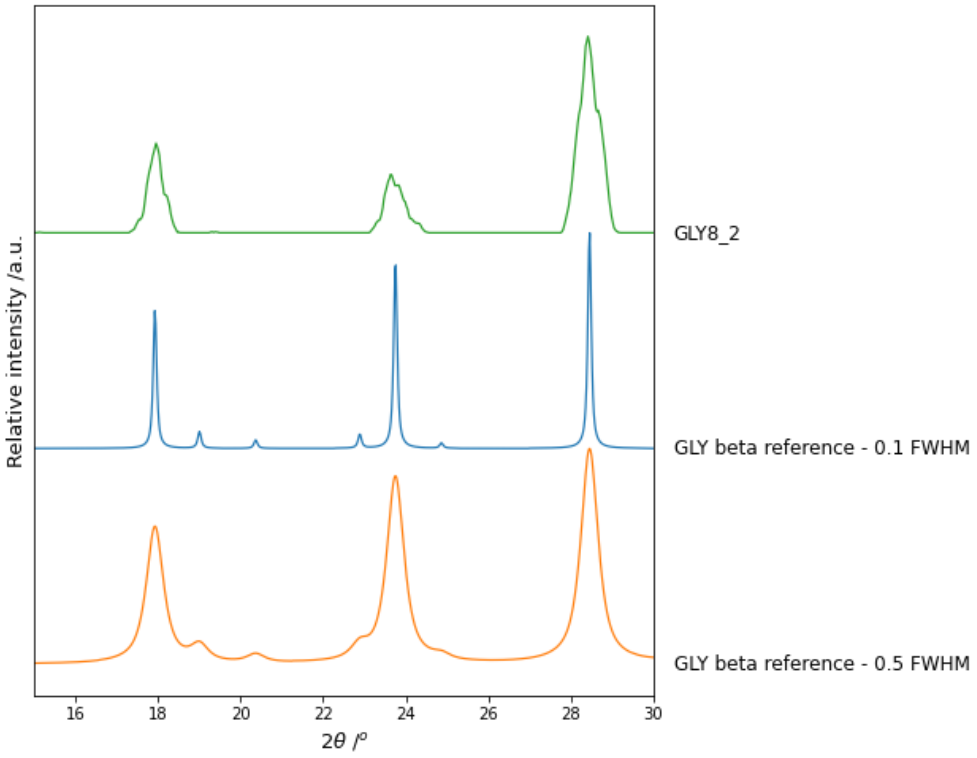

Figure 4.16: PXRD patterns of GLY8_2 dataset against GLY beta reference for 0.1 ° and 0.5 ° 2θ FWHMs.[12–14]

4.4.2 – L-glutamic acid crystallisations

As previously stated, all six LGA conditions produced crystallisation and data collection was attempted with all conditions. Using the processing regime discussed in Chapter 3, the LGA frames were filtered using the Frame Selector tool in CrysAlisPro developed by Rigaku for the Flow-Xl project and visually inspected by the user. Out of the 20 datasets collected during LGA conditions, 6 datasets contained no diffraction, 5 datasets had only a single diffraction spot noted for thousands of frames collected, and 2 datasets had notable diffraction due to an encrustation in the Kapton X-ray window tube. The remaining 7 datasets had a few diffraction spots noted in the resultant overlaid diffraction pattern. Full details on frame selection are summarised in Appendix A4.2.

An example of the appearance of the LGA X-ray datasets with minimal diffraction spots is shown below in Figure 4.17 with representative diffraction frames, the overlaid diffraction frame with signal extracted in CrysAlisPro, and the processed 1D integrated PXRD pattern, as processed with the workflow discussed in Chapter 3, Figure 3.27. The LGA data was processed with calculated 50.42 mm detector distance calibration for the 70 mm detector setting data. The diffraction datasets with a single spot recorded were unable to be processed due to poor signal-to-noise.

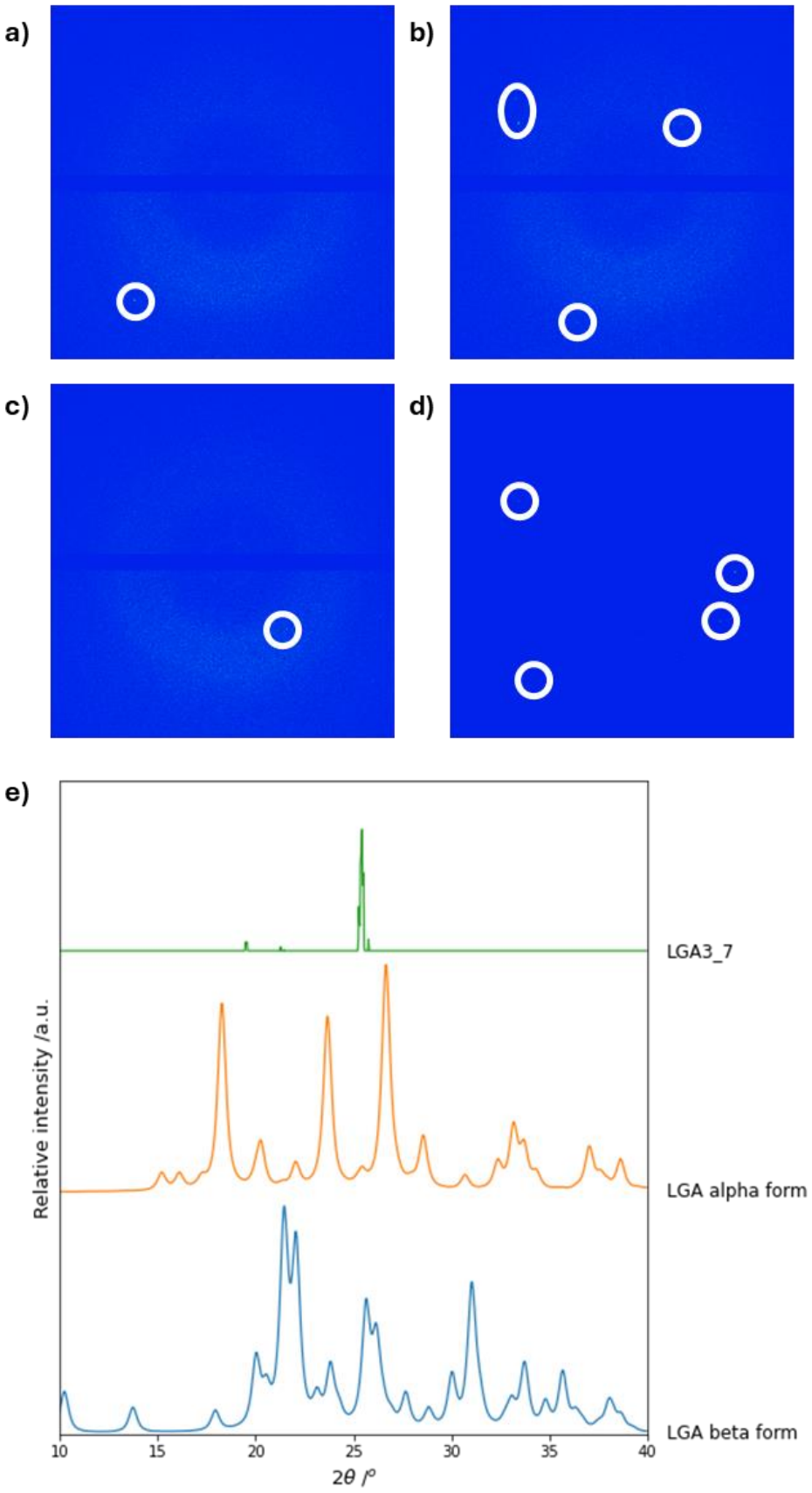

Figure 4.17: a – c) example diffraction frames collected for LGA3 conditions (dataset LGA3_7), d) overlaid 2D diffraction frame for LGA3_7 generated with the processing technique described in Figure 3.27. Diffraction spots circled on images e) processed diffraction pattern for LGA3_7 against Mercury generated LGA reference forms.[4,5]

The PXRD data gathered during encrustation of LGA on the Kapton window were processed and are shown below in Figure 4.18. The LGA6_3 encrustation whilst visual inspection of the X-ray window showed a slight encrustation, the diffraction frames contained only a single spot maintaining position for ~ 700 frames with only one peak on the resultant PXRD pattern. This indicates that the X-ray beam was not focused on the bulk of the encrustation. The LGA3_5 encrustation showed strong diffraction and peak positions for 337 frames; the data capture was ended to clear the encrustation. The LGA3_5 appears to show the stable β-LGA polymorph. The literature shows that low ethanol loadings and higher nucleation temperatures promote the nucleation of the stage β-LGA form.[8–10] The relatively low ethanol fraction (0.300) with low supersaturation levels promoted the growth of the stable LGA form. The intermediate temperatures used for crystallisation (14 – 25 °C) do not promote the metastable α-LGA. These crystallisation results correlate with literature studies of LGA anti-solvent and cooling crystallisation.

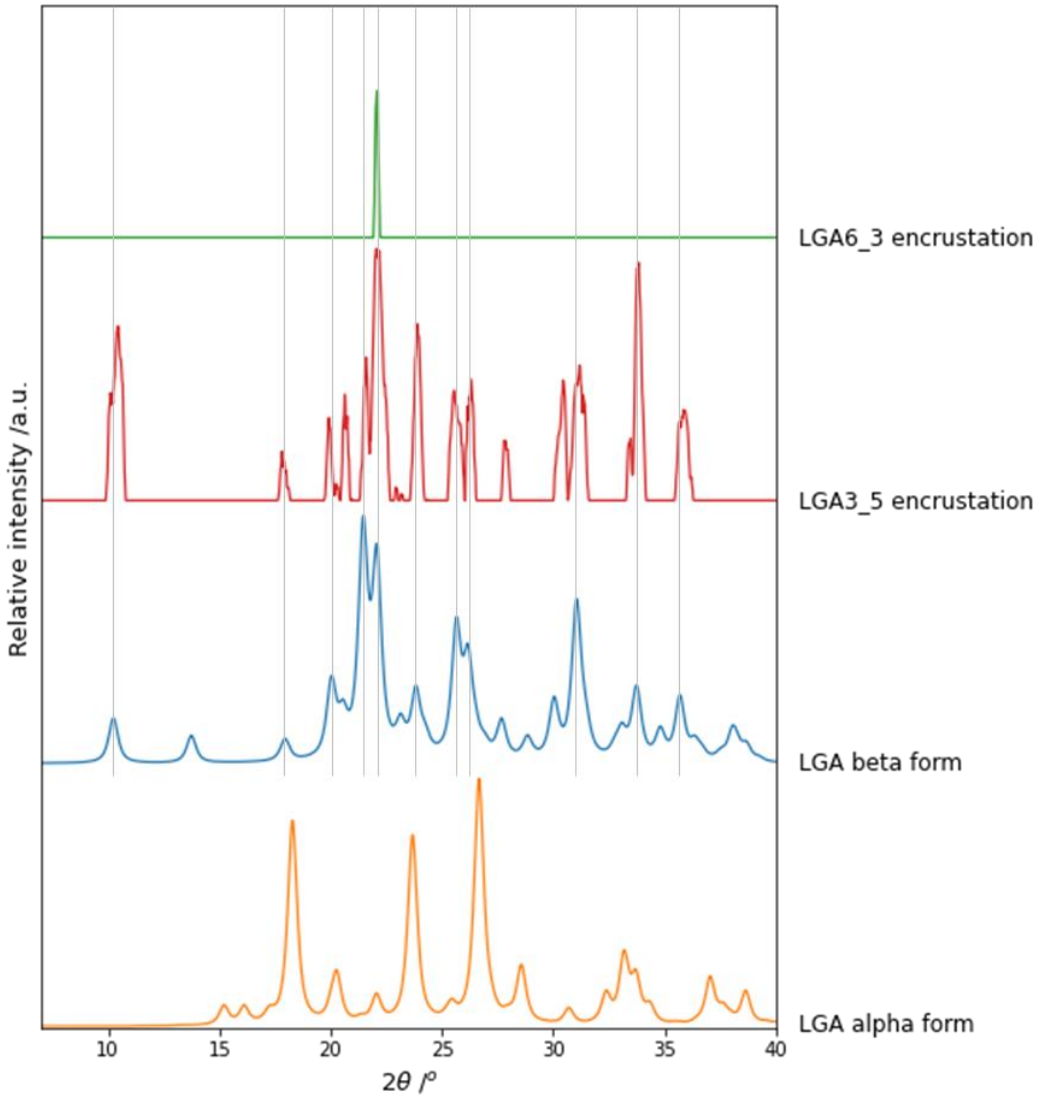

Figure 4.18: PXRD patterns of LGA encrustations, compared against the 0.5 ° 2θ FWHM Mercury generated LGA reference patterns. Line annotations show key β-LGA peak positions.

The LGA3_5 resultant pattern has strong signal but incomplete peak shapes due poor powder averaging from preferred orientation of the encrustation not accounting for the full powder rings or ring thickness present at the lab-source system. The broader X-ray peaks are the result of several instrumental factors, including the larger beam size and imperfect monochromacy compared to synchrotron sources. The variation in sample-to-detector distance of the sample in the 1/8" ID Kapton tube is equivalent to the synchrotron KRAIC systems; however, the peak broadening effect is exacerbated by the different beam optics. The number of peaks in the LGA references and broadness of peaks highlight the challenges of lab-source *in situ* XRD, with complex systems may struggle to achieve phase identification in the KRAIC-Xl system as a result.

The processed patterns for the LGA collections with a few diffraction spots are shown below in Figure 4.19. The LGA diffraction patterns with minimal diffraction signal have too few diffraction spots to form the diffraction peaks of the appropriate width of the instrument system to identify the polymorphic form. The lack of quality diffraction for LGA datasets is likely due to a combination of too few crystals in-beam, crystal density shown previously in Figure 4.11, and poor targeting of crystals in the X-ray tubing. At synchrotron experiments, varying the stage height focus on the X-ray window and observing the resulting diffraction usually indicates the best position for targeting crystals, however, varying the stage height on the X3 window of the KRAIC-Xl did not result in the observation of strong diffraction. The targeting the X-ray windows was done by eye, with observation of crystalliser height and detector frames: frames with high Kapton scattering were deemed to be hitting the top or bottom edge of tubing, thus not targeting the crystals in slug. No heights with strong diffraction were observed, leading to the conclusion that the crystal density was not high enough.

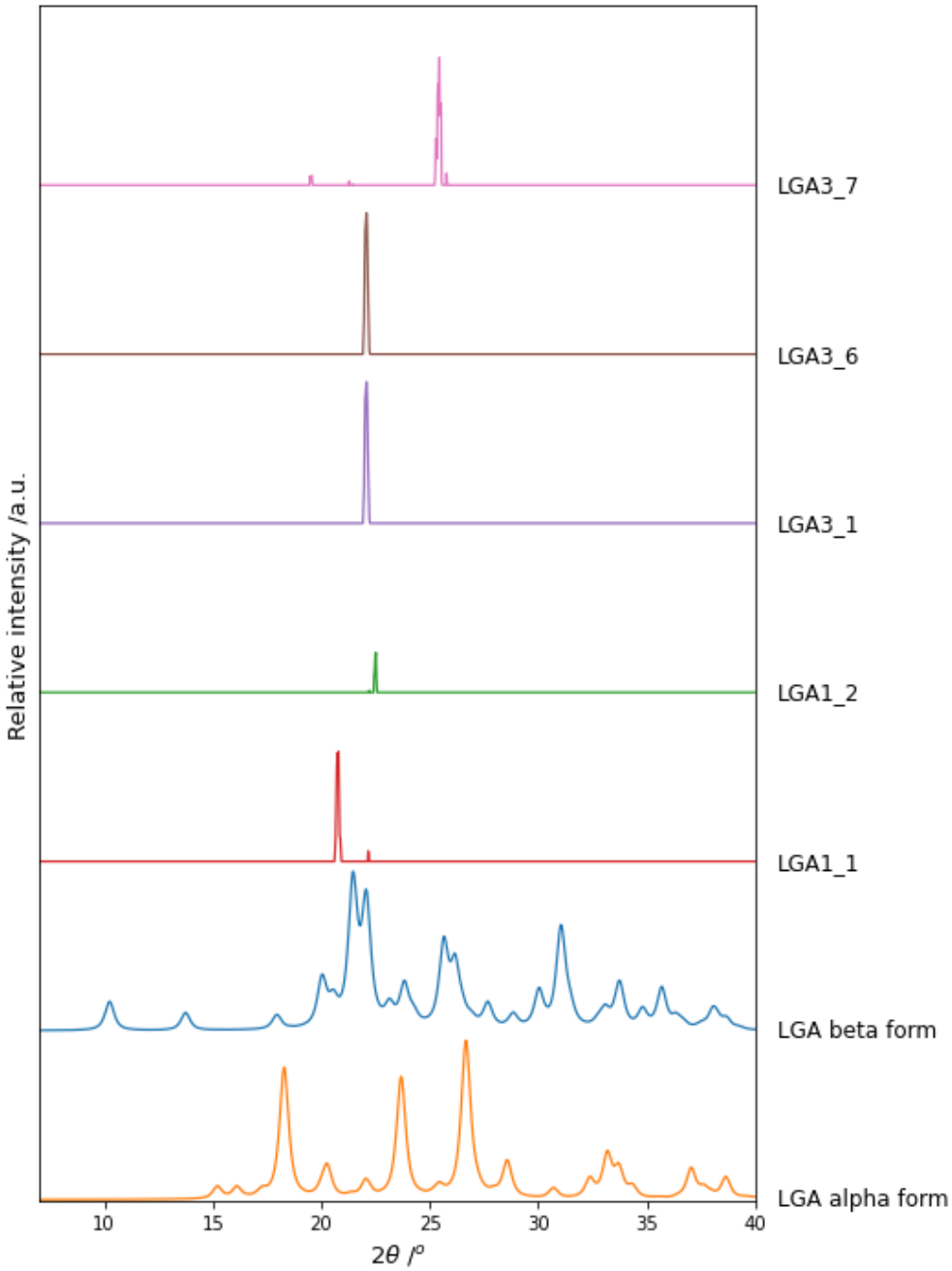

Figure 4.19: PXRD patterns of low signal diffraction frames from LGA crystallisation in the KRAIC-XI against LGA Mercury generated reference patterns.

4.4.3 – Glycine crystallisations

As previously stated, crystallisation was achieved at all GLY conditions, however the crystallisation levels were low for GLY1-4 conditions, with data collected only at GLY1. The segmentation set-up for GLY1 produced encrustation and inconsistent pumping of the crystal slurry: this uneven loading of slugs resulted in high enough crystal densities in some slugs to achieve X-ray diffraction data, despite the lower ethanol loading (0.430). The higher ethanol anti-solvent loadings of GLY5-9 resulted in increased crystallisation levels, as shown in Figure 4.15. Data for GLY1, and GLY5-8 was collected at X3 only, with

GLY9 looking at time-resolved crystallisation with X1 to 3 analysis. Using the processing regime discussed in Chapter 3, the GLY frames were visually inspected and sorted using the Frame Selector tool in CrysAlisPro developed by Rigaku for the Flow-Xl project. The results are summarised in Table 4.08 below.

Table 4.08: Summary of Frame Selector results for GLY datasets during GLY crystallisations in the KRAIC-Xl.

Dataset Identifier	Number of frames	Used frames	Percentage of "Used frames"
GLY1_1_variable	3600	240	6.7%
GLY5_1	2478	121	4.9%
GLY6_1_variable	3600	490	13.6%
GLY6_2_variable	3600	820	22.8%
GLY7_1_variable	14400	3580	24.9%
GLY7_2	14400	5205	36.1%
GLY7_3	14400	2479	17.2%
GLY8_1	7200	1590	22.1%
GLY8_2	1231	455	37.0%
GLY9_1_X3	14400	5851	40.6%
GLY9_2_X2_variable	5893	796	13.5%
GLY9_3_X2	14400	3392	23.6%
GLY9_4_X1_variable	7200	373	5.2%
GLY9_5_X1_variable	7771	1993	25.6%

The processing method with visual inspection by the user ensured that the majority of “used frames” to form the total overlaid diffraction frame contained diffraction, filtering out the background noise only. The vertical stage variable collections showed reduced percentage of used frames due to a higher proportion of the frames containing background scattering as the user attempted to target crystal diffraction more affectively. The initial GLY9_4_X1_variable has a lower percentage of frames used (5.2%) due to the larger range of stage heights tested (71.0 - 77.0) rather than the slight adjustment (76.25 – 76.50) used for the final GLY9_5_X1_variable dataset (25.6%). Varying the stage height during collection resulted in improved targeting of the bulk of crystalline material for improved diffraction signal. The lower beam divergence collections (4 mR) for GLY7_3 and GLY8_1 did not improve the collection of diffraction frames, slightly decreasing the percentage of selected frames in comparison to the wider beam divergence (10 mR) equivalent datasets. The d70 detector settings for GLY1_1_variable to GLY6_1_variable may have slightly reduced the number of Used Frames achieved; however, it is more likely the unoptimized vertical stage heights produced the lower percentage of Used Frames.

The quality of diffraction for the GLY data was significantly improved compared to the LGA diffraction. Representative diffraction frames are shown below in Figure 4.20.

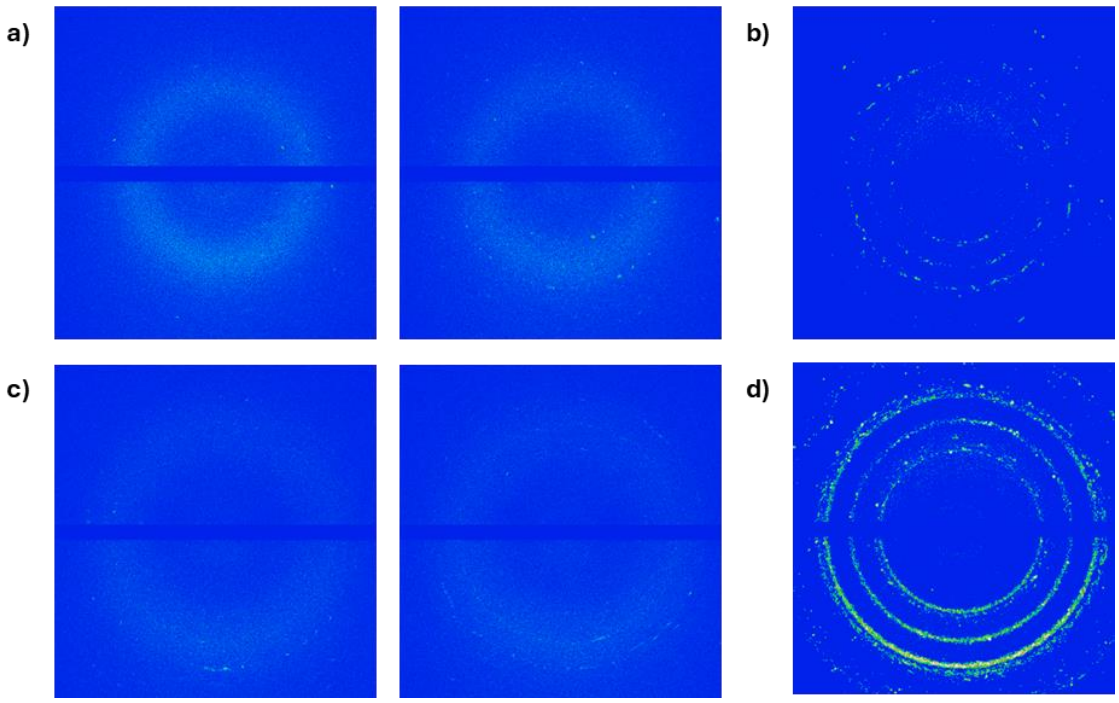

Figure 4.20:Two single 100 ms acquisition diffraction frames from a) GLY1_1_variable with a d70 stage setting, and c) GLY9_1_X3 for a d80 stage position. Overlaid diffraction frames using selected frames from the Frame Selector tool in CrysAlisPro for b) GLY1_1_variable, and d) GLY_1_X3.

The single diffraction frames collected for GLY conditions, shown in Figure 4.20a+c, often showed multiple spots per frame, with some frames starting to show the powder ring appearance. The increase detector distance setting used for GLY9_1_X3 compared to GLY1_1_variable show an expansion of the diffraction and background scattering. The resulting overlaid diffraction frames created with the used frames from the Frame Selector tool were processed with the corrected detector frames using the Python workflow described in Chapter 3, examples shown in Figure 4.20b+d. The overlaid diffraction pattern for GLY9_1_X3 shows significantly stronger intensities and clearer powder rings than GLY1_1_variable due to the higher proportion of Used Frames forming the overlaid pattern: 5851 compared to 240. The overlaid powder rings illustrate the thickness of powder rings achieved with the lab-source X-ray instrument, resulting in broad FWHM diffraction peaks. The resultant plots for GLY1-8 are shown below in Figure 4.21.

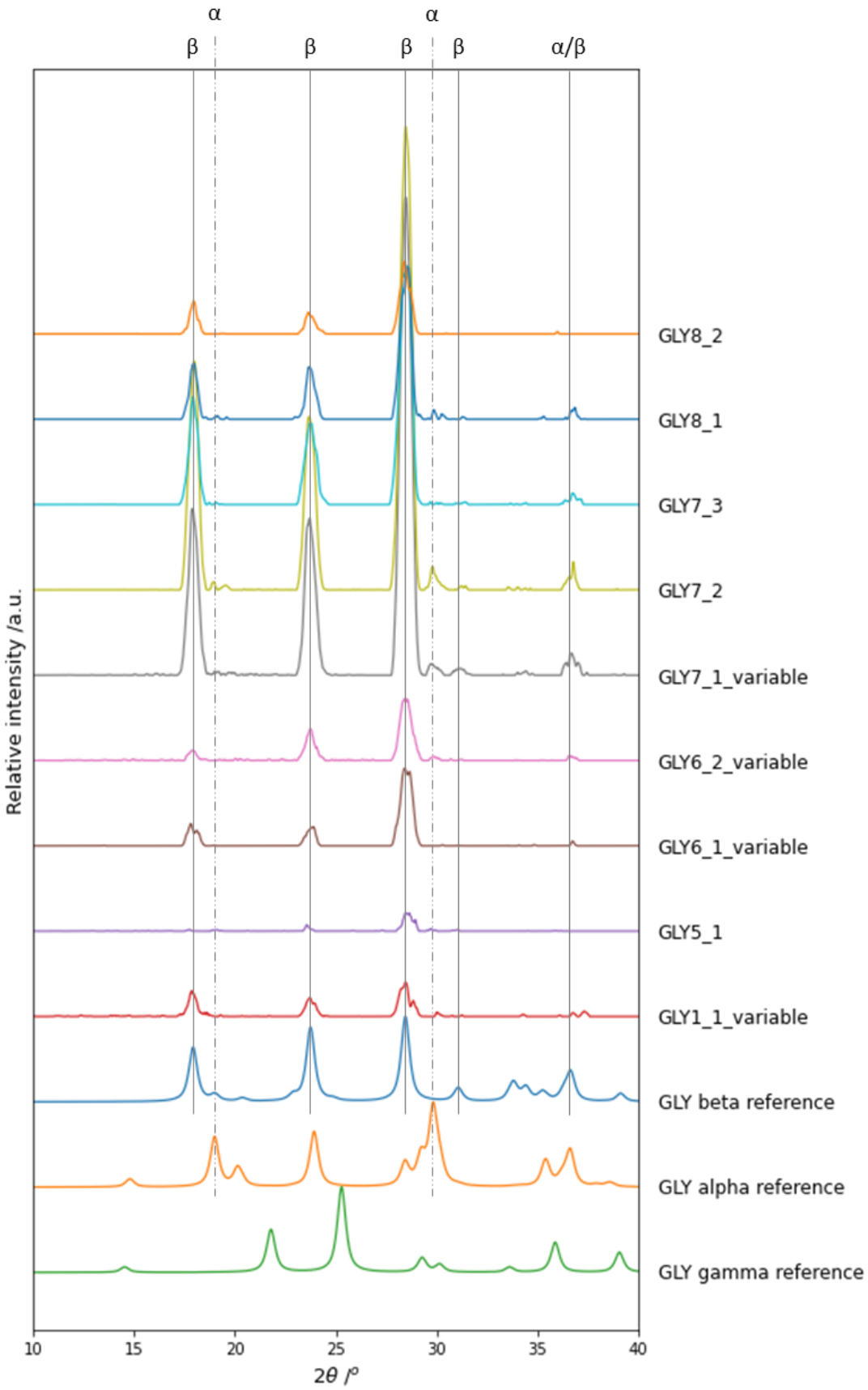

Figure 4.21: PXRD patterns of GLY1-8 conditions against Mercury generated 0.5 ° 2θ FWHM GLY reference patterns. Key β-GLY and α-GLY peaks are annotated on the plot. Processed GLY patterns shown with the same intensity scaling.

All diffraction frames show predominant β-GLY presence with key β-GLY peaks at 17.9 °, 23.7 °, and 28.5 ° 2θ. GLY1_1_variable, GLY5_1, GLY6_2_variable, GLY7_1_variable, GLY7_2, GLY7_3, and GLY8_1 also show a key α-GLY peak at 29.8 ° 2θ. The predominant β-GLY with some α-GLY correlates with literature behaviour for ethanol anti-solvent crystallisation of GLY; β-GLY in literature is shown to commonly crystallise from alcohol anti-solvent systems, with known crystallisation of α-GLY in the presence of water, or transformation of β-GLY to α-GLY in the presence of water.[16,17]

GLY1_1_variable to GLY6_2_variable and GLY8_2 PXRD patterns generally show lower intensity with peak splitting or uneven peak shapes due to poor powder averaging. This is due to the low number of selected frames (121 – 820) and incomplete powder rings, like shown in Figure 4.20b. The patterns with over 1000 frames start to show improvement in peak shapes, and clearer α-GLY peaks appearing. As a result, the data collection required for a crystal density as shown in Figure 4.15 for X3 position to achieve reasonable data quality was minimum of 7200 frames and 1000 resultant Used Frames, for a total collection time of 12 min minimum. Collections of 14400 frames achieved the best results, for collection times of 24 minutes.

The time resolved analysis for GLY9 conditions is shown below in Figure 4.22. The PXRD patterns for the time resolved pattern show predominant β-GLY at all three X-ray windows for the 17.9 °, 23.7 °, and 28.5 ° 2θ, with α-GLY presence appearing at the X2 window (19.2 °, 20.2 ° and 29.8 ° 2θ), with a stronger presence of α-GLY developing by the X3 analysis point. GLY9_4_X1_variable shows poor signal due to the variable stage height used to target maximum diffraction signal resulting in only 373 frames of diffraction. After targeting the bulk of crystal density, the increased diffraction results in 1993 diffraction frames for similar collection times: this increased signal produces a PXRD pattern with good powder averaging and clear β-GLY presence with no α-GLY. The lack of α-GLY indicates a non-detectable level of α-GLY, rather than poor data quality due to the high number of diffraction frames collected and good powder averaging achieved. The variable height collections generally show poorer signal to noise and poor powder averaging due to the lower overall used frames achieved. However, the variable collections do give a good initial indication of the polymorphic presence.

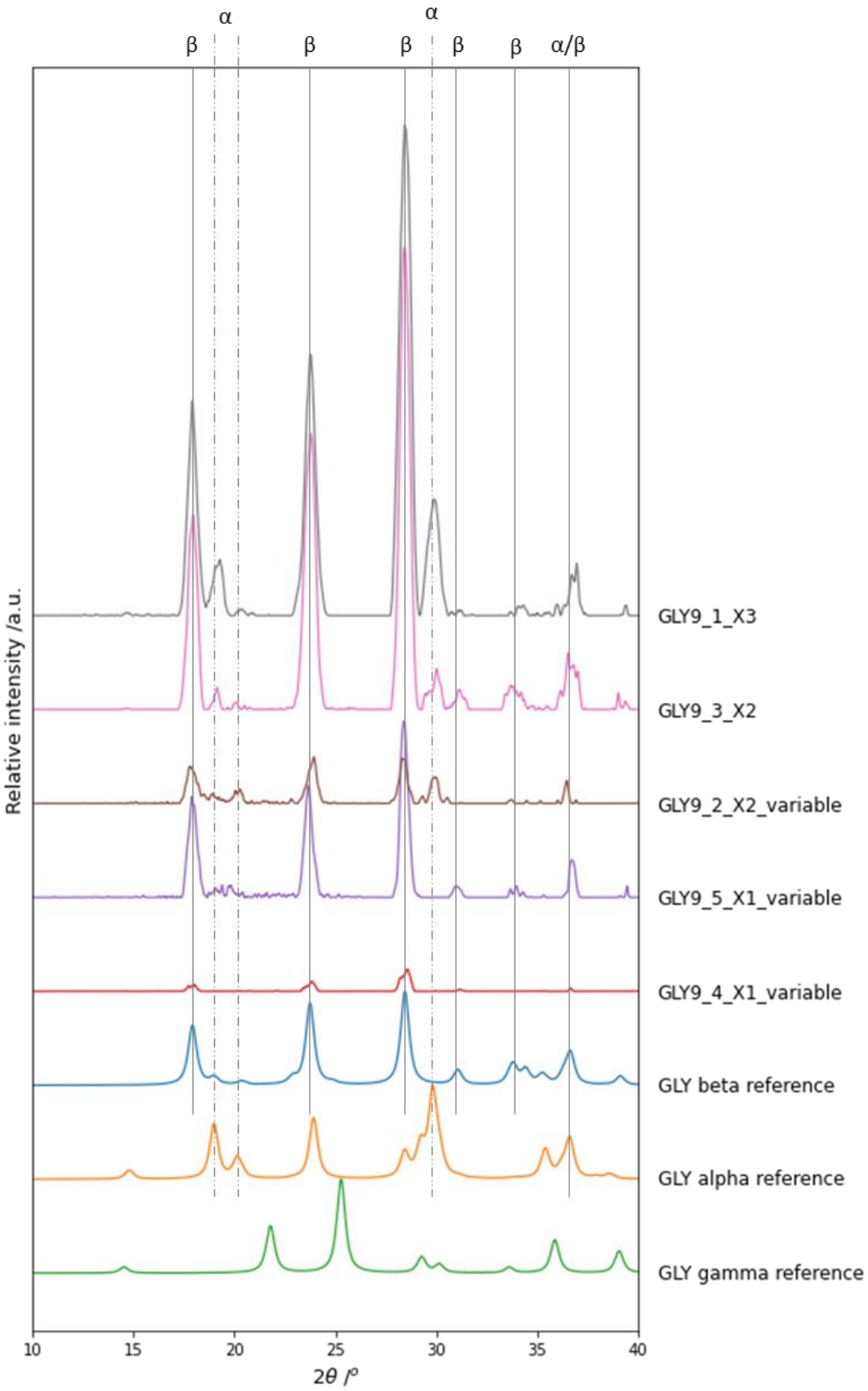

Figure 4.22: PXRD patterns from GLY9 crystallisation conditions in the KRAIC-XI at X1-3 analysis points against Mercury generated GLY reference patterns. Key β-GLY and α-GLY peak positions are annotated.

The crystallisation of the least stable, metastable β-GLY initially on anti-solvent addition with a high supersaturated state agrees with literature sources for GLY crystallisation. β-GLY is known to rapidly recrystallise to α-GLY through solvent mediated phase transitions in the presence of water, with timescales in the region of minutes to hours, dependent on the crystallisation environment.[16,17] Bouchard *et al*. found the induction time for recrystallisation of β-GLY to α-GLY at 37 °C to detectable levels by Raman spectroscopy is dependent on the anti-solvent used and proportion of anti-solvent to water; transformation with acetone and IPA anti-solvents is rapid, with ~0.5 volume fractions resulting in transformation within minutes.[17] Increased IPA and acetone (~0.7) reduced the presence of water, increasing the induction time to ~ 10 min. With ethanol and methanol anti-solvents, lower volume fractions (~0.5) resulted in induction times within minutes, but high volume fractions ethanol and methanol (~0.7) resulted in slower induction times of 50 min and 120 min respectively. The KRAIC-Xl GLY 0.50 ethanol fraction crystallisation appears to show initial β-GLY crystallisation after 2:40 min at X1, with β-GLY partially transforming to detectable α-GLY at 4:25 min total crystallisation time, a further 1:45 min from the initial analysis point. The final analysis window, X3, shows significant α-GLY content with majority β-GLY after 6:21 min, an additional 1:56 min transformation time from X2. The KRAIC-Xl results do not appear to show concomitant nucleation, rather, initial β-GLY nucleation and transformation to α-GLY over time. The timescales for the GLY solvent mediated phase transition in the KRAIC-Xl are rapid, with non-detectable α-GLY to considerable detectable levels after 1:45 min, agreeing with the literature for the detection of α-GLY within minutes at 0.500 volume fractions.

4.5 – Conclusions

Lab-source *in situ* PXRD analysis during meso-scale, tri-segmented flow has been achieved with the development of the KRAIC-Xl at the Flow-Xl facility, University of Leeds. The model system glycine was studied during ethanol anti-solvent crystallisation of aqueous GLY solution at room temperature (~25 °C). Ethanol fractions of 0.400 - 0.440 produced a lower, inconsistent crystal densities of GLY. Higher ethanol fractions of 0.500 – 0.520 produced a high crystal density in slugs, with X-ray diffraction achieved at X-ray analysis times at 6:21 min, 7.5 m along the crystalliser length at analysis window 3 (X3). Processing of data was achieved with a novel processing methodology developed for this work, discussed in Chapter 3. Data processing used CrysAlisPro, the Rigaku XRD software, for the Frame Selector tool to separate background scattering only frames and frames with diffraction signal termed “Used Frames”. On filtering the used frames, an overlaid diffraction frame of overlaid signal from the Used Frames is exported to a Jupyter Notebook for Python scripted calibration, 1D integration, and baseline correction. The GLY data found that for the crystal density present, minimum collection times of 12 min, equivalent to 7200 frames, were required for the minimum 1000 Used Frames to achieve good signal-to-noise and powder averaging of the resulting 1D PXRD pattern. The processed GLY data at the X3 data capture position

showed crystallisation predominantly of the metastable β-GLY polymorph, with a small quantity of α-GLY present. A crystallisation run of GLY with 0.50 fraction of ethanol was studied at three analysis windows at lengths of 3.1 m, 5.3 m and 7.5 m for crystallisation times of 2:40 min, 4:25 min, 6:21 min respectively. PXRD analysis of the first X-ray window showed β-GLY only, with X2 showing predominant β-GLY and some α-GLY, and finally X3 showing β-GLY with a higher quantity of α-GLY, achieving a time-resolved study of crystallisation in the meso-scale system. β-GLY commonly crystallises from alcohol anti-solvent crystallisations and is known to rapidly transform to α-GLY in aqueous conditions: this study of GLY crystallisation concurs with literature sources with the phase transition of β- to α-GLY occurring over short 1:45 min timescales.

Crystallisation experiments of aqueous L-glutamic acid with ethanol anti-solvent additions (ethanol fractions of 0.300 – 0.500) for temperature conditions of 60 – 14 – 25 °C produced crystallisation, however, adequate X-ray diffraction was not acquired during flow conditions. The LGA crystal densities produced were lower than seen for GLY, especially at 0.300 – 0.350 volume fraction ethanol loadings, potentially causing the lower diffraction signal. Another cause may be the poor targeting of crystals with the X-ray beam, however, lack of visualisation of the sample position hindered crystal targeting. PXRD analysis of diffraction data collected from an encrustation of LGA in the analysis window showed the stable β-LGA polymorph, likely due to the low supersaturation achieved by the ethanol loadings and nucleation temperatures favouring crystallisation of the stable polymorph. The complexity of the LGA diffraction patterns shows a limitation of the lab-source technique: the broad 0.5 ° 2θ FWHM diffraction peaks present for the KRAIC-Xl system may struggle to achieve phase identification of polymorphic systems with many forms, or polymorphs with distinctive peaks in similar 2θ regions.

Whilst PXRD with a lab-source X-ray instrument of meso-scale segmented flow diffraction has been achieved, the comparison of LGA and GLY diffraction achieved highlights the limitations of the technique. The specific conditions required to achieve diffraction patterns in the KRAIC-Xl, in terms of quantity of crystalline material in beam and the high “ambient” temperature of the X-ray enclosure (25 °C), limits the scope of experiments at the Flow-Xl facility. For example, larger scale screenings of GLY crystallisation conditions with a range of anti-solvent ratios would be unfeasible due to the lower anti-solvent loadings producing less crystallisation and resulting diffraction signal, potentially to non-detectable levels. However, the advantages of the Flow-Xl facility are the ease-of-use of the crystalliser and X-ray equipment, requiring less rigorous safety controls due to the lower energy X-rays for easier access into the enclosure in the event of blockage. The results of the GLY *in situ* diffraction data shows that synchrotron X-rays are not required in all situations, and that the Flow-Xl facility and KRAIC-Xl provide an alternative, and potentially easier route for obtaining *in situ* data, reducing the demand for synchrotron resources. The initial data acquired at Flow-Xl could provide the preliminary data for synchrotron beamtime applications if further detailed information is required at a larger range of conditions, such as lower anti-solvent loadings, reducing

crystallisation and crystal density. The results from the LGA *in situ* diffraction analysis show that a synchrotron source is necessary for some *in situ* analysis experimental conditions. The Flow-Xl data provides a good basis for beamtime proposals with preliminary data highlighting the necessity of synchrotron data improving the chances of beamtime application success. The KRAIC-Xl crystalliser and peripheral equipment is available for future users of the Flow-Xl facility to conduct their own experiments, as is the Python processing script.

4.6 – Future Work

Now that proof-of-principle has been achieved, the system would greatly benefit from engineering enhancements to improve ease-of-use and data quality. Crystal targeting was an unknown factor in the data acquisition, with the lack of LGA data likely caused by poor crystal targeting. The inclusion of close-up camera on or near the beam position would greatly assist with targeting crystals in slugs and improve crystal targeting for high crystal density systems also. The current set up in the Flow-Xl enclosure uses moveable lighting that could be used for visualisation of crystals in the X-ray tubing, so no additional equipment would be required. The Flow-Xl facility also has *in situ* Raman spectroscopy functionality; whilst it was out of scope for this work, adding Raman spectroscopy would benefit the analysis of systems with overlapping PXRD peaks, should the Raman spectra be suitably different.

The KRAIC-Xl system suffered from poor calibration due to poor quality silver behenate calibrant files collected at the X3 sample position. Future work with the KRAIC-Xl should focus on getting higher quality calibrant files at all X-ray window positions. Putting the silver behenate powder in the Kapton tube X-ray window may improve the calibration of the detector distance. Also, the X-ray windows should have the same detector distance, however, any slight tilt to the crystalliser body should be accounted for by proper calibration of the X-ray positions. Furthermore, the system could be modified to use the typical sample position, enabling PXRD processing in the CrysAlisPro software. Adjustment to the vertical stage posts would enable X4 to be accessed for future experiments also.

A further method to improve data quality would be adapt the slug triggering mechanism, previously developed for the KRAIC-S for single crystal XRD, as the data acquisition methodology. The slug triggering mechanism uses stage translation backwards at the same rate the flow is moving forward in the X-ray analysis window to artificially suspend the crystals in beam for a prolonged period. The slug triggering method was applied for PXRD for the first time on the KRAIC-T crystalliser system, discussed in Chapter 5, to great affect for improving signal-to-noise and distinction of polymorphic peaks in areas of high background scattering. Applying the slug triggering mechanism for the KRAIC-Xl would be challenging due to the compact space of the X-ray enclosure and translation requirements of the large KRAIC-Xl body. Slug triggering would require translation stages, a laser-photodiode system, and a targeting camera installing with computer communications and scripting required. The benefits

for the resultant data quality would be considerable, potentially allowing for analysis with lower levels of crystal density, enabling a wider range of feasible experiments to be conducted at the Flow-Xl facility.

The KRAIC-Xl main body is currently not temperature controlled and limits the experimental conditions for crystallisation due to the 25 °C temperature of the enclosure seen with the GLY and LGA experiments. Additional temperature control to the KRAIC-Xl main body through Peltier cooling elements and heating pads could enable fully temperature controlled crystallisation experiments, widening the scope of feasible experiments with the KRAIC-Xl system. Furthermore, temperature cycling could be achieved by separately controlling the heating elements for the different tubing rungs. The main body of the KRAIC-Xl is able to be modified with additional equipment, and a further KRAIC-Xl body piece is available should further modifications be required in the future also.

Now that the KRAIC-Xl system has been commissioned and made available for users, it should be tested with a range of different system with more complex X-ray patterns to fully investigate the limitations of the technique. Furthermore, the KRAIC-Xl can be used to explore the crystallisation pathways of new materials with time-resolved studies of crystallisation. The KRAIC-Xl at the Flow-Xl facility provides a more streamlined access route for meso-scale *in situ* PXRD analysis compared to synchrotron facilities. Lab-source studies also provide basis for further synchrotron beamtime analysis with a wider range of crystallisation conditions available with the KRAIC-T and KRAIC-S systems.

4.7 – References

1. Simmance, K., Van Beek, W. & Sankar, G. Time resolved in situ X-ray diffraction study of crystallisation processes of large pore nanoporous aluminophosphate materials. *Faraday Discuss* **177**, 237–247 (2015).

2. Llewellyn, A. V., Matruglio, A., Brett, D. J. L., Jervis, R. & Shearing, P. R. Using in-situ laboratory and synchrotron-based x-ray diffraction for lithium-ion batteries characterization: A review on recent developments. *Condens. Matter* **5**, 1–28 (2020).

3. Turner, T. D. *et al.* Flow-Xl: a new facility for the analysis of crystallization in flow systems. *J. Appl. Cryst.* **57**, (2024).

4. Hirayama, N., Shirahata, K., Ohashi, Y. & Sasada, Y. Structure of α Form of l-Glutamic Acid. α-β Transition. *Bull Chem Soc Jpn* **53**, 30–35 (1980).

5. Marcoin, W., Duda, H., Kusz, J., Bzowski, B. & Warczewski, J. Structure refinement of L-glutamic acid with the aid of the X-ray 4- circle diffractometer. in *Proceedings of the 17th Applied Crystallography Conference* 40 (Poland World Scientific Pub Co Inc, 1999).

6. Kee, N. C. S., Tan, R. B. H. & Braatz, R. D. Selective crystallization of the metastable α-form of L-glutamic acid using concentration feedback control. *Cryst. Growth Des.* **9**, 3044–3051 (2009).

7. Hatakka, H., Alatalo, H., Louhi-Kultanen, M., Lassila, I. & Hæggström, E. Closed-loop control of reactive crystallization Part II: Polymorphism control of L-glutamic acid by sonocrystallization and seeding. *Chem. Eng. Technol.* **33**, 751–756 (2010).

8. Srinivasan, K. & Dhanasekaran, P. Separation and nucleation control of α and β polymorphs of L-glutamic acid by swift cooling crystallization process. *Amino Acids* **40**, 1257–1260 (2011).

9. Srinivasan, K. & Dhanasekaran, P. Nucleation control and crystallization of l-glutamic acid polymorphs by swift cooling process and their characterization. *J Cryst Growth* **318**, 1080–1084 (2011).

10. Shi, H. *et al.* Screening and Manipulation of l-Glutamic Acid Polymorphs by Antisolvent Crystallization in an Easy-To-Use Microfluidic Device. *Ind. Eng. Chem. Res.* **59**, 6102–6111 (2020).

11. Alieva, A., Boyes, M., Vetter, T. & Casiraghi, C. Selective polymorphism of α-glycine by acoustic levitation. *CrystEngComm* **22**, 7075–7081 (2020).

12. Iitaka, Y. The crystal structure of β-glycine. *Acta Crystallogr* **13**, 35–45 (1960).

13. Iitaka, Y. The crystal structure of γ-glycine. *Acta Crystallogr* **14**, 1–10 (1961).

14. Marsh, R. E. A refinement of the crystal structure of glycine. *Acta Crystallogr* **11**, 654–663 (1958).

15. Jit, P. & Feng, W. Solubility of amino acids in water and aqueous solutions by the statistical associating fluid theory. *Ind. Eng. Chem. Res.* **47**, 6275–6279 (2008).

16. Ferrari, E. S., Davey, R. J., Cross, W. I., Gillon, A. L. & Towler, C. S. Crystallization in polymorphic systems: The solution-mediated transformation of β to α glycine. *Cryst. Growth Des.* **3**, 53–60 (2003).

17. Bouchard, A., Hofland, G. W. & Witkamp, G. J. Solubility of glycine polymorphs and recrystallization of β-glycine. *J. Chem. Eng. Data* **52**, 1626–1629 (2007).

18. Levenstein, M. A. *et al.* Supplementary Information: Dynamic Crystallization Pathways of Polymorphic Pharmaceuticals Revealed in Segmented Flow with Inline Powder XRD. *Anal. Chem.* **92**, 7754–7761 (2020).

19. Levenstein, M. A. *et al.* Dynamic Crystallization Pathways of Polymorphic Pharmaceuticals Revealed in Segmented Flow with Inline Powder X-ray Diffraction. *Anal. Chem.* **92**, 7754–7761 (2020).

20. Rigaku Oxford Diffraction. CrysAlisPro. *Version 171.43.109a* (2024).

21. Kluyver, T. *et al.* Jupyter Notebooks—a publishing format for reproducible computational workflows. in *Positioning and Power in Academic Publishing: Players, Agents and Agendas - Proceedings of the 20th International Conference on Electronic Publishing, ELPUB 2016* 87–90 (2016). doi:10.3233/978-1-61499-649-1-87.

22. Kieffer, J., Valls, V., Blanc, N. & Hennig, C. New tools for calibrating diffraction setups. *J Synchrotron Radiat* **27**, 558–566 (2020).

23. Erb, D. pybaselines: A Python library of algorithms for the baseline correction of experimental data (v1.1.0). Preprint at https://doi.org/10.5281/zenodo.10676584 (2024).

24. Perez-Pueyo, R., Soneira, M. J. & Ruiz-Moreno, S. Morphology-Based Automated Baseline Removal for Raman Spectra of Artistic Pigments. *Appl Spectrosc* **64**, 595–600 (2010).

Chapter 5 – Development of the KRAIC-T, a temperature cycling crystalliser coupled with *in situ* PXRD on Beamline I11

This chapter discusses the development of the KRAIC-T, a crystalliser designed by Dr Lois Wayment and Dr Karen Robertson with Diamond Light Source technicians Jonathan Potter and Stuart Gurney. The KRAIC-T is based on the work on the KRAIC-D system developed by Dr Wayment, Dr Robertson, Dr Mark Levenstein, and Dr Pierre-Baptiste Flandrin. Research into *ortho*-aminobenzoic acid crystallisation conducted with contribution from Dr Elena Simone.

5.1 – Introduction

To achieve PXRD analysis of concomitant polymorphic systems in segmented flow, Levenstein *et al.* developed the KRAIC-D (KRAIC for diffraction) in collaboration with Beamline I11, the high resolution PXRD beamline at Diamond Light Source.[1] The KRAIC-D used the typical 1/8" ID FEP tubing used for previous KRAIC systems, with an alternately wound arrangement between two columns to present the sample in-beam, shown in Figure 5.01a. Due to the high background scattering of FEP, X-ray analysis windows (Xs) were designed using X-ray transparent Kapton tubing with PTFE connection pieces (Figure 5.01b): the Kapton windows required hydrophobic coating to maintain wetting for the segmented flow.

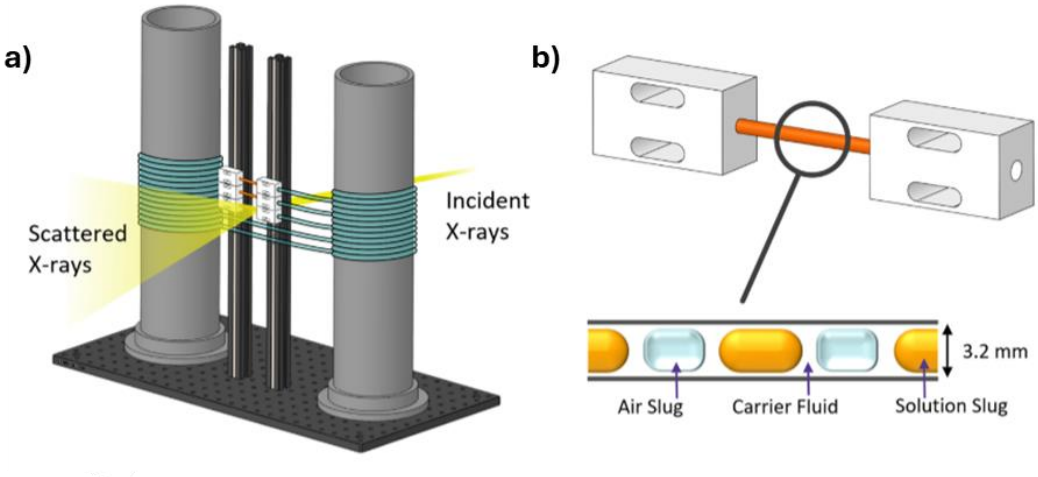

Figure 5.01: a) Representation of the KRAIC-D with alternately wound tubing arrangement around two columns, with multiple X-ray windows for time-resolved analysis. b) Kapton tube X-ray window with PTFE unions. Figure adapted from [1].

By installing X-ray windows at various points along the crystallisers length, this enabled the time-resolved study the concomitant crystallisation of multiple polymorphic systems. The initial KRAIC-D study by Levenstein *et al.* investigated two model pharmaceutical compounds, a urea:barbituric acid co-crystal (UBA)

and carbamazepine (CBZ). The UBA system has three known polymorphs, the stable Form I, and metastable Forms II and III, with concomitant production of Forms I and III. CBZ has five crystal polymorphs, often with concomitant nucleation of the stable CBZ Form III and a metastable form, CBZ Form II. The time-resolved *in situ* PXRD studies in the KRAIC-D identified that UBA Form III nucleated initially as a kinetic metastable polymorph, transforming to UBA Form I during the course of the crystallisation process, shown in Figure 5.02b. For the crystallisation of CBZ, the metastable Form II was shown to nucleate and remain stable during the full crystallisation process, but when seeding with the thermodynamic Form III post-nucleation of Form II, a transformation occurred to Form III, Figure 5.02c.

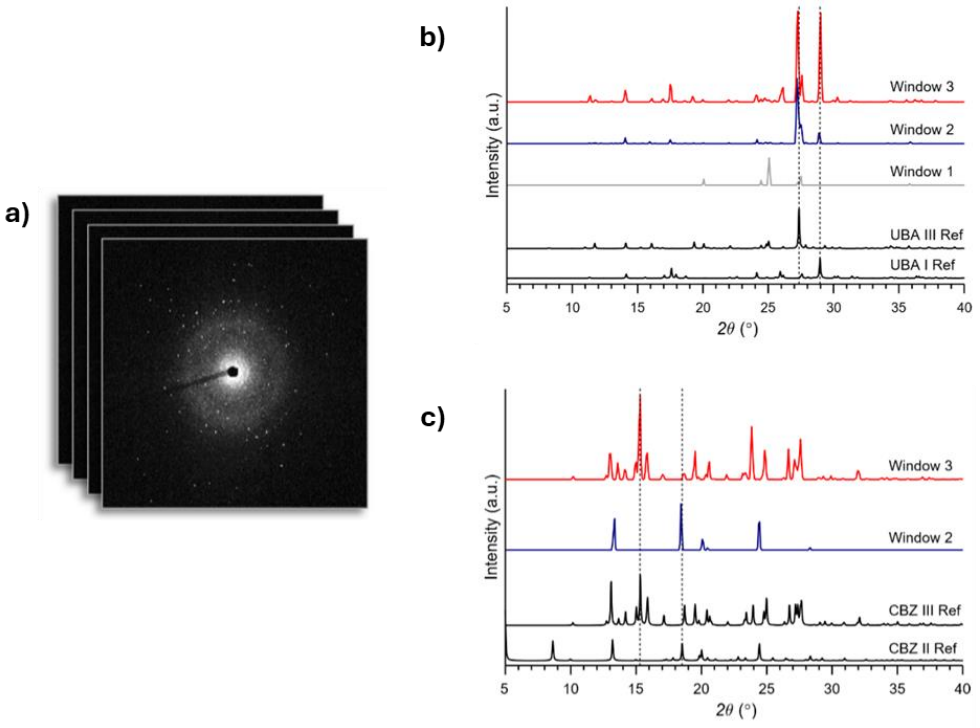

Figure 5.02: a) Representative 100 ms acquisition diffraction frames used to from the composite diffraction patterns: b) PXRDs of UBA cooling crystallisation showing initial Form III formation and transformation to Form I over time, and c) seeded CBZ cooling crystallisation showing initial CBZ Form II crystallisation and transformation to Form III after seeding. Figures adapted from [1].

The development of the KRAIC-D showed the benefit of *in situ* XRD for elucidating the polymorphic landscape and gaining understanding of the polymorphic pathways in complex systems. The research provides an excellent foundation for further research and development of the system to address some drawbacks: the KRAIC-D used 100 ms continual acquisitions (Figure 5.02a) during segmented flow, collecting diffraction frames and background scattering frames from the gas bubbles and solution slugs with no crystals in-beam. Combination of several diffraction frames were required to achieve a PXRD pattern for analysis. The processing procedure for separation of diffraction frames, and diffraction extraction and integration were time-consuming also.

The KRAIC-T (Kinetically Regulated Automated Input Crystalliser – for Temperature cycling) is a segmented flow crystalliser for *in situ* PXRD studies

during temperature cycling segmented flow crystallisation. The KRAIC-T is a development of the KRAIC-D design, using a 15 m length of 1/8” ID FEP tubing alternately wound between two independently temperature-controlled aluminium columns to produce the temperature cycling during segmented flow (Figure 5.03).

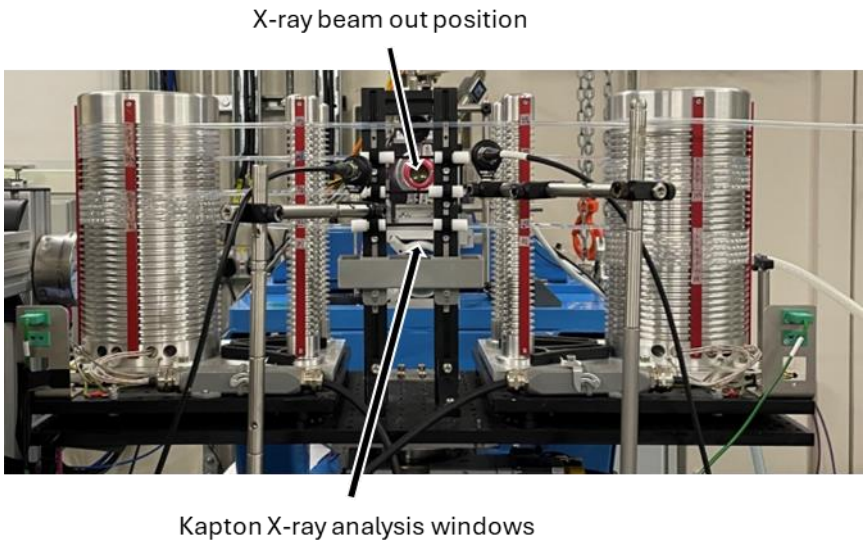

Figure 5.03: Image of the KRAIC-T in Beamline I11 EH2 (Experimental Hutch 2) at Diamond Light Source.

The machined tubing path on the aluminium columns aim to provide efficient heat transfer to the tubing and enable easy modification to the tubing configuration. The hollow columns leave a void space for ice baths to facilitate sub-ambient conditions during crystallisation. The KRAIC-T, pictured in Figure 5.03 in its basic configuration features four heating zones (HZs) alternating between the aluminium columns (C) and four X-ray analysis windows (X), schematic shown below in Figure 5.04.

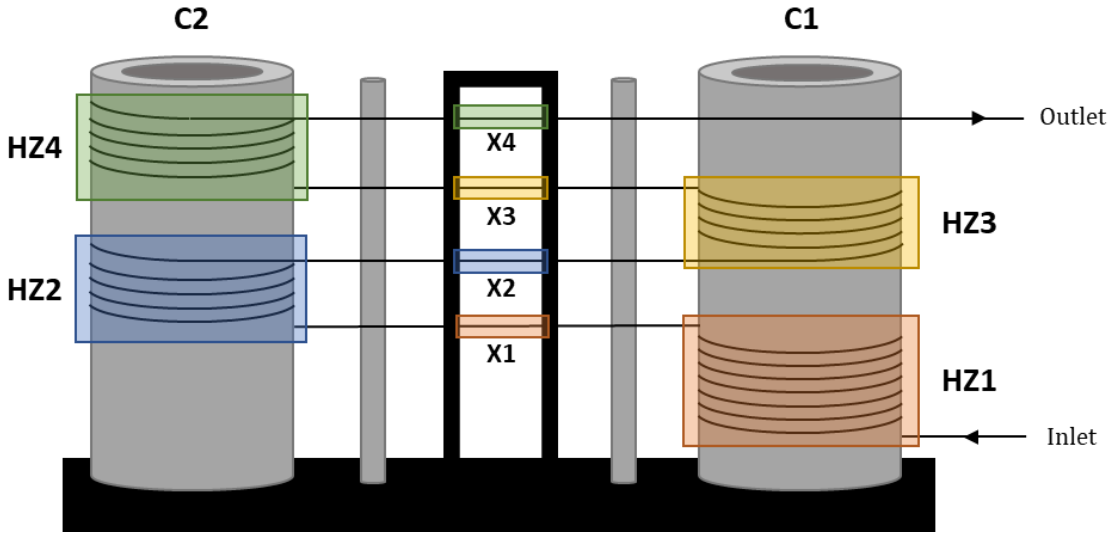

Figure 5.04: Schematic representing the KRAIC-T with Columns (C), Heating Zones (HZs) and corresponding X-ray windows (X) annotated. Temperature heating range of 30 – 60 °C investigated, with sub-ambient temperature control (9 – 12 °C) also investigated.

Temperature cycling crystallisation, introduced in Chapter 1, uses successive heating and cooling cycles during crystallisation to provide greater control over nucleation and crystal growth than typical cooling crystallisation.[2] Cooling the solution promotes nucleation and crystal growth, with heating the solution redissolving smaller nuclei and reducing crystal size, for a greater control over resultant crystal size distribution and overall crystal size. The temperature cycling process can also achieve improved control over polymorphic form and crystal morphology. The KRAIC-T aims to achieve greater control over flow crystallisation processes compared to previous KRAIC iterations through enhanced temperature control and use of temperature cycling during segmented flow crystallisation to optimise flow processes and crystalline products in terms of crystal size distribution, crystal size and morphology, and polymorphic form.

Coupling the KRAIC-T with *in situ* PXRD analysis aimed to enable investigations into temperature dependent polymorphic transitions to further elucidate the polymorphic landscape of crystalline systems. Specific aims for the KRAIC-T as a sample environment on Beamline I11 are as follows:

- To enable PXRD studies during temperature cycling segmented flow crystallisation or slurrying.
- To improve data quality, in terms of signal-to-noise, and efficiency of data collection compared to the KRAIC-D.
- To integrate the data collection system into GDA (Generic Data Acquisition software), the Diamond data collection software to improve ease-of-use of the system for non-expert Diamond users.
- To improve the efficiency of the data processing methodology, also improving the ease-of-use for non-experts.

Section 5.2 of this chapter focuses on the commissioning of the KRAIC-T crystalliser through temperature profile studies, a case study on succinic acid (SCA) crystallisation, and development heat sink column insert for improved sub-ambient temperature control.

Following this, Section 5.3 discusses the development of the crystalliser as a sample environment on Beamline I11, through adaptation and development of the slug triggering mechanism for data acquisition to enhance data quality, and data collection efficiency, and its integration into the GDA software.

Commissioning of the sample environment is discussed further in Section 5.4 with a KRAIC-T beamtime of I11 for temperature cycling flow slurrying of *ortho*-aminobenzoic acid (*o*ABA) to evaluate improvements to the system. The efficacy of the slug triggering mechanism is assessed, with the data used to develop the processing methodology for PXRD data, discussed further in Chapter 3.

5.2 – Commissioning of the KRAIC-T crystalliser system

5.2.1 – Heated temperature profile studies

5.2.1.1 – Introduction

To investigate the temperature operating range and functional limits of the KRAIC-T, temperature mapping studies were conducted with a range of column temperature settings and liquid flow rates to assess heat transfer to solution. Understanding the operational limits of the KRAIC-T are of key importance for future experimental planning to be able to target labile temperatures for the targeted crystallisation of polymorphs, or control of crystallite size through temperature control in the metastable zone. Furthermore, for PXRD studies, targeting of polymorphic transitions during crystallisation requires an understanding of temperature settings and resultant operational temperatures of the KRAIC-T

5.2.1.2 – Methodology

The KRAIC-T system was temperature mapped for each tubing rung in a heating zone and X-ray window with a FLIR E5 thermal imaging camera. The KRAIC-T set up for temperature profile studies is shown below in Figure 5.05. The crystalliser system uses a hotplate with round bottom flask adapter for heating the feedstock, with temperature controlled transfer tubing between the feedstock container to HZ1. The jacketed tubing uses a temperature controlled water circulator system to maintain solution temperature pre-crystalliser columns.

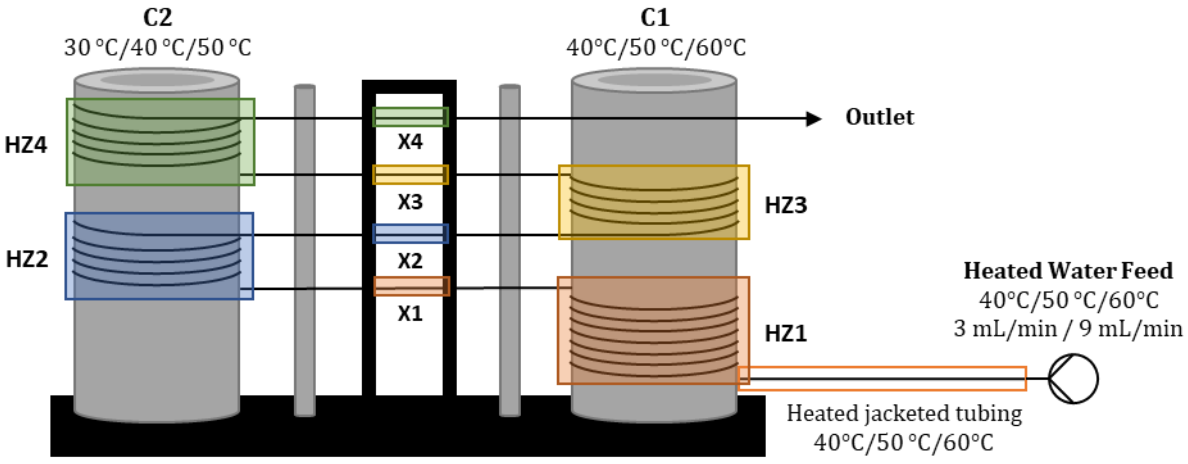

Figure 5.05: Schematic diagram of the KRAIC-T set up for temperature profile studies with variable temperature settings, flow rates, temperature HZs and Xs annotated.

Total flow rates typical in KRAIC experiments are between 3 – 9 mL/min: to test the effect on resultant temperature, feed solution of unsegmented heated water flow at 3 and 9 mL/min was used for the temperature studies. Settings for C2 temperatures were 30, 40, and 50 °C, with C1 temperatures of 40, 50, and 60 °C. The hotplates for heated water flow and hot jacketed transfer tubing matched the temperature setting for C1. The upper temperature limit is 60 °C due to safety limitations: above 60 °C extra shielding is required due to the risk of

solution spray which is not ideal during *in situ* PXRD studies due to any changes to Kapton window unions requiring easy, hands-on access to the system.

Given the variable flow rates and columns temperatures, twelve different variable temperature and flow rate conditions were studied in total. Temperature mapping was completed with the FLIR E5 for all HZs at the front and back of the column on each tubing rung, for each X-ray window, and for the transfer tubing sections between each HZ and X-ray window.

5.2.1.3 – Results and Discussion

The twelve variable temperature and flow rate conditions were temperature mapped, with one condition repeated on separate days to investigate the effect of room temperature on the temperature profile. The quoted temperatures are readings from visual inspections of the tubing with IR camera, it is assumed the fluid temperature is equivalent to the tubing thermal reading. When discussing these conditions, an example condition name of "60:30_3_18.7RT" indicates a C1 temperature, water hotplate, and jacketed transfer tubing circulator settings of 60 °C, with a C2 temperature of 30 °C, a heated water flow rate of 3 mL/min, and a room temperature (RT) of 18.7 °C. Example images of the visual inspection of tubing rungs is shown below in Figure 5.06.

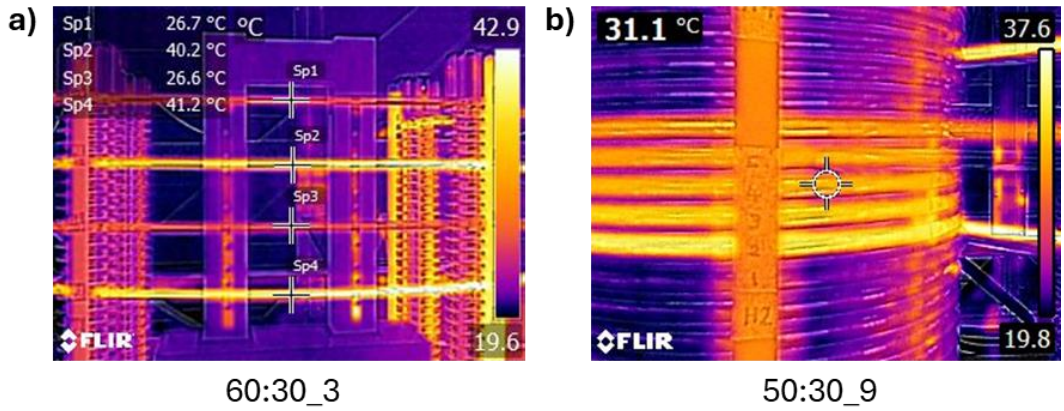

Figure 5.06: FLIR IR images for a) X-ray windows for temperature mapping run 60:30_3 with annotated temperature readings, and b) heating zone 2 for temperature mapping run 50:30_9 with tubing rungs showing gradual cooling on C2.

The temperature profiles for the 40:30 conditions are shown in Figure 5.07. Key features of the 40:30 °C conditions are the apparent fluctuations in temperature within the heating zones: this is due to the auto calibration of the FLIR adjusting the temperature readout between the front and back of the column measurements. This auto calibration cannot be turned off, leaving a temperature variation on average of ±1.5 °C, however this reading is also affected by emittance of the material the IR camera is focussed on; the back of the columns was shadowed, generally giving lower readings.

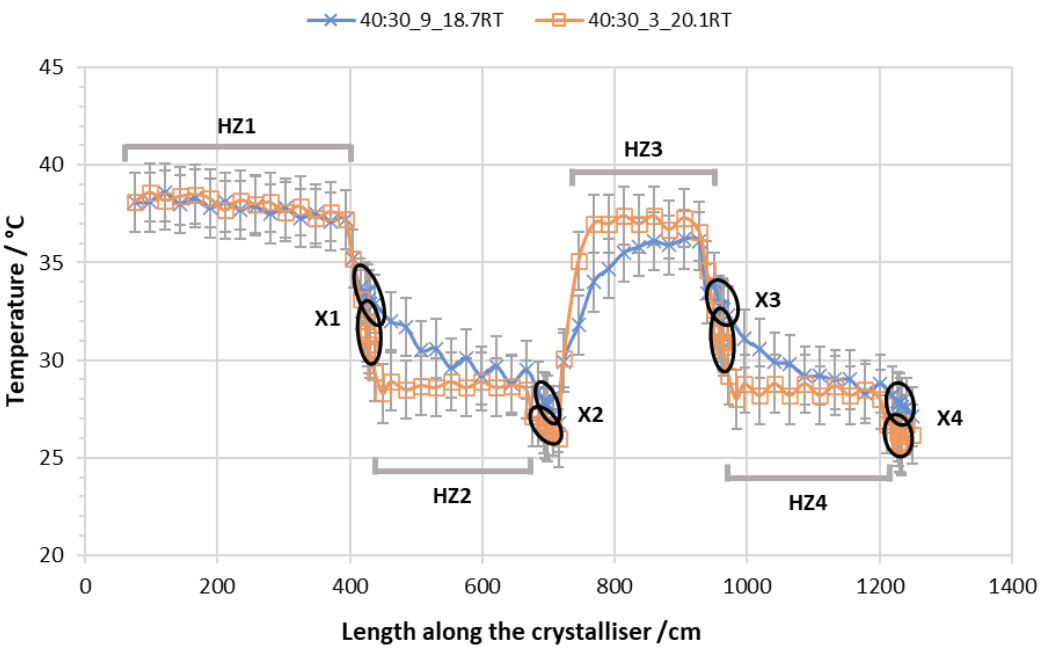

Figure 5.07: Temperature profile for 40:30 temperature settings with 3 mL/min and 9 mL/min flow rate. HZs and Xs are annotated on the graph. ±1.5 °C error bars are shown on the temperature profiles.

The effect of flow rate on temperature profile is considerable: with faster flow rates causing a slower heat transfer and less overall air cooling. The faster flow rate (9 mL/min) had a reduced temperature loss in the HZ1 to HZ2 and HZ3 to HZ4 sections. Furthermore, the 9 mL/min solution does not reach as high a temperature on HZ3 due to the slower heat transfer from increases flow rate, and the 1.4 °C lower room temperature during data collection. The HZ exit temperatures and X temperature readings for all conditions are summarised in Table 5.01 below.

*Table 5.01: Temperature readings for the final measurements in a heating zone for the various temperature and flow rate conditions. Heating zones (HZs) and X-ray windows (Xs) locations detailed in Figure 5.05. *Repeated 50:40_9 conditions differing room temperatures.*

	Temperatures readings /°C							
Temperature mapping conditions/ C1:C2_flowrate_RT	**Final HZ1**	**Final HZ2**	**Final HZ3**	**Final HZ4**	**X1**	**X2**	**X3**	**X4**
40:30_3_20.1RT	37.2	29.5	36.6	28	31.2	26.4	31	25.8
40:30_9_18.7RT	37.2	28.5	36.1	28.8	33.3	27.8	32.8	27.6
50:30_3_18.3RT	45.6	28.7	43.8	28.3	35.5	26.3	35.9	25.8
50:30_9_19.4RT	44.6	30.2	43.1	30.2	40.6	28.8	39.1	28.4
50:40_3_18.1RT	44.7	34.3	43.3	32.7	34.6	29	33.8	27.6
50:40_9_18.6RT*	44.5	34.9	43.6	33.6	39.4	32.3	38.5	31.1
50:40_9_20.5RT*	45.6	37.9	44.1	37.4	40.4	34.7	39.9	34.7
60:30_3_18.7RT	53.2	28.6	51.5	28.3	40.9	26.7	40.2	26.3
60:30_9_19.2RT	52.5	30.7	50	30.4	45.2	28.8	43.6	28.9
60:40_3_19.4RT	53.8	37.5	52.1	35.9	40.9	31.8	40.4	31.7
60:40_9_19.4RT	53.5	38.4	51.4	38.1	46.9	35.4	45.3	35
60:50_3_20.1RT	53.3	45.6	52.2	44.5	41.2	38	40.4	37.3
60:50_9_20.7RT	53.9	46	52.1	44.7	46	41	46.2	40.4

Temperature profiles for all conditions not shown in this chapter (50:30, 50:40_3, 60:30, 60:40, and 60:50) are in Appendix A5.1. In general, the temperature settings of the columns did not fully equate to the temperature of the solution. The average temperature deficit is 10% of the set value for the C1 heating zones. Due to room temperature cooling for the transfer from C1 heating zones to the X-ray windows X1 and X3, there is significant temperature loss from the C1 temperature with a range of 9 – 15% loss of temperature from the C1 heating zone final temperatures for 9 mL/min flow. For 3 mL/min flow rates the temperature loss from the final C1 column temperature was a range of 15 – 24 %. There was no general trend in resultant C2 heating zones temperatures as they were affected by both the C1 temperature and flow rate. The heat loss during transfer from C2 to the X-ray windows X2 and X4 resulted in a 2 – 17% loss of temperature from the final C2 heating zone temperatures.

Given the effect of room temperature on temperature profiles, and the 2.6 °C variation in room temperature in the non-temperature controlled laboratory, a repeat run of 50:40_9 conditions were trialled on different days with an approximate ~ 2 °C room temperature difference to directly compare the effect of variable room temperature on the thermal profile of the crystalliser, shown in Figure 5.08. The heat loss present in the system and the resulting influence of room temperature will impact temperature-controlled crystallisation processes and may limit the reproducibility of those crystallisations based on room temperature.

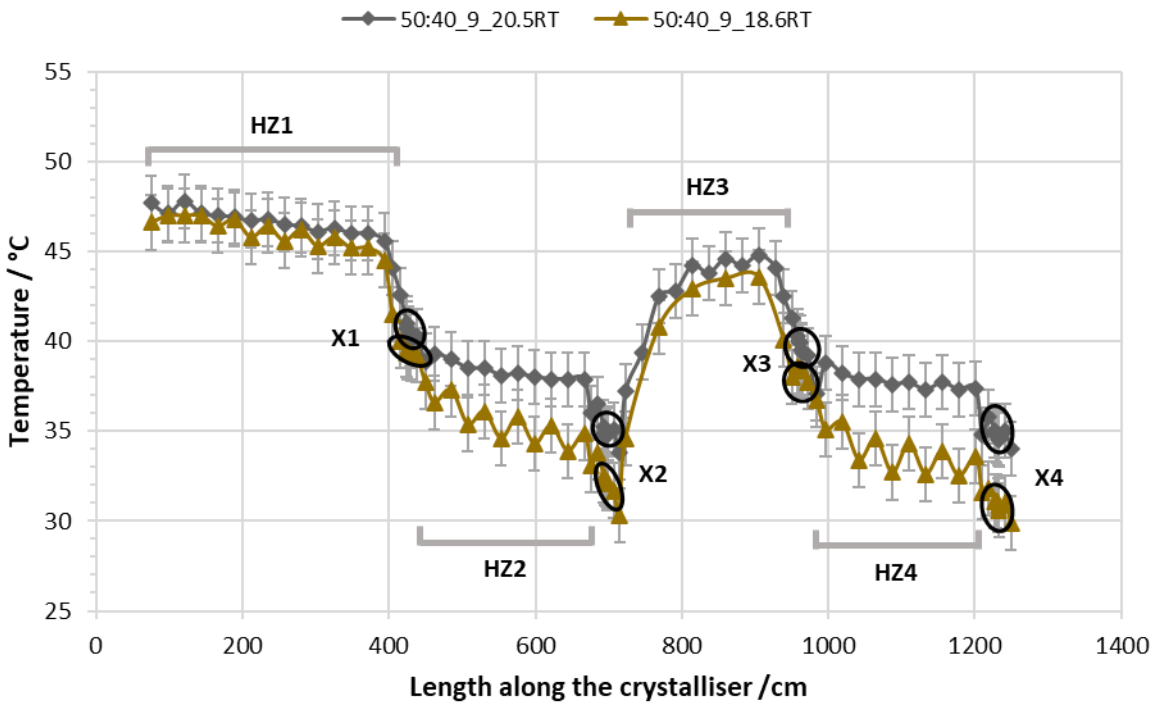

Figure 5.08: Temperature profile for 50:40_9 conditions for temperature cycling water flow between 50 °C and 40 °C at 9 mL/min for two room temperatures, 20.5 °C and 18.6 °C. HZs and Xs are annotated on the graph. ±1.5 °C error bars are shown on the temperature profiles.

The heating curves for the two room temperatures show similar results for the column temperatures in HZ1 and HZ3. The flattening of the temperature profiles at the HZ2 and HZ4 temperature zones for both runs indicate the water flow continued cooling on the C2 40 °C column until reaching equilibrium: this shows the room temperature does effect the temperature of the flow on the columns also. The large surface area of tubing exposed to the air room temperature, rather than contact with the KRAIC-T columns, does influence the overall temperature on the columns. The effect of room temperature is also considerable for the cooling of solution from the transfer of columns to X-ray windows. The difference in X1 and X3 temperatures 1.2 °C and 0.6 °C respectively are within the range of error, however the difference in X2 and X4 temperatures of 3.5 °C and 2.7 °C are outside ±1.5 °C. This effect on the temperature profile would affect a crystallisation process, with increased crystallisation or crystal growth with lower C2 temperatures found for the 50:40_9_15.36RT example.

Given the operational limit of 60 °C for safety reasons, the temperature settings could be increased to temperature setting limit of 65 °C for flow rates above 3 mL/min as this would equate to a maximum temperature reading of ~58 °C, under the overall 60 °C limit.

As a result of the influence of room temperature on the temperature profile, insulated tubing sections were trialled during the *o*ABA KRAIC-T commissioning beamtime, discussed further below in Section 5.4. However, these insulation

blocks prevented quick access to Kapton X-ray window changes in the event of a blockage, therefore were unsuitable for use during beamtimes.

The laboratory in Nottingham in which these experiments took place are not temperature controlled, causing the room temperature variation and effect on temperature profiles. This limits the reproducibility of the KRAIC-T system for the control of temperature-dependent crystallisation processes. The KRAIC-D is a non-temperature controlled crystalliser system entirely reliant on the cooling of solution to room temperature for cooling crystallisation processes; this did not allow for the direct transfer of crystallisation processes from the university laboratories to I11 EH2. As a result, significant periods of beamtime were used optimising crystallisations for the conditions in the I11 experimental hutch. The KRAIC-T temperature control partially mitigates this effect with additional temperature control on the columns, however, does not eliminate this issue entirely. Thorough pre-experimental crystallisation trials with the KRAIC-T with a range of temperature cycles to understand the crystallisation behaviour of the material could further mitigate this issue. Whilst some time to optimise the process would still be required, in terms of modifying column temperature settings to target crystallisation temperatures, this should be reduced in time compared to the KRAIC-D system.

5.2.2 – Temperature cycling mediated segmented flow crystallisation of succinic acid

5.2.2.1 – Introduction

In order to fully commission the KRAIC-T crystalliser, crystallisation trials with aqueous succinic acid were used to assess crystalliser function. Succinic acid (SCA) is challenging material for flow crystallisation given its high propensity to block due to a fast crystal growth rate and large resultant crystals. SCA has two polymorphic forms, the stable β-SCA and metastable α-SCA. The molecular structure of SCA and the crystal structures of the polymorphs are shown below in Figure 5.09, with the crystallographic information summarised in Table 5.02.

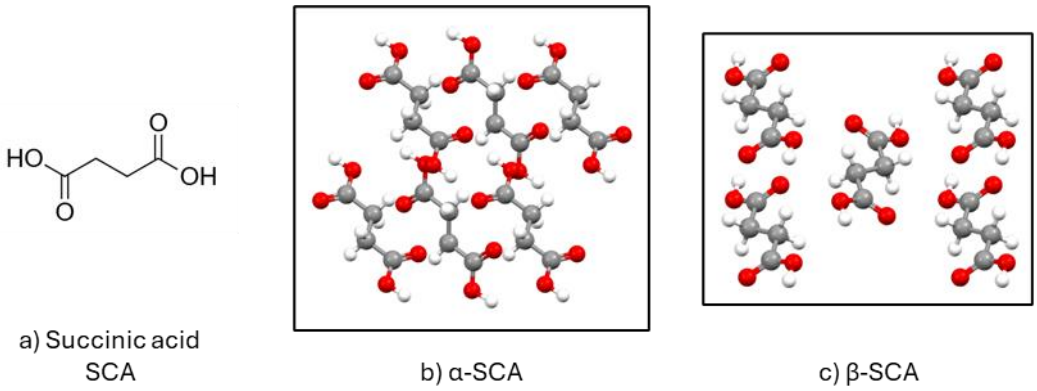

Figure 5.09: a) molecular structure of succinic acid with crystal structures of b) α-SCA, refcode SUCACB07, viewed down the a-axis, and c) β-SCA, refcode SUCACB02, viewed down the a-axis. Crystal structure information taken from the Cambridge Structural Database.[3,4]

Table 5.02: Summary of crystallographic information for SCA polymorphs, taken from the Cambridge structural database.[3,4]

SCA polymorph	α-SCA	β-SCA
Refcode	SUCACB07	SUCACB02
Space Group	P $\bar{1}$	P 2_1/c
Lattice Type	Triclinic	Monoclinic
a /Å	6.867	5.519
b /Å	7.198	8.862
c /Å	5.727	5.101
α /°	109.1	90
β /°	97.18	91.59
γ /°	101.84	90
Cell Volume /Å^3	256.092	249.391

SCA has shown previous interesting polymorphic effects during cooling crystallisation in KRAIC systems: typically, during solution-based crystallisation, pure β-SCA is produced; analysis with *in situ* Raman spectroscopy in the KRAIC-R, SCA crystallisation showed α-SCA and β-SCA concomitant nucleation with transformation to predominant β-SCA.[5] Previous KRAIC cooling crystallisation of 130 g/L SCA aqueous solution cooled from 40 °C dissolution temperature to room temperature. The estimated cooling curve for crystallisation is shown in Figure 5.10.

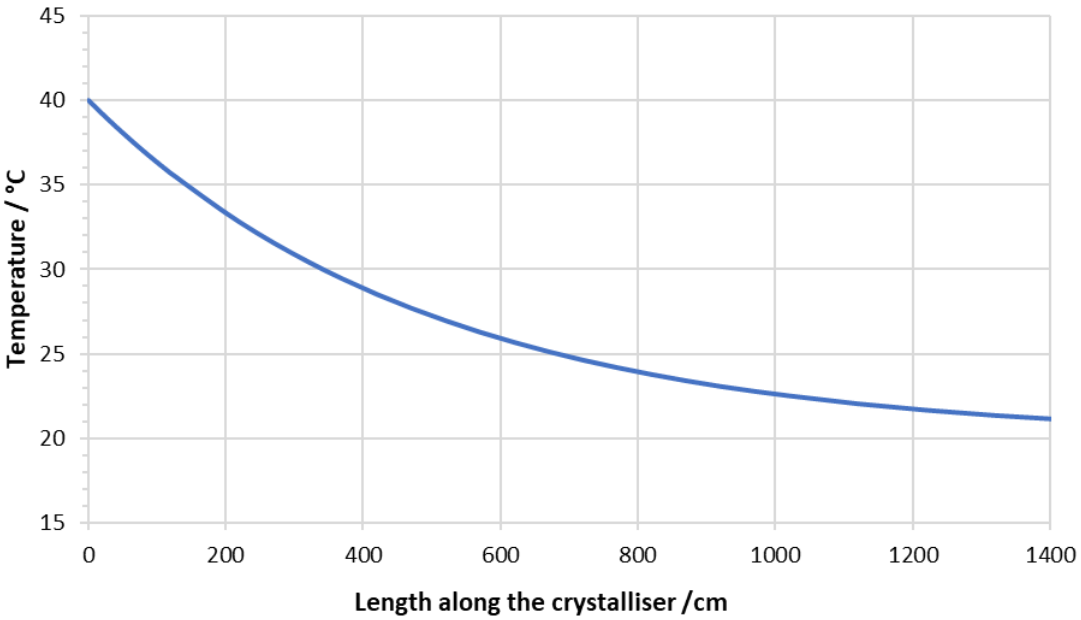

Figure 5.10: Estimated cooling curve for the crystallisation of aqueous 130 g/L succinic acid from 40 °C to room temperature.

This crystallisation can be maintained for several residence times; however, SCA tends to block due to the fast crystal growth rate. To further establish the temperature cycling capabilities of the KRAIC-T, crystallisation of SCA was undertaken with ice bath temperature control in Column 2 over a range of C1 temperatures. The aims of the experiment were:

- To investigate the effects of sub-ambient temperature cycling on the challenging SCA crystallisation material to see if it can mitigate blocking.
- To investigate SCA polymorphic crystallisation behaviour in the KRAIC-T to see if β-SCA with trace α-SCA is maintained.
- To test sub-ambient ice bath temperature control in the KRAIC-T with temperature mapping to further determine KRAIC-T temperature operational parameters.

5.2.2.2 – Experimental

A schematic diagram summarising the KRAIC-T set up for aqueous succinic acid crystallisations is shown below in Figure 5.11.

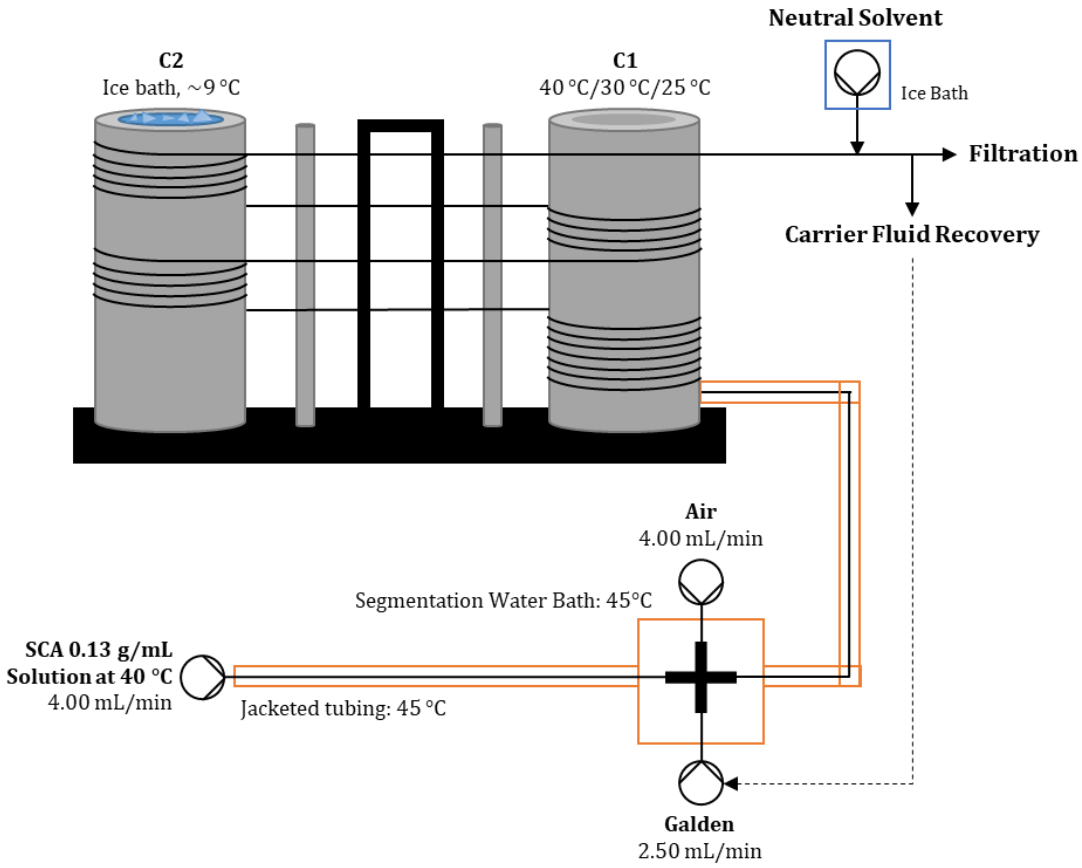

Figure 5.11: Schematic diagram of the KRAIC-T set up for succinic acid crystallisations with flow rates and temperature settings noted for the range of conditions.

The solution of 130 g/L SCA in DI water was prepared at 40 °C, with 45 °C jacketed transfer tubing and segmentation bath temperatures to maintain dissolution prior to the KRAIC-T temperature controlled columns. Vapourtec SF-10 peristaltic pumps were used for air, Galden (carrier fluid), and SCA solution flow with flow rates of 4.00 mL/min, 2.50 mL/min, and 4.00 mL/min respectively. The measured residence time of the SCA crystallisations was 10 min 37 s. An ice bath in C2 was maintained during crystallisations at a temperature of approximately 9 °C measured with a thermocouple. Variable C1 temperatures of 25, 30, and 40 °C were used during the three crystallisation runs. At the

endpiece, carrier fluid was recycled, and neutral solvent flow (cold DI water) was used to aid crystal removal into a Buchner funnel to collect and dry the crystals. The system was primed with heated water segmented flow prior to solution flow.

The sub-ambient operation of the KRAIC-T was temperature mapped with a thermal imaging camera (FLIR E5) during the three temperature cycling runs. The front of the columns and X-ray windows were temperature mapped only.

5.2.2.3 – Results and Discussion

For the total flow rate of 10.5 mL/min, the residence time was measured to be 10 min 37 s for the 30:icebath run. The crystallisation runs ended without issues, running for approximately 4, 4.5, and 5 residence times for 40:icebath, 30:icebath, and 35:icebath, respectively. For all temperature conditions, SCA crystallisation was observed, and output crystals collected. The temperature profiles for the three conditions are shown below in Figure 5.12.

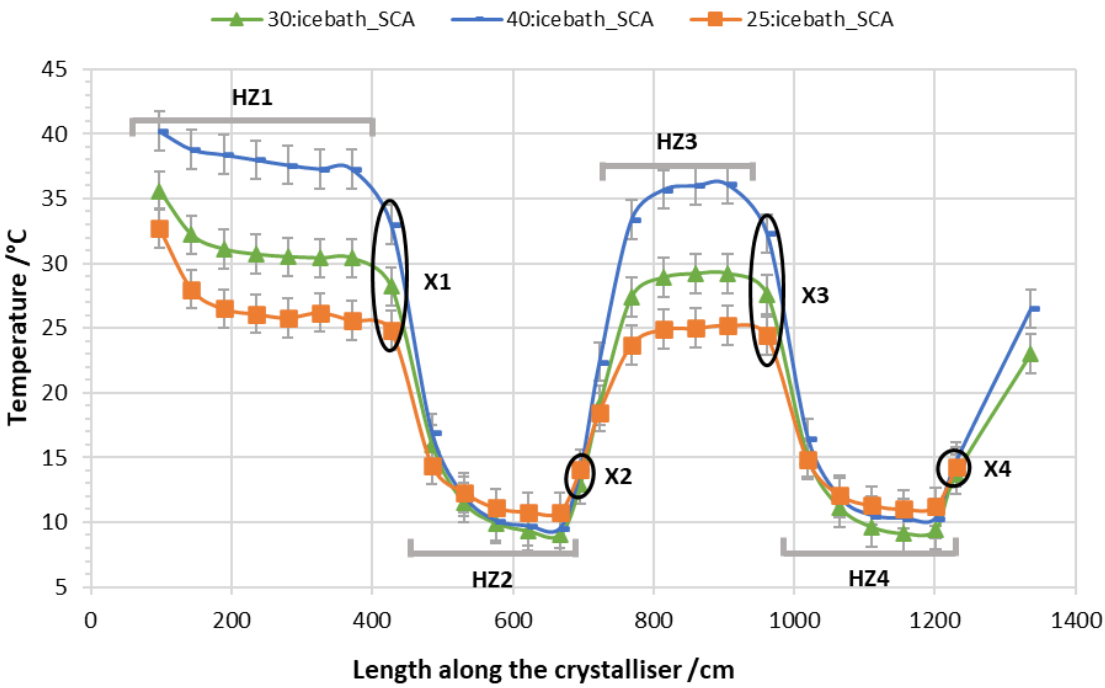

Figure 5.12: Temperature profiles for SCA temperature cycling crystallisation runs with ±1.5 °C error bars for 25:icebath, 30:icebath, and 40:icebath. X-ray window and HZs annotated on the plots.

For the temperature profiles, the 25:icebath and 30:icebath C1 HZ1 have final temperatures of 25.6 °C and 30.41 °C respectively, and final HZ3 temperatures of 25.2 and 29.2 °C respectively with likely errors of ±1.5 °C as previously established. These show good correlation with the C1 temperature settings. The 40:icebath have final C1 temperatures of 37.3 and 36.1 °C for HZ1 and HZ3 respectively. This shows that above a 30 °C temperature setting, the KRAIC-T does not heat to the set temperature as heat loss to the surroundings; a higher temperature setting is required to achieve the desired temperature cycle. X1 temperatures of 24.8, 28.7, and 33.0 °C were achieved for the 25:icebath,

30:icebath, and 40:icebath runs respectively, with 24.4, 27.6, and 32.3 °C for X3. The effect of heat transfer due to room temperature is seen for all temperature profiles due to the non-temperature controlled tubing sections between C1 and X-ray windows, however this is mitigated by the overall 10.5 mL/min flow rate.

With the C2 ice bath, final C2 temperatures of a range of 9.0 – 11.2 °C were achieved during SCA temperature cycling with resultant 12.9 – 14.7 °C X-ray window temperatures due to room temperature heating. The C2 column temperature variation was due to ice bath melting causing fluctuations in the ice bath temperature: the heat transfer from the aluminium columns rapidly warms and melts the ice bath. The effect is rapid, with the ice bath requiring frequent addition of ice to maintain temperature. The ice bath temperature control is not suitable for long, continuous use due to the constant monitoring and ice addition required and resultant variation in temperature profiles. This is not suitable for beamtime operation of the KRAIC-T as the *in situ* XRD requires the system to be contained in the experimental hutch for long periods for data acquisition.

For the SCA crystallisation, the effect of sub-ambient temperature cycling showed improvement to the segmented flow crystallisation process: all three temperature conditions did not block in the KRAIC-T for run times of 4 – 5 residence times. Microscope images of SCA crystals for the three temperature cycling runs are shown below in Figure 5.13b-d, compared against SCA crystals from the original KRAIC paper, Figure 5.13a.[6]

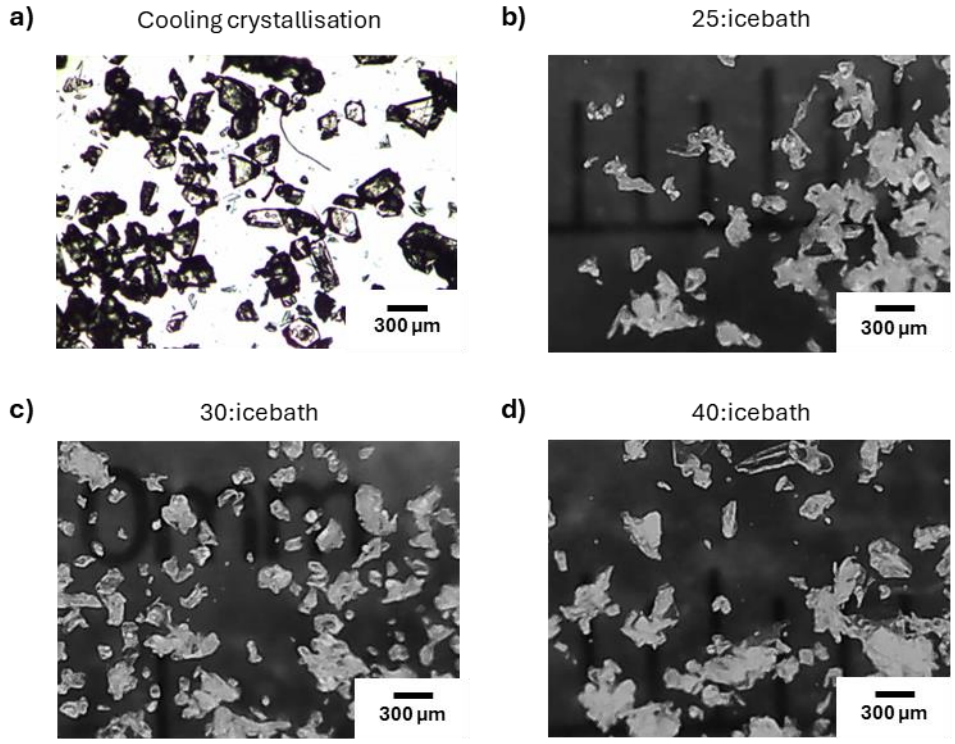

Figure 5.13: Microscope images of SCA crystals from a) produced by cooling crystallisation in the KRAIC, figure adapted from [6], and from temperature cycling in the KRAIC-T for b) 25:icebath, c) 30:icebath, and d) 40:icebath crystallisation runs in the KRAIC-T.

The SCA crystals produced through temperature cycling show a range of resultant crystal sizes with partial agglomeration caused by drying on the filter paper. The 40:icebath run produced larger SCA crystals (~ 300 µm) than other temperature cycles; this can be attributed to the temperature cycling regime preferentially redissolving smaller particles and promoting growth of larger crystals on the colder column. Both cooling and temperature cycling examples show similar rod-like morphology with some agglomeration present. Comparing the size of SCA cooling and SCA temperature cycling crystals, from the small sample size in these microscope images, there does not appear to be a significant change in crystal size (~250 µm). The temperature mitigation of nucleation and crystal growth likely prevented the crystal growth of significantly larger crystals, preventing blockages in the system during temperature cycling.

Residence time yields of SCA crystals were calculated for the 25:icebath and 40:icebath crystallisation runs; 25:icebath had an average residence time yield of 3.2% (4.1 g/L), and 40:icebath showed an average of 2.7% (3.4 g/L). The lower yield for the 40:icebath run can be attributed to the higher level of dissolution of fines on the hotter 40 °C column, reducing the overall mass of crystals produced. The higher yield for the 25:icebath run can also be attributed to the earlier nucleation in the crystallisation process when supersaturated on the lower C1 temperature HZ1. No crystals were collected for 30:icebath conditions. Previous cooling crystallisation of succinic acid in the KRAIC produced a 2% residence time yield for the same concentration of SCA (130 g/L) and reactor length (15 m) with a slower overall flow rate (8.3 mL/min).[6] The sub-ambient temperature control on the KRAIC-T promotes rapid nucleation compared to gradual cooling crystallisation, and blockages are mitigated by dissolution cycles to control the overall crystal growth. This rapid nucleation and growth control also increases the residence time yield compared to a typical cooling experiment.

Offline PXRD of the temperature SCA cycling crystal samples are shown below in Figure 5.14. The PXRD samples were prepared without grinding as this can convert β-SCA to α-SCA, as a result the patterns show poor powder averaging and relative peak heights. The 30:icebath shows predominant β-SCA with partial α-SCA peaks, correlating with previous KRAIC experimental results.[5,6] The 25:icebath and 40:icebath SCA patterns do not show a strong α-SCA characteristic 20.95 ° 2θ peak, however this is likely due to the poor powder averaging from lack of grinding during sample preparation. Temperature cycling of SCA in the KRAIC-T has shown no apparent changes to the polymorphic outcome, only on the resultant crystal size and flow blockage prevention.

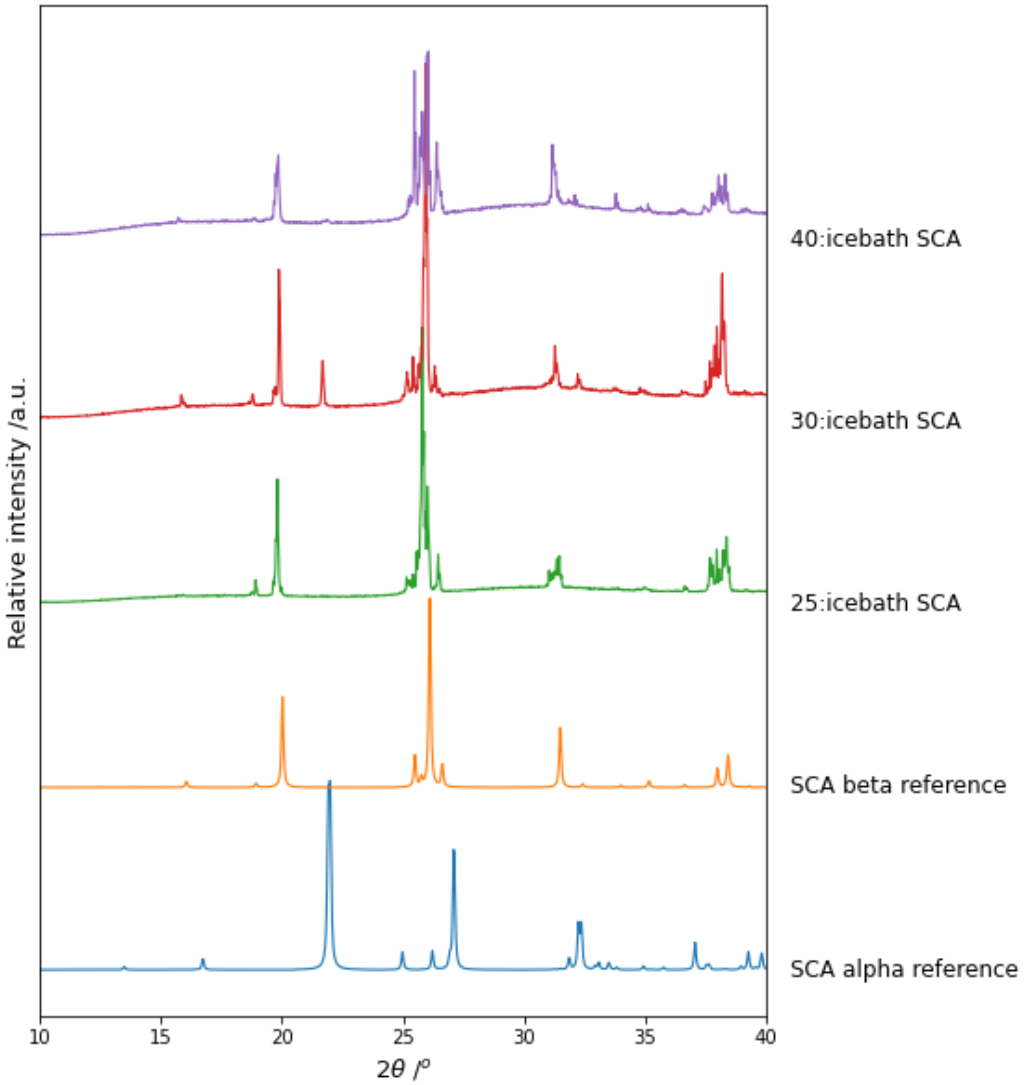

Figure 5.14: PXRD plot of SCA crystals from sub-ambient temperature cycling experiments against Mercury generated α-SCA and β-SCA references, SUCACB07 and SUCACB02 respectively.[3,4] Data collected on lab source X-ray instrument at 1.5406 Å.

5.2.3 – Development of a column heat sink for sub-ambient temperature control

5.2.3.1 – Introduction

Sub-ambient temperature cycling is a key operational area for the KRAIC-T due to the enhanced ability to control nucleation and crystal growth, illustrated by blockage prevention in the sub-ambient temperature cycling crystallisation of the challenging SCA material. However, the use of an ice bath in C2 to achieve sub-ambient temperatures was found to produce variable temperature profiles due to the fast ice melt requiring frequent ice addition into the column. Even with frequent ice additions, variation in temperature profiles of 2.2 °C was found. This causes long duration flow processes, such as beamtimes, to be unfeasible with ice bath temperature control.

This section discusses the design and use of a column heat sink insert with a refrigerated water circulator system for sub-ambient temperature control in the KRAIC-T. This aims to produce sub-ambient temperatures more sustainably in the KRAIC-T, enabling reproducible temperatures without the need for constant management of an ice bath.

5.2.3.2 – Design and Experimental

The heat sink insert is a copper piping coil made with 3 mm ID and 6 mm OD copper piping, made to fit the dimensions of the KRAIC-T column hollow; copper coil is approximately 10.5 mm by 9.0 mm, shown below in Figure 5.15a .

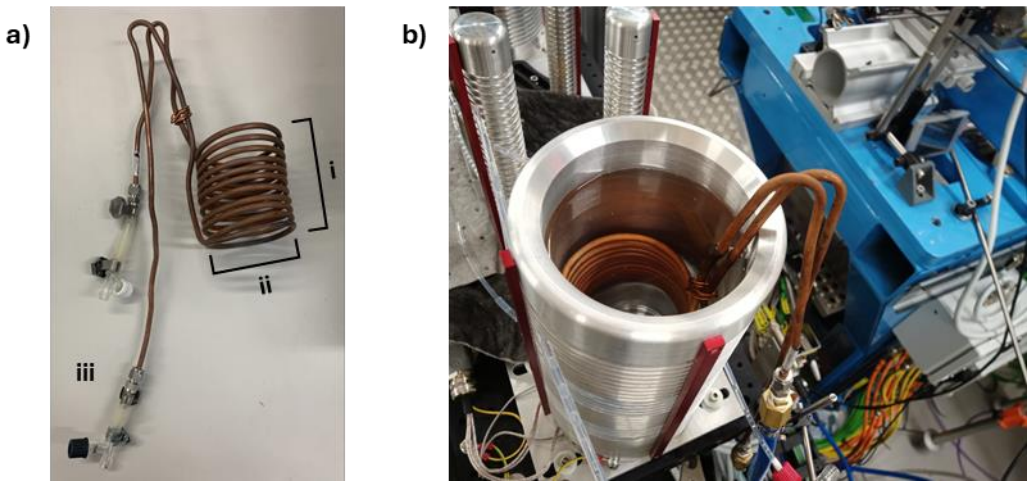

Figure 5.15: a) image of the copper heat sink insert of approximate dimensions height (i) 10.5 cm and width (ii) 9.0 cm. Fluidic adapters for connection to temperature controlled water circulator are shown at (iii). b) image of the heat sink in position in KRAIC-T column 1 with water bath in column.

As shown in Figure 5.15b, the copper heat sink fits into a KRAIC-T column filled with a water bath for heat transfer to the column and KRAIC-T tubing. The copper tubing connects to a refrigerated water circulator limited to 5 °C to prevent ice build-up. The transfer tubes to and from the heat sink are insulated to limit temperature increase from the circulator to the heat sink. The thin copper piping with 11 coils creates a high surface area to enhance heat transfer to and from the column water bath.

The heat sink was trialled for temperature control during segmented flow conditions with a temperature setting of 6 °C for C1 and no temperature setting for C2. The C1 temperature was given time to equilibrate during system priming until the temperature had stabilized. The feedstock entered C1 at 25.5 °C, having cooled from the segmentation bath temperature of 57 °C due to a nucleation promoter jacketed tubing section. The total flow rate was 5.19 mL/min for the segmented flow, with a room temperature of approximately 24 °C. The temperature profile was examined with an E5 FLIR thermal imaging camera.

5.2.3.3 – Results and Discussion

The temperature profile for 6:RT (6 °C C1 and heat sink to C2 at room temperature conditions of ~24 °C) is shown below in Figure 5.16.

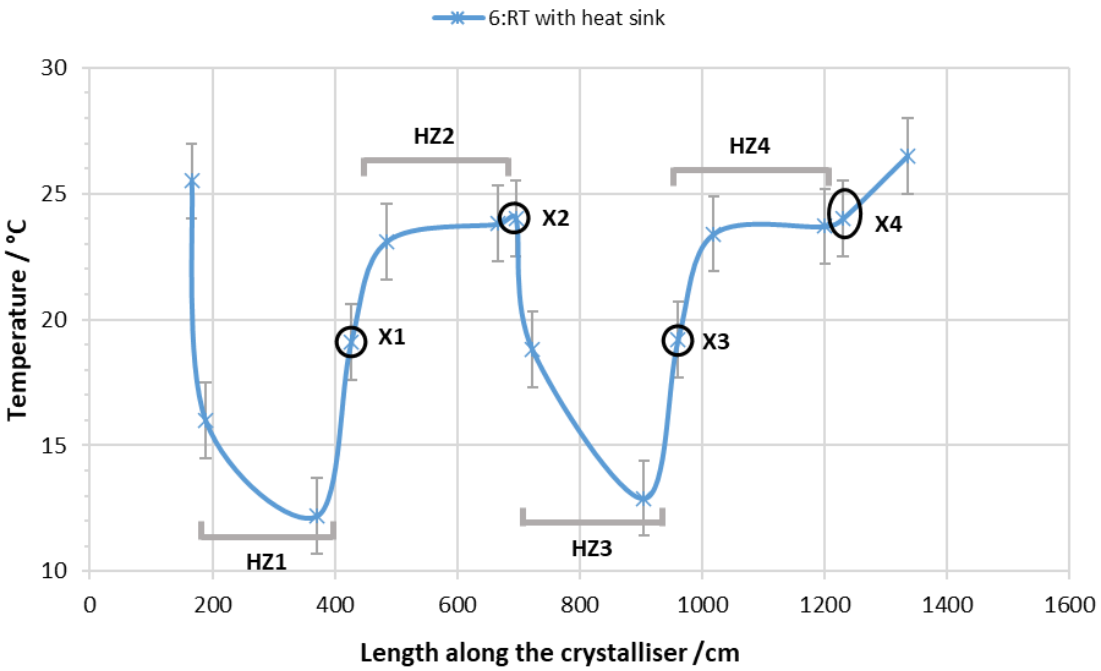

Figure 5.16: Temperature profile of KRAIC-T with heat sink in C1 set to 6 °C and no temperature control for C2 during segmented flow, with ±1.5 °C error bars. Heating zones and X-ray windows are annotated.

With a heat sink temperature setting of 6 °C, C1 temperatures of 12.2 °C were achieved on HZ1 and 12.9 °C on HZ3. This temperature difference is within the approximate error of the FLIR camera of ±1.5 °C. During run conditions over 40 min no temperature fluctuations were observed. Room temperature heating to 23.7 °C on HZ2 and HZ4 for the room temperature reading of approximately 24 °C. Heat transfer from the surroundings for the transfer tubing sections from C1 to X1 and X3 result in X-ray window temperatures of 19.1 °C and 19.2 °C respectively.

Whilst the sub-ambient temperature achieved with the heat sink is higher than achieved with an ice bath (9 °C), the temperature control is improved, with no temperature fluctuations observed over a 40 min runtime. Furthermore, the heat sink required no management as was present with the ice bath requiring constant ice addition to maintain lower temperatures, improving the overall ease-of-use of sub-ambient temperature control in the KRAIC-T.

5.3 – Slug triggering data acquisition adaptation for the KRAIC-T on Beamline I11

5.3.1 – Introduction

The data acquisition method used for the KRAIC-D on Beamline I11 was continual 100 ms acquisitions through Kapton tubing X-ray analysis windows. The segmented flow caused the majority of detector frames to contain background scattering only due to the high proportion of air, carrier fluid, or solution in-beam. This section discusses the adaptation of the slug triggering mechanism as the data acquisition technique for the KRAIC-T on Beamline I11. The slug triggering mechanism is a data acquisition technique developed for SCXRD data acquisition on Beamline I19 with the KRAIC-S, to suspend a single crystal in segmented flow in-beam for a prolonged period of time to gather wedges of SCXRD data for serial crystallography structure solution. See Chapter 6 and 7 for more detail.

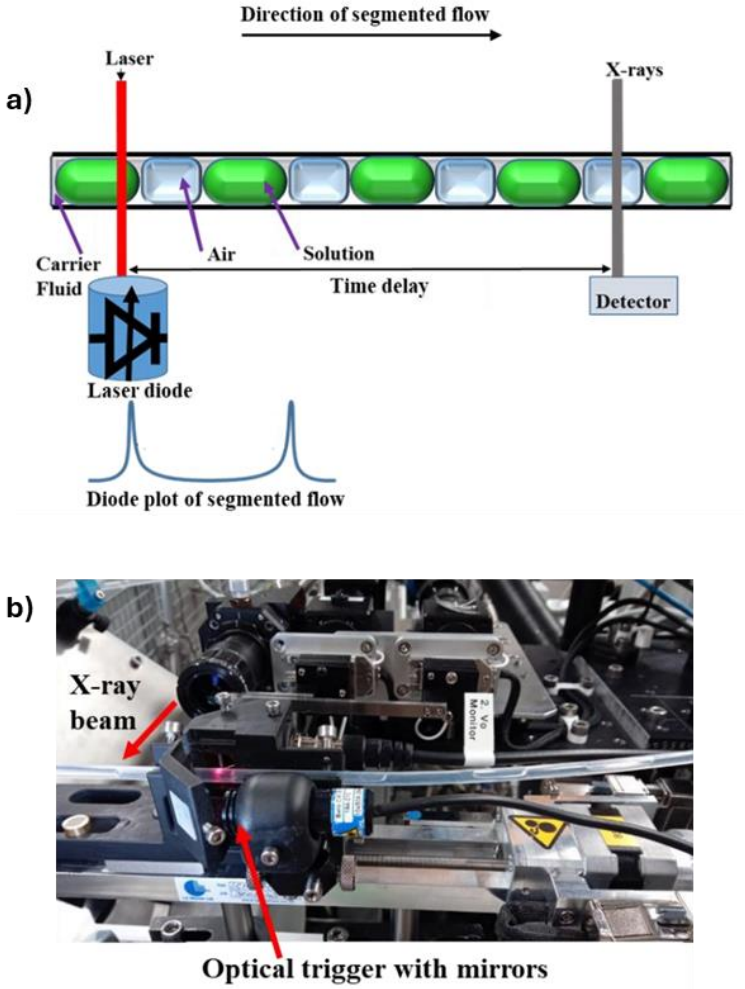

Figure 5.17: a) Schematic diagram describing the slug triggering mechanism with the laser-photodiode sensor and resulting plot due to segmented flow. b) shuttle analysis module developed for the KRAIC-S. Images taken from [7].

The Beamline I19 slug triggering system used a shuttle analysis module (Figure 5.17b): the analysis module had a 60 mm section of the crystalliser FEP tubing

as the X-ray analysis window in-beam, translating the tubing backwards, matching the approximate forwards flow speed, to suspend the crystals in beam. The slug triggering technique uses a laser-photodiode pair as a segmented flow sensor (Figure 5.17a) with fluctuations in the photodiode readout based on the segmented flow: solution peaks and gas bubble troughs. The laser-photodiode segmented flow sensor for the KRAIC-S system used a class 2 red laser and an X-ray sensitive photodiode directed through the tubing with short path distance. Slug triggering was controlled through Python scripts: one script for reading the photodiode intensity and plotting over a set period, and another for controlling the slug triggering data collections. Slug triggering activates when a user-set photodiode value is reached which corresponds to the rear edge of the slug, where the crystals typically reside; this triggers the stage movement backwards, X-ray shutter, and detector capture.

The KRAIC-T layout with multiple Kapton X-ray windows is not suitable for the shuttle analysis slug triggering method: the X-ray analysis windows have two directions of flow, requiring a minimum of two laser-photodiode sensors prior to the X-ray windows. This work proposed to achieve slug triggering through mounting the KRAIC-T on the large motion stage in Beamline I11 EH2, translating the whole crystalliser during triggering, rather than a single tubing section. The laser-photodiode flow rate sensors therefore require positioning at a distance to the X-ray analysis regions to enable access to all X-ray windows. This section discusses the adaptation of the slug triggering mechanism for the KRAIC-T for both flow directions, investigating if the increased laser-to-tubing and tubing-to-photodiode are able to achieve slug triggering in the Beamline I11 experimental hutch 2.

Slug triggering as the data acquisition technique for the KRAIC-T aims to improve the hit-rate of crystals by ensuring crystals are in-beam during data collection through the Kapton tubing X-ray windows. The slug triggering data acquisition method aims to also improve data quality by following multi-crystalline slugs for prolonged periods, whilst the crystals undergo rotations in beam due to turbulence to improve powder averaging. To improve the ease-of-use of the system for future non-expert users on Beamline I11, the slug triggering control script was incorporated into the Generic Data Acquisition (GDA) software.

5.3.2 – Methodology

5.3.2.1 – Initial analysis shuttle integration

To initially test the requirements for slug triggering in Experimental Hutch 2 (EH2) on Beamline I11, the KRAIC-S analysis shuttle was installed onto the large motion stage, shown in Figure 5.18. With the analysis module in-place and using basic segmented flow with water, the Python control scripts were adapted to the beamline, making modifications to the previous Beamline I19 scripts.

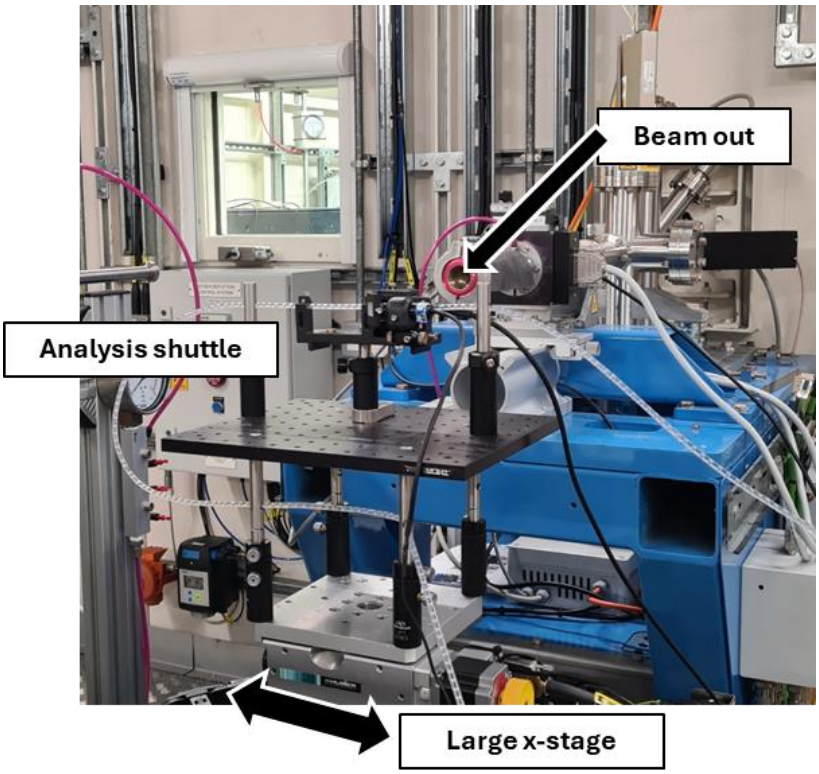

Figure 5.18: Slug triggering shuttle analysis module mounted to larger x-stage on Beamline I11 EH2.

Initial testing with segmented flow in EH2 used the KRAIC-S analysis shuttle module to integrate the control scripts into the beamline for the control of:

- Photodiode readout graph
- Slug triggering activation from photodiode triggering value
- X-ray shutter control
- Detector capture
- Motion stage movement

5.3.2.2 – KRAIC-T integration

Following this initial shuttle analysis testing, the KRAIC-T was installed on the large motion stage in EH2 (Figure 5.19). The large stage features a y-stage (Figure 5.19iii) to translate the crystalliser between the X-ray windows, and the x-stage (Figure 5.19iv) for slug triggering translation.

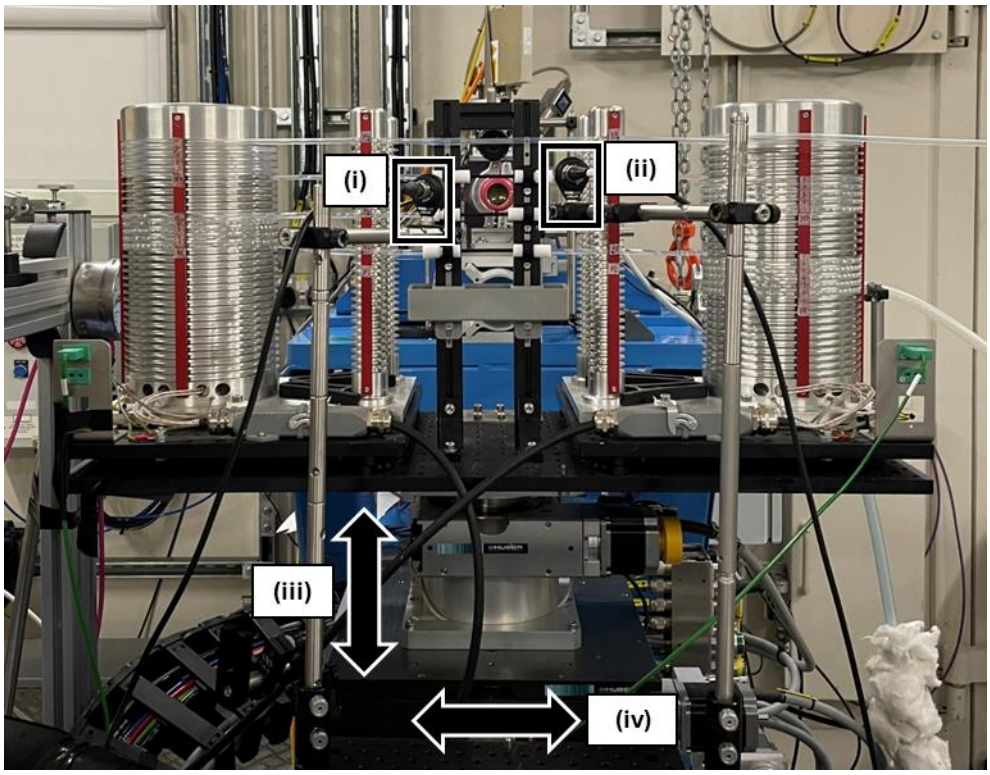

Figure 5.19: Image of the KRAIC-T in Beamline I11 EH2; X3 aligned to X-ray beam. Annotations for (i) slug triggering photodiodes for X2 and X4 flow directions, (ii) and X1 and X3 directions. (iii) shows y-stage movement for X-ray analysis window targeting, with (iv) annotating x-stage for slug triggering stage movement for crystal suspension.

The shuttle analysis module for the KRAIC-S used an X-ray sensitive photodiode; given the increased laser-to-tubing and tubing-to-photodiode distances required for the KRAIC-T slug triggering layout this would likely not be sensitive enough to detect the laser intensity fluctuations. Furthermore, two laser-photodiode sensors are required for the two flow directions, shown above in Figure 5.19 with (i) for X2 and X4 flow direction, and (ii) for X1 and X3 flow direction. For each of the two slug triggering sensors, a Class 2 635 nm red laser (Thorlabs PL202) with a visible light 350 – 1100 nm responsive photodiode (Thorlabs SM1PD1A) was used. Alignment of laser-photodiode pairs are prior to the Kapton X-ray window, as close as possible to the window to minimise delay from slug triggering monitoring to the X-ray capture start point. Careful positioning of the photodiodes aimed to minimise detector shadowing of the diffraction signal.

EH2 at Beamline I11 does not have an on-axis camera to record a video feed during slug triggering acquisitions, as with I19. However, a camera was installed above the X-ray beam focussed on the Kapton window position, aiming to record slug triggering collections and closely observe segmented flow conditions.

The aims of testing slug triggering with the KRAIC-T are to assess if increased laser-to-tubing and tubing-to-photodiode distances are effective for slug triggering and to define any limitations of the methodology. Furthermore, in collaboration with Diamond Software Engineers, the slug triggering scripts were

incorporated into the GDA software for improved ease-of-use for slug triggering control.

5.3.3 – Results and Discussion

5.3.3.1 – Initial analysis shuttle integration

The initial analysis shuttle integration was successful, with the photodiode able to communicate to the beamline computers through an existing femto amplifier. The Python control scripts for plotting photodiode readout and for slug triggering movement were adapted to I11 with the scripts able to:

- Trigger the collection based on the photodiode triggering value specified by user
- Open and close the X-ray beam shutter at the beginning and end of collections
- Specify detector settings and collect detector frames
- Trigger stage movement for specified stage limits for the large x-stage

The Thales Pixium Area Detector (RF4343) used settings of pixel size of 296 x 296 µm with 1441 x 1440 px detector area. The detector operates with continual acquisition during the slug triggering collection, resulting in a single detector frame per collection. This contrasts to the I19 KRAIC-S data collection which collected at 100 ms acquisitions over the prolonged data collection period, giving multiple frames per slug triggering collection. The single frame method was chosen for I11 operation as successive frames showing diffraction spot rotation is not necessary for the PXRD technique. Furthermore, the single frame method removes computer processing time to save the individual frames during the collection, maximising data collection time for the suspended crystals. Total collection time is specified by the stage limits for the X-ray window and stage motor speed: the x-stage speed is limited to a maximum of 15 mm/s. Using Equation 5.01 below, this corresponds to an approximate maximum total flow rate of ~7.1 mL/min.

Equation 5.01: For converting linear stage velocity (v) in mm/s to approximate flow rate in mL/min for tubing of a specified internal diameter (ID) in mm.

$$Flow\ rate \approx \frac{v\pi\left(\frac{ID}{2}\right)^2}{6000}$$

Equation 5.01 does not take into account pressure in the system which affects the flow rate, so the calculated flow rate is an estimated value, not the total flow rate output by the pump settings.

Overall, the initial analysis shuttle integration into EH2 has shown that slug triggering is feasible on I11, adapting the slug triggering control scripts to function on the beamline. The adaptation of the slug triggering methodology to the KRAIC-T is discussed further in Section 5.4.

5.3.3.2 – KRAIC-T integration

With the KRAIC-T installed on the large x-stage, the two new lasers and visible light sensitive photodiodes were set up in EH2 to establish if increased laser-tubing and tubing-photodiode distances are feasible for slug triggering with the KRAIC-T. A second femto amplifier was added to EH2 to read the second photodiode. Stage translation limits of -530 mm to -500 mm were established for the Kapton X-ray window zone, giving 30 mm maximum travel during slug triggering collections. For a total flow rate of 7.1 mL/min, this would equate to a stage movement speed of 15 mm/s for a collection time of 2 s of multi-crystalline slugs.

Air bubble and slug size is often variable, with segments not spanning the full height of the tubing: for this reason, laser alignment at the top half of the tubing was found provide the greatest distinction between air and solution slugs, as illustrated below in Figure 5.20a. Furthermore, the scattering pattern of the laser was observed to show the maximum difference between air and slug when aligned with the top or bottom of the scattered region, shown below in Figure 5.20b.

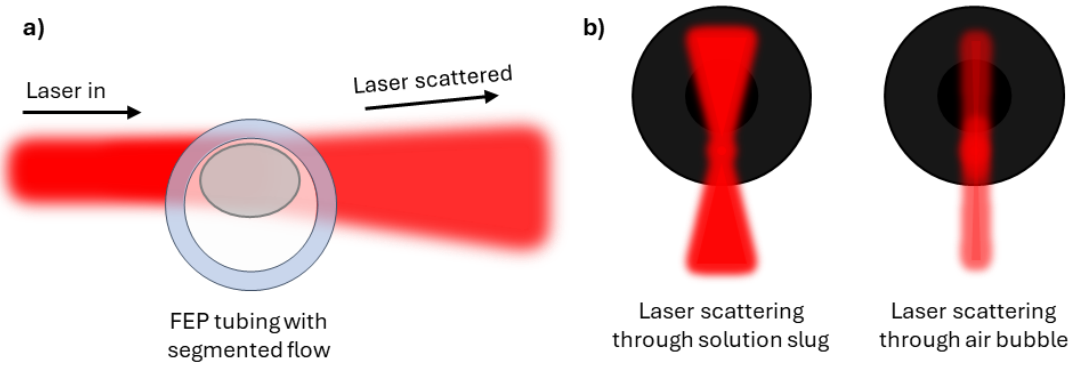

Figure 5.20: Diagrams of a) the laser alignment to tubing focussing on slugs and air bubbles in the upper tubing region, and b) optimised photodiode alignment focusing on the upper laser scattered regions, rather than central point.

The increased tubing-photodiode distance of ~20cm with the new visible light photodiodes were able to produce detailed photodiode readout graphs, using the alignment shown in Figure 5.20b. The increased laser-tubing distance of ~1 m had no impact on the photodiode readout plots compared to Beamline I19 examples, due to the visible light sensitive photodiode and optimised laser and photodiode alignment with the tubing.

The photodiodes support posts were aligned in a manner to avoid detector shadowing and blocking of diffraction signal cones, the results of this is shown with beamtime detector frames discussed in the following Section 5.4. The addition of the above-axis camera assisted with the alignment of the X-ray beam to the approximate X-ray window heights and stage start and end positions. However, the Kapton tubing was too dark to visualise the segmented flow during beamtime, discussed further in Section 5.4.

Two sets of Python scripts were made for slug triggering in I11 EH2 for control of slug triggering in the two required directions. The control scripts were adapted

and made available in GDA for improved ease of use for non-expert users. The GDA slug triggering requires the same user inputs for slug triggering variables and a single command for activating slug triggering collections. The main benefits are that GDA displays the photodiode readout during slug triggering collections, automatically displays the most recent collected detector frame, and displays the auto processed 1D diffraction pattern, shown in Figure 5.21. This enables real-time assessment of the slug triggering efficacy through observation of diffraction in the detected frames.

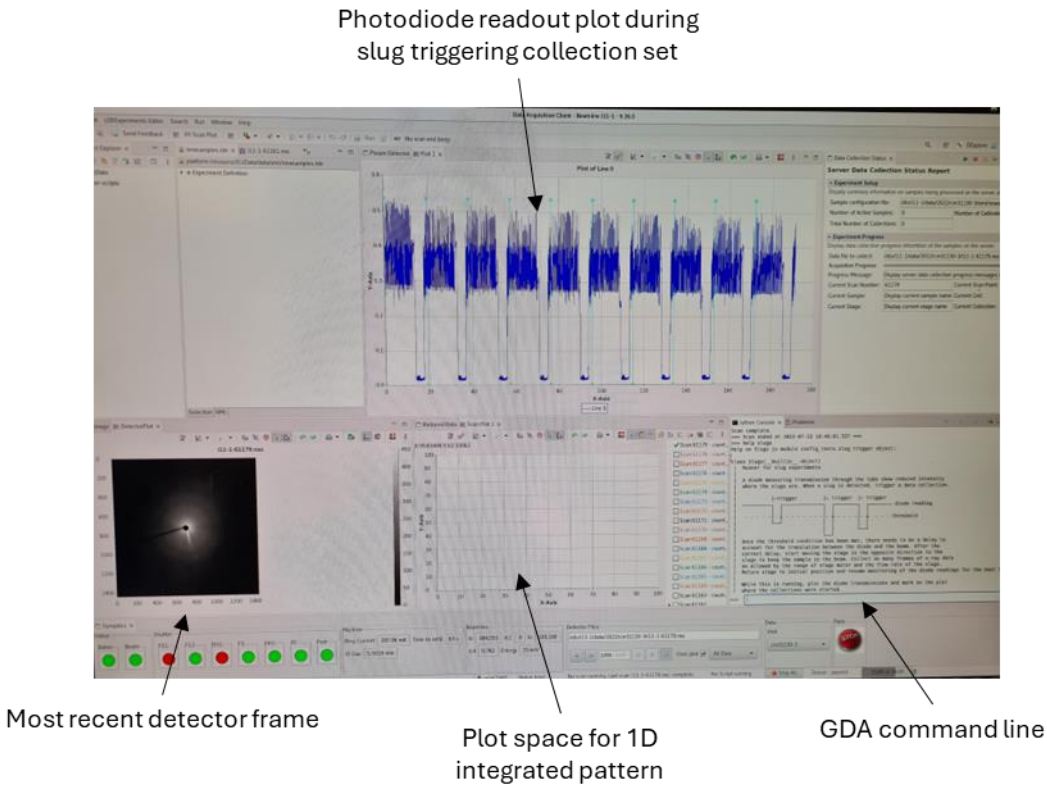

Figure 5.21: Screen image of GDA with slug triggering control, with simultaneous view of detector frame, integrated raw 1D plots, photodiode readout during collections, with GDA command line and slug triggering "help" information.

5.4 – Study of *o*ABA segmented flow crystallisation and slurrying with *in situ* PXRD at Beamline I11

5.4.1 – Introduction

Ortho-aminobenzoic acid (*o*ABA), also known as Anthranilic acid, is a compound used as a starting material for heterocycle synthesis and commonly used for the production of dyes, pigments, and perfumery materials.[8,9] *o*ABA, the molecular structure shown in Figure 5.22a, has three polymorphic crystal forms: Form I, the stable form; Form II, a metastable form with an enantiotropic transition to Form I at 60 °C and monotropically related to Form III; and Form III, a more stable metastable form with an enantiotropic transition to Form I at 50 °C.[10] The relative stabilities of the polymorphic forms and transition temperatures are shown in a proposed phase diagram in Figure 5.23.

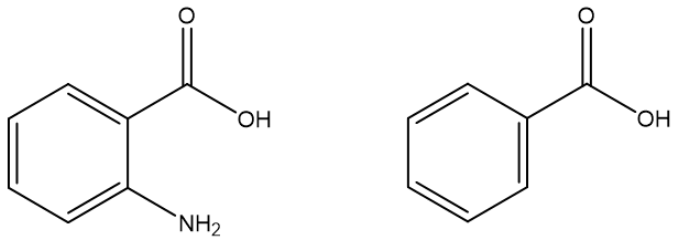

Figure 5.22: Molecular structure of ortho-aminobenzoic acid (oABA) and structurally similar benzoic acid (BA) additive.

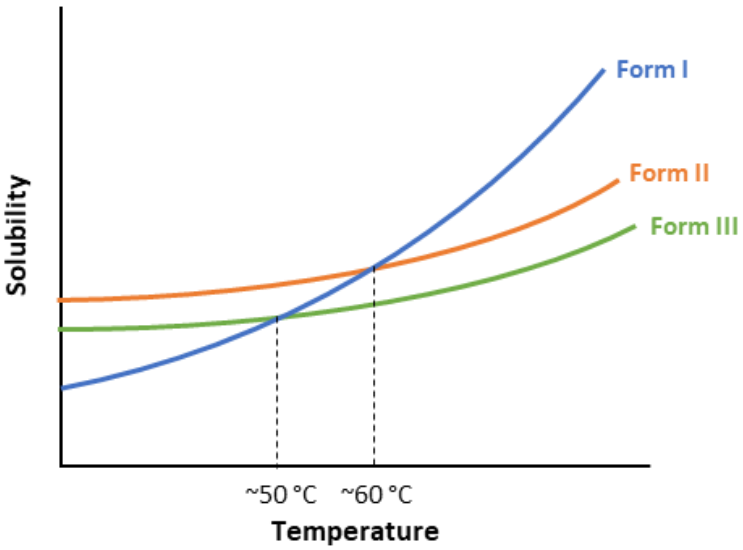

Figure 5.23: Proposed phase diagram for oABA with marked transition points, adapted from [11].

Form I has a prism-like morphology and is the only *o*ABA polymorph to present zwitterions in the crystal structure so is therefore preferentially nucleated from aqueous solutions. Mixtures of IPA and water, which promote non-ionised molecules in solution, support the nucleation of the needle morphology,

metastable Form II.[10,12] The crystal structures for *o*ABA polymorphic forms are shown below in Figure 5.24.

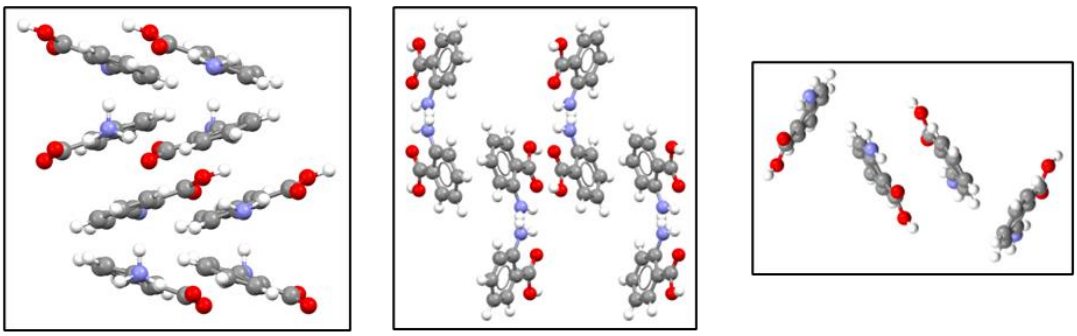

a) *o*ABA Form I b) *o*ABA Form II c) *o*ABA Form III

*Figure 5.24: Crystal structures of o*ABA *taken from Cambridge Structural Database for a) orthorhombic Form I, refcode AMBACO01, viewed down the a-axis showing zwitterionic o*ABA*, b) orthorhombic Form II, refcode AMBACO03, viewed down the c-axis showing dimers of o*ABA*, c) monoclinic Form III, refcode AMBACO06, viewed down the c-axis showing o*ABA *dimers.*[13–16]

Form III is generally not observed during solution-based cooling crystallisation, however, additive controlled solution-based crystallisation with the structurally similar benzoic acid (BA, Figure 5.22b) in high ratios (0.35) has been shown to favour the growth of the plate-like morphology *o*ABA Form III.[10] Temperature cycling crystallisation of *o*ABA has been shown to achieve polymorphic purity of Form I through a controlled dissolution cycle to eliminate metastable Form II crystals.[17]

*o*ABA has been subject to in-depth studies during batch solution-based crystallisation with the polymorphic forms of *o*ABA showing a clear distinction in the powder patterns and unit cell parameters. Therefore, it is an ideal model compound for *in situ* PXRD studies for the commissioning the KRAIC-T as a sample environment on Beamline I11. The unit cell parameters for the *o*ABA polymorphic forms are shown below in Table 5.03, extracted from entries in the Cambridge Structural Database.[16] The Mercury generated PXRD patterns from the *o*ABA database references with refcodes AMBACO01, AMBACO03, and AMBACO06 for Form I, II, and III respectively are compared against the *o*ABA starting material in Figure 5.26.[13–15]

*Table 5.03: Unit cell parameters and crystal data for polymorphs of o*ABA*, obtained from the Cambridge Structural Database.* [13–16]

***o*ABA polymorph**	**Form I**	**Form II**	**Form III**
Refcode	**AMBACO01**	**AMBACO03**	**AMBACO06**
Space Group	$P2_1cn$	Pbca	$P2_1/a$
Lattice Type	Orthorhombic	Orthorhombic	Monoclinic
a /Å	12.868	15.973	12.226
b /Å	10.772	11.605	15.336
c /Å	9.325	7.162	7.56
α /°	90	90	90
β /°	90	90	152.56
γ /°	90	90	90
Cell Volume /Å^3	1292.58	1327.6	653.204

Form I and Form II are feasible in the temperature range achievable by the KRAIC-T (12.2 - 53.9 °C) in water and IPA solvent mixture, with addition of BA additive to potentially nucleate Form III. In the commissioning beamtime, the crystallisation of *o*ABA from an IPA and water solvent mixture, aimed to investigate the crystallisation of Form I and II, and influence of temperature cycling on polymorphic purity, with *in situ* diffraction. Furthermore, BA additive crystallisation aims to study the control of polymorphic crystallisation in segmented flow, similarly studied with *in situ* PXRD. Over-saturated slurrying of *o*ABA in segmented flow with temperature cycling aims to investigate the effects of solvent-mediated phase transitions of *o*ABA.

The crystallisation and slurrying trials aimed to commission the KRAIC-T as a sample environment on Beamline I11 and provided the opportunity to test the slug triggering mechanism for data acquisition, assessing the efficacy though hit rate analysis of multi-crystalline slugs in beam. The PXRD data outputs from the beamtime were also used for the development of the PXRD processing methodology, detailed further in Chapter 3. The polymorphic diffraction patterns provided a reasonable complexity to develop the processing technique and to understand the limitations of data analyses.

5.4.2 – Methodology

The *o*ABA starting material; Anthranilic acid 98+%, was purchased from Thermo Scientific. The starting material was analysed with PXRD capillary data collection at 0.824 Å in Experimental Hutch 1 (EH1) on Beamline I11; comparison against *o*ABA references shown in Figure 5.26. Rietveld refinement of the starting material (Figure 5.25) shows majority Form III at 78.4% polymorphic percentage, with some Form II (21.6%), and no Form I present.

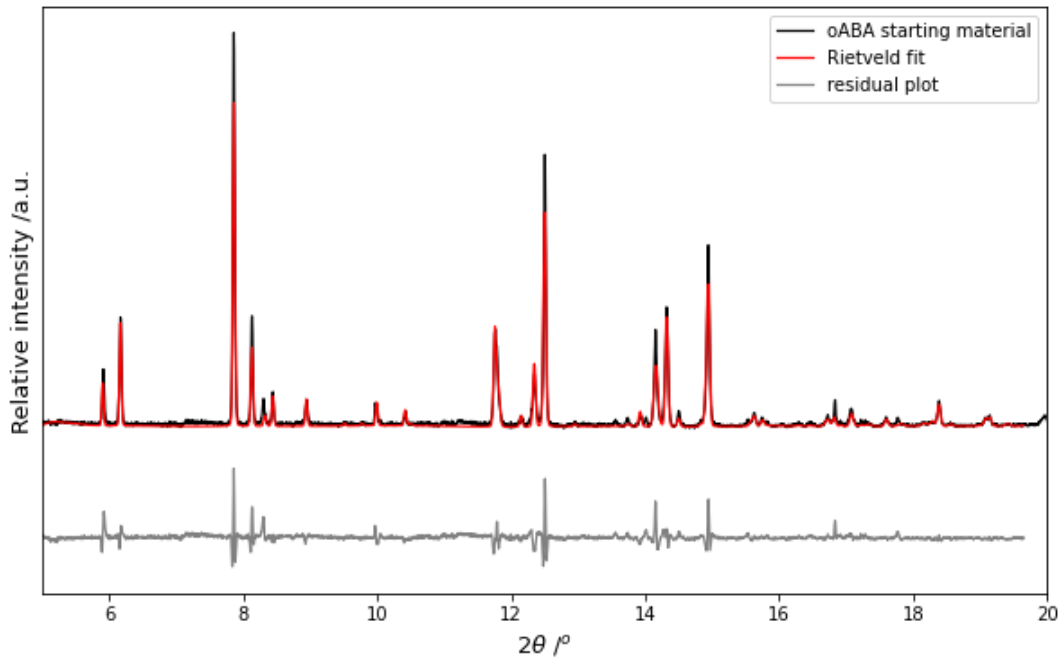

Figure 5.25: Rietveld refinement of oABA starting material fitted against oABA references.

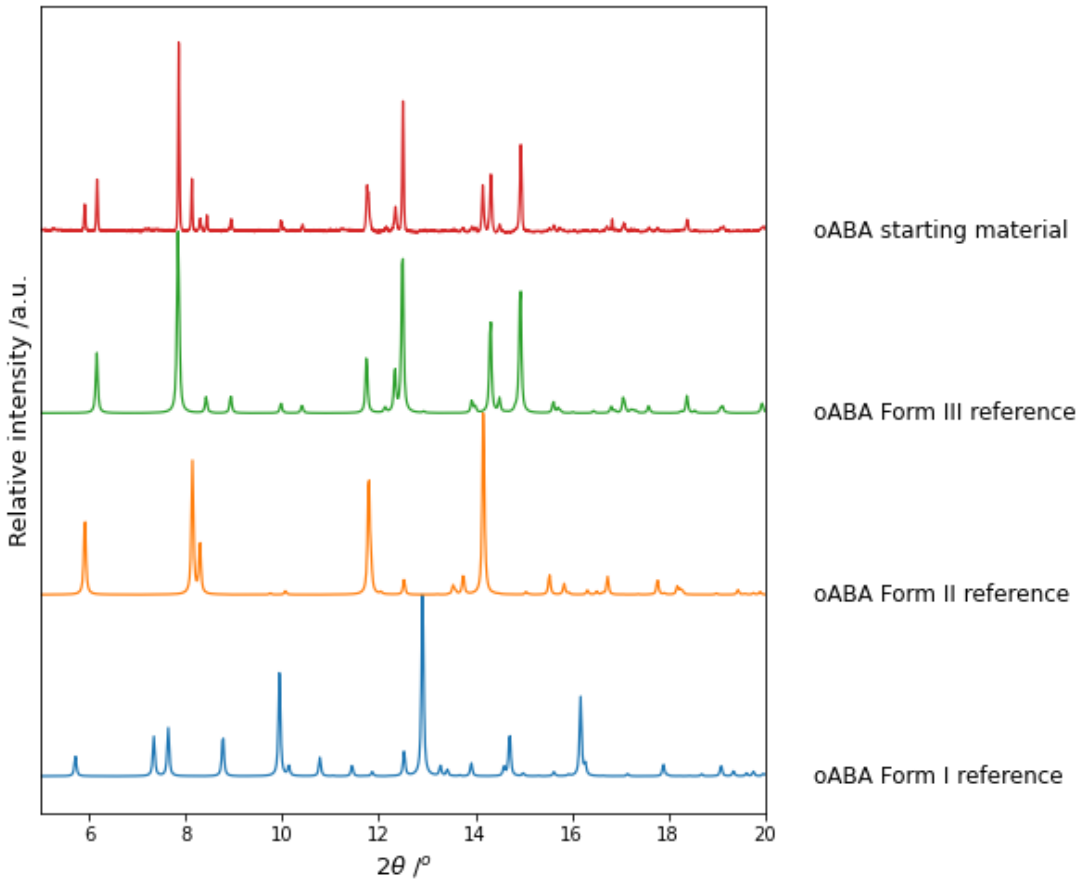

*Figure 5.26: PXRD pattern displayed at 0.824 Å of oABA starting material against Mercury generated reference o*ABA *polymorphic forms AMBACO01, AMBACO03, and AMBACO06 for Forms I-III respectively.*[13–15] *N.B. starting material shows presence of Form II and III of o*ABA.

The crystallisations and slurrying experiments were developed using the solubility data of Form II oABA in 90:10 wt/wt H_2O:IPA data adapted from [12], and converted to v/v and g/L, shown in Figure 5.27. No equivalent Form III solubility could be found in the literature.

Pre-beamtime crystallisation experiments were conducted in the KRAIC-T using 15 m of continuous 1/8" ID FEP tubing without Kapton windows installed. The pre-beamtime experiments used 19 g/L *o*ABA in 90:10 volume/volume (v/v) deionised water:IPA solution (H_2O:IPA), prepared at 60 °C. The KRAIC-T was set up with nucleation promoter jacketed tubing prior to HZ1, and temperature controlled with a refrigerated water circulator set to 10 °C. The temperature settings for the columns were set to 30 °C and 55 °C for C1 and C2 respectively. The solution pump used was an unheated Vapourtec SF-10 with a flow rate of 3.5 mL/min, and flow rates of 1.5 mL/min and 1.2 mL/min for air and Galden carrier fluid respectively.

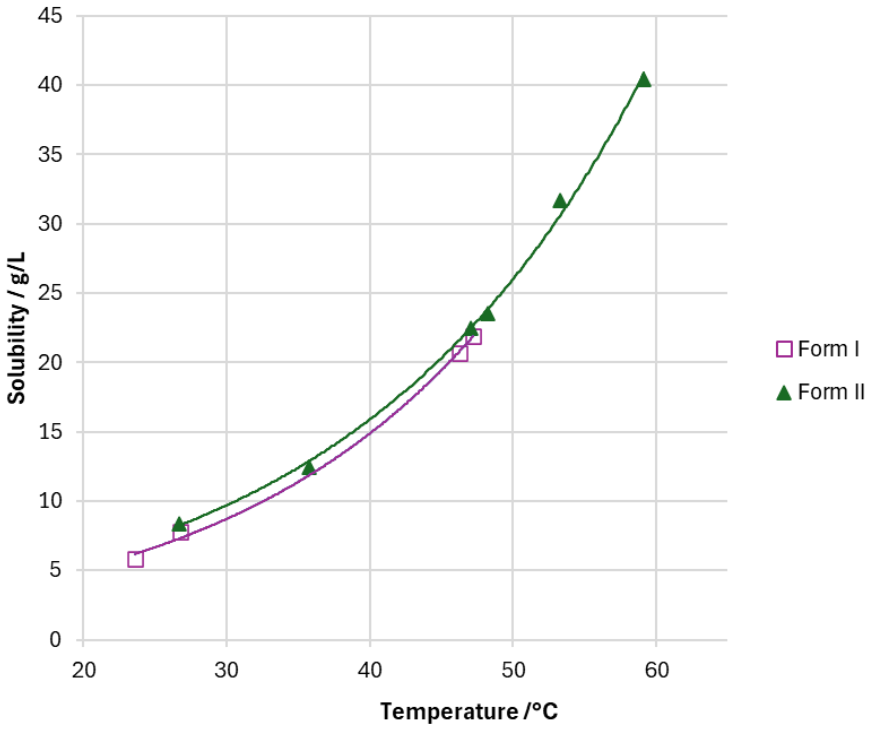

*Figure 5.27: Solubility curve for o*ABA *Form II and Form I in 90:10 v/v H_2O:IPA solvent mixture, adapted from* [12].

The pre-beamtime experiments showed a tendency to form brown, needle-like *o*ABA crystals which often caused blockages due to the crystals growing to the width of the tubing; the needle morphology of the crystals indicated formation of the metastable Form II. The peristaltic solution pump blocked often, likely due to the temperature change from 60 °C solution to room temperature pump head causing nucleation and crystal growth. Due to time limitations, no further experiments to optimise the crystallisation of *o*ABA prior to the beamtime were carried out.

The KRAIC-T was set up on the large motion stage in I11 EH2, with the slug triggering laser-photodiode alignments established in Section 5.3.3.2. The slug triggering acquisitions were controlled through the GDA scripts for data collection, using a Thales Pixium Area Detector (RF4343) settings of pixel size of 298 x 298 µm with 1441 x 1440 px detector area, with an X-ray beam wavelength of 0.8247935 Å (15 keV), calibrated using a 100 µm sample of CeO_2 (NIST certified standard SRM674b).

5.4.2.1 – Kapton X-ray analysis window preparation

The 1/8" ID Kapton tubes require preparation with a hydrophobic coating to maintain fluid wetting and segmentation. Kapton preferentially wets solution rather than carrier fluid, disrupting the tri-segmented flow. Each Kapton tube was prepared using the methodology previously developed for the KRAIC-D: the tube was cut, then underwent Quorum sputter coater 30 s negative glow discharge to prepare the Kapton surface. The tubing was then submerged in

Aquapel, adhering the hydrophobic coating. Kapton tubes with minimal water beading when tested with water indicate a good adherence of the hydrophobic layer. Tubes are then glued with silicone sealant into the PTFE unions and left to dry.

*5.4.2.2 – o*ABA *crystallisations*

The KRAIC-T experimental set up for *o*ABA crystallisations in 90:10 v/v H_2O:IPA is shown below in Figure 5.28. The KRAIC-T features 15 m of 1/8" ID FEP tubing with Kapton unions installed for X1 to X3 as X4 was inaccessible for this beamtime due to y-stage limitations and the tubing configuration of the KRAIC-T. X-ray window positions of X1-X3 were at lengths of 4.3 m, 7.0 m, and 9.6 m along the crystalliser respectively. Insulation blocks between the heating zone tubing sections and X-ray windows were trialled to reduce temperature decrease from regions outside of temperature control. The KRAIC-T set up, represented in Figure 5.28, used a dilution and solution stream meeting at a 1.5 mm thruhole PEEK IDEX "Y" mixer piece to vary the resultant *o*ABA solution concentration. The diluted solution flow segments with the pre-segmented air and carrier fluid at a further 1.5 mm thruhole "Y" mixer.

An experiment identifier of "0.1_18.9_oABA_30:55_15" indicates *o*ABA with no BA additive, the "0.1_18.9" indicating the first crystallisation run used a resultant oABA concentration of 18.9 g/L oABA solution with "30:55_15" showing C1 temperature of 30 °C, C2 at 55 °C, and 15 °C setting for the cold water circulator for the nucleation promoter jacketed tubing. Using four variations of the dilution stream and solution flow rate ratios equalling a total solution flow of 3.5 mL/min (crystallisation runs 0.1 – 0.4), four concentrations of *o*ABA ranging from 18.9 – 22.0 g/L were trialled during beamtime. Runs 0.1 – 0.3 used air and carrier fluid flow rates of 1.5 mL/min and 1.2 mL/min respectively, for a total flow rate of 6.2 mL/min and a recorded residence time of 18 min 35 s. Runs 0.5 – 0.8 were *o*ABA with a 0.4 ratio BA loading. Runs 0.4 – 0.8 used air and carrier fluid flow rates of 1.5 mL/min and 1.4 mL/min respectively, for a total flow rate of 6.4 mL/min, slightly increasing the flow rate to give faster movement through the X-ray windows which were prone to blocking. Full experimental details with experiment identifiers, flow rates, resultant concentrations, and temperature settings are described in Appendix A5.2 of the appendix. The "0.8_18.9_oABA_BA_45:50_13" conditions of *o*ABA with BA additive crystallisations used the HZ1-X1-HZ2 sections of tubing only, disconnecting from the X2 window to create a new outlet point due to large needle build up at the increased blockages in the system. Temperature settings for the flow conditions are described in the Figure 5.28 and in Appendix A5.2.

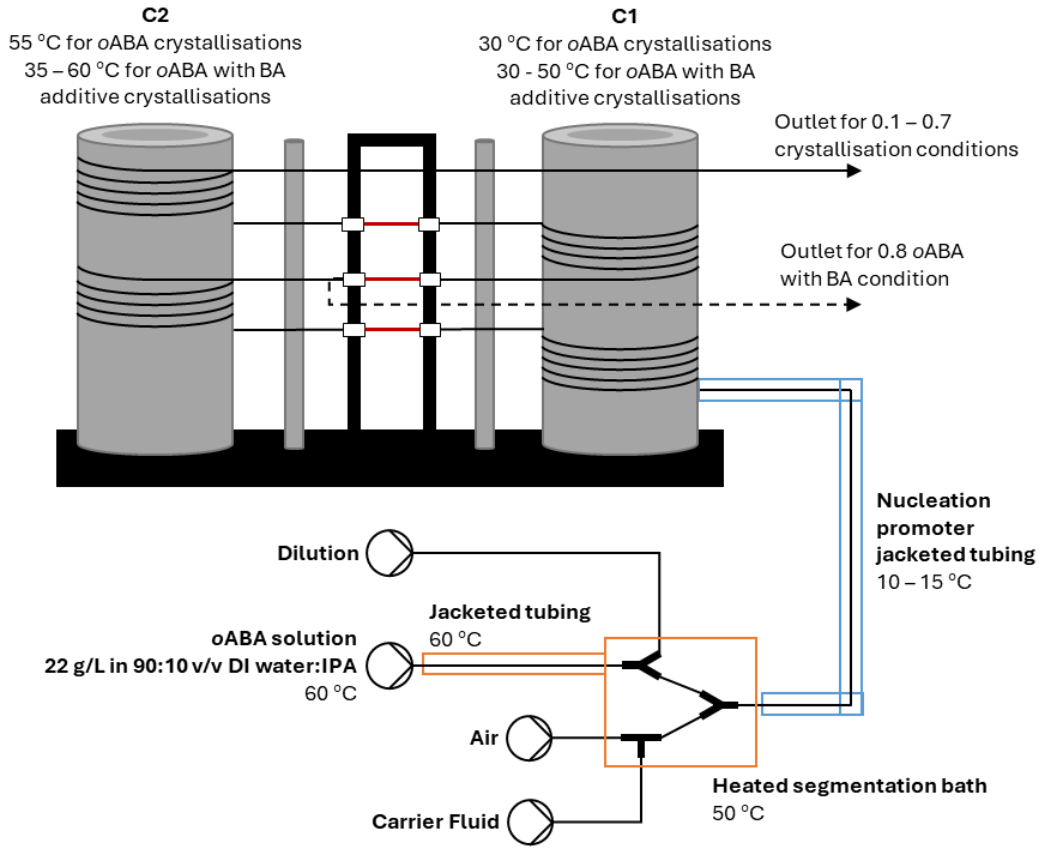

Figure 5.28: Schematic diagram for the experimental set up of the KRAIC-T during the oABA and oABA with BA additive crystallisations during beamtime in I11 EH2. Temperatures settings for run conditions annotated for column temperatures, jacketed tubing water circulator temperatures, and hotplate temperatures. Alternative outlet for the " 0.8_18.9_oABA_BA_45:50_13" oABA with BA additive crystallisation noted.

5.4.2.3 – oABA slurrying conditions

The KRAIC-T set up for the slurrying of *o*ABA in 90:10 v/v H_2O:IPA is shown below in Figure 5.29. The segmentation was modified from the *o*ABA crystallisation to use large bore mixer pieces and using a bypass stream to maintain flow in the KRAIC-T event of a blockage in the slurry pump or transfer tubing. The KRAIC-T had X-ray window positions of X1-X3 at lengths of 4.3 m, 7.0 m, and 9.6 m along the crystalliser respectively. The segmentation set up was modified to use larger bore Y-pieces (3.175 mm) to prevent blockages caused by encrustation of the slurry during segmentation. The segmentation bath temperature was set to 45 °C, above the 40 °C *o*ABA slurry feedstock temperature to ensure heat transfer to the slurry to prevent further crystallisation.

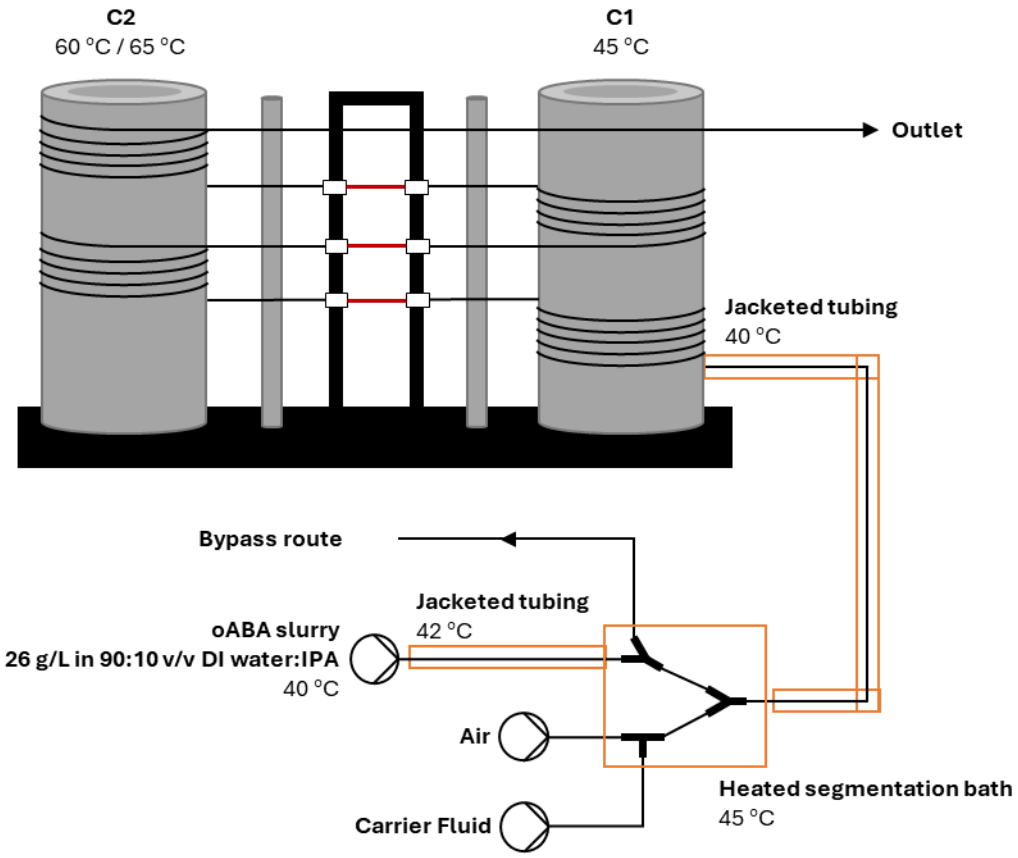

*Figure 5.29: Schematic diagram of the KRAIC-T for o*ABA *slurrying experiments during beamtime on I11. Temperature settings for the slurrying conditions are annotated.*

Slurries of *o*ABA in 90:10 H_2O:IPA were prepared with a loading of 26 g/L at 40 °C, a 10 g/L excess on the 16 g/L saturation at 40 °C, shown with the Form II solubility curve in Figure 5.27. Using Equation 1.01 and the *o*ABA solubility at 40 °C to give a supersaturation ratio of 1.6.

Equation 1.01: For calculation of supersaturation ratio, S, using concentration, c, and current solubility, c, based on conditions present (temperature).*

$$S = \frac{c}{c^*}$$

The first slurry was prepared prior to 1_*o*ABA_45:60_1 slurrying run, and used for the following 2_*o*ABA_45:65_1 run. The second slurry was prepared immediately prior to 3_*o*ABA_45:60_2 slurrying run, then used for the following 4_*o*ABA_45:65_2 run. The suspensions were maintained through rapid mixing, with an SF-10 peristaltic pump at 3.5 mL/min used for slurry flow. Flow rates of 1.5 and 1.4 mL/min were used for air and carrier fluid respectively for a total flow rate of 6.4 mL/min. Due to time constraints, only a residence time was recorded for the 0.1_18.9_*o*ABA_30:55_15 *o*ABA crystallisation conditions: 18 min 35 s residence time was recorded for a total flow rate of 6.2 mL/min. With the 6.4 mL/min total flow rate and the same KRAIC-T layout, the residence time was estimated to be 18 min for the *o*ABA slurrying runs. X-ray windows at flow slurrying times of 5 min 35 s, 8 min 50 s and 12 min 25 s respectively for X1-3.

Temperature settings for the flow conditions are shown above in Figure 5.29: the slightly higher jacketed tubing temperatures and heated segmentation bath temperatures were used to prevent blockages in the slurry flow tubing pre-segmentation. Two temperature cycling conditions were used for *o*ABA slurrying in the KRAIC-T due to time constraints: 45 – 60 and 45 – 65 °C. Two repeats were completed for each temperature cycling condition.

PXRD data were collected using the slug triggering mechanism as discussed in Section 5.3, using the slug triggering control functionality in the GDA software. The slug triggering mechanism used a photodiode threshold level to trigger the stage movement to maintain the multi-crystalline slugs in-beam. The user defined the stage speed and photodiode threshold level. The camera installed above the X-ray beam position was used to set x-stage positions for the slug triggering translation and set the x-stage translation velocity based on the visual suspension of slugs through test stage movements. Temperature mapping was completed for some conditions with a FLIR E5 IR thermal imaging camera, shown in the following sections in Figure 5.37, Figure 5.39, and Table 5.07.

5.4.3 – Results and Discussion

5.4.3.1 – Crystallisation results and discussion

Crystallisation of *o*ABA at 18.9 – 22 g/L concentrations with 30 – 55 °C C1 – C2 temperature settings were unsuccessful in the KRAIC-T during beamtime. A residence time of 18 min 35 s was recorded for the 6.2 mL/min total flow rates. Despite using similar conditions in terms of total flow rate, concentration, and temperature settings as offline *o*ABA crystallisations, the crystallisation runs failed due to persistent blockages in Kapton windows. In the initial crystallisation runs, the insulation blocks were found to be bulky and prevent the change of Kapton windows so were removed and not used for the remainder of beamtime. With the majority of conditions, no crystallisation was observed on the KRAIC-T columns, only blockages in the X-ray windows. Higher oABA concentrations produced a small amount of *o*ABA crystals, inconsistent in the slugs, however, similarly rapidly blocked in the X-ray windows. These failed crystallisation attempts indicate *o*ABA is likely dominated by surface-dependent nucleation during crystallisation; the segmented flow conditions provide a liquid-liquid interface for nucleation which is unfavoured by *o*ABA, inhibiting nucleation. In the offline experiments, the lack of Kapton windows meant that primary nucleation, not dependent on a solid interface, occurred in the segmented flow, enabling crystal growth in the KRAIC-T. However, with the Kapton windows installed, slight perturbations to the tubing surface in the X-ray windows exist in areas of poor hydrophobic coating. Furthermore, the PTFE Kapton union, shown in Figure 5.30, has an area where the segmented flow changes from FEP to PTFE to Kapton tubing: whilst the union has been designed to fit the two tubing types well, any imperfections in the tubing fit may leave a ledge where crystals may get stuck, causing an encrustation that leads to blockages. Any defects in the exposed PTFE section from the machining of the

PTFE to shape may also provide areas for rapid heterogeneous nucleation and crystal growth, blocking the flow.

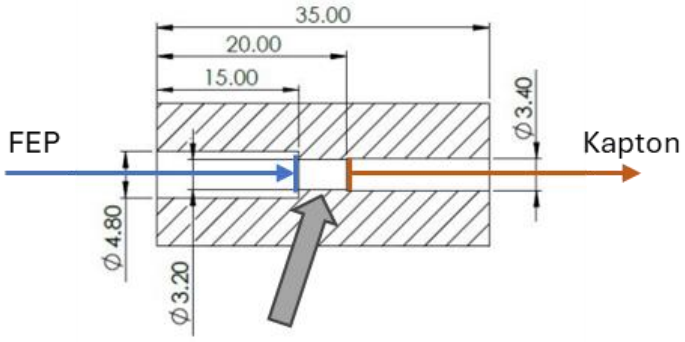

Figure 5.30: CAD drawing of the PTFE Kapton union with FEP and Kapton tubing and flow direction annotated. Measurements in mm. Arrow to indicate region potentially causing blockage issues. Image adapted from [18].

For all crystallisation runs of *o*ABA with the BA additive, needle crystals were often observed in the nucleation promoter. The needle morphology is consistent with *o*ABA Form II growth, however, with the BA additive needle crystals have also been seen for the typically prism-like Form I.[10] At concentrations of 18.9 – 19.5 g/L where no crystallisation was observed for *o*ABA without BA additive, crystallisation was observed with BA additive and similar experimental conditions, indicating that the BA additive promotes the nucleation of *o*ABA and reducing the need for surface interaction for initial nucleation. However, all crystallisation of *o*ABA with BA produced blockages in the Kapton windows. Despite the BA additive promoting nucleation and crystal growth, the surface effects in the Kapton unions may also have contributed to the window blockages. The needle habit of *o*ABA likely contributed to the blockages in the Kapton window joins. The additive may have been promoting the growth of *o*ABA Form III, like seen in literature examples,[10] which may be less reliant on surfaces for nucleation. *o*ABA crystallisation without the BA additive may favour Form I and II crystallisation which may be more reliant on surfaces for nucleation. No X-ray data suitable for processing was acquired to verify BA polymorphic control of *o*ABA.

The Aquapel coating of the Kapton X-ray window tubes was often poor, with a high number of rejects due to inconsistent coating. This likely contributed to the surface-dependent nucleation of *o*ABA in the X-ray windows. The preparation and sputter regime remained the same methodology used with the KRAIC-D; a possible cause for the poor hydrophobic coating is a potential Aquapel reformulation causing weaker adherence to the Kapton. The atmospheric humidity levels during the coating were high, often 80% humidity during the preparation period; the preparation lab should be temperature and humidity controlled but was not monitored, so humidity may have contributed to the poor Aquapel coating. Humidity should be monitored during future Kapton preparation to assess if this is a potential cause.

*5.4.3.2 – o*ABA *slurrying results and discussion*

For each slurrying condition of *o*ABA in 90:10 v/v H_2O:IPA, X-ray diffraction data was collected at multiple X-ray windows. When discussing slurrying results, the slurrying run "2_*o*ABA_45:65_1" refers to the second slurrying run completed for temperature settings of 45 °C for C1 and 65 °C for C2, the first repeat of these conditions. When discussing the X-ray data, "X1_01" refers to a collection set of slug triggering data collections at the X1 analysis window for the first repeat of collections at this window.

The slurries of *o*ABA maintained suspension in the feedstock vessel and pumped well, producing multi-crystalline slugs with *o*ABA. The slurry slugs generally flowed well through the Kapton windows; occasionally a window required replacing due to a build-up of crystals in areas of poor hydrophobic coating, or at the Kapton union join. There was a high level of crystalline material in slugs coming from HZ1 and HZ3 on the 45 °C C1 column, shown in Figure 5.31a. The C2 temperatures of 60 °C and 65 °C showed a reduction of crystalline material due to dissolution on HZ2 and HZ4, shown in Figure 5.31b. As a result, X1 and X3 windows generally showed high hit rates and higher signal-to-noise for the resultant PXRD patterns. The reduced crystalline material in-beam for X2 slug triggering collections slightly reduced the hit rates and reduced the diffraction intensity. The slurry density for X2 slurry flow (Figure 5.31b) is more equivalent to the crystalline density that would be present in typical crystallisation experiments.

Figure 5.31: Images from the above-axis camera showing slurry density for a) X1, and b) X2 windows.

The above-axis camera improved the ease of beam alignment to the X-ray windows and helped define stage start and end positions, preventing the X-ray beam from hitting the silicone glue. A video image from the beamtime is shown below in Figure 5.32. The video feed of the segmented flow prior to the Kapton union assisted with monitoring for blockages through visual disturbances in the flow rate, and for setting the slug triggering stage velocity to match the flow rate. However, segmented flow and crystals were not visible through the Kapton windows to aid slug triggering optimisation.

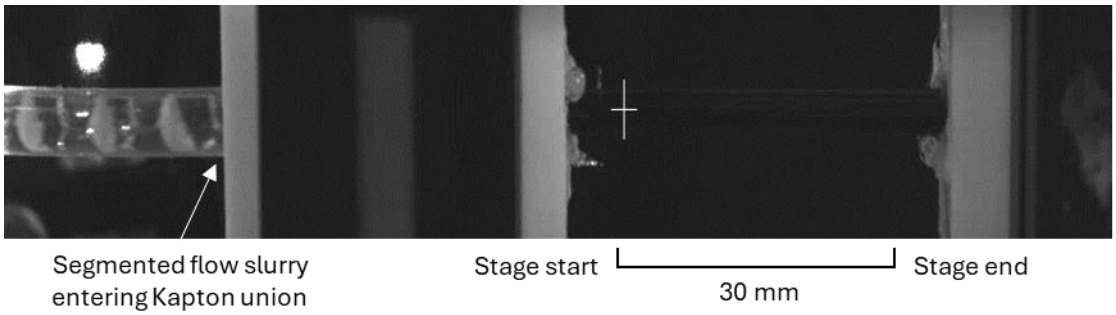

Figure 5.32: Still of the video feed captured during a slug triggering collection. "+ " on image indicates the approximate beam position horizontally, vertical position not shown due to parallax from the above axis camera.

Slug triggering through GDA enabled control of the slug triggering data collection for non-expert users with real-time viewing of the collected diffraction frames. The basic raw integration to 1D PXRD patterns provided a general overview of the slug triggering hit rate, quantity of data, and diffraction signal for each collection. Compared to slug triggering control with a Python command line, the detector image and raw 1D pattern is the main benefit for users with the immediate feedback on beamtime results.

The x-stage velocity for the 30 mm slug triggering translation used a median value of 12.75 mm/s for the 6.4 mL/min total flow rate. The slug triggering mechanism suspended crystal in-beam for an average of 2.3 s acquisitions, with the captured detector frames often containing powder rings as opposed to individual spots as seen with KRAIC-D data: comparison with KRAIC-D 100 ms data is shown below in Figure 5.33.

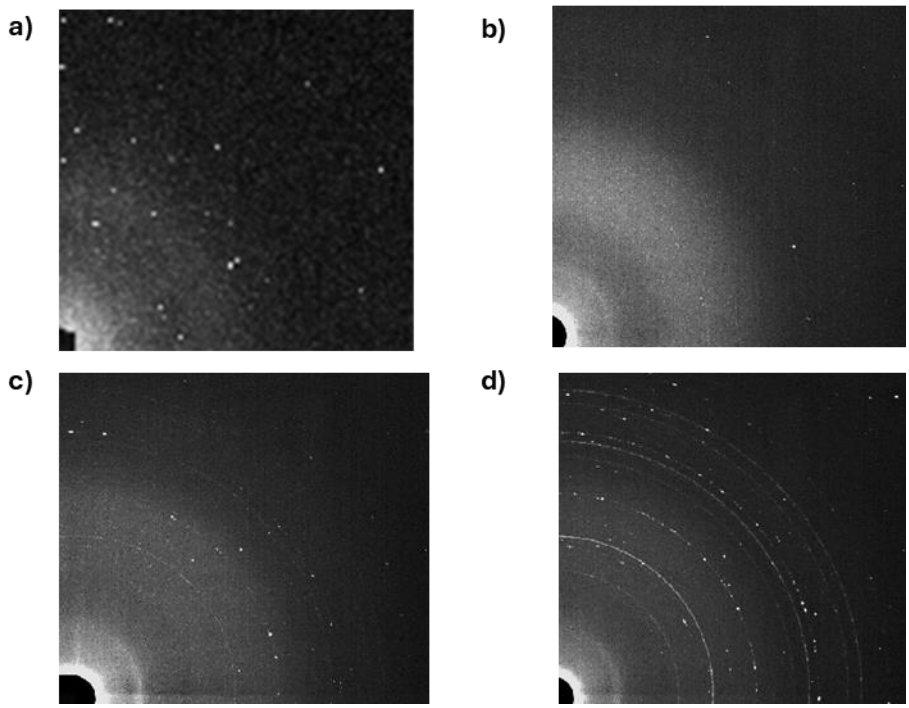

*Figure 5.33: Sections of diffraction frames of a) 100 ms acquisition of carbamazepine in the KRAIC-D, and b-d) diffraction frame images captured for 2.3 s during slug triggering of o*ABA *in the KRAIC-T. b) shows low level of diffraction captured with a few spots present, c) shows weak powder rings with strong diffraction spots, with d) showing strong powder diffraction rings and spots.*

The KRAIC-D detector frame (Figure 5.33a) was considered an exceptional diffraction frame with a high number of spots compared to the bulk of diffraction frames collected. With slug triggering, collections are now able to achieve powder rings due to the prolonged data capture of multi-crystalline material rotating in beam due to flow turbulence. The majority of frames captured at X1 and X3 were equivalent to the Figure 5.33c+d example diffraction frames. The majority of frames from X2 collections were equivalent to Figure 5.33c. The slug triggering photodiode and support frame produced minimal detector shadowing in the main resolution range of the detector frame.

The hit rates for the slug triggering collections were calculated with the developed diffraction sorting workflow (diffraction_sorting.py), discussed further in Chapter 3. The slug triggering collection set diffraction frames were processed with the multi-frame baseline correction processing methodology, developed using the *o*ABA data and also discussed further in Chapter 3. The results for the different *o*ABA slurrying conditions are discussed below.

5.4.3.2.1 – 1_*o*ABA_45:60_1 slurrying

The first repeat of the 45 °C to 60 °C temperature settings *o*ABA slurrying conditions successfully ran for 1 hr 20 min with the first *o*ABA slurry feedstock, ending due to time constraints necessitating a change in conditions. The temperature profile for all runs performed at 45 – 65 °C temperature cycling can be presumed to be equivalent due to the stable ~24 °C room temperature. A temperature profile was recorded for 3_*o*ABA_45:60_2 repeated conditions and is shown in Figure 5.37. The length along crystalliser, equivalent temperatures (from 3_*o*ABA_45:60_2), and calculated supersaturation is shown below in Table 5.04.

*Table 5.04: Temperature measurements for heating zone temperatures during o*ABA *slurrying (1_o*ABA*_45:60_1), taken from Figure 5.37, with calculated supersaturation for Form II, S_{II}, and Form I, S_I.*

	Approximate length along crystalliser /cm	**Temperature /°C**	**S_{II}**	**S_I**
Start of HZ1	189	42.2	1.47	1.55
End of HZ1	371	43.1	1.40	1.48
Start of HZ2	462	49.9	1.00	1.03
End of HZ2	667	53.3	0.85	0.86
Start of HZ3	723	40.8	1.57	1.67
End of HZ3	905	41.3	1.53	1.63

The slug triggering hit rate was calculated for each slug triggering collection set, shown in Table 5.05. The slug triggering collection sets showed a high level of hit rate of crystals, with an average of 93% of slug triggering collections containing diffraction.

Table 5.05: Number of detector frames collected, containing diffraction, and overall hit rate for each slug triggering collection set in the 1_oABA_45:60_1 slurrying run. Collection sets are displayed in the order of collection, with start of acquisition time noted.

			Number of detector frames		
		Approximate start of collection time /hr:min	**Collected**	**With diffraction**	**Hit rate**
Collection Sets for 1_*o*ABA_45:60_1	**X1_01**	00:15	7	7	100%
	X2_01	00:20	30	27	90%
	X3_01	00:45	19	19	100%
	X2_02	00:57	18	18	100%
	X1_02	01:13	8	6	75%
		Total	82	77	93%

The processed PXRD patterns for each collection set are shown below in Figure 5.34 against the *o*ABA polymorph reference patterns. The PXRD patterns for the 1_*o*ABA_45:60_1 slurrying run were processed as an average of the individual slug triggering collections; the X2 collection sets show a reduced average diffraction intensity compared to the X1 and X3 collection sets. This is due to the reduced crystalline material in-beam due to X2 position after the hot 60 °C HZ2 dissolved the *o*ABA slurry. The X1_02 collection set shows high intensity diffraction signal: this is due to one individual frame with a particularly good hit of crystals in slug, and due to the low number of frames averaged this shows at a high average intensity.

Visual inspection of the PXRD patterns shows a high proportion of Form III in all collections with Form I present in all and trace Form II. This is similar to the *o*ABA feedstock used, shown in Figure 5.26, which was dominant Form III with Form II present and no Form I. X1_01 featuring Form I indicates a transformation of *o*ABA in the feedstock. When analysed using Rietveld refinement in the TOPAS software the percentage balance of *o*ABA polymorphic forms were calculated, shown below in Table 5.06.[19] An example Rietveld refinement plot is shown in Figure 5.35; the residual plot is representative of the residuals of all processed datasets shown in this chapter.

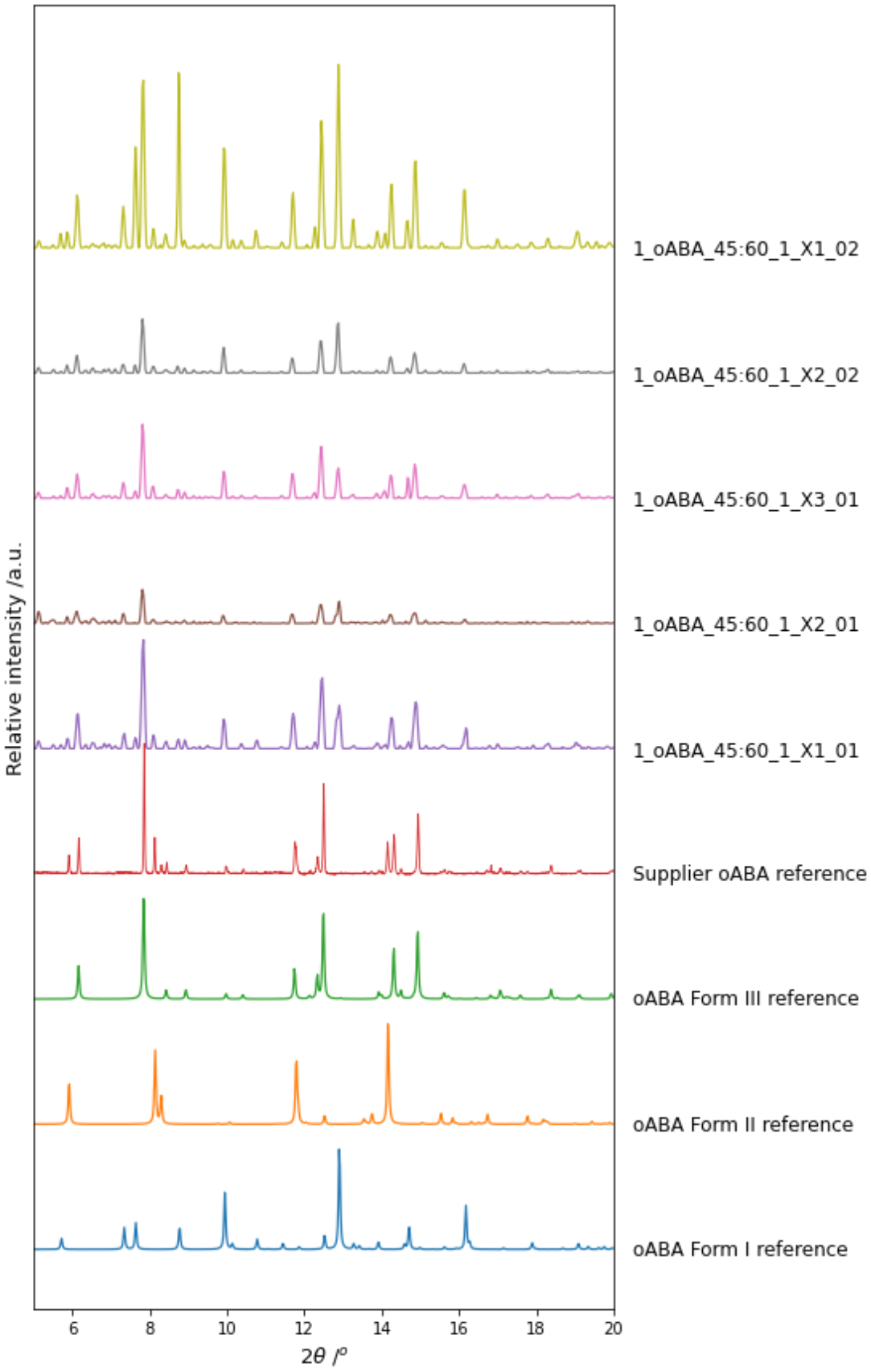

Figure 5.34: PXRD patterns of oABA *reference patterns against 1_*oABA*_45:60_1 slurrying patterns processed using the multi-frame baseline correction technique for each X-ray window collection set.*

Table 5.06: Collection sets of 1_oABA_45:60_1 with experimental collection time against oABA polymorphic form percentage, with calculated R-factors for the Rietveld refinement. Compared against Rietveld results for oABA supplier reference polymorph percentage.

			***o*ABA polymorph percentage /%**			
		Approximate start of collection time /hr:min	**Form I**	**Form II**	**Form III**	**r_wp**
Collection Sets for 1_*o*ABA_45:60_1	**X1_01**	00:15	26.7	6.1	67.3	29.867
	X2_01	00:20	14.7	9.0	76.3	41.100
	X3_01	00:45	27.5	10.0	62.5	27.604
	X2_02	00:57	24.4	8.6	67.1	29.578
	X1_02	01:13	33.5	3.4	63.2	22.244
	***o*ABA supplier reference**		-	21.6	78.4	56.590

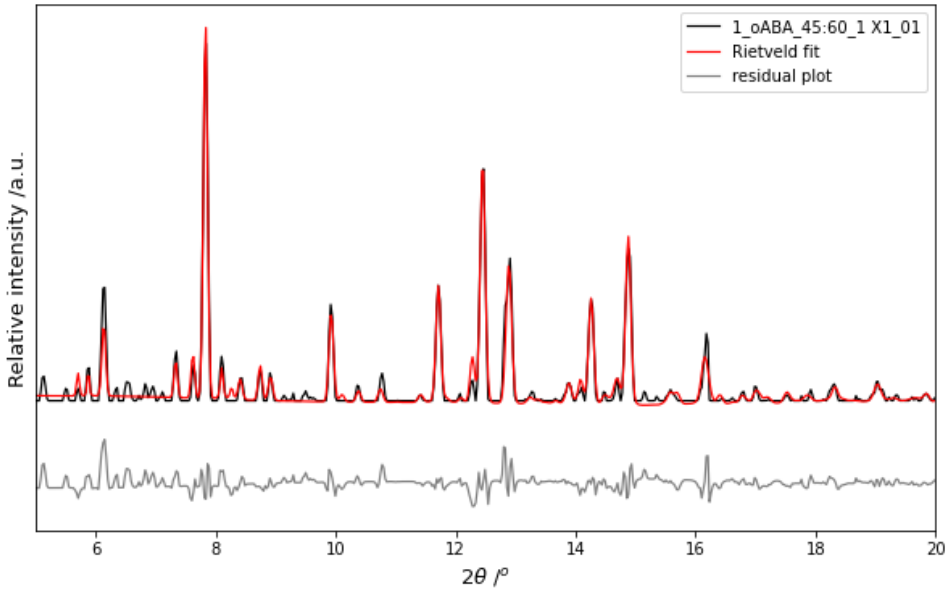

Figure 5.35: Rietveld refinement of 1_oABA_45:60_1 X1_01 against oABA references.

The refinement required the use of a preferred orientation correction to minimise the residual plot due to incomplete powder averaging. The slug triggering acquisitions, whilst improving powder averaging through following multiple, tumbling micro-crystals in-beam for a prolonged period, do not fully account for the full powder averaging affect, leading to a preferred orientation style effect. As a result, the Rietveld refinement cannot be used for conclusive analysis of polymorphic form changes due to the relationship between complete powder averaging and polymorphic ratio calculations. However, it can be used for reliable identification of polymorphic form, rather than just visual inspection. The *o*ABA polymorphic percentage shows a poor correlation between repeated X-ray window collections; X1_02 and X2_02 shows reduction in Form II and Form III, with an increase in Form I compared to X1_01 and X2_01. This either shows the error in refinement polymorphic balance for these datasets collected in the high background noise *in situ* environment or indicates

a further transformation of the feedstock from Form II and Form III to Form I, during the hour between data collections. The Form I percentage was reduced for the X2 windows compared to the X1 and X3 values; both Form I and Form II show undersaturation at the ~53 °C HZ2, supersaturation ratio shown above in Table 5.04, indicating dissolution of Form I and II. The temperature is approximately at the Form I – III transition point at 50 °C, potentially showing a slight transformation on HZ2, correlating with the calculated X2 polymorphic percentages. The Form II percentage is slightly increased at X2: this may be an error or may be caused by the overall reduced crystalline density due to dissolution with the further transformation of I to III increasing the overall percentage of Form II, despite partially dissolving. Overall, the *o*ABA Form I percentage shows a slight increase over the crystalliser length, corresponding to slurrying run time, indicating a potential solvent-mediated transition of Form III to Form I. The unit cell parameters (summarised in Appendix A5.3.1) for 1_*o*ABA_45:60_1 show good agreement with the literature values shown in Table 5.03 with low errors for the polymorphs of *o*ABA. The unit cell volumes are 7.8 – 38.9 $Å^3$ higher than quoted in the literature, however, this can be attributed to the thermal expansion of the unit cell in the increased temperatures for data collection in the KRAIC-T.

5.4.3.2.2 – 2_*o*ABA_45:65_1 slurrying

The second *o*ABA slurring run used the first *o*ABA slurry feedstock, temperature cycled with C1 and C2 temperature settings of 45 °C and 65 °C respectively. The flow slurrying ran for 1 hr 15 mins, finishing due to a slight encrustation in the slurrying pump requiring cleaning with solvent. Full temperature mapping of the temperature conditions was not completed due to time constraints, partial temperature readings with the FLIR E5 IR camera were taken and shown below in Table 5.07. Temperature readings are compared to full temperature mapping completed for 2_*o*ABA_45:65_2 repeated conditions below in Section 5.4.3.2.2.

*Table 5.07: Temperature measurements for heating zone temperatures during o*ABA *slurrying (2_o*ABA*_45:65_1) in EH2 Beamline I11, with calculated supersaturation ratios for Form I and Form II.*

	Approximate length along crystalliser /cm	**Temperature /°C**	**S_{II}**	**S_I**
Start of HZ1	189	41.5	1.52	1.61
End of HZ1	371	42.5	1.44	1.53
Start of HZ2	462	45.0	1.28	1.33
End of HZ2	667	57.0	0.71	0.70
Start of HZ3	723	41.5	1.52	1.61
End of HZ3	905	42	1.48	1.57

Slug triggering data collections were acquired at all three X-ray windows, with a repeated collection set for X2. The calculated hit rates are shown below in Table 5.08 with an average hit rate of 86% of frames collected containing diffraction.

The average hit rate is lower than 1_*o*ABA_45:60_1 due to the reduced crystalline material in the slugs in X2 caused by dissolution of the *o*ABA forms due to solution undersaturation on the 57 °C HZ2.

Table 5.08: Number of detector frames collected, containing diffraction, and overall hit rate for each slug triggering collection set in the 2_oABA_45:65_1 slurrying run. Collection sets are displayed in the order of collection, with start of acquisition time noted.

			Number of detector frames		
		Approximate start of collection time /hr:min	**Collected**	**With diffraction**	**Hit rate**
Collection Sets for 2_*o*ABA_45:65_1	X1_01	00:16	35	34	97%
	X2_01	00:27	19	13	68%
	X3_01	00:39	20	19	95%
	X2_02	00:52	20	17	85%
		Total	94	83	86%

The collection sets for 2_*o*ABA_45:65_1 was processed using the multi-frame baseline correction procedure, the resultant PXRD patterns are shown below in Figure 5.36 against *o*ABA polymorphic form references.

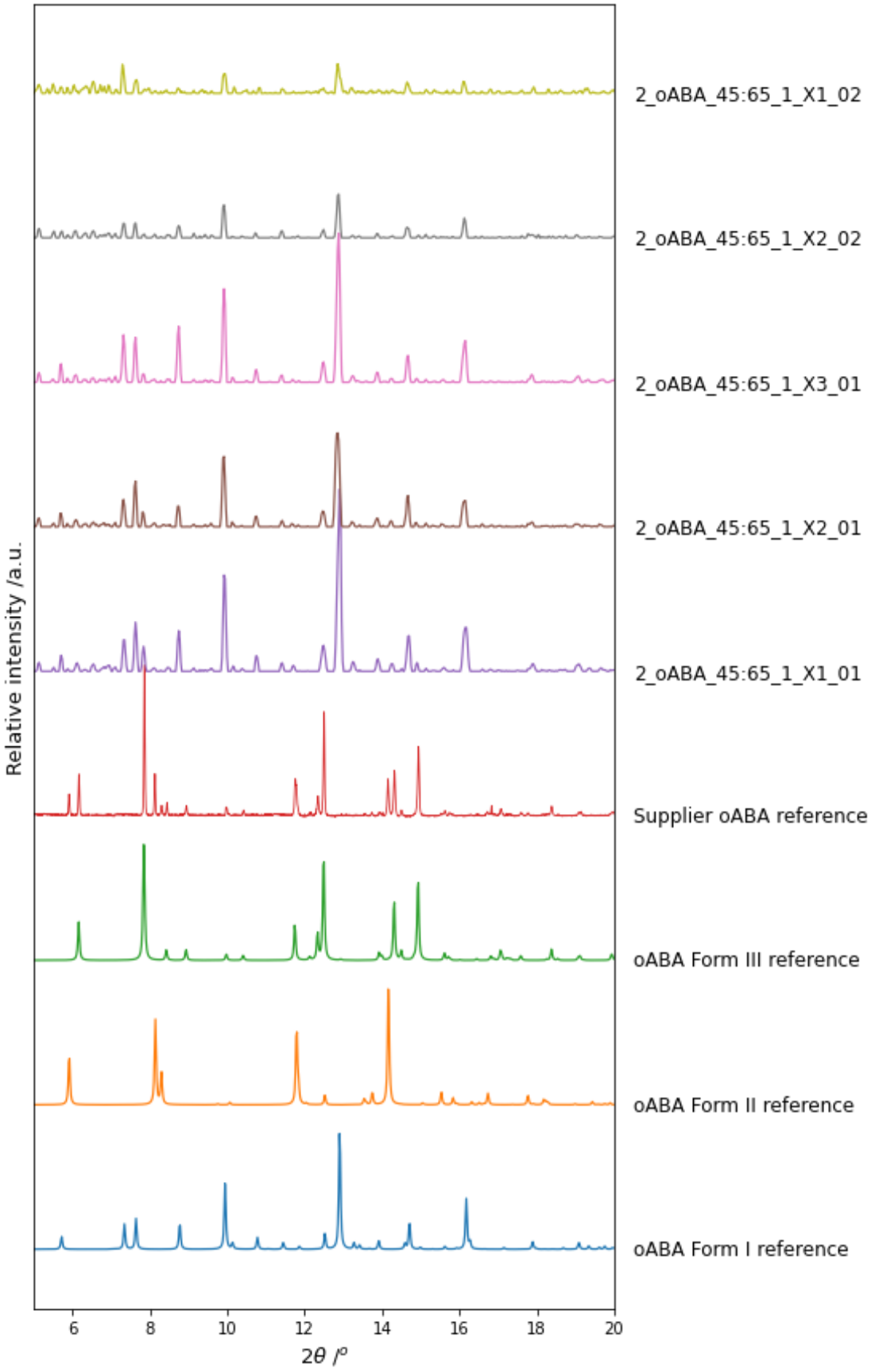

Figure 5.36: PXRD patterns for the 2_oABA_45:65_1 slurrying conditions slug triggering collection sets against the oABA Mercury generated references.

The PXRD patterns for the 2_*o*ABA_45:65_1 slurrying run show dominant Form I with small amounts of Form III shown by the Form III peak at 7.84 ° 2θ. No Form II can be confirmed with visual inspection alone. This contradicts the results for 1_*o*ABA_45:60_1 in which the slurry entering the crystalliser under the same temperature conditions showed dominant Form III, with Form I and trace Form II at X1_01. In the solid state, Forms II and III transition to the stable Form I at 60 °C and 50 °C respectively, however, the comparison of the first and second *o*ABA slurrying results indicate solvent-mediated phase transitions of Form II and III in the feedstock slurry at 40 °C during the 4.5 hr lifespan of the slurry. The slurry would likely transition fully to Form I if left at 40 °C for a prolonged period. The difference in polymorphic percentage of 1_*o*ABA_45:60_1 for X1_01 and X1_02 (Table 5.06) from 26.7% to 33.5% Form I and reduction in Form II and III indicate this transition had progressed in the starting material during the 1 hr time difference in collection times, rather than an error in calculation for the Rietveld refinement. The Rietveld refinement polymorphic percentages are shown below in Table 5.09.

*Table 5.09: Collection sets of 2_o*ABA*_45:65_1 with experimental collection time against o*ABA *polymorphic form percent, with calculated R-factors for the Rietveld refinement. Compared against Rietveld results for oABA supplier reference polymorph percentage.*

			***o*ABA polymorph percentage /%**			
		Approximate start of collection time /hr:min	**Form I**	**Form II**	**Form III**	**r_wp**
Collection Sets for 2_*o*ABA_45:65_1	X1_01	00:16	88.0	0.6	11.5	26.080
	X2_01	00:27	88.1	1.1	10.8	31.378
	X3_01	00:39	93.6	0.8	5.7	25.214
	X2_02	00:52	90.4	1.5	8.1	35.453
	***o*ABA supplier reference**		-	21.6	78.4	56.590

The Rietveld refinement potentially shows a small presence of Form II: including Form II for the X1_01 refinement slightly reduces the R-factor from 26.159 to 26.080. However, the unit cell parameters for Form II, summarised in Appendix A5.3.2, have a high error (±17.9 $Å^3$ for volume for X3_01) compared to the Form II results from 1_*o*ABA_45:60_1 (±2.0 $Å^3$ for volume for X3_01). The unit cell parameter errors could not be calculated for Form II for X1_01. The high error involved in Form II calculations for 2_*o*ABA_45:65_1 indicate Form II was likely not present in the slurry. The Rietveld refinement compared to 1_*o*ABA_45:60_1 gives further evidence for the feedstock solvent-mediated phase transition to Form I, with considerable increases in Form I and reduction in Form II and III. The polymorphic form ratios are relatively consistent with maximum deviation of 5.8% which is likely to be within the error of the Rietveld calculations for this technique, showing no phase transformation due to temperature cycling influence in the KRAIC-T.

5.4.3.2.3 – 3_*o*ABA_45:60_2 slurrying

For the repeat of 45 °C C1 and 60 °C C2 temperature settings for the slurrying of *o*ABA, the second *o*ABA slurry was used with the same 26 g/L *o*ABA loading in 90:10 v/v H_2O:IPA solvent mixture at 40 °C. The slurrying run completed 2 hr 08 min of run time, ending due to a potential blockage. The temperature profile is shown below in Figure 5.37.

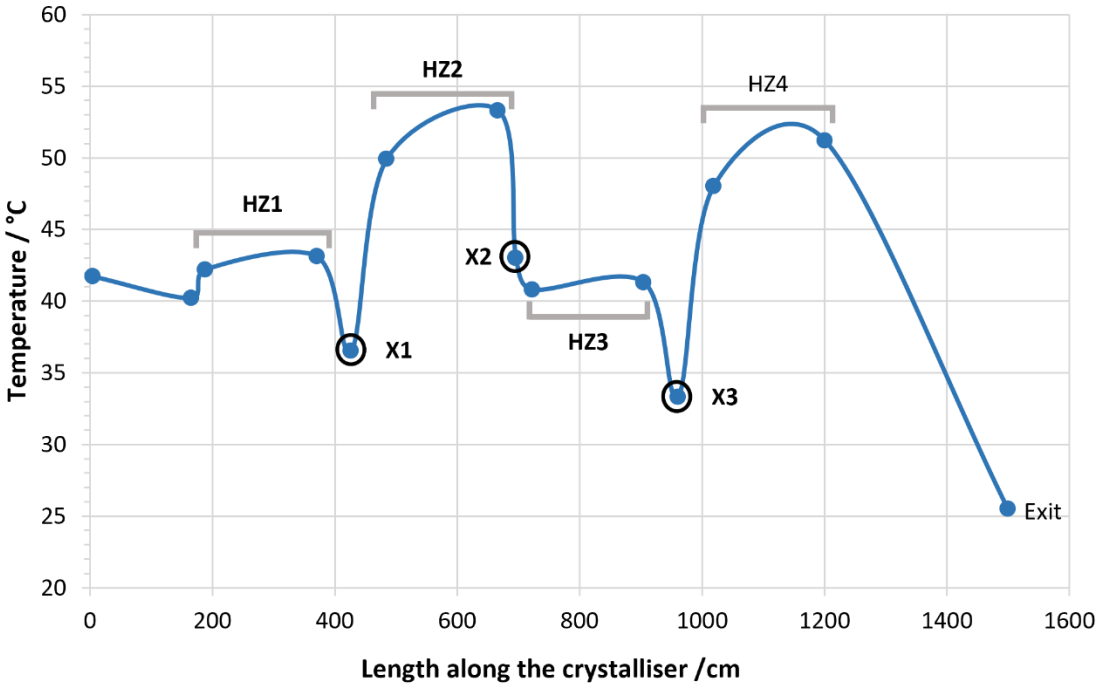

Figure 5.37: Temperature profile for the slurrying of oABA between column settings of 45 °C and 60 °C for C1 and C2 respectively.

The temperature measurements for the HZ1 and HZ3 temperatures correlate well with the equivalent measurements on 2_*o*ABA_45:65_1, shown in Table 5.07, for the same C1 temperature setting of 45 °C. These measurements correlate well with the temperature profile commissioning of the KRAIC-T, above in Section 5.2. The temperature readings and resultant supersaturation ratios are previously described in Table 5.04.

The hit rate calculations are shown below in Table 5.10. Collections stopped for X3_02 due to a potential second blockage ending the slurrying run. Hit rates for the 3_*o*ABA_45:60_2 conditions were high with an average of 95% of frames containing diffraction.

*Table 5.10: Number of detector frames collected, containing diffraction, and overall hit rate for each slug triggering collection set in the 3_o*ABA*_45:60_2 slurrying run. Collection sets are displayed in the order of collection, with start of acquisition time noted. *Increased time between start of collection times due to unblocking X2.*

			Number of detector frames		
		Approximate start of collection time /hr:min	**Collected**	**With diffraction**	**Hit rate**
Collection Sets for 3_*o*ABA_45:60_2	X1_01	00:16	15	15	100%
	X2_01	00:25	29	26	90%
	X3_01	00:47	30	27	90%
	X1_02	*01:47	35	33	94%
	X3_02	02:08	5	5	100%
		Total	114	106	95%

The collection set diffraction frames for the 3_*o*ABA_45:60_2 slurrying conditions were processed using the multi-frame baseline correction processing methodology, with resultant PXRD patterns shown below in Figure 5.38. Visual inspection of the X3_02 frames showed powder rings, like shown in Figure 5.33d, however with minimal changes to diffraction spots, indicating a blockage. Visual inspection of the PXRD patterns shows dominant Form III with Form II present. The X1_02 collection set shows some presence of Form I with the peaks at 7.63 ° and 12.87 ° 2θ.

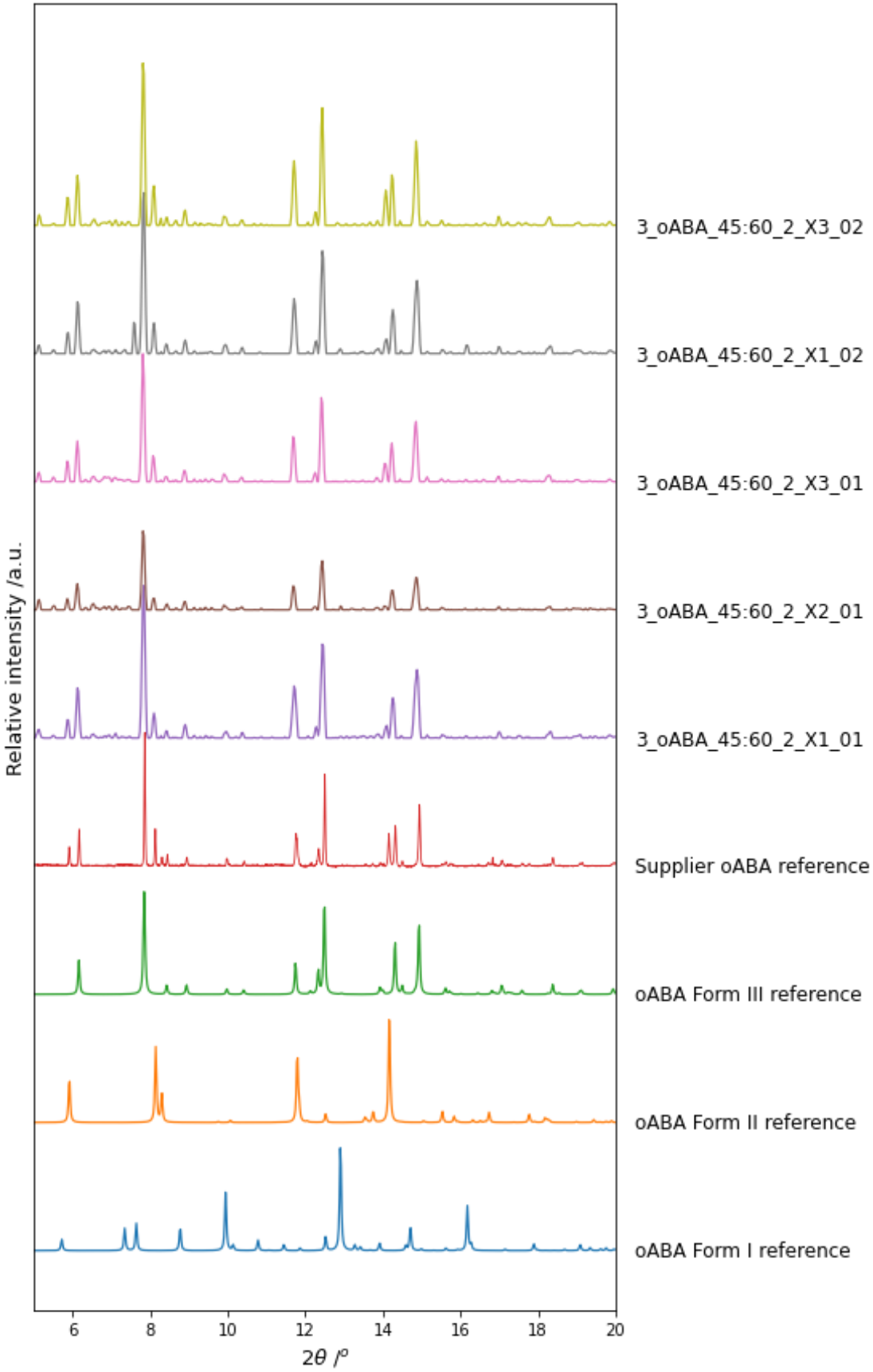

Figure 5.38: PXRD patterns for the slug triggering collection sets from the I11 beamtime on the 3_oABA_45:60_2 slurrying conditions in the KRAIC-T. Patterns displayed against the Mercury generated oABA references.

The polymorphic percentage results for the Rietveld analysis of the collection set PXRD patterns are summarised below in Table 5.11.

*Table 5.11: Collection sets of 3_o*ABA*_45:60_2 with experimental collection time against o*ABA *polymorphic form percentage, with calculated R-factors for the Rietveld refinement. *Increased time between start of collection times due to unblocking X2. Compared against Rietveld results for oABA supplier reference polymorph percentage.*

			***o*ABA polymorph percentage /%**			
		Approximate start of collection time /hr:min	**Form I**	**Form II**	**Form III**	**r_wp**
Collection Sets for 3_*o*ABA_45:60_2	X1_01	00:16	-	14.3	85.7	30.300
	X2_01	00:25	-	10.4	89.6	31.562
	X3_01	00:47	-	13.7	86.3	28.007
	X1_02	01:47*	33.3	19.2	47.5	28.715
	X3_02	02:08	-	19.4	80.6	27.853
	***o*ABA supplier reference**		-	21.6	78.4	56.590

The polymorphic percentage results agree with visual analysis of the PXRD patterns with predominant Form III and Form II with no Form I for the majority of collections. The diffraction patterns and Rietveld percentage are similar to the *o*ABA starting material pattern (Figure 5.26), with predominant Form III, some Form II with no Form I detected. The 1hr between starting collections for X3_01 and X1_02 due to unblocking the crystalliser are likely to account for the increase in Form I: it may have allowed for transformation of the fresh feedstock to Form I, as seen previously, or the disruption to flow during unblocking caused some Form I formation. This Form I presence should be visible in the X3_02 pattern, however the collection set only contained 5 diffraction frames of a blockage in the X-ray windows, the blockage formed of Form III and II. The unit cell parameters for the oABA forms at each collection window (summarised in Appendix A5.3.3) show low error, correlating with the results from 1_*o*ABA_45:60_1.

5.4.3.2.4 – 4_*o*ABA_45:65_2 slurrying

The repeated *o*ABA slurring run with 45 °C and 65 °C column temperature settings for C1 and C2 respectively ran for 1 hr 6 min, ending due to blockages in the Kapton windows. The temperature profile of the KRAIC-T was collected for 4_*o*ABA_45:65_2 slurrying conditions and is shown and compared against 2_*o*ABA_45:65_1 below in Figure 5.39.

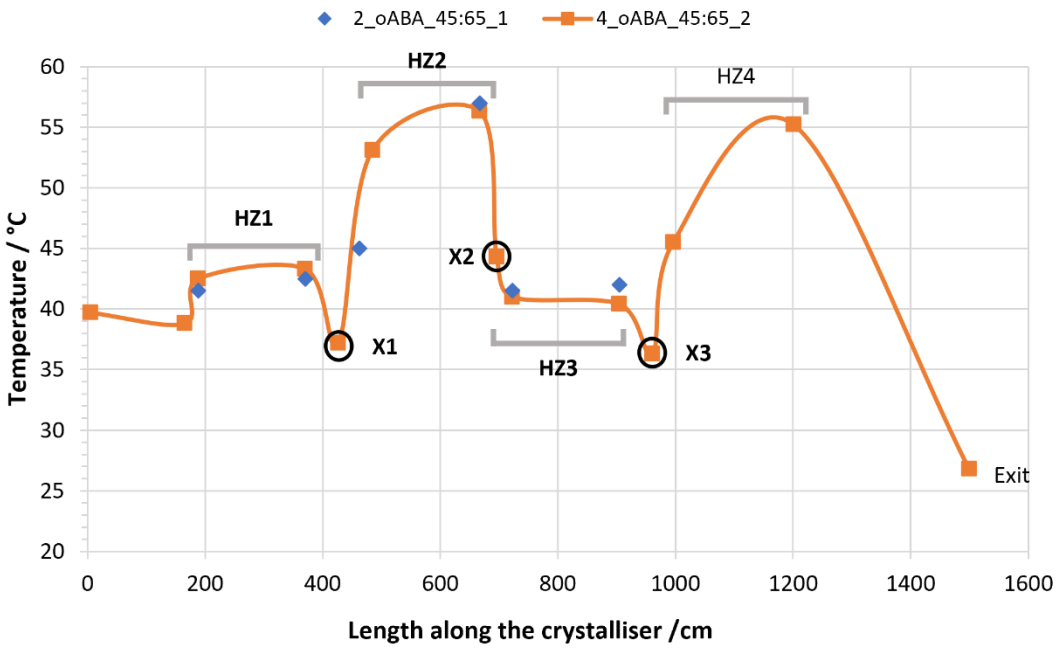

Figure 5.39: Temperature profile for the slurrying of oABA with 45 °C and 65 °C column temperature settings for C1 and C2 respectively. Full temperature profile for the second repeat of conditions, with the partial temperature data collected for 2_oABA_45:65_1 shown for comparison. Heating zones and X-ray analysis windows are annotated.

The temperature measurements for the first and second repeats of the temperature conditions show good correlation. The calculated supersaturation ratios are equivalent to those shown for 2_*o*ABA_45:65_1 shown in Table 5.07. The hit rates for the slug triggering collection sets for the 4_*o*ABA_45:65_2 slurrying conditions are shown below in Table 5.12.

Table 5.12: Number of detector frames collected, containing diffraction, and overall hit rate for each slug triggering collection set in the 4_oABA_45:65_2 slurrying run. Collection sets are displayed in the order of collection, with start of acquisition time noted.

			Number of detector frames		
		Approximate start of collection time /hr:min	**Collected**	**With diffraction**	**Hit rate**
Collection Sets for 4_*o*ABA_45:65_2	X1_01	00:14	23	20	87%
	X2_01	00:34	6	2	33%
	X2_02	01:05	10	4	40%
		Total	39	26	53%

The hit rates were low for this slurrying run due to persistent blockages in the Kapton windows. The slurrying run was towards the end of beamtime, with only poorly coated Kapton tubes remaining, which likely caused the increased frequency in blockages. No further data could be acquired. The processed PXRD patterns are shown below in Figure 5.40.

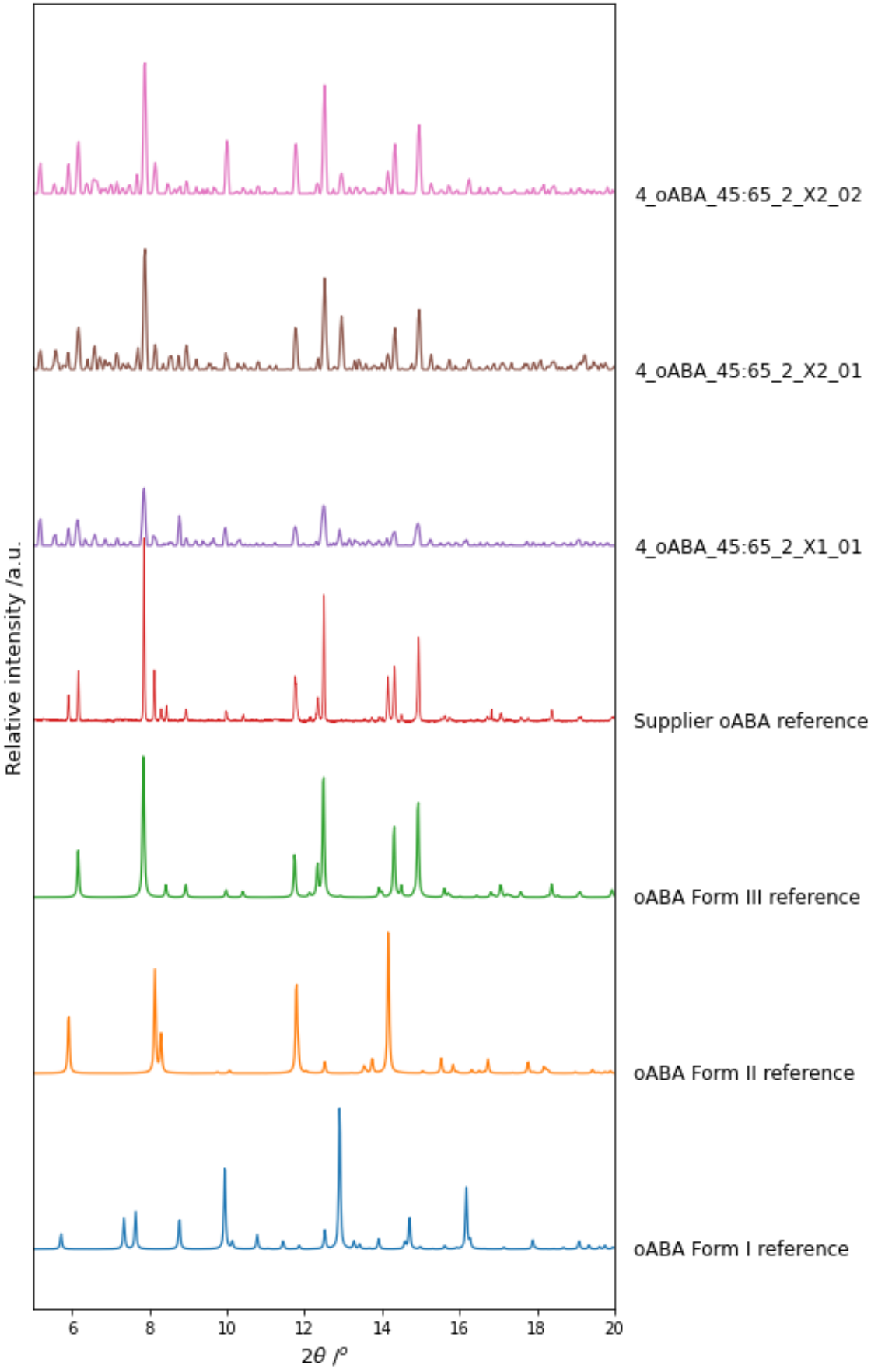

Figure 5.40: PXRD patterns for the 4_oABA_45:65_2 slurrying run collection sets against the oABA Mercury generated reference patterns.

The resulting PXRD patterns show a high quantity of noise in comparison to the other slurrying runs: the X2 collections have high noise due to the low number of slug triggering collections completed. Despite 20 diffraction frames for the X1 collection and 87% hit rate, the data also shows a high level of noise, indicating poor slug triggering crystal hits: whilst some diffraction was captured, the beam was not hitting the bulk of crystals in the slug. This highlights the issues with slug triggering on I11 with the lack of visualisation of the Kapton windows making it difficult to effectively target the crystals should the slug triggering be sub-optimal.

The PXRD patterns show predominant Form III with some presence of Form II and Form I. This is validated by the Rietveld refinement results for polymorphic percentages, shown below in Table 5.13.

Table 5.13: Collection sets of 4_oABA_45:65_2 with experimental collection time against oABA polymorphic form percent, with calculated R-factors for the Rietveld refinement. Compared against Rietveld results for oABA supplier reference polymorph percentage.

			***o*ABA polymorph percentage /%**			
		Approximate start of collection time /hr:min	**Form I**	**Form II**	**Form III**	**r_wp**
Collection Sets for 4_*o*ABA_45:65_2	X1_01	00:14	26.1	8.2	65.7	44.374
	X2_01	00:34	22.3	9.7	68.0	39.702
	X2_02	01:05	18.7	13.8	67.6	34.820
	***o*ABA supplier reference**		-	21.6	78.4	56.590

The polymorphic mixture with predominant Form III, alongside Form I and Form II concurs with the visual inspection, with no considerable change in polymorphic balance. The poorer quality of the data with high noise is highlighted by the high R-factors due to the residual noise after the Rietveld refinement. The unit cell parameters for X2_01 and X2_02, summarised in Appendix A5.3.4, do not follow the same trends as the other slurrying runs, often with cell volumes smaller than the reference data, also indicating a high error in the calculations. The unit cell volumes were expected to be larger due to thermal expansion, as seen for the other slurry results. X1_01 shows unit cell parameters in line with previous results, likely due to the increased quantity of diffraction frames collected resulting in improved signal-to-noise. There is an increase in Form I compared to 3_*o*ABA_45:60_2 and the *o*ABA reference material percentages, following the hypothesis of the feedstock undergoing solvent mediated phase transitions (SMPT) to Form I: at this stage the feedstock slurry was several hours old.

5.5 – Overall Conclusions

The temperature operational conditions of the KRAIC-T with two flow rates have been established through temperature mapping experiments. For a temperature setting range of 30 – 60 °C, the KRAIC-T was measured with an IR thermal imaging camera and shown to have an operational range of 25.8 – 53.8 °C ±1.5 °C for a water flow rate of 3 mL/min, and 27.6 – 53.9 °C ±1.5 °C for a water flow rate of 9 mL/min. Cooling in the transfer tubing sections from the Column Heating Zones to X-ray windows due to room temperature influenced the temperature profiles. The faster flow rate showed reduced overall cooling due to decreased residence times in these sections. Understanding these operational parameters and limitations was key to enabling experimental planning for targeting temperature-dependent transitions for crystallisation or solvent-mediated phase transitions for future experiments.

Crystallisation of succinic acid with ice bath sub-ambient temperature control in C2, and heated C1 temperatures of 25 °C, 30 °C, and 40 °C were shown to have positive effects on blockage prevention of the fast growth rate SCA crystals during crystallisation runs for 4 – 5 residence times. Successive cooling and heating cycles mediated succinic acid crystal growth through successive nucleation and crystal growth, and dissolution of fine particles and crystals. The resultant residence time yields for 25:icebath and 40:icebath of 3.2% and 2.7% respectively showed improvement on the average 2% yield for cooling of succinic acid. The temperature cycling does not appear to effect the polymorphic outcome in this instance, with predominant β-SCA with trace α-SCA seen for the 30:icebath conditions. The ice bath temperatures achieved 9.0 – 11.2 °C during succinic acid crystallisation, however, temperatures fluctuated due to rapid ice bath melt. The ice bath temperature control is not sustainable for long experimental periods due to the constant management required.

The integration of a heat sink temperature insert into the KRAIC-T system has successfully enabled sub-ambient temperature control, reaching a minimum of 12.2 °C. This enables a controlled, consistent temperature operating window of the KRAIC-T from 12.2 – 53.6 °C corresponding to temperature settings of 6 °C and 60 °C respectively. The temperature was limited by the use of water as the heat transfer media, limiting the circulator temperature to 5 °C to prevent ice blockages in the system. However, heat transfer to and from the surroundings still remains an operational limitation: transfer tubing sections from column temperature control to the X-ray windows for analysis gradually warms the liquid flow from sub-ambient column temperatures. The heat sink insert offers a significant advantage by enabling a broader range of sub-ambient temperatures beyond the limited ice bath temperature. With the current configuration, temperatures from 12 – 25 °C are likely achievable using the heat sink water circulator control, thereby enhancing the flexibility of the KRAIC-T system for a range of applications. The KRAIC-T provides enhanced temperature control, rather than complete reliance on room temperature, and offers the ability to cycle temperatures during crystallisation – a key process for optimising

crystallisation processes for improved crystalline products in terms of crystal size distribution, crystallite size, morphology, and polymorphic form.

Commissioning of the KRAIC-T as a sample environment aimed to investigate the model polymorphic compound *ortho*-aminobenzoic acid through crystallisation and slurrying in segmented flow with *in situ* PXRD analysis. *o*ABA temperature controlled crystallisation during beamtime was unsuccessful due to the tendency of blockage formation in the Kapton windows, whilst minimal crystallisation is occurring in segmented flow. The blockages formed due to rapid crystal nucleation and growth in the X-ray analysis windows, likely due to heterogeneous primary nucleation from the solid interfaces present in the windows from poor hydrophobic coating and imperfect FEP-Kapton tube joins. Crystallisation of *o*ABA with the BA additive promoted crystallisation in segmented flow, however, similarly blocked due to rapid crystallisation in the X-ray windows. It is proposed that *o*ABA crystallisation is controlled through surface-dependent nucleation, whilst the additive BA *o*ABA crystallisation more readily undergoes primary nucleation. The may be due to the formation of a different polymorph of *o*ABA in the presence of the BA additive: as seen in the literature, the BA additive can promote the crystallisation of *o*ABA Form III which is typically difficult to nucleate from solution.[10] Due to the strong surface dependence for *o*ABA nucleation and rapid crystal growth, it is not a good candidate for segmented flow crystallisation, especially with *in situ* analysis requiring Kapton windows.

The starting material of *o*ABA contained predominant Form III with Form II: both slurry feedstocks underwent solvent mediated phase transitions to the stable Form I when consistently stirred at 40 °C over the course of several hours. If slurrying was continued for several hours, it would have likely transformed to Form I only. As a result of the SMPT in the feedstock slurries, the effect of temperature cycling on the polymorphic balance could not be reliably monitored as repeated conditions and collection sets showed no correlation in results due to continual transformation of the feedstock.

Slurrying run 1_*o*ABA_45:60_1 shows some potential temperature cycling effect on polymorphic ratio with a substantial decrease (12%) in the Rietveld refinement results for Form I X2_01 compared to X1_01 and X3_01. This may be due to error associated with the Rietveld refinement caused by substantial preferred orientation in the collection set that was not accounted for; shown by the high R-factor (41.100) compared to the other collection sets (22.244 – 29.867). Another cause may be the dissolution of Form I on the 53 °C HZ2, as shown by the supersaturation ratio indicated a undersaturated solution at these conditions. Form II should also be undersaturated at this point, however, shows an increase in polymorphic ratio: this may be due to the total crystalline material decreasing due to undersaturation, but Form I decreasing the most through dissolution and transformation to Form III at the 50 °C transition temperature. This effect could not be fully verified by a repeat X2 collection set due to the increased Form I in the feedstock. Further work to evaluate the quality and quantity of slug triggering collections required to achieve low R-factors in the KRAIC-T sample environment would be beneficial to optimise the

data collections required for quality analysis for future beamtimes. Number of slug triggering collections required to achieve quality data is likely dependent on the crystal density per slug; beamtime studies in the KRAIC-T on a material with easily controllable crystal density per slug, such as anti-solvent crystallisation of glycine discussed in Chapter 4, would enable investigation into the amount of data collections required for a certain crystal density. The maximum number of data collections at a single window for *o*ABA was 35, with 34 containing diffraction: trialling collections up to 50 and 100 and comparing the data for different crystal densities would help to determine the minimum diffraction frames required for a given crystal density.

Introduction of the slug triggering mechanism as the data acquisition technique for *in situ* PXRD of *o*ABA slurrying in segmented flow was successful, with an average hit rate of 82% of detector frames containing diffraction for a 2.4 s collection. The slug triggering diffraction frames also showed improved signal-to-noise from the KRAIC-D collections, with powder rings often visible for a single collection. At this stage of development, the slug triggering mechanism functioned through a simple photodiode triggering level that caused the slug triggering to follow either the front or rear of a slug. The amount of crystalline material in slugs during *o*ABA slurrying provided a high hit rate, regardless of which part of the slug was targeted.

PXRD data collected through the 100 ms method with the KRAIC-D when processed and merged were unable to be analysed through Rietveld refinement for polymorph identification and polymorphic percentage information: the analysis software struggles with the low signal intensities and flat baseline for processing. The ability to perform Rietveld refinements for polymorphic form presence and analysis demonstrates the considerable improvement in data quality for the KRAIC-T slug triggering data processed with the multi-frame baseline correction technique. The polymorphic percentage data from the Rietveld refinement likely has error due to the preferred orientation correction required: this preferred orientation is due to the short collections times of non-microcrystalline material compared to typical PXRD experiments and full powder averaging is not achieved. The Rietveld refinement cannot be used to make conclusions based on small changes in the percentage values for polymorphic balance but can be used to verify the presence of polymorphs, rather than reliance on visual analysis. For this system with three polymorphs present, the Rietveld refinement was used to confirm significant changes in polymorphic percentages; for example, an average 25% Form I and 67% Form III in 1_*o*ABA_45:60_1 to 90% Form I and 9% Form III for 2_*o*ABA_45:65_1, confirming the transformation of the *o*ABA feedstock to the stable Form I. Furthermore, the Rietveld refinement assisted the identification of small quantities of Form II (~10%).

Addition of an above-axis camera feed during beamtime assisted beam-alignment to the X-ray windows and monitoring flow conditions for blockages. The camera view also allowed the user to set the x-stage velocity to match the flow rate for the slug triggering collections. However, the segmented flow was not visible through the dark Kapton windows which hindered adjustment of the

slug triggering settings to improve the targeting of crystalline material, demonstrated by the poor signal-to-noise for X1_01 in 4_*o*ABA_45:65_2.

Tubing insulation blocks were developed in response to temperature profile studies in Section 5.2, aiming to mitigate heat transfer due to room temperature in the non-temperature controlled tubing sections. The insulation blocks were trialled during *o*ABA crystallisations during beamtime but were bulky and prevented quick changes of the X-ray windows in the event of a blockage. Previously, the KRAIC-T was limited to 60 °C for safety reasons, however, temperature profile studies showed this resulted in solution temperatures of 53.9 °C, within the 60 °C limit. With a temperature setting of 65 °C for C2, temperatures of 56.3 °C were achievable, for an updated operating range of 12.2 – 56.3 °C. The upper limit of temperature control increased by 2.4 °C for a setting increase of 5 °C: the KRAIC-T would benefit from further insulation on the columns to increase the upper limit of temperature control, rather than temperature setting increases which has minimal success.

The slug triggering mechanism has been adapted the KRAIC-T on Beamline I11 EH2. Through use of the KRAIC-S shuttle analysis module, initial adaptation of the slug triggering control scripts was successfully achieved to work with I11 equipment. Slug triggering with the KRAIC-T was achieved with two separate laser-photodiode flow sensors enabling slug triggering for both directions of flow for X1 and X3, and X2 and X4 respectively. Visible light responsive (350 – 1100 nm) photodiodes were required for this purpose due to the increased tubing-photodiode distance (~20 mm) for which the previous X-ray response photodiode used with the KRAIC-S analysis shuttle would be too weak.

The limits for KRAIC-T slug triggering are a x-stage movement speed of 15 mm/s, equating to an approximate flow rate of ~7.1 mL/min. Stage translation is limited to the individual lengths of Kapton windows, which vary due to inconsistency with the window preparation. The maximum translation achievable is 30 mm, limited by the Kapton window frame, for stage translation limit at 15 mm/s giving a total collect time of 2 s for the fastest flow rates achievable for the system in EH2. Optimised laser-tubing and photodiode alignments with aligning the tubing with the top half of the tubing ensures distinction between solution and air segments. Alignment of the photodiode with the strongly scattered regions of the laser beam provides strong contrast between air and solution segments. Incorporation of a camera into EH2 on the approximate sample position assisted with alignment of the crystalliser in-beam and setting x-stage limits for the translation of the crystalliser. However, the Kapton unions were too dark to show the segmented flow during the trial data collections, future work would benefit from enhanced lighting of the X-ray windows to visualise flow conditions during data capture. Incorporation of slug triggering data collections into the GDA software, enables improved ease-of-use for slug triggering, not requiring detailed knowledge of the technique or experience with Python. GDA simultaneously visualises the photodiode readout, detector frames, and 1D integrated raw PXRD patterns for immediate feedback of crystal hit success.

5.6 – Future Work

Whilst the KRAIC-T shows enhanced temperature control compared to previous KRAIC systems, the system remains somewhat dependent on room temperature, with temperature variation caused by changes in room temperature. Ideally, future work in the KRAIC-T in a temperature controlled laboratory would mitigate this effect for more reproducible crystallisation experiments. The experimental hutches at Diamond are temperature controlled but can be affected by the experimental apparatus increasing the overall room temperature during KRAIC experiments: the average room temperature in EH2 at Beamline I11 during the heat insert testing was 25.5 °C due to the 55 °C hotplates in use for feedstock preparation. For preparation of crystallisation experiments for beamtime, preparation lab temperature ~25 °C for conditions in the 55 °C feedstock range would reduce temperature profile deviations when transferring the process from laboratory to experimental hutch. The KRAIC-T design has a high surface area of tubing exposed to air on the columns. As a result, the column temperatures were affected by room temperature variations. In future designs, minimising air contact or additional insulation could improve upon this design to minimise the effect of air temperature.

The heat sink insert was limited by the operational temperatures of water as the heat transfer liquid. Future work where below zero temperatures are required during temperature cycling for non-aqueous crystallisations, alternative heat transfer liquids could be used in the refrigerated circulator and column bath to improve sub-ambient temperature control.

Succinic acid temperature cycling trials showed success in mitigating blockages during segmented flow through controlled nucleation and dissolution cycles. Further experiments for crystal size and distribution analysis could benefit from inline imaging analysis of crystals in flow to assess crystal growth at various crystallisation stages post-heating zones, or offline particle characterisation with static image analysis to quantify crystal size changes with temperature cycling.[20,21] Further experiments with the heat sink insert for more controlled sub-ambient temperatures with increased run times to fully assess blockage mitigation over hour timescales would provide further insight into the temperature cycling blockage mediation.

Future adaptations to the Python processing scripts could look to assess unoptimized slug triggering through real-time hit analysis during beamtime to evaluate the quality of data acquired so users could perform more data collections for windows with poor collections. Furthermore, incorporation of auto-processing with the baseline correction technique, established in Chapter 3, into the GDA software could provide users with immediate feedback on the quality of the X-ray data and for optimising the slug triggering crystal-hit. Modifying the lighting to the Kapton windows could improve the visualisation of flow through the window and allow the user to optimise collections through modifying slug triggering parameters.

Slurrying of *o*ABA often resulted in solvent-mediated phase transitions to the stable polymorphic form; batch slurrying experiments of polymorphically pure

starting material could investigate this behaviour and any temperature-dependence. *o*ABA crystallisation showed a strong preference for secondary nucleation on surfaces, whilst BA promoting nucleation during segmented flow. Experimental work to investigate the polymorphic forms crystallising in these environments would provide further insight into this effect. Full analysis of *o*ABA polymorphic form transformations during slurrying in segmented flow was not able to be achieved due to time constraints during beamtime. Future *in situ* studies of *o*ABA crystallisation could investigate the surface-dependent crystallisation seen in this work and the influence of BA additive. Whilst unsuited for segmented flow studies with the Kapton windows, other environments such as acoustic levitation could provide a surface-less environment to study the crystallisation of *o*ABA from solution.[22] Segmented flow slurrying of Form I *o*ABA in the KRAIC-T would enable temperature cycling studies to investigate if the potential Form I dissolution on the 60 °C column was producing crystallisation of other polymorphic forms.

Observations from the commissioning of a KRAIC-S v2, discussed in Chapter 6, found that the triggering was taking place from the front and rear of the slugs due to the photodiode triggering value not discriminating between the front or rear of the slug. By adjusting the script to require a photodiode high level be achieved before reaching the triggering value, it helped improve triggering from the rear interface of the slugs. The adapted slug triggering method with the high level functionality was not available for this initial KRAIC-T work but should be employed for future beamtimes to improve targeting of the rear edge of slugs.

The Kapton windows showed poor Aquapel hydrophobic coating, despite following the same coating procedure as developed previously. Future work should investigate the Kapton coating behaviour against the lab humidity levels or using a separate batch of Aquapel and assessing the results, potentially moving towards a different X-ray window solution should the coating continue to perform poorly.

5.7 – References

1. Levenstein, M. A. *et al*. Dynamic Crystallization Pathways of Polymorphic Pharmaceuticals Revealed in Segmented Flow with Inline Powder X-ray Diffraction. *Anal. Chem.* **92**, 7754–7761 (2020).

2. Bakar, M. R. A., Nagy, Z. K. & Rielly, C. D. Seeded batch cooling crystallization with temperature cycling for the control of size uniformity and polymorphic purity of sulfathiazole crystals. *Org Process Res Dev* **13**, 1343–1356 (2009).

3. Leviel, J.-L., Auvert, G. & Savariault, J.-M. Hydrogen bond studies. A neutron diffraction study of the structures of succinic acid at 300 and 77 K. *Acta Crystallogr* **B37**, 2185–2189 (1981).

4. Dodd, I. M., Maginn, S. J., Harding, M. M. & Davey, R. J. SUCACB07 - Succinic acid alpha polymorph. *CSD Communication* Preprint at (1998).

5. Pallipurath, A. R., Flandrin, P.-B., Wayment, L. E., Wilson, C. C. & Robertson, K. In situ non-invasive Raman spectroscopic characterisation of succinic acid polymorphism during segmented flow crystallisation. *Mol. Syst. Des. Eng* **5**, 294–303 (2020).

6. Robertson, K., Flandrin, P.-B., Klapwijk, A. R. & Wilson, C. C. Design and Evaluation of a Mesoscale Segmented Flow Reactor (KRAIC). *Cryst. Growth Des.* **16**, 4759–4764 (2016).

7. Wayment, L. E. Continuous flow for materials synthesis, assembly and crystallisation at Diamond: discovery and delivery of high value materials. (University of Bath, Bath, 2020).

8. Wiklund, P. & Bergman, J. The Chemistry of Anthranilic Acid. *Curr Org Synth* **3**, 379–402 (2006).

9. Yadav, G. D. & Krishnan, M. S. An Ecofriendly Catalytic Route for the Preparation of Perfumery Grade Methyl Anthranilate from Anthranilic Acid and Methanol. *Org Process Res Dev* **2**, 86–95 (1998).

10. Simone, E., Steele, G. & Nagy, Z. K. Tailoring crystal shape and polymorphism using combinations of solvents and a structurally related additive. *CrystEngComm* **17**, 9370–9379 (2015).

11. Jiang, S., Jansens, P. J. & Ter Horst, J. H. Control over Polymorph Formation of o-Aminobenzoic Acid. *Cryst. Growth Des.* **10**, 2541–2547 (2010).

12. Simone, E. & Nagy, Z. K. A link between the ATR-UV/Vis and Raman spectra of zwitterionic solutions and the polymorphic outcome in cooling crystallization. *CrystEngComm* **17**, 6538–6547 (2015).

13. Hardy, G. E., Kaska, W. C., Chandra, B. P. & Zink, J. I. Triboluminescence-structure relationships in polymorphs of hexaphenylcarbodiphosphorane

and anthranilic acid, molecular crystals, and salts. *J. Am. Chem. Soc.* **103**, 1074 (1981).

14. Boone, C. D. G., Derissen, J. L. & Schoone, J. C. Anthranilic acid II (o-aminobenzoic acid). *Acta Cryst.* **B33**, 3205–3206 (1977).

15. Brown, C. J. The crystal structure of anthranilic acid. *Proc. Roy. Soc. A.* **302**, 185–199 (1968).

16. Groom, C. R., Bruno, I. J., Lightfoot, M. P. & Ward, S. C. The Cambridge Structural Database. *Acta Cryst.* **B76**, 171–179 (2016).

17. Simone, E., Saleemi, A. N., Tonnon, N. & Nagy, Z. K. Active Polymorphic Feedback Control of Crystallization Processes Using a Combined Raman and ATR-UV/Vis Spectroscopy Approach. *Cryst. Growth Des.* **14**, 1839–1850 (2014).

18. Levenstein, M. A. *et al.* Supplementary Information: Dynamic Crystallization Pathways of Polymorphic Pharmaceuticals Revealed in Segmented Flow with Inline Powder XRD. *Anal. Chem.* **92**, 7754–7761 (2020).

19. Bruker AXS. TOPAS. *Version 4.2* (2009).

20. Vancleef, A., Maes, D., Van Gerven, T., Thomassen, L. C. J. & Braeken, L. Flow-through microscopy and image analysis for crystallization processes. *Chem Eng Sci* **248**, (2022).

21. Gamble, J. F. *et al.* Morphological distribution mapping: Utilisation of modelling to integrate particle size and shape distributions. *Int J Pharm* **635**, 122743 (2023).

22. Alieva, A., Boyes, M., Vetter, T. & Casiraghi, C. Selective polymorphism of α-glycine by acoustic levitation. *CrystEngComm* **22**, 7075–7081 (2020).

Chapter 6 – Design of an integrated segmented flow crystalliser for *in situ* SCXRD on Beamline I19

This chapter discusses the development of the KRAIC-S crystalliser based on work on the original KRAIC-S v1 by Dr Lois Wayment, Dr Karen Robertson, Dr Mark Warren, Senior Beamline Scientist at Beamline I19. The KRAIC-S v2 in this chapter was developed in collaboration with Dr Mark Warren, and the KRAIC-S v3 was designed in collaboration with James Hawkins, I19 Beamline Technician.

6.1 – Introduction and Aims

Serial crystallography is a key technique for protein structure solution: proteins do not often grow large crystals so require synchrotron light source for diffraction experiments on the protein micro-crystals. However, protein crystals can be radiation-sensitive causing radiation damage by the high energy synchrotron X-rays, so a full dataset for structure solution cannot be obtained from a single crystal.[1] Serial crystallography uses data collection from multiple micro-crystals for partial "wedges" of reciprocal space, merging the partial datasets to form a more complete reciprocal space dataset. The wedges of diffraction data from multiple crystal orientations increases the completeness of the diffraction until the structure can be solved. Delivery of crystals for serial crystallography uses a range methodologies used including fixed target sample holders, droplet injection, microfluidic systems, and acoustic levitation.[2–5] Specialist software is used to extract the diffraction spots, index, refine, integrate, and merge the datasets for structure solution.[6]

Radiation sensitivity is becoming an increasingly prevalent problem in small molecule crystallography due to the increased flux densities at third generation synchrotron sources.[7] With the current advancement to fourth generation synchrotron sources, there will likely be an increasing demand for serial crystallography style techniques for small molecule systems.[8] The segmented flow conditions in the KRAIC style crystallisers have the potential to provide the sample delivery conditions for small molecule single crystals during crystallisation, enabling time-resolved structural analysis of the crystallisation process. The original KRAIC-S (KRAIC for single crystal XRD) was developed by Dr Lois Wayment, Beamline scientist Dr Mark Warren at Beamline I19: the small molecule single crystal diffraction beamline at Diamond Light Source. The KRAIC-S sample environment aims to achieve single crystal X-ray diffraction (SCXRD) from single crystals in segmented flow, with crystal rotation in the turbulent flow providing conditions to collect wedges of data from multiple single crystals to achieve structural solution in a serial crystallography style methodology.

The original KRAIC-S, referred to as the KRAIC-S v1 in this chapter, featured a continuous 11 m length of 1/8" ID FEP tubing. In contrast to the *in situ* PXRD KRAIC systems discussed in previous chapters, the KRAIC-S did not use X-ray

transparent windows due to the experimental complexity it would add. Furthermore, the close proximity of the detector to the sample environment in I19 experimental hutch 2 (EH2) would put the detector at risk of spray during the switching of X-ray windows due to blockages. The high X-ray energy (Ag K edge 25.5140 keV, 0.4859 Å) at I19 enabled penetration through the FEP tubing walls to achieve diffraction from flow crystallisation of paracetamol.

Paracetamol (PCM) is a polymorphic crystal system with the stable Form I and the metastable Form II. The molecular structure and crystal structures of PCM is shown below in Figure 6.01, with the crystallographic information summarised in Table 6.01. The elusive and highly metastable Form II is known to be challenging to crystallise in flow environments due to the rapid solvent mediated phase transition to the stable Form I.[9] Due to the instability of Form II, only the stable Form I is discussed in this Chapter.

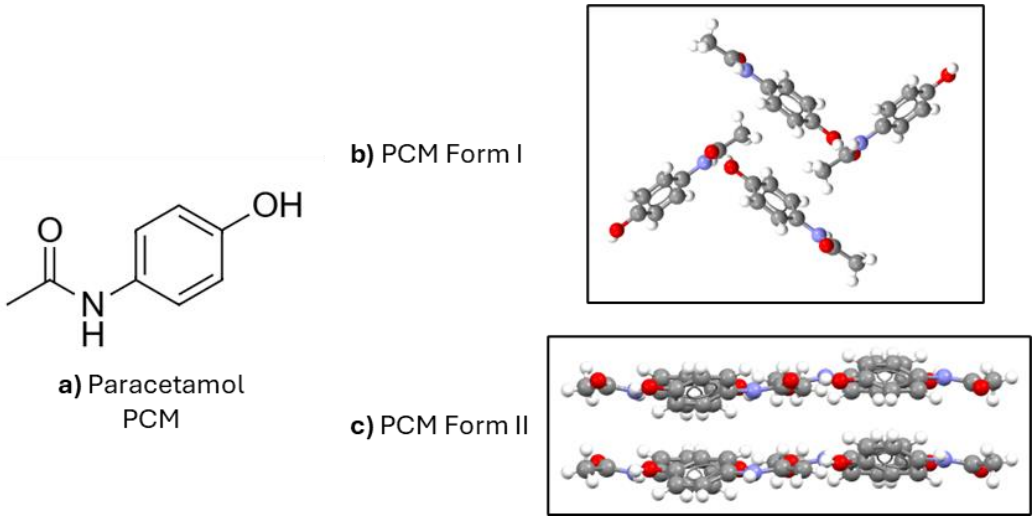

Figure 6.01: a) the molecular structure of paracetamol with the two crystal polymorphic structures taken from the Cambridge Structural Database; b) PCM Form I, refcode HXACAN04, viewed down the a-axis, c) PCM Form II, refcode HXACAN, viewed down the a-axis.[10,11]

Table 6.01: Summary of the crystallographic information for paracetamol polymorphs, taken from the Cambridge Structural Database.[10,11]

PCM polymorph	**Form I**	**Form II**
Refcode	**HXACAN04**	**HXACAN**
Space Group	P 2_1/n	Pcab
Lattice Type	Monoclinic	Orthorhombic
a /Å	7.0939	11.805
b /Å	9.2625	17.164
c /Å	11.657	7.393
α /°	90	90
β /°	97.672	90
γ /°	90	90
Cell Volume /Å^3	759.093	1497.98

PCM is known to often grow a single crystal per slug in KRAIC cooling, segmented flow crystallisation, and was used in the development of the KRAIC-S v1. The KRAIC-S v1 PCM cooling crystallisation used a 254 g/L feedstock of PCM in 60:40 v/v H_2O:IPA binary solvent mixture, cooling from 50 °C to room temperature (~24 °C) to produce single crystals in slugs. The solubility curve for PCM Form I in 60:40 v/v H_2O:IPA is shown below in Figure 6.02. The produced PCM Form I polymorph crystals from KRAIC cooling crystallisation are known to grow two morphologies, rhombohedral and parallelopiped, despite both being the stable PCM Form I.[12]

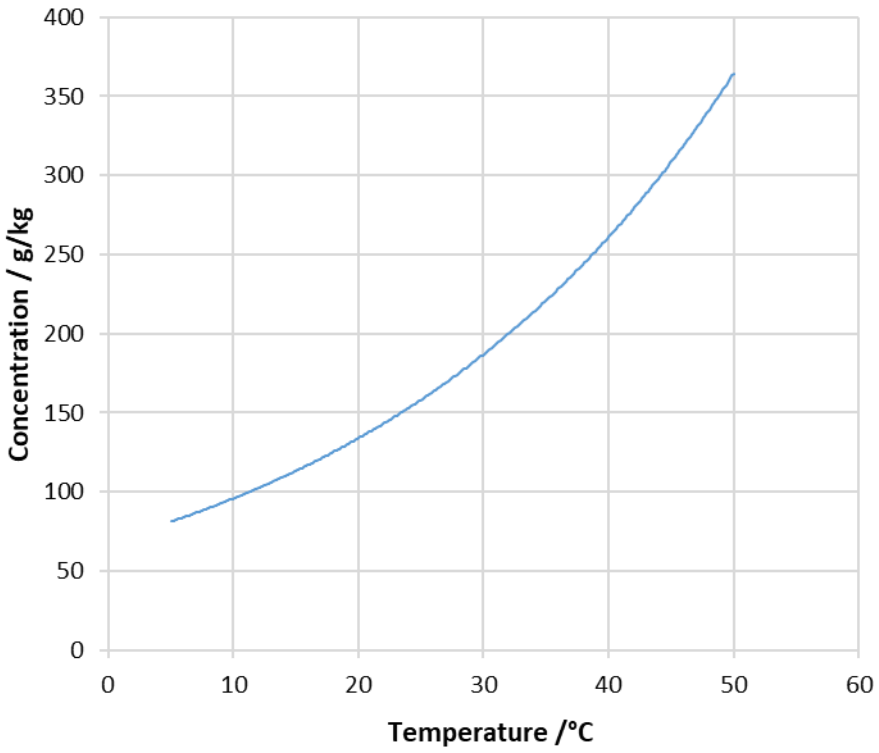

Figure 6.02: Solubility curve for PCM Form I in 60:40 v/v H_2O:IPA, adapted from [9,13].

The KRAIC-S v1 used a shuttle-analysis module and a slug triggering mechanism to translate an X-ray analysis tubing length backwards at the same rate the flow was travelling forwards, to artificially suspend a PCM single crystal in-beam for as prolonged period. The KRAIC-S v1 analysis shuttle is shown below in Figure 6.03. The slug triggering mechanism, introduced in Chapter 5 with the KRAIC-T, uses a laser-photodiode pair as a segmented flow monitor prior to the X-ray analysis FEP tubing length of 60 mm. Python scripting monitors the segmented flow and is controlled through a user threshold that corresponds to the rear-edge of the slug where the crystals typically reside; the threshold value triggers the translation stage movement backwards for crystal suspension in the X-ray beam during X-ray data acquisition.

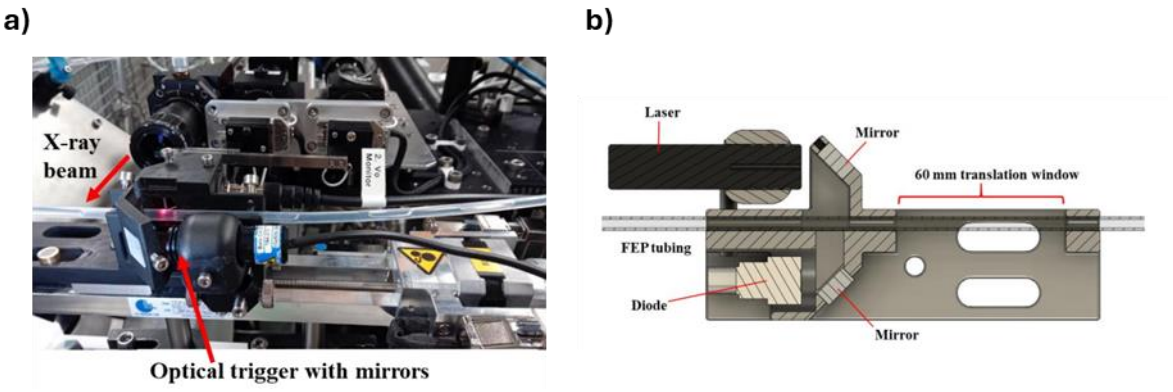

Figure 6.03: a) image of the KRAIC-S v1 analysis shuttle in the sample collection position in EH2 Beamline I19, and b) CAD drawing of the analysis module with the 60 mm translation window. Figure adapted from [13].

The slug triggering Python control script triggers the X-ray shutter, detector capture, on-axis camera video capture, and stage movement for the data acquisition methodology. The laser-photodiode pair are situated before the X-ray analysis point creating a delay from the triggering point to the X-ray analysis point. The script calculates the delay based on the set laser-photodiode to X-ray beam point with the set stage translation speed. The delay ensures the mechanism moves the slug in-beam from which the photodiode readout triggered with the threshold value. The factors required to optimise the slug triggering data acquisition method are:

- User threshold level
- Diode to X-ray analysis point delay
- Translation stage speed to match the segmented flow rate
- Vertical stage targeting height for crystal position in tubing

With segmented flow crystallisation, tubing length equates to crystallisation time, and so X-ray diffraction at different tubing lengths probes different points along the crystallisation process for a time-resolved style of analysis. Two crystalliser lengths were studied for PCM crystallisation in the KRAIC-S v1: 6.7 m and 8.7 m for crystallisation times of 8:12 min and 10:54 min respectively. The key drawback of the analysis shuttle KRAIC-S v1 was the inability to easily change between X-ray analysis lengths: to change the analysis point required pulling the tubing through the shuttle to the desired analysis point and rearranging the other tubing lengths in EH2.

The slug triggering mechanism enabled prolonged data capture (4.2 s) for a total flow rate of 6.2 mL/min for single, rotating crystals in-beam. The crystals were reported to be stable in-beam for datasets collected during optimised conditions. 60 datasets in total were collected, 16 datasets at the 6.7 m position and 44 datasets at the 8.7 m crystalliser length. One in twenty (5%) slug triggering collections resulted in successful beam hit of a crystal. The data processing technique for the KRAIC-S v1 data used the following methodology in DIALS:[6,13]

1. **Importing**: importing the frame and fixing the instrument model.
2. **Spot finding**: extraction of diffraction spots from dataset frames.

3. **Indexing:** indexing of reflections using a reference unit cell. KRAIC-S v1 used the creep indexing technique: an individual frame is indexed to determine the orientation of the crystal, the next frame is assumed to be related by a small rotation, aiding in the refinement of successive frames for the whole dataset.
4. **Refining**: Final crystal model unit cell from the indexed reflections. This step also produces a scan-vary orientation parameter plot to calculate the rotation values for the crystal in-beam.
5. **Integration:** measuring the intensity of diffraction spots on frames.
6. **Scaling:** Dataset is scaled, producing the merging statistics for the single dataset.
7. **Merging:** All processed datasets are merged, producing the final merged dataset and merging statistics.
8. **Exporting and structure solution:** production of SHELX input and hkl files, with structure solution in Olex2.[14,15]

All datasets with diffraction did not process fully, with a 50% success rate of dataset processing. Datasets can fail due to too few reflections to process in the indexing, refinement and integration stages. Due to each dataset containing limited data, the instrument model, input unit cell and space group is constrained.

The crystals collected at the shorter crystallisation time (6.7 m) were generally smaller with crystal rotation analysis calculating an average compound rotation of ~25 °; the highest rotation recorded for a single dataset was 58.6 °. The datasets collected at the 8.7 m crystalliser length were larger crystals resulting in an average compound rotation of ~10 °, with the highest rotation for a single dataset at 33.4 °. The smaller crystals also rotate faster in segmented flow, with the higher rotation datasets producing a large wedge of reciprocal space for a single dataset with 7 % for a 6.7 m example dataset and 2 % for data obtained at the 8.7 m crystalliser length. The best 13 datasets from the 8.7 m sample collection length were merged with the merging statistics shown below in Table 6.02.

Table 6.02: Merging statistics from the 13 best datasets of PCM from the 8.7 m analysis point acquired with the KRAIC-S v1 analysis shuttle

Total Reflections	2138
Unique reflections	936
Completeness (%)	56.8
Mean I/σ (I)	7.37
Min D	0.8004
Max D	7.3619
R int	0.1859

The merged datasets produced an overall 56.8 % completeness with 0.8 Å restraints. The solved paracetamol structure is shown in Figure 6.04. The asymmetric structure is of poor quality and is not at a publishable level.

However, it shows that the technique has potential as a serial crystallography methodology, requiring further study and optimisation.

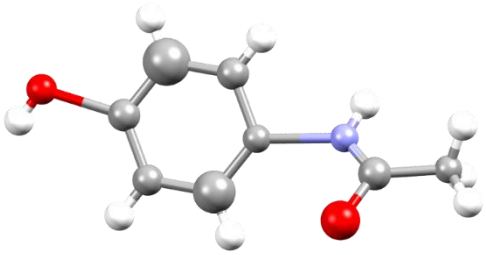

Figure 6.04: Image of the Form I PCM structure solved in Olex2.[14]Structure solved from the merged 13 best datasets from 8.7 m crystalliser length acquired with the shuttle analysis KRAIC-S v1. Atoms are shown by C – grey, O – red, N – blue, and H – white.

The main aims of this project are to develop an integrated crystalliser design to easily change between crystalliser lengths for analysis and to improve data acquisition with an increased X-ray acquisition window length, attempting to obtain a greater completeness from a single crystal. Sections 6.2 and 6.3 of this chapter features the development of a 3D printed KRAIC-S v2 prototype design with a two column arrangement similar to the KRAIC-D and KRAIC-T systems. The crystalliser design was assessed through commissioning beamtime on Beamline I19 in Experimental Hutch 2 (EH2) with the crystallisation of paracetamol to compare to the previous analysis shuttle KRAIC-S v1. Following results from the commissioning of the prototype KRAIC-S v2, an updated KRAIC-S v3 was developed, discussed in Section 6.4. The KRAIC-S v3 design was used for further beamtimes, including beamtime on the non-photochemical laser induced nucleation of potassium chloride in segmented flow, discussed in Chapter 7.

6.2 – KRAIC-S v2 design

The design aims for the crystalliser were to improve the ease-of-use of the system, particularly with changing the X-ray analysis point and arrangement of the tubing in the hutch, whilst ensuring that the slug triggering data capture mechanism is not compromised. To fit in the limited space for sample environments in EH2 Beamline I19, a compact two-columned KRAIC-S v2 was designed in CAD. The design featured main column pieces and X-ray window support posts, shown below in Figure 6.05.

The slug triggering translation stage used was the same as used for the KRAIC-S v1, a motorised screw drive linear stage with a 15 mm/s maximum translation speed and a 0.5 s acceleration time to velocity. The KRAIC-S v2 main body pieces were designed to be attached directly to the slug triggering translation stage. The design was developed to use 3D printing as the manufacturing technique to test the two column design. The KRAIC-S v2 design assembled on the stage with the beamline apparatus is shown below in Figure 6.06.

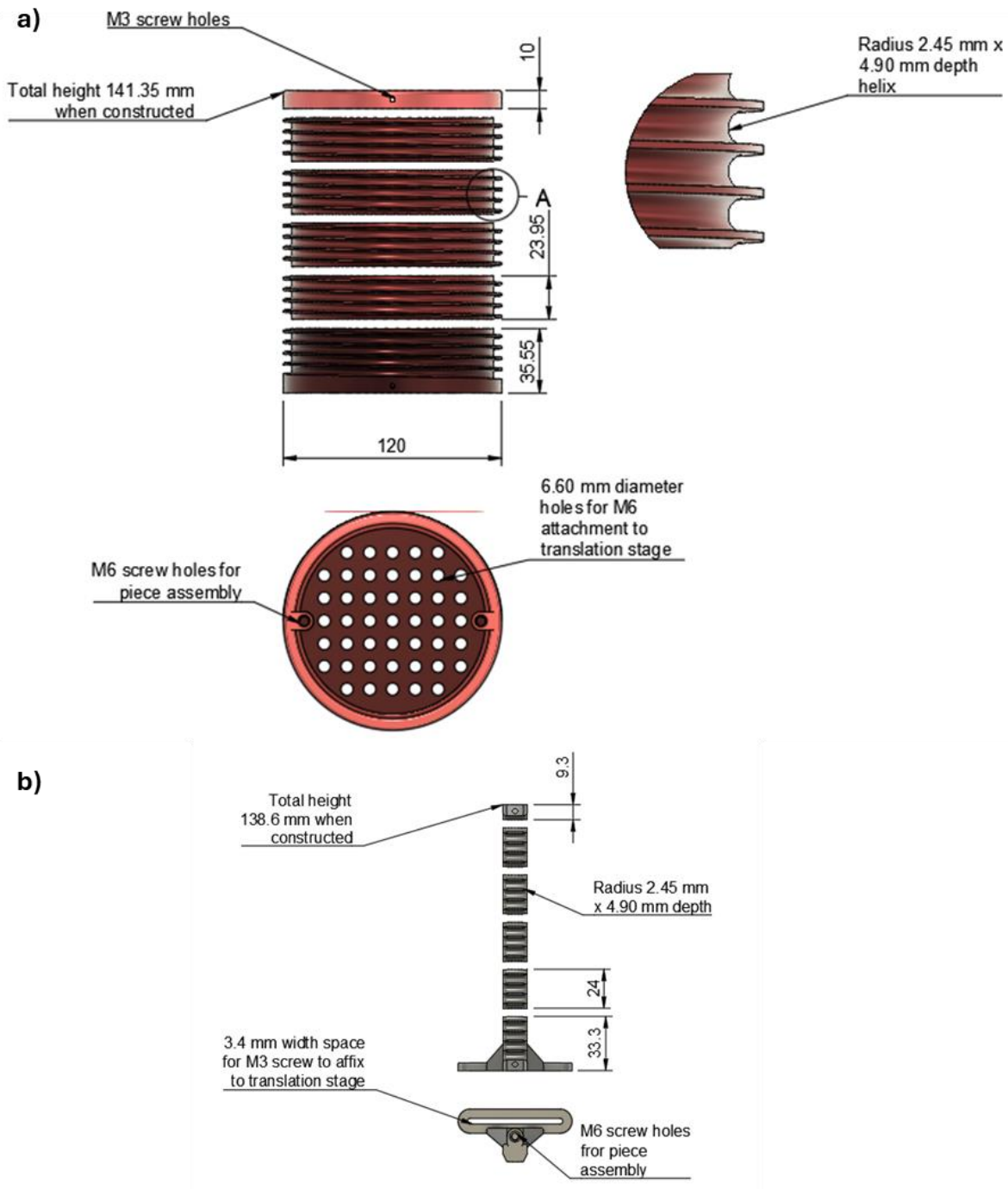

Figure 6.05: CAD drawings of a) KRAIC-S v2 column pieces with inset helix tubing guiding path with front and top view, and b) KRAIC-S v2 X-ray support posts with straight inset tubing guiding paths. Measurements displayed in mm units. Design is modular to enable 3D printing and designed to be constructed with M6 screws. Tubing held in place using post supports screwed into M3 screw holes in the column and X-ray window support posts.

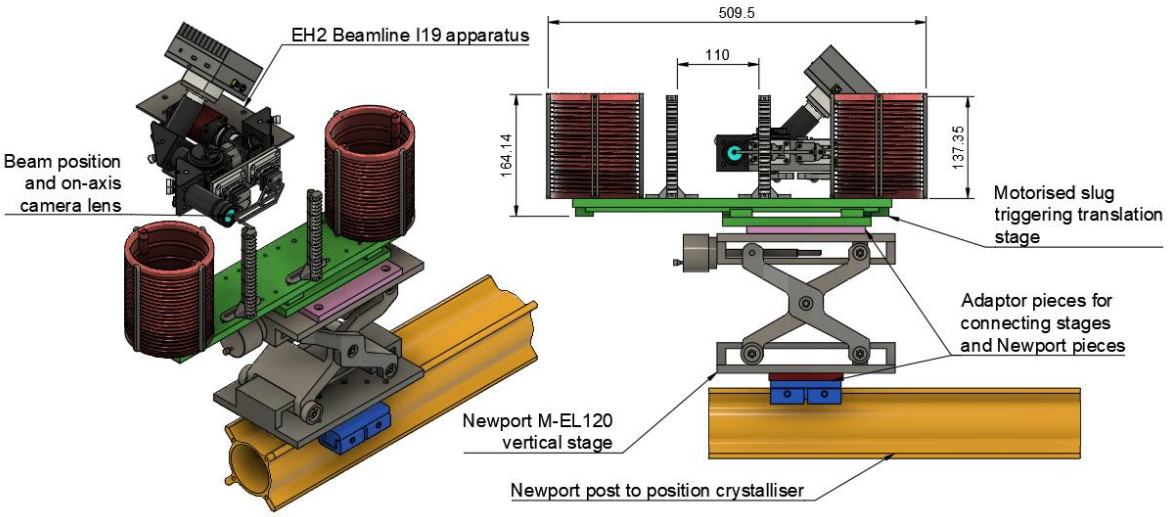

Figure 6.06: CAD drawing of the full KRAIC-S v2 design and assembly in EH2 I19 with beamline apparatus from front on and side view. Measurements displayed in mm.

The crystalliser layout was designed so every loop of tubing around the main body pieces has an X-ray analysis length every ~ 50 cm along the length of the crystalliser for a total of 20 analysis windows. The length of the X-ray analysis windows was increased to 110 mm from the 60 mm used previously for the KRAIC-S v1. Given the limited space in the hutch this was the maximum X-way analysis length achievable. Despite the compact size of the crystalliser, 13 m of 1/8" ID FEP tubing fits on the column design, with 1 m lengths of tubing for the inlet and outlet pieces for a total of ~15 m continuous length of 1/8" ID FEP tubing. To translate between the X-ray windows, the motorised translation stage is attached to a vertical translation stage, a Newport M-EL 120 lab jack. The vertical translation stage has a 120 mm travel range, covering the majority of the 124.9 mm height of the X-ray window analysis region. The Newport vertical stage is manual only, enabling 4.2 µm adjustments to the crystalliser height to target crystal position.

The KRAIC-S v2 main body pieces were stereolithography resin 3D printed with the Formlabs Form2 using Black Resin V4. Black resin was chosen to provide contrast to growing crystals: with the KRAIC-T system (Chapter 5) it was found to be challenging to identify crystals in slugs due to the poor contrast of small, pale crystals with the reflective aluminium surface. The fully printed 3D printed KRAIC-S v2 assembled on the translation stage is shown below in Figure 6.07. The offset X-ray window regions were required to maximise X-ray translation window length in-beam, limited by the beamline goniometer position to the left of the crystalliser system.

Figure 6.07: Images of the assembled KRAIC-S v2 on the translation stage with a) front on view, b) top down view, and c) view of top-down X-ray analysis region with bowing tubing on every return loop.

The crystalliser tubing was held in position with post supports screwed into the 3D printed crystalliser body pieces. However, the screw threads did not print precisely, requiring tapping of the screw holes. Due to the relatively brittle crystalliser material, two of the tapped screw holes were stripped of thread during the construction process. The stripped screw holes were replaced with alternative tapped plastic material, glued into a bore hole. The post supports could not tightly hold the tubing enough in the X-ray analysis region for every other X-ray window, shown in Figure 6.07c. The bowing of the X-ray windows for the return flow direction was due to the curved tubing input and output of the return X-ray windows causing increased force on the tubing as it approaches the bending radius limit of 19.05 mm. The bowing of the tubing in the X-ray windows would cause unacceptable additional deviation in the sample-to-detector distance. Consequently, the return X-ray windows were not used for the commissioning beamtime discussed in the following section: the resulting 10 X-ray window positions along the continual tubing length is summarised below in Table 6.03.

Table 6.03: Summary of position on crystalliser against length of crystalliser continuous tubing in metres, with cumulative residence time recorded for flow conditions discussed in Section 6.3 for a total flow rate of 6.20 mL/min.

Position on crystalliser	X-ray window length along crystalliser tubing /m	Residence time / mm:ss
X1	1.0	01:12
X2	2.5	03:07
X3	3.9	05:04
X4	5.4	07:01
X5	6.9	08:57
X6	8.3	10:53
X7	9.8	12:49
X8	11.2	14:45
X9	12.7	16:40
X10	14.2	18:35
Outlet	15.2	21:35

The original KRAIC-S v1 used a 635 nm Class 2 laser aimed through the crystalliser tubing with a photodiode sensitive to X-rays used to detect the laser signal. The X-ray sensitive photodiode had issues with signal detection accuracy, particularly in distinguishing peaks and troughs in the readout plots due to a high level of background noise and limited sensitivity of the photodiode. Testing of the slug triggering for the KRAIC-T on Beamline I11 (Chapter 5) used an Thorlabs SM1PD1A, which is responsive to a broader range of visible light (350 – 1100 nm). This wider spectral response allowed for better detection of the laser light, reducing background noise, and improving the accuracy of the signal detection. Fine-tuned laser and photodiode positioning, previously shown in Figure 5.19, improved the distinction between solution (peaks) and gas bubbles (troughs) in the photodiode readout. The KRAIC-T testing found that slug triggering could be achieved at increased laser-to-tubing and tubing-to-photodiode distances; this increased separation enabling the slug triggering apparatus to be mounted separately from the translating part of the crystalliser, enabling movement between analysis points on the crystalliser. The KRAIC-S v2 design makes use of these developments to the understanding of the slug triggering mechanism, using a separately mounted laser-photodiode pair enabling access to the ten X-ray windows.

6.3 – KRAIC-S v2 commissioning experiments

6.3.1 – Experimental

The KRAIC-S v2 was commissioned using flow crystallisation of PCM during beamtime at Beamline I19. The KRAIC-S v2 was set up in Beamline I19 Experimental Hutch 2 as described in Section 6.2 with the motorised slug triggering translation stage, manual vertical translation stage for X-ray window

modification and targeting, and with slug triggering laser-diode aligned at the X-ray windows, shown below in Figure 6.08.

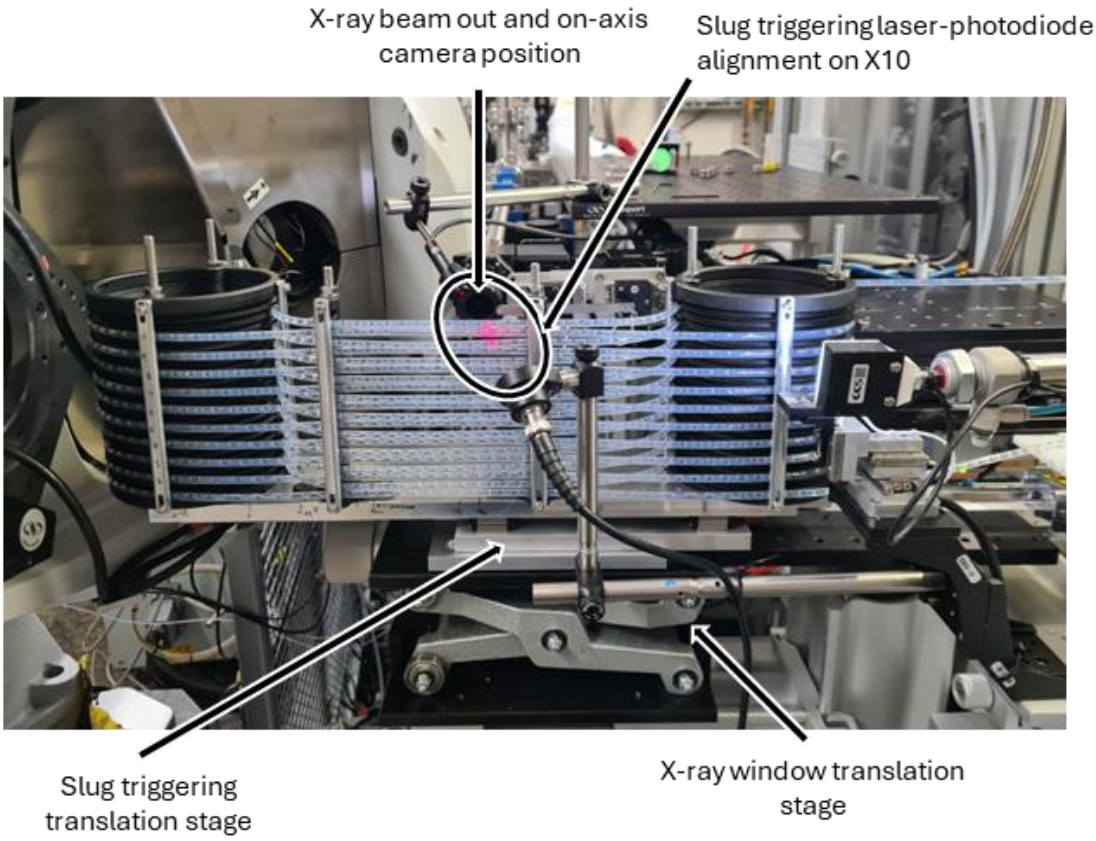

Figure 6.08: Annotated image of the KRAIC-S v2 installed on the I19 beamline in EH2. Annotations show key features of slug triggering laser-photodiode alignment and motorised translation stage, and manual translation stage for changing X-ray windows or changing alignment for crystal targeting.

The schematic for the KRAIC-S v2 set up during PCM cooling crystallisation experiments is shown below in Figure 6.09. Three undersaturated feedstocks of PCM dissolved in 60:40 v/v deionised water:IPA (H_2O:IPA) at 50 °C were used during beamtime at 250 g/L, 260 g/L, and 265 g/L. The flow rates for the nitrogen mass flow controller and Galden carrier fluid were 2.50 mL/min and 1.00 mL/min respectively. The KRAIC-S v2 used a dilution stream of H_2O:IPA solvent mixture with varied dilution and solution flow rate ratios to modify resultant PCM concentrations, shown in Table 6.04. The total solution flow rate was 2.70 mL/min with an overall segmented flow rate of 6.20 mL/min. The 6.20 mL/min total flow rate resulted in a recorded residence time of 21:40 min and crystallisation times of 12:50 min and 18:36 min for X-ray analysis windows (Xs) of X7 and X10 respectively.

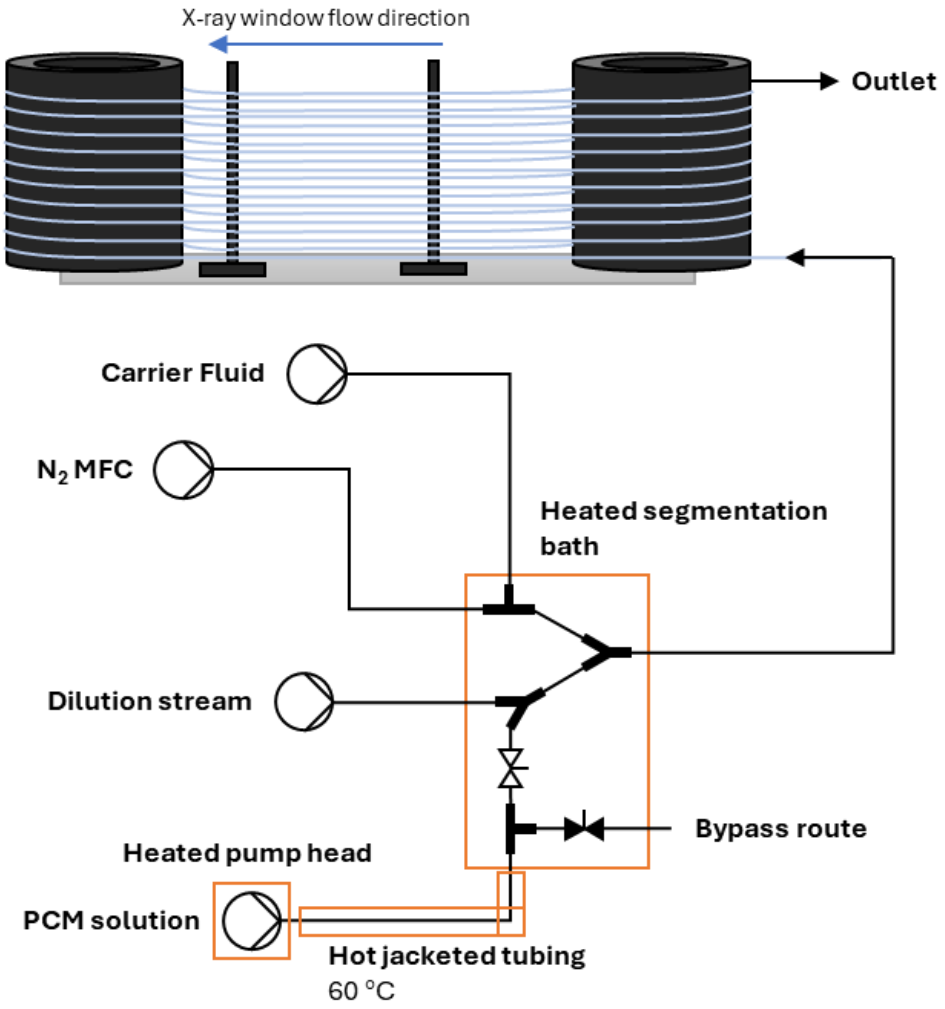

Figure 6.09: Schematic of KRAIC-S v2 conditions for segmented flow crystallisation of PCM during beamtime on I19. Schematic shows segmented flow mode, reverse stopcock valves status bypassed PCM flow to waste.

Table 6.04: Summary of Flow rates for varied PCM concentrations during flow crystallisation of PCM during commissioning experiments in the KRAIC-S v2.

		Flow rates /mL/min		
Crystallisation run name	**PCM feedstock concentration / g/L**	**Solution**	**Dilution**	**Diluted PCM concentration / g/L**
PCM1	250	2.65	0.05	245.4
PCM2	250	2.70	0	250.0
PCM3	260	2.65	0.05	255.2
PCM4	260	2.70	0	260.0
PCM5	265	2.65	0.05	260.1
PCM6	265	2.63	0.07	258.1
PCM7	265	2.63	0.07	258.1
PCM8	265	2.64	0.06	259.1
PCM9	265	2.64	0.06	259.1

The Vapourtec SF-10 pump used for the solution stream used a PID (Proportional Integral Derivative) controller with heating pads fitted to the pump head to heat the solution in the pump, temperatures shown in Table 6.05. The system used jacketed transfer tubing temperature controlled with a heated water circulator set to 60 °C to prevent blockages in the transfer tubing prior to segmentation in the heated segmentation water bath. The bypass route, shown in Figure 6.09, used stopcocks to divert solution flow in the event of a blockage in the main crystalliser body, to not leave stagnant PCM solution to crystallise in the transfer tubing or pump head: in bypass mode the dilution stream flow was increased to the total solution flow rate of 2.70 mL/min to maintain flow rate in the crystalliser body and to dissolve any encrusted crystals.

Table 6.05: Summary of temperature conditions for PCM crystallisation runs during commissioning beamtime of the KRAIC-S v2.

Crystallisation run name	Segmentation bath temperature / °C	Pump head temperature reading / °C
PCM1	40	-
PCM2	40	-
PCM3	45	39.1
PCM4	50	39.4
PCM5	50	39.5
PCM6	50	39.9
PCM7	50	39.5
PCM8	50	40
PCM9	50	40

A temperature profile was collected for PCM8 conditions with a FLIR E5 thermal imaging camera for a room temperature of 21.5 °C, temperature profile shown below in Figure 6.10. The temperature profile is assumed to be equivalent for differing PCM conditions, except for different starting temperatures due to segmentation bath temperatures. Final PCM temperatures were monitored and found to be equivalent for conditions PCM1 and PCM3.

PCM1+2 conditions at resultant concentrations of 245.4 g/L and 250.0 g/L resulted in no crystallisation after 2-3 residence times despite the solution being supersaturated at the final ~23 °C crystalliser temperature reached by around 700 cm of crystalliser length at the X5 position (Supersaturation, $S \approx 1.64 – 1.67$ based on Equation 1.01 and Figure 6.02). This demonstrates the effect seen for segmented flow conditions where the lack of the solid interface for nucleation causes a widening of the metastable zone width resulting in a supersaturated but not labile PCM solution.

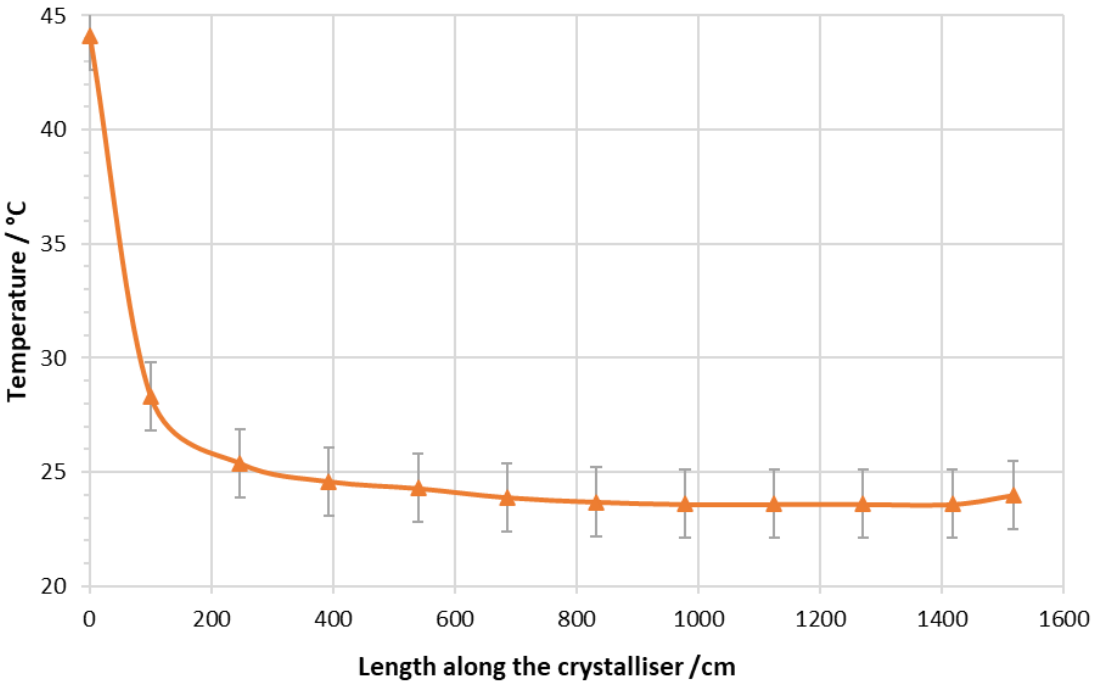

Figure 6.10: Temperature profile for PCM8 flow crystallisation conditions in the KRAIC-S v2 during commissioning beamtime. Error bars for ± 1.5 °C calculated FLIR E5 error.

PCM3 flow conditions (255.2 g/L, S ≈ 1.70) produced crystallisation of PCM but ended in a blockage in the segmentation bath after 6 residence times, resulting in the increased 50 °C segmentation bath temperature for PCM4-9 conditions. Data collection was attempted for PCM3 at the X10 position, but no diffraction was achieved due to unoptimized vertical stage targeting and slug triggering settings. The PCM4 crystallisation conditions (260.0 g/L, S ≈ 1.73) resulted in crystallisation and ran for 4 residence times. The crystallisation run ended due to no PCM solution remaining. Similarly, no data was collected due to unoptimized slug triggering settings triggering in the gas bubble or front edge of slugs, missing the crystals.

PCM5 conditions (260.1 g/L, S ≈ 1.74) ran for 5.5 residence times, ending due to a severe blockage in the KRAIC-S v2 main tubing. Slug triggering data acquisitions acquired data from X10 during PCM flow before blockage. The sizable blockage could not be unblocked through pumping pure solvent through the system or applied pressure with a syringe. As a result, the KRAIC-S v2 main body was removed from the hutch for the system to replace the tubing. Due to the attachment of the KRAIC-S v2 main body to the stage equipment, it could not be detached and removes from EH2 without the removal of the main body and the slug triggering translation stage and vertical stages and disassembly of the slug triggering laser-photodiode. During PCM5 it was noted that the slug triggering often triggered from the front boundary of the slug as well as the rear boundary: the slug triggering threshold does not distinguish between the increasing photodiode value corresponding to the front edge and decreasing value corresponding to the rear edge. The script was adapted for subsequent PCM6-9 crystallisation runs to require a high level be achieved before triggering from a decreasing threshold value, illustrated in Figure 6.11.

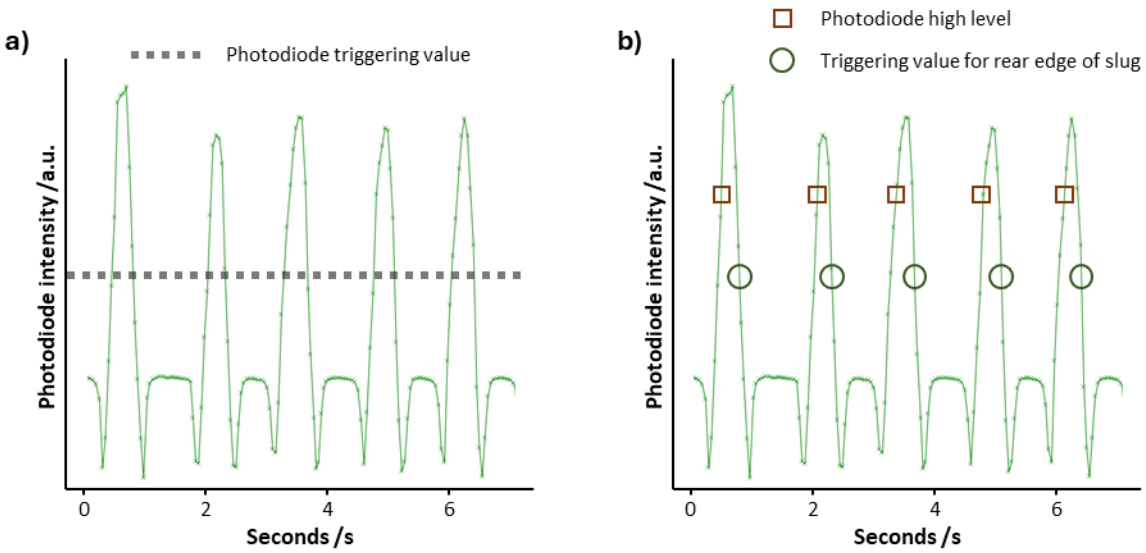

Figure 6.11: Photodiode readout plots during segmented flow in the KRAIC-S v2. a) represents the photodiode triggering value cutoff that triggers from both the front and rear of slugs. b) shows the adjusted high level triggering mode where a set high level must be reached before triggering at the triggering value, ensuring rear edge only.

The system was reassembled and re-aligned for PCM6 and run with a lower PCM concentrations with PCM6+7; 258.1 g/L, S ≈ 1.72, and PCM8+9; 259.1 g/L, S ≈ 1.73. The decrease in saturation aimed to decrease the propensity of the system to block. Furthermore, the crystallisation run time was limited to a maximum 4-5 residence times for all subsequent PCM runs. X-ray data was collected for PCM6-9 at X10 position and for a short period of time at the X7 position during PCM9. The X7 and X10 analysis points were at crystallisation times of 12:49 min and 18:35 min respectively. Slug triggering collections used an average motor speed of 11.1 mm/s for prolonged acquisition times of 7.3 s, achieving 73 diffraction frames per collection dataset.

6.3.2 – Results and Discussion

On average 7.3 s continual acquisitions were achieved in the KRAIC-S v2, an increase from the 4.2 s previously with the KRAIC-S v1 for equivalent 6.2 mL/min total flow rate. The increased acquisition time was due to the increased usable X-ray window length of 100 mm in the X-ray analysis window, an increase on the 60 mm used originally. All the full 110 mm window length in the KRAIC-S v2 design was not accessible due to ~10 mm of length used by the laser-photodiode alignment region.

The KRAIC-S v2 system enabled an improved ease-of-use of the crystalliser sample environment system due to the vertical stage allowing easy modification of the X-ray targeting for different analysis lengths and arrangement of tubing in the experimental hutch. However, slight modifications to the X-ray analysis height to improve the targeting of crystals in the slug was time consuming due to the manual translation stage: when necessary, it required the opening of the experimental hutch and movement of the detector out of sample collection

position to modify, causing a loss of 5 min of active beam each time. The 4.2 µm sensitivity of the vertical stage was suitable for the minor modifications required to target the crystals.

The considerable blockage during PCM5 required the KRAIC-S v2 to have the tubing replaced. However, the connections of the crystalliser main body to translation and vertical stages required the full system to be removed from the beamline from the Newport post. The entire system needed to be disassembled, rethreaded, reassembled, and laser-photodiode to be realigned taking a total of 2.5 hours, a considerable loss of active beamtime.

Overall, 63 datasets containing diffraction were acquired: 2 datasets at the X7 position and 61 datasets at the X10 position. Of the acquired datasets, only 35 datasets (56%) passed the DIALS data processing procedure, following the same processing methodology as the previous KRAIC-S work.[13] The processing procedure is summarised in the Appendix A6. The 56% pass rate of datasets through the processing workflow follows the trend from the previous KRAIC-S v1 data, with only 50% of collections able to pass the processing technique. A total of 21 datasets resulted merging statistics with acceptable R_{int} values to proceed with processing. The processing procedure fails if there are too few reflections captured for a dataset, or if the crystal is moving significantly in-beam with large variation of the sample-to-detector distance which cannot be processed with the DIALS technique. The on-axis camera videos were inspected for the presence of crystals in the slug and assessed against the number of datasets containing diffraction, shown below in Table 6.06.

*Table 6.06: Summary of slug triggering collections for PCM conditions with number of on-axis videos containing diffraction, and number of diffraction datasets achieved. *PCM6 on-axis camera view was not recorded due to equipment failure: this was fixed for subsequent conditions.*

Crystallisation run identifier	Number of slug triggering collections	Crystal visible in slug from on-axis camera view	Datasets containing diffraction	Processed datasets
PCM5	138	55	34	27
PCM6	107	n/a*	10	2
PCM7	126	15	9	5
PCM8	94	10	5	1
PCM9 - X7	66	2	2	0
PCM9 - X10	57	5	3	0

For PCM5 conditions, the percentage of datasets where a crystal or crystals were visible for a slug triggering collection on the on-axis camera view was 40%. This is an increase of the 3% of slugs containing crystals found for the KRAIC-S v1. PCM5 had 25% of slug triggering collections containing diffraction, compared to 5% for the KRAIC-S v1. However, this was due to the increased concentration of PCM5 (260.1 g/L compared to 254 g/L) and increased crystallisation time at the X10 analysis point of 18:35 min compared to 10:54 min for the 8.7 m KRAIC-S v1 data. The high concentration caused increased

nucleation of PCM with the increased crystallisation time growing larger crystals of PCM, improving the overall hit rate.

For the lower concentrations of 258.1 g/L for PCM6-9, the number of slug triggering collection visually showing a crystal in the slug decreased significantly to between 9 – 12 % at the X10 analysis point. The slug triggering mechanism appeared to trigger from the rear edge of the slug more frequently due to the changes of the control script, however this cannot be fully assessed against the PCM5 hit rates due to the lower level of crystallisation in PCM6-9 conditions. The X7 analysis point (12:49 min crystallisation time) for PCM9 showed a 3% appearance of collections showing a crystal on the video. This is approximately equivalent to the KRAIC-S v1 conditions with 254 g/L and 3% of slugs containing crystals. This demonstrates that the slug triggering efficacy is maintained with the KRAIC-S v2 design, and the and the increased laser-tubing-photodiode distances have not been detrimental to the data acquisition methodology.

The larger size of the PCM crystals resulted in only small rotations of the PCM crystals in-beam, resulting in an average completeness of the 21 best processed datasets of 2.3 % for the processed datasets collected at the X10 position (14.2 m crystalliser length and 18:35 min crystallisation time). The average completeness for datasets collected with the KRAIC-S v1 were 7 % and 2 % for datasets collected at 6.7 m (8:12 min crystallisation time) and 8.7 m (10:54 min crystallisation time) respectively. The overall completeness is equivalent to the 8.7 m KRAIC-S v1 analysis point despite the increased slug triggering collection time.

When the best 21 datasets were merged to attempt to solve the crystal structure it resulted in considerably low completeness (29 %) and unique reflections (787) and could not be solved to find the PCM structure. When using all the 35 datasets, the completeness appears higher (71.6 %), however the other processing statistics, such as I/sigma and R_{int} values are significantly worse. The 35 merged datasets also do not result in a structural solution. A comparison of the KRAIC-S v1 13 merged dataset, and KRAIC-S v2 21 and 35 datasets are shown in Table 6.07.

Table 6.07: Merging statistics for the original KRAIC-S v1 data, and KRAIC-S v2 data with all merged 35 datasets, and 21 datasets where R int < 0.100.

	KRAIC-S v1 - 13 datasets	**KRAIC-S v2 - 35 datasets**	**KRAIC-S v2 - 21 datasets**
Total Reflections	2138	6791	1896
Unique reflections	936	1653	787
Completeness (%)	56.8	71.6	29.1
Mean I/σ (I)	7.37	4	31.9
Min D	0.8004	0.74	0.7
Max D	7.3619	9.62	6.56
R int	0.1859	0.682	0.108

To understand the poor completeness of the merged datasets for the KRAIC-S v2 the crystal rotation was calculated from the scan varying parameters using the technique developed for the KRAIC-S v1.[13] Furthermore, the on-axis video captures were inspected and compared the KRAIC-S v1 frames, shown in Figure 6.12. The small PCM crystals from the 8.7 m analysis point in the KRAIC-S v1 rotate in-beam with an average ~10 ° compound rotation due to the turbulence in the segmented flow, still image from a slug triggering collection video shown in Figure 6.12a. Whilst only 2% completeness was obtained from the 4.2 s acquisition, the random orientations of the crystal ensured high completeness overall when merged. For the 21 best datasets of KRAIC-S v2 data, the average compound rotation was calculated to be 15 °, a similar value to the ~10 ° for KRAIC-S v1 8.7 m datasets. However, the large PCM crystals sit at the bottom of the slug and minimally move, providing an average 2.3 % completeness despite the long 7.3 s acquisition. The calculated rotation for morphologies is shown below in Table 6.08. The large crystals in the KRAIC-S v2 data acquisition appear to exhibit a "preferred orientation" in segmented flow, shown in Figure 6.12b, producing a preferred orientation like effect for the SCXRD data. Both morphologies show slightly increased rotation in the a-axis, with minimal rotation in the b and c axis. As such, when the datasets are merged the average completeness is poor and cannot be solved for the PCM structure.

*Table 6.08: Average a-, b-, c-axis, and compound rotation for parallelopiped, rhombohedral crystal. *multi-crystal slugs processed but do not know the exact crystal morphology hit.*

		Rotation / °			
Morphology	**Datasets**	**a-axis**	**b-axis**	**c-axis**	**Compound**
Rhombohedral platelet	5	6.77	2.57	1.72	11.06
Parallelopiped	6	10.60	2.87	3.12	14.22
Multi-crystal slug*	10	9.17	3.95	3.31	16.42

Offline face-indexing of the two morphologies of PCM produced in flow showed that the rhombohedral and parallelopiped morphologies share the same growth faces but have different aspect ratios and thicknesses of the crystals (Figure 6.12c). The parallelopiped and rhombohedral crystals both were positioned at the bottom of the slugs but in slightly different "preferred orientations". The two main orientations of the PCM morphologies in-beam (Figure 6.12d) likely improved the overall completeness present due to the two crystal orientations present.

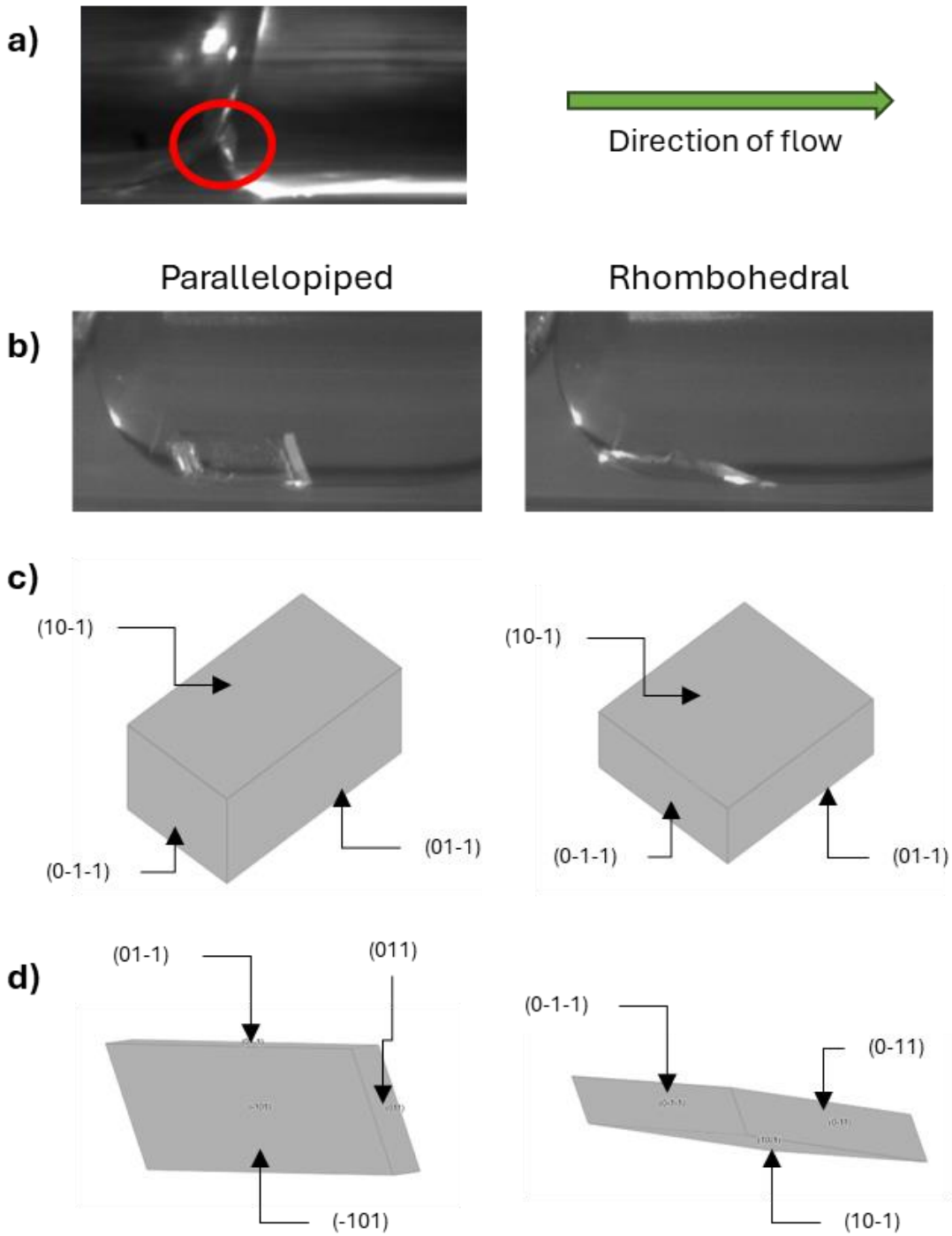

Figure 6.12: a) video still image of a small PCM crystal in flow in the KRAIC-S v1, adapted from [13]. Annotations show circled crystal and direction of flow for KRAIC-S v1 and KRAIC-S v2 images. b) KRAIC-S v2 video still from slug triggering in the KRAIC-S v2 for the two morphologies, parallelopiped and rhombohedral. c) face indexed crystals of the two morphologies displayed in the same orientation, grow faces annotated. d) face indexed crystals of the two morphologies in the beam collection orientations, displaying the different faces present in-beam during data collection.

It was believed prior to the beamtime that despite reduced rotation of the larger crystals and reduced movement of the crystal, that the orientation of the crystals would be random resulting in high completeness from the merged dataset of many individual collections. However, the large crystal sizes show a preferred orientation in the slugs due to localised eddies and low turbulence from the relatively flow overall flow rate. The lack of random rotation for the large

crystals resulted in low overall completeness: this is a serious limitation of the KRAIC-S v2 serial crystallography technique in segmented flow analysis. This limitation was not known prior to this study and is a key finding for future experiments to ensure that data capture is prioritised on crystals with sufficient rotation. The KRAIC-S v2 design with multiple accessible windows should aid with targeting of crystals with the appropriate size and rotation. This limits the scope of time-resolved SCXRD feasible in the system due to the dependence on crystal size for data quality.

The KRAIC-S set-up lends itself to the development of *in situ* morphological analysis given the built in on-axis camera which captures videos during the data acquisition process. Typical process analytical technologies (PAT) with image analysis for morphology and particle size analysis typically have carefully considered analytical windows to achieve distinction between the background and particles for image processing.[16] The videos captured from the KRAIC-S are non-ideal, with the flashing lights in the experimental hutch and the slug triggering laser providing a poor background lighting for image analysis. To test the feasibility of morphological analysis in the KRAIC-S system, 75 PCM still frames from the KRAIC-S v2 beamtime were collated and assigned shape identifiers (rhombohedral platelet, parallelopiped, unidentified shape single crystal, or agglomerate/cluster). In collaboration with Dr Chris Boyle and Dr Javier Cardona at the University of Strathclyde, the training set of 75 images were used to develop a custom deep learning algorithm. The algorithm was then used to identify the shape crystals on 1900 images. The example output of the shape identification algorithm is shown below in Figure 6.13.

The short feasibility test was highly successful in distinguishing between multiple crystals in a slug, a single crystal per slug, and agglomerate shapes despite the light distortion present in the system. The algorithm was adept at identifying crystal presence, as seen for Figure 6.13d where a small unidentified crystal shape is positively identified, despite being difficult to spot with the naked eye. The algorithm was less proficient in distinguishing between rhombohedral or parallelopiped morphology, as seen with the unidentified crystal shapes in Figure 6.13d. However, given the non-ideal sample environment for *in situ* image and small algorithm training set, the successful identification of crystals shows the technique has promise for larger scale studies in the KRAIC-S system.

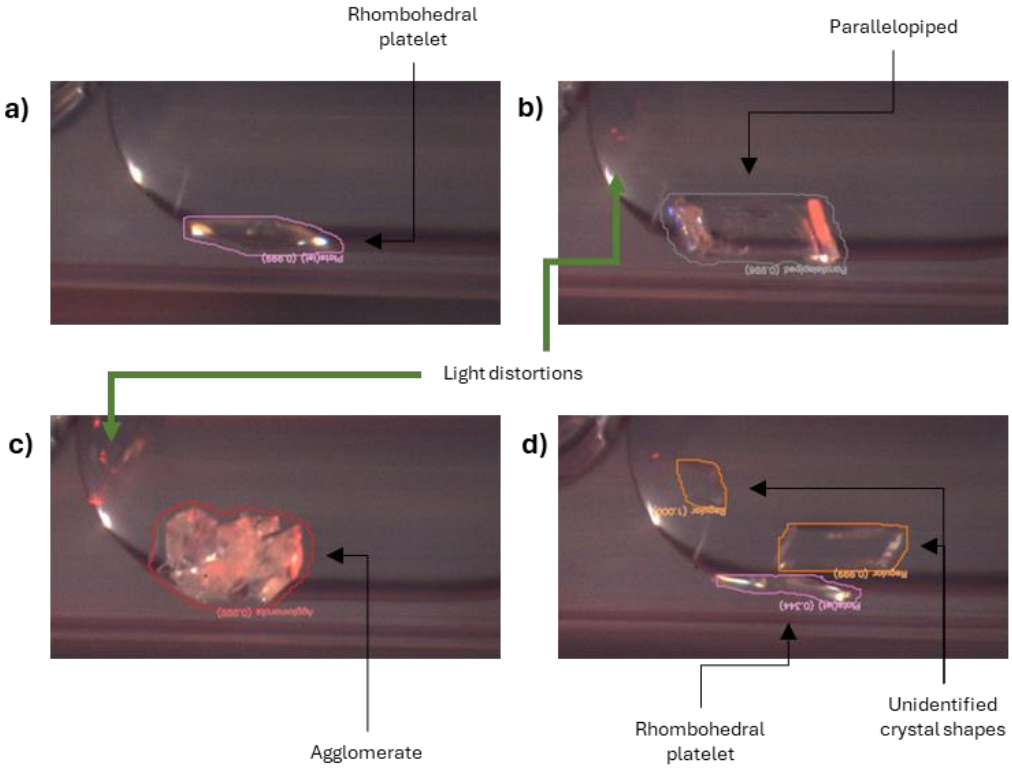

Figure 6.13: Still images from PCM slug triggering acquisitions in the KRAIC-S v2 with deep learning algorithm results from the 75 image training set for a) a rhombohedral platelet crystal, b) a parallelopiped crystal, c) agglomerate PCM crystal cluster, and d) multi crystalline slug with two unidentified morphology crystals and one identified rhombohedral crystal. Key regions of light distortion annotated.

6.4 – KRAIC-S v3 design

The KRAIC-S v2 configuration showed improvements from the initial KRAIC-S analysis shuttle proof-of-principle system with improved ease-of-use of the crystalliser arrangement in the hutch and easy modification of the X-ray window position. However, the KRAIC-S v2 columns and support posts being directly attached to the slug triggering translation stage, and translation stage directly attached to the vertical stage required removal of the full system from the hutch to rethread the tubing during a blockage in PCM5 conditions. This caused the loss of a considerable amount of beamtime and made it clear that the KRAIC-S must allow for easy change of the crystalliser body and main tubing without full disassembly and realignment to ensure efficient beam usage. Whilst the 3D printed design was suitable for testing the new arrangement of tubing for the KRAIC-S v2 system, the material was brittle causing the screw holes to deteriorate first use of the system during the commissioning beamtime. A new design was proposed using a hardwearing, machinable material: black acetal plastic. The columns and support posts were redesigned in CAD by I19 Beamline Technician Jim Hawkins to be machinable, rather than the KRAIC-S v2 design which was tailored to 3D printing. The new KRAIC-S v3 design is shown below in Figure 6.14. The tubing guiding posts were redesigned to be slightly wider to improve the direction of the tubing in the X-ray analysis region to prevent bowing of the tubing.

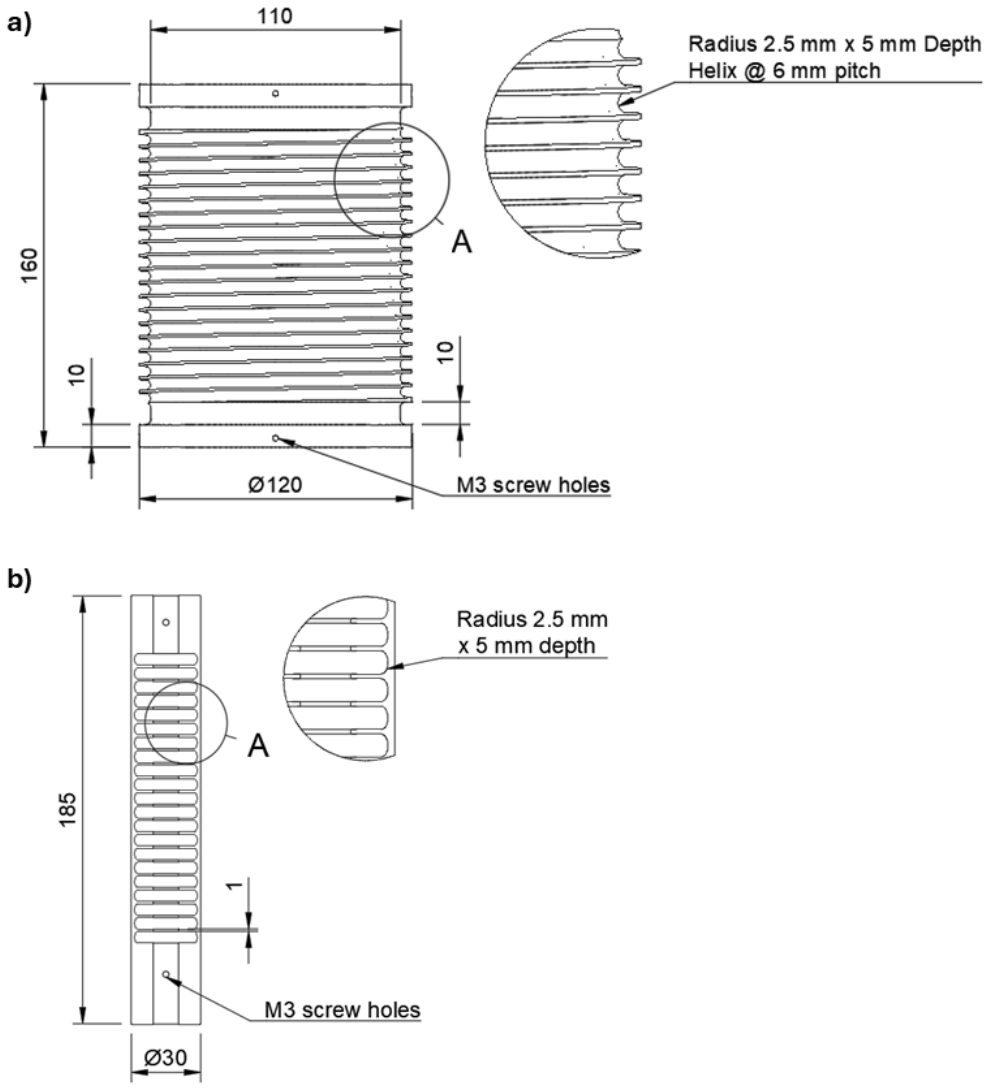

Figure 6.14: CAD drawing of KRAIC-S v3 parts, measurements shown in mm of a) the main column with continually increasing height helix for tubing, and b) X-ray guiding posts for the X-ray windows. Clamp bars for holding tubing in place screw into M3 screw holes in crystalliser.

To account for the unblocking issue caused by the KRAIC-S v2 design, two full crystalliser bodies were made and attached to two removable baseplates. The removable baseplates, made of lightweight aluminium, attach to the slug triggering translation stage through two alignment notches. Therefore, in the event of a blockage, the new KRAIC-S v3 main body can be removed from the data analysis position without also removing the translation stage or vertical stage. As a result, the system should not need realignment of the slug triggering laser-photodiodes if unblocking and rethreading the system is required. The only requirement during unblocking is the replacement of the second main crystalliser body and reattachment to segmentation pieces and endpiece arrangements. The KRAIC-S v3 CAD design and crystalliser set-up in Beamline I19 EH2 is shown below in Figure 6.15. The KRAIC-S v3 when threaded with tubing had no bowing in the X-ray analysis region, enabling X-ray analysis from either flow direction for future experiments.

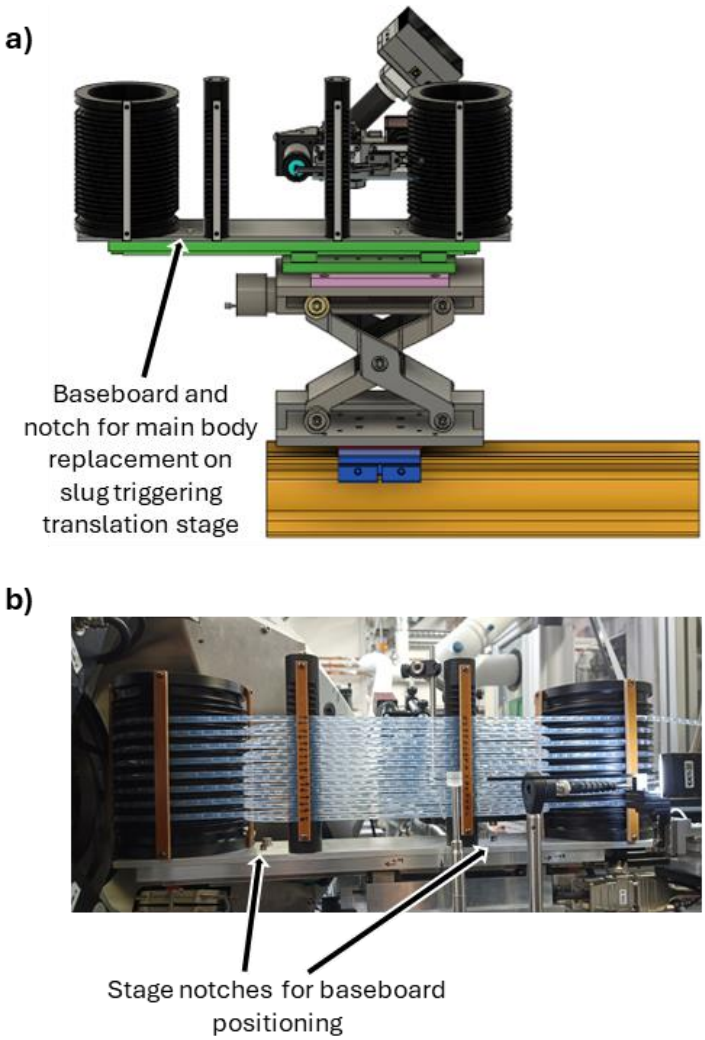

Figure 6.15: a) CAD design of the KRAIC-S v3 with full mounting arrangement, and b) image of the KRAIC-S v3 during beamtime on I19 discussed further in Chapter 7. Annotations show design differences from the KRAIC-S v2, with baseboard and notches for alignment on the slug triggering stage, and sturdy post supports which does not allow for tubing bowing in the X-ray window.

The KRAIC-S v3 is used for the first time during beamtime on I19 for the non-photochemical laser induced nucleation of potassium chloride in segmented flow with *in situ* X-ray diffraction, discussed in Chapter 7. The KRAIC-S v3 has since been used for a beamtime by the author for the development of a dual-imaging camera system for coupling morphology analysis and *in situ* XRD, building on the promising results from the PCM machine learning morphology identification. The development of the dual-imaging system was conducted in collaboration with researchers from the University of Strathclyde, Dr Chris Boyle and Dr Javier Cardona Amengual. The flexible set-up for the KRAIC-S v3 design enabled a modified tubing configuration for the dual imaging system, demonstrating the versatility of the system. The KRAIC-S v3 has been made available for Diamond users and the system has been used for two beamtimes by members of the Robertson group, University of Nottingham; one beamtime required the unblocking of the system and used the secondary KRAIC-S v3 main body to rapidly replace the blocked system, reducing beam downtime to 40 minutes, from the 2.5 hr previously required to fully disassemble, replace the tubing, reassemble and realign the system.

6.5 – Conclusions

The KRAIC-S v2 segmented flow crystalliser for *in situ* single crystal X-ray diffraction was developed based on the work of Dr Lois Wayment and Dr Mark Warren on the initial KRAIC-S v1. The KRAIC-S v2 built on the successes of the initial prototype shuttle analysis module system by developing a fully integrated 3D printed two column design for easy modification of the X-ray analysis length and improved layout of the crystalliser in Beamline I19 experimental hutch. The KRAIC-S v2 layout with increased X-ray analysis window lengths aimed to collect improved data from the *in situ* SCXRD of paracetamol during flow crystallisation.

The cooling crystallisation of paracetamol from 50 °C to ~ 23 °C room temperature was analysed with X-ray diffraction with prolonged 7.3 s continual data acquisition with the 100 mm analysis windows on the KRAIC-S v2, an improvement from the 4.2 s achieved with the 60 mm shuttle analysis length with version 1. The commissioning beamtime with the KRAIC-S v2 achieve 63 datasets with an average of 50 % of the datasets passing the DIALS processing procedure for diffraction spot indexing, refinement, integration, and scaling. The average dataset collected at the crystalliser length of 14.2 m and a crystallisation time of 18:35 min resulted in a 2.3 % completeness of reciprocal space for paracetamol Form I. This equivalent to the 2 % collected at 8.7 m length, 10:54 min crystallisation time for the KRAIC-S v1 data.

Merging of the 21 best datasets in a serial crystallography style technique resulted in a total completeness of only 29.1 %, a significantly lower completeness than the 56.8 % achieved from the best 13 datasets from the prior KRAIC-S v1 work. As a result, the structure of paracetamol could not be solved from the low completeness data. The rotation data and inspection of the data acquisition videos collected from the on-axis camera revealed that the large paracetamol crystals grown at increased crystallisation times resulted in a preferred orientation style effect where each morphology of paracetamol, rhombohedral and parallelopiped, has a preferred orientation in the slug, and therefore minimal orientations were achieved from the crystal movement in beam. This demonstrates that the serial crystallography technique in the KRAIC-S v2 is currently limited to smaller crystals with increased random orientations in beam from turbulent flow, a previously unknown limitation of the technique.

The KRAIC-S system was investigated for it potential *in situ* imaging analysis through feasibility studies with the paracetamol data acquisition videos from the on-axis camera. A training set of 75 images were described with parallelopiped, rhombohedral, unidentified single crystal, and agglomerate identifiers and used to train a deep learning algorithm. The algorithm was then applied to 1900 images of the paracetamol data; the algorithm resulted in highly successful identification of single, multi-crystal, or agglomerate occupancy of slugs. It showed promising results for morphology identification given the small training set of images applied and the non-optimised imaging environment.

The KRAIC-S v2 during commissioning beamtime experienced a severe blockage during PCM5 high concentration (260.1 g/L) paracetamol conditions,

requiring new tubing for the crystalliser. The design of the KRAIC-S v2 and the attachment to the translation and vertical stages required full removal of the system from the beamline, disassembly, and rethreading with new tubing. On reassembly, it also required realignment of the slug triggering laser-photodiode flow rate monitor. Overall, this process resulted in a 2.5 hr downtime during beamtime. From the issues experienced with the KRAIC-S v2 design, an improved crystalliser design was developed, termed the KRAIC-S v3. The KRAIC-S v3, made with a durable black acetal plastic, used the two column layout which was the main advantage of the KRAIC-S v2 system, with analysis points accessible at a 13 m region of the crystalliser length. However, two KRAIC-S v3 bodies were made with a detachable baseplate. As such, any subsequent beamtimes will have access to two threaded KRAIC-S v3 bodies available to easy detach and re-attach during beamtime, maximising beam usage. The KRAIC-S v3 design has been used for non-photochemical laser induced nucleation in flow, discussed in Chapter 7. Furthermore, the KRAIC-S v3 design has been used for the development of a dual-imaging system coupled with *in situ* SCXRD based on the results from the feasibility study conducted with paracetamol data collection videos. The KRAIC-S v3 design has been used for two further beamtimes by users from the Robertson group, University of Nottingham; one beamtime resulted in a blockage in the crystalliser and replacement of the main body, a process which took 40 minutes, a significant reduction in beam downtime. The KRAIC-S v3 design is available for users on I19 for investigation of crystallisation through *in situ* SCXRD with a serial crystallography approach.

6.6 – Future Work

The KRAIC-S serial crystallography technique is currently limited by the size and therefore rotation of crystals during data collection. Future experiments should focus on small crystal sizes to achieve a greater overall completeness of the merged data for structure solution. The easy access to multiple X-ray windows with the vertical translation stage can assist with targeting the appropriate size of crystals. The vertical translation stage could be improved through motorisation and remote operation to enable micro-adjustment of stage height for improved targeting of crystals during data collection. This would maximise beam usage by removing the necessity to enter the hutch and move the detector during data collection, eliminating the 5 min downtime required per manual stage height adjustment. A motorised vertical stage must have a similar 4.2 µm sensitivity for crystal targeting which was a key benefit of the Newport M-EL120 manual lab jack used for the KRAIC-S v2 system.

The rotation of crystals for data collection is currently limited by the 15 mm/s stage translation speed during data collection. A faster motorised stage would enable faster flow rates during segmented flow to induce a greater rotation during turbulent flow in slugs; this would improve the overall completeness of datasets collected and reduce the preferred orientation effect to achieve a great merged completeness overall. A faster flow rate may decrease the overall hit

rate but the benefit of the improved completeness of the wedge datasets would likely outweigh the reduction in datasets collected. The 0.5 s time for acceleration and deceleration with the current stage results in 14 % of the data collection time with incorrect speed matching to the crystal in flow. A faster acceleration for an updated translation stage could also improve the length of slug triggering data collection. However, this should be investigated during future beamtime set up stages to find the maximum acceleration speed that does not disrupt the segmented flow: systems with lower water content have reduced surface tension during segmented flow and may be susceptible to segmented flow collapse during higher speed acceleration.

A significant proportion of beamtime during PCM3+4 conditions were spent optimising the slug triggering mechanism to achieve the suspension of crystals in beam: the stage translation speed matching was a considerable portion of that as the stage speed matching also effects the delay calculated from the slug triggering laser-diode point to the X-ray beam centre to initiate data collection. A flow rate sensor developed by A. Harvie *et al.* used offset light emitting diode (LED)-photodiode sensor pairs to monitor segmented flow, using the offset of the LED-photodiode pairs to calculate the localised flow rate.[17] The sensor can also monitor the uniformity of flow, notifying the user if the flow uniformity deviates, such as in the event of a blockage in the system disrupting the flow rate of segmented flow or uniformity of slug and air bubble lengths. This concept could be adapted to the KRAIC-S system, using a flow rate sensor immediately before the X-ray window data collection point to read in the flow rate and required translation speed into the slug triggering control scripts to automatically set the speed, to improve the efficiency of data collection.

To improve the capabilities of the KRAIC-S system, a dual-imaging addition to the KRAIC-S v3 design has been trialled during beamtime at I19. The dual-imaging system aimed to couple morphological analysis with *in situ* SCXRD analysis based on the promising output of feasibility studies with the morphological analysis of PCM video stills from the KRAIC-S v2 experiments. The dual camera view provides side-on and top-down views during particles during slug triggering in flow, providing greater morphological information to potentially create a 3D projection of the particles, like seen in literature examples with 3D morphology modelling used to identify polymorphs during crystallisation.[18] The dual-camera system was commissioning using glass beads in flow with slug triggering and used for the first time during the anti-solvent flow crystallisation of DL-methionine, a model system with polymorphic-dependent morphologies (beamtime reference CY33055-1). Figure 6.16 shows the dual-imaging set up of the KRAIC-S v3 and resulting video stills from the commissioning of the system with glass beads and first beamtime with DL-methionine with on-axis camera view and top-down camera view.

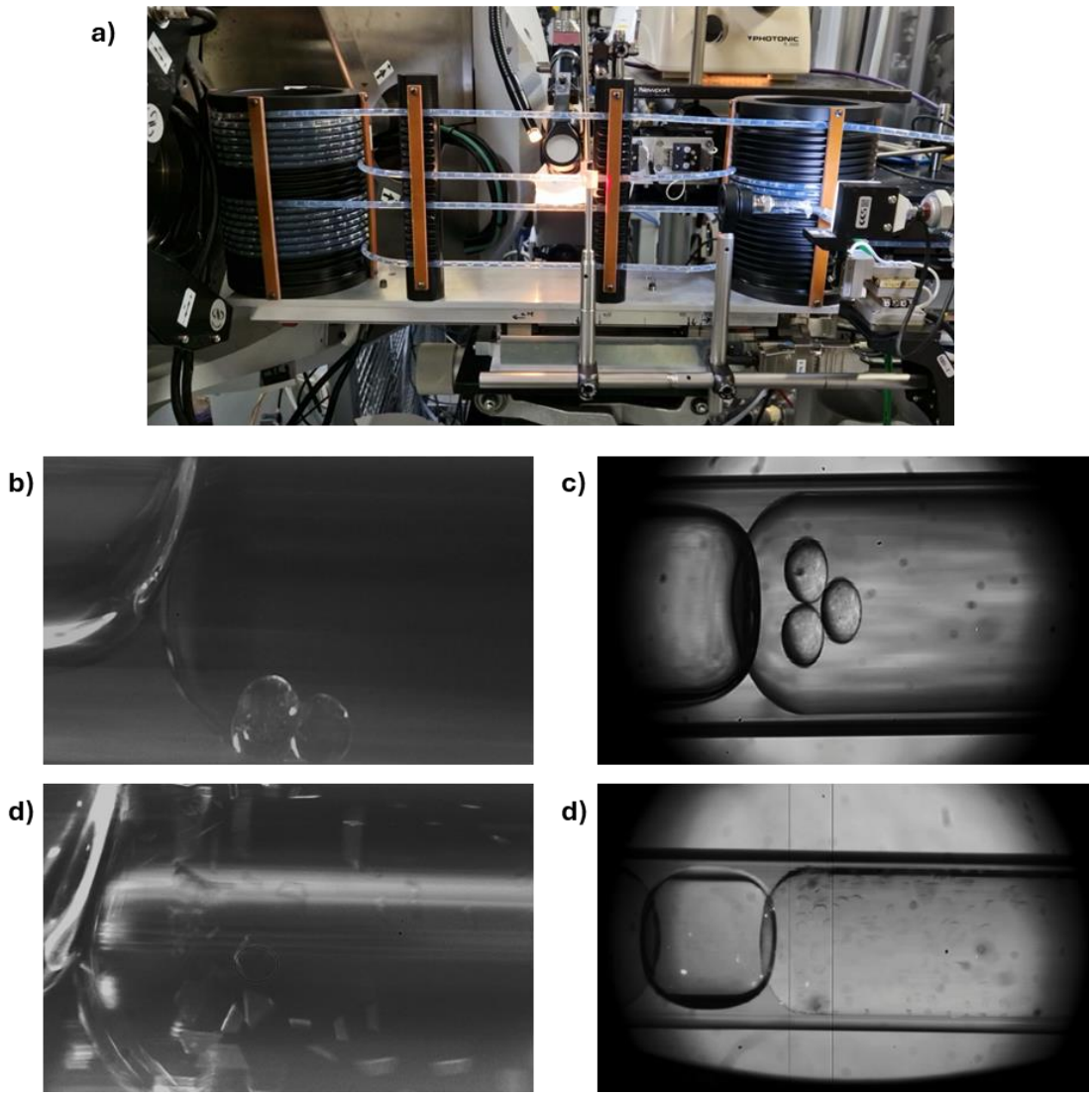

Figure 6.16: Image of the KRAIC-S v3 with dual imaging camera set up during DL-methionine beamtime. b) on-axis camera view of glass beads during dual-camera commissioning with c) the top-down dual-camera view. d) on-axis camera view of DL-methionine crystals with d) the top-down camera view during acquisition of the DL-methionine crystals.

The DL-methionine experiment focussed on smaller crystals with a greater movement and random rotation of crystals in-beam, however, featured multiple crystals in a slug with potentially multiple crystals in-beam during data collection, as seem by the slug triggering video stills shown in Figure 6.16d+e. The beamtime aims to investigate the limits of the DIALS processing to see if the data can be processed with multiple single crystals in beam and see if the data can be used to identify the DL-methionine polymorph(s) present. Furthermore, if the data is able to process, does data from a multi-crystalline slugs improve the overall completeness of the diffraction data to achieve structural solution of the DL-methionine polymorph(s).

Experiments with the KRAIC-S have been limited to systems where only a few single crystals per slug are crystallised: the maximum ~ 3 crystals seen per slug for paracetamol. These conditions limit the scope of the KRAIC-S system as they are not representative of the majority of crystallisation behaviours of small

molecule systems. The DIALS processing techniques were developed for protein serial crystallography where a slurry of protein crystals is injected in-beam: the DIALS processing extracts the strongest matching spots to the reference space group and unit cell and may be able to process systems where multiple crystals are in beam. This work aims to investigate if it is possible to use this technique for small molecules where there are potentially 2 to 3 crystals in beam, which would potentially have significant benefits on the applicability of the technique and data quality extracted. Future work includes the advancement of the deep learning algorithm to identify crystals in slugs and the morphology of the DL-methionine crystals from the video collections with collaborators at the University of Strathclyde. The data processing is ongoing and therefore is out of scope for this thesis. The KRAIC-S v3 system has been made available for Diamond Light Source users, with beamtime planned for users from the Robertson group, University of Nottingham.

6.7 – References

1. Zhao, F. Z. *et al.* A guide to sample delivery systems for serial crystallography. *FEBS Journal* **286**, 4402–4417 (2019).
2. Oghbaey, S. *et al.* Fixed target combined with spectral mapping: Approaching 100% hit rates for serial crystallography. *Acta Cryst.* **72**, 944–955 (2016).
3. Sonker, M. *et al.* Electrically stimulated droplet injector for reduced sample consumption in serial crystallography. *Biophysical Reports* **2**, 1–15 (2022).
4. Stubbs, J. *et al.* Droplet microfluidics for time-resolved serial crystallography. *IUCrJ* **11**, 237–248 (2024).
5. Morris, R. H. *et al.* Non-Contact Universal Sample Presentation for Room Temperature Macromolecular Crystallography Using Acoustic Levitation. *Sci Rep* **9**, (2019).
6. Winter, G. *et al.* DIALS as a toolkit. *Protein Science* **31**, 232–250 (2022).
7. Christensen, J. *et al.* Radiation damage in small-molecule crystallography: Fact not fiction. *IUCrJ* **6**, 703–713 (2019).
8. Chapman, H. N. Fourth-generation light sources. *IUCrJ* vol. 10 246–247 Preprint at https://doi.org/10.1107/S2052252523003585 (2023).
9. Agnew, L. R. *et al.* Continuous Crystallization of Paracetamol (Acetaminophen) Form II: Selective Access to a Metastable Solid Form. *Cryst Growth Des* **17**, 2418–2427 (2017).
10. Haisa, M., Kashino, S. & Maeda, H. The orthorhombic form of p-hydroxyacetanilide. *Acta Crystallogr* **B30**, 2510–2512 (1974).
11. Naumov, D. Y., Vasilchenko, M. A. & Howard, J. A. K. The Monoclinic Form of Acetaminophen at 150K. *Acta Crystallogr* **C54**, 653–655 (1998).
12. Robertson, K., Seeberger Bc, P. H. & Gilmore, K. Rapid optimisation of API crystallisation in a segmented flow reactor with a continuous, variable temperature gradient. *React. Chem. Eng.* **8**, 77–83 (2023).
13. Wayment, L. E. Continuous flow for materials synthesis, assembly and crystallisation at Diamond: discovery and delivery of high value materials. (University of Bath, Bath, 2020).
14. Dolomanov, O. V., Bourhis, L. J., Gildea, R. J., Howard, J. A. K. & Puschmann, H. OLEX2: A complete structure solution, refinement and analysis program. *J Appl Crystallogr* **42**, 339–341 (2009).
15. Sheldrick, G. M. A short history of SHELX. *Acta Crystallogr* **A64**, 112–122 (2008).

16. Vancleef, A., Maes, D., Van Gerven, T., Thomassen, L. C. J. & Braeken, L. Flow-through microscopy and image analysis for crystallization processes. *Chem Eng Sci* **248**, (2022).

17. Harvie, A. J. & deMello, J. C. Optical determination of flow-rate and flow-uniformity in segmented flows. *Chemical Engineering Journal* **394**, (2020).

18. Huo, Y. *et al*. In Situ Measurement of 3D Crystal Size Distribution by Double-View Image Analysis with Case Study on L-Glutamic Acid Crystallization. *Ind. Eng. Chem. Res.* **59**, 4646–4658 (2020).

Chapter 7 – Non-photochemical laser-induced nucleation of potassium chloride in segmented flow with *in situ* XRD on Beamline I19

The non-photochemical laser induced nucleation research presented in this chapter in collaboration with Dr Karen Robertson and Dr Mark Warren, Senior Beamline Scientist at Beamline I19, as well as Dr Andrew Alexander, University of Edinburgh, Dr Martin Ward, University of Strathclyde, and Dr Gabriel Karras, Beamline Scientist (Laser) at Diamond Light Source.

7.1 – Introduction

Non-photochemical laser-induced nucleation (NPLIN) is a process where short laser pulses in the visible and near-infrared range trigger the formation of nuclei in a metastable solution.[1] The use of NPLIN to control nucleation offers a unique method to investigate nucleation mechanisms and crystal growth due to the ability to trigger nucleation remotely in closed systems. NPLIN can produce the nucleation and crystal growth of crystalline phases from the supersaturated, metastable solution.

The KRAIC-S system is a segmented flow crystalliser for *in situ* SCXRD analysis on Beamline I19. The SCXRD analysis uses a serial crystallography style approach to merge datasets collected from multiple single crystals for crystal structure solution. The KRAIC-S v3 design, developed in Chapter 6, uses a two column crystalliser design with multiple accessible X-ray windows to probe different points along the crystallisation process with *in situ* XRD.

The aim of this work was to establish NPLIN in segmented flow coupled with *in situ* XRD analysis for phase identification. NPLIN demonstrates polymorphic control in certain circumstances, however, the mechanism of nucleation phase control is not well understood. The KRAIC-S system offers an *in situ* XRD sample environment with repeatable volumes of supersaturated solution for the study of NPLIN mechanics. Furthermore, KRAIC crystallisations generally have a broadening of the metastable zone width (MSZW) for supersaturated solutions from the lack of a solid interface in segmented flow, limiting primary heterogeneous nucleation. This broad MSZW results in far higher supersaturations required to produce nucleation than typical batch experiments. The ability of NPLIN to nucleate metastable, but not labile supersaturated solutions could widen the scope of KRAIC studies to probe areas of the polymorphic landscape previously inaccessible with typical KRAIC conditions. Coupling non-photochemical laser-induced nucleation with crystallisation in the KRAIC-S with *in situ* XRD would improve the capabilities of the system for the study of the crystallisation landscape of polymorphic, solvate, and co-crystalline materials. The aim of this work was to achieve NPLIN in segmented flow with *in situ* XRD analysis to enable future experimentation on

nucleation mechanisms or polymorphic crystal landscape studies in a high-throughput, repeatable manner.

NPLIN has been observed for the laser-induced nucleation of carbon dioxide bubbles from aqueous solution, however, it is more commonly studied for the nucleation of solid particles from a metastable solution.[2] NPLIN is a form of primary nucleation, but the potential mechanisms for NPLIN are not well understood. Key observations from systems that undergo NPLIN are:[1]

- A minimum threshold pulsed laser power density is required for the NPLIN of a system
- Probability of nucleation increases as supersaturation of the solution increases
- There is a linear dependence of probability of nucleation and laser power density, above the minimum threshold
- A single, nanosecond pulse can induce nucleation, including the nucleation of a single crystal in some cases
- The polarisation of the laser (linearly or circularly polarised) can affect NPLIN, in terms of polymorphic form and efficacy of NPLIN for a system
- Nanoparticle impurities can increase the probability of NPLIN

Systems that undergo NPLIN require have different threshold peak power densities required to induce nucleation. Peak power density is a measure of a pulsed laser power, the calculation for a Gaussian beam profile is shown below in Equation 7.01. Supersaturation is another key property in the discussion of NPLIN, as the solutions are in the metastable supersaturated state, but not labile with no spontaneous nucleation. The equation to calculate supersaturation (S) has been shown previously in Chapter 1 and is repeated here for clarity (Equation 1.01).

Equation 7.01: Calculation of pulsed laser peak power density from laser average power, repetition rate, pulse duration, and beam area. Multiplication by 2 to convert from a flat-top beam to a Gaussian beam profile.

$$Peak\ power\ density\ (W/cm^2) = \frac{Average\ power\ (W)}{Repetition\ rate\ (Hz) \times Pulse\ duration\ (s) \times Beam\ area\ (cm^2)} \times 2$$

Equation 1.01: For calculation of supersaturation ratio, S, using concentration, c, and current solubility, c, based on conditions present (temperature).*

$$S = \frac{c}{c^*}$$

The two main nucleation mechanisms, introduced in Chapter 1, are classical nucleation theory (CNT) and two-step nucleation theory (TSN). Key differences of the two theories are that TSN proposed the formation of dense, liquid-like amorphous clusters which require an energy barrier to be overcome to rearrange into viable crystalline clusters for crystal growth. Whereas CNT proposes a solid cluster formation with the likelihood of nucleation and crystal

growth dependent on the size of clusters formed. The mechanism for non-photochemical laser-induced nucleation is not well understood; initially the optical Kerr effect (OKE) with the TSN model appeared to explain the phenomenon. The optical Kerr mechanism explains that non-crystalline clusters formed with the TSN could interact with the electric field of the pulse laser light inducing a dipole moment to align molecules in the field direction to assist with rearrangement into viable crystalline nuclei.[3,4] However, NPLIN has been observed for systems with no preferred axis for alignment with the laser for the OKE mechanism, such as potassium chloride. The mechanism proposed by Alexander *et al.,* collaborator on this project, is for Isotropic Dielectric Polarisation (IDP) based on CNT or TSN wherein the pulse laser causes a dielectric polarisation of the solid/amorphous cluster, lowering the free energy and promoting nucleation kinetics.[5] Both OKE and IDP do not explain the observations that the NPLIN effect is inhibited with the filtering and removal of impurities in solution. This observation lead to the proposal of a third nanoparticle heating mechanism, where impurities heat on laser irradiation causing a vapour cavity; various mechanisms nanoparticle heating causing nucleation are proposed including vapour cavity collapse inducing nucleation, or the liquid interface of the cavity providing regions of higher supersaturation to promote nucleation.[1] Polarisation of the NPLIN laser, with circularly polarised or linearly polarised light, has been shown to influence the polymorphic form nucleated, with examples of polarisation switching for glycine, sulfathiazole, carbamazepine, and L-histidine.[6–9] The mechanism for polymorphic control through polarisation switching is not well understood with supersaturation, temperature, and solvent choice impacting the nucleated phase. There are debates surrounding if polarisation switching is indeed an NPLIN phenomena or controlled by the other factors.[10]

Overall, the study of NPLIN is twofold with experiments attempting to rationalise the phenomenon through mechanism studies, and the use of NPLIN to externally control and induce nucleation in a closed sample environment. The ability to induce nucleation in atypical environments has implications for the study of pharmaceutical materials, for example, for the discovery of new crystal forms and understanding the crystal landscape of novel materials.

For the development of the NPLIN KRAIC-S system, it was proposed to use potassium chloride (KCl), a model material in the NPLIN field. KCl NPLIN crystallisation has been well-studied in batch, levitator, and microfluidic crystallisation environments.[11–13] KCl is a monomorphic crystal system with a rock salt-like crystal structure with the $Fm\bar{3}m$ space group and cubic unit cell: a, b, c = 6.28 Å, α, β, γ = 90 °, and volume = 248.12 Å^3.[14,15] Whilst ideally the system is aims to achieve phase resolution of polymorphic systems, the complexity of the proposed experiment necessities reduced variables for this initial NPLIN in segmented flow study. KCl is known to produce a single crystal per laser pulse at low laser powers, providing they are above a threshold power density. The threshold power density required for KCl NPLIN varies based on the irradiated volume, sample container, supersaturation, temperature, and laser wavelength. A summary of literature data of KCl NPLIN examples are shown

below in Table 7.01. KCl slightly favours a 532 nm pulsed laser wavelength, with reduced power threshold required for crystal NPLIN. KCl NPLIN has been demonstrated to occur for a general range of supersaturation ratio, S = 1.05 – 1.10 for glass vial experiments. The solubility data for aqueous KCl is shown below in Figure 7.01 and used for supersaturation ratio calculations.

Table 7.01: Literature data on the NPLIN of potassium chloride with varying laser and KCl solution conditions.

Sample environment	Laser wavelength /nm	KCl sample volume /cm^3	Supersaturation, S	Temperature /°C	Threshold laser power / MW/cm^2
Electric field levitator[13]	532	8×10^{-9}	1.20	21 - 23	3
Glass vials[11]	532	3.8	1.06	23	5.6
	1064	3.8	1.06	23	8.2
	1064	3.8	1.06	33	7.7

Sample container may influence the threshold intensity through slight absorption of the laser pulse requiring higher laser powers, however, NPLIN of KCl in a levitated droplet, essentially a "containerless" environment, found a threshold intensity of 3 MW/cm^2 for S = 1.20; NPLIN was not observed below S = 1.20. This demonstrated the relationship between the sample environment, resulting sample volume, and supersaturation on the required threshold power density for NPLIN. Decreased sample volume irradiated decreases the number of nucleation events, requiring a higher supersaturation for NPLIN to occur.[5] The NPLIN mechanism initially proposed for KCl was the IDP mechanism, however, IDP does not account for the fact that filtering of the KCl solution reduces the nucleation probability: this provides strong evidence for the nanoparticle heating mechanism.[1,5]

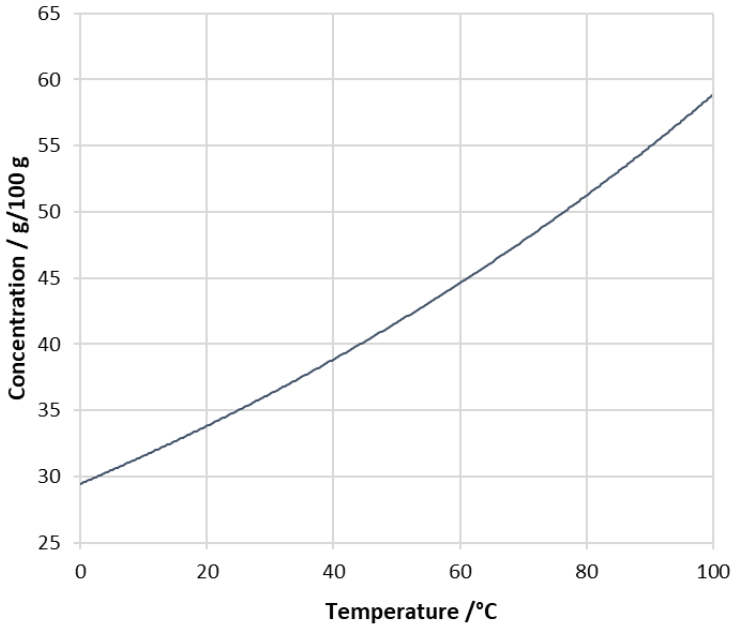

Figure 7.01: Solubility data for aqueous potassium chloride solubility, adapted from [16].

To achieve NPLIN in segmented flow, initial feasibility experiments (Section 7.2) were conducted to test if NPLIN could be achieved with the nano-second pulsed Nd:YAG laser available for beamtime on Beamline I19. These feasibility studies included initial testing with varied KCl supersaturated solutions in glass vials and FEP laser tubing damage studies to see if NPLIN can be achieved without modifying the KRAIC-S apparatus. Further feasibility studies induced NPLIN of KCl in the KRAIC-S FEP tubing, to see what threshold laser power and supersaturation is required in the different "sample container" present. Furthermore, the slug triggering mechanism was adapted to achieve a single laser pulse per slug, with the aim of inducing single crystals of KCl per slug for a serial crystallography style analysis. Section 7.3 discusses the beamtime of KCl segmented flow with laser pulse triggering of a single crystal per slug (~ 55 µL solution volume per slug) with *in situ* XRD.

7.2 – NPLIN feasibility studies

7.2.1 – Batch KCl NPLIN

The initial feasibility studies aimed to define the conditions of KCl NPLIN to occur with the Class IV laser available for experiments on Beamline I19. The laser used was the Opotek Vibrant He 355 II Nd:YAG laser. The pulsed laser has a 10 Hz repetition rate and used the 532 nm wavelength marginally preferred for KCl NPLIN. The pulse duration for the laser an approximate 10 ns and will be used for subsequent calculations in this chapter. The KCl NPLIN tests used the highest supersaturation previously tested in glass vials, S = 1.10 for a room temperature in the hutch of 23 °C, a concentration 38.59 g/100 g. The KCl solution was prepared at 40 °C and left to cool to room temperature. The solution was loaded into in 1.75 mL volume glass vials. A camera was set up to monitor the crystal growth of KCl as a result of the laser pulses. A summary of conditions trialled is shown below in Table 7.02.

Table 7.02: Summary of laser pulse characteristics for KCl NPLIN testing with the Vibrant laser, and if NPLIN occurred. Gaussian peak power density calculated with Equation 7.01.

Identifier	Laser average power /mW	Approximate beam diameter /mm	Gaussian peak power density / MW/cm^2	NPLIN occurred?
KCl_vial1	110	3.8	19.4	Yes
KCl_vial2	50	3.8	8.8	Yes
KCl_vial3	180	3.8	31.7	Yes

All three test conditions trialled with the Vibrant laser produced NPLIN, which was expected given the high peak power densities used, above the threshold peak power density of 5.6 MW/cm^2 used in literature for similar experimental conditions. Still images from the video collections post-laser pulse are shown in Figure 7.02. The still images show the first crystals visible by eye on the video at timeframes between 7 – 11 s after laser pulse. The nucleation and crystal

growth are rapid, significantly faster than the minutes to yield visible crystals in the similar literature study. This is attributed to the high supersaturation and higher peak power density used for these tests. In the first 120 s after the laser pulse, block morphologies of KCl are grown, however, large needle-like crystals are observed to grow in the KCl_vial2-3 examples post 120 s. More needle crystals are present in the KCl_vial2 example (8.8 MW/cm^2 power density) compared to KCl_vial3 (31.7 MW/cm^2 power density) . This may be due to the higher laser pulse power inducing a greater number of nucleation events, which grow into the block morphology. Any secondary nucleation that occurs grows a needle shape morphology, with the lower pulse power having a greater number of secondary nucleation events. However, this cannot be concluded from three tests and would require further experimental investigation.

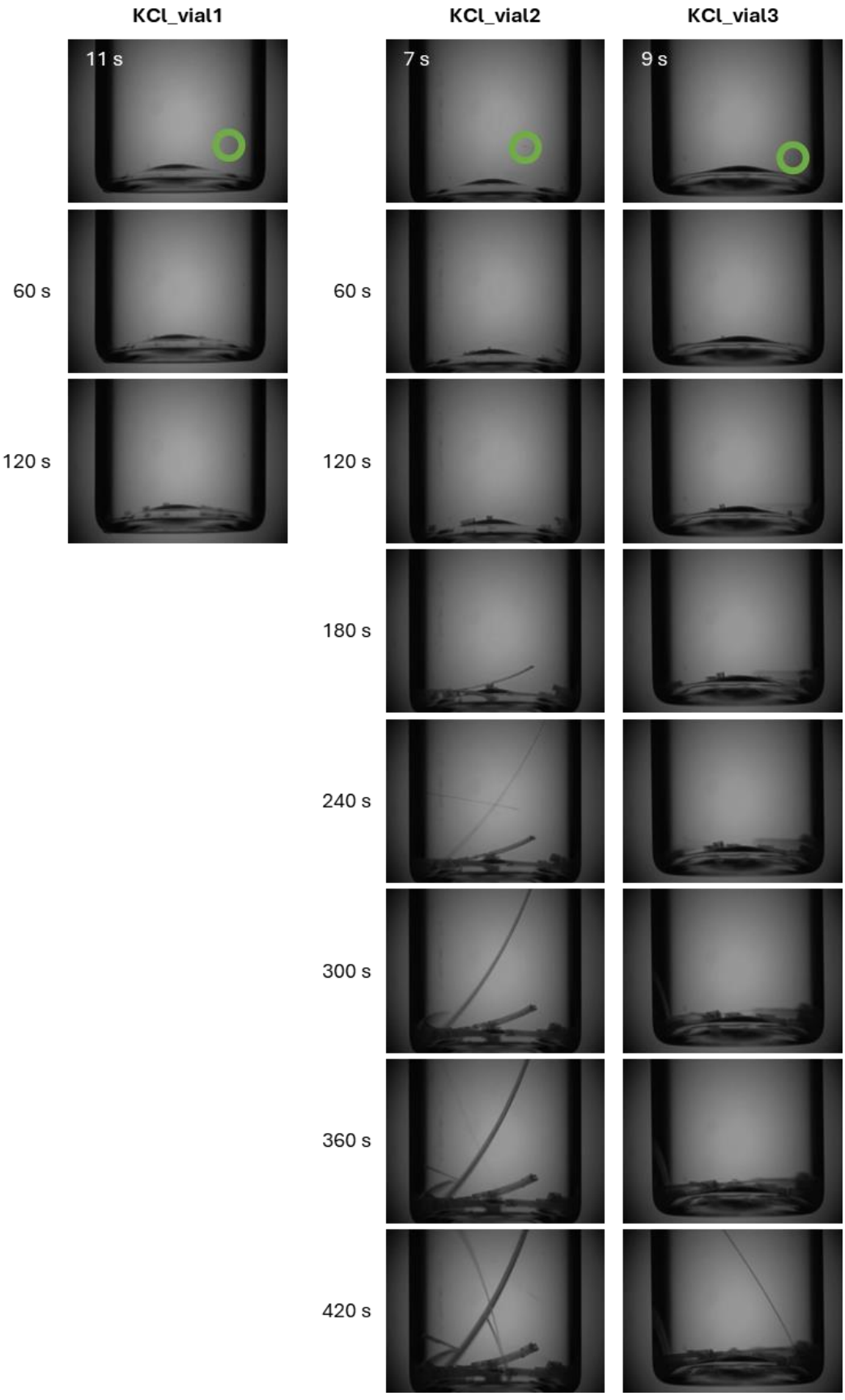

Figure 7.02: Still images from the video collections during NPLIN of KCl in glass vials during feasibility testing, with frames and corresponding time since laser pulse for KCl_vial1-3. Annotations circle the first crystal visible by eye and the corresponding growth time. Note: KCl_vial1 was only recorded for 2 min, other two recorded for 7 mins to observe crystal growth.

7.2.2 – Laser tubing damage

To mitigate any potential cause of blockages in the system, the KRAIC-S experiment aimed to use a continuous length of 1/8" inner diameter (ID) FEP tubing. However, it was unknown if the FEP would withstand the laser power required for NPLIN. Any tubing damage may alter the surface properties of the FEP, potentially interrupting the segmented flow. To investigate potential tubing damage, sections of FEP tubing were subjected to exposure to a set number of laser pulses at various peak power densities and inspected under a microscope for damage. Laser parameters of repetition rate (10 Hz), wavelength (532 nm) and pulse duration (~10 ns) remained unchanged from the KCl NPLIN testing in the previous section. The summary of conditions trialled and if damage was observed is summarised below in Table 7.03. Example microscope images of tubing damage shown in Figure 7.03.

Table 7.03: Summary of tubing laser damage tests for modified laser parameters, variable tubing exposure times and resulting laser pulses. Peak power density calculated with Equation 7.01. Resulting tubing damage observation noted.

Identifier	Approximate beamsize	Laser power average /mW	Gaussian peak power density / MW/cm^2	Tubing exposure /s	Number of laser pulses	Tubing damage observed?
LD_1	5 mm diameter	120	12.2	10	100	No
LD_2	5 mm diameter	120	12.2	100	1000	Yes
LD_3	5 mm diameter	120	12.2	600	6000	Yes
LD_4	5 mm diameter	50	5.1	600	6000	No
LD_5	< 3.2 mm diameter	63	15.9	1	10	Yes
LD_6	7 mm x 5 mm	68	4.9	60	600	No
LD_7	7 mm x 5 mm	68	4.9	600	6000	Minor

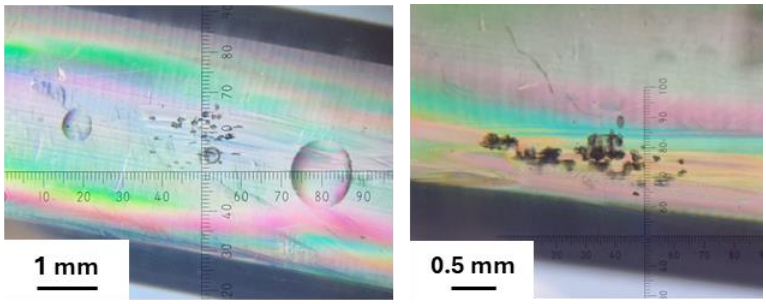

Figure 7.03: Microscope images with scale bar showing laser tubing damage caused by exposure to high powered laser pulses.

Tubing damage was found to be dependent on laser power density and number of pulse exposures: 100 laser pulses at 12.2 MW/cm^2 resulted in no visible tubing damage, whereas above 1000 laser pulses at the same laser power density resulted in tubing damage, like shown in Figure 7.03. Ten pulses at 15.9 MW/cm^2 similarly resulted in damage. Tubing exposure at 4.9 – 5.1 MW/cm^2 results in minimal tubing damage with 6000 pulses, however, appears to be on the limit with the 4.9 MW/cm^2 6000 pulses showing initial signs of tubing

damage. Laser power should be ideally kept within the 5.0 MW/cm^2 range and under 6000 exposures to limit the effects of tubing damage on the flow process.

7.2.3 – NPLIN of KCl in FEP tubing

To investigate the limitations of FEP tubing for producing NPLIN in comparison to a glass vial, tubing sections of FEP were filled with 100% supersaturated solution of aqueous KCl. The KCl solutions were prepared at 40 °C and syringed into ~10 cm tubing sections and sealed (~ 800 µL of KCl solution). The tubing sections were then submerged in a 40 °C water bath to ensure no crystalline material remained after the transfer process, and left to cool to room temperature, 23 °C. The prefilled tubing sections were exposed to single laser pulses at different power densities, supersaturation ratio and laser conditions summarised in Table 7.04. Still images from a 7 min video recorded after the single laser pulse for KCl_FEP1 conditions is shown below in Figure 7.04.

Table 7.04: Summary of KCl NPLIN conditions tested for KCl solutions in FEP tubing for a single laser pulse.

Identifier	KCl supersaturation, S	Laser average power /mW	Approximate beam diameter /mm	Gaussian peak power density / MW/cm^2	NPLIN?
KCl_FEP1	1.10	50	3.8	8.8	Yes
KCl_FEP2	1.06	70	3.8	12.3	No
KCl_FEP3	1.06	90	3.8	15.9	No

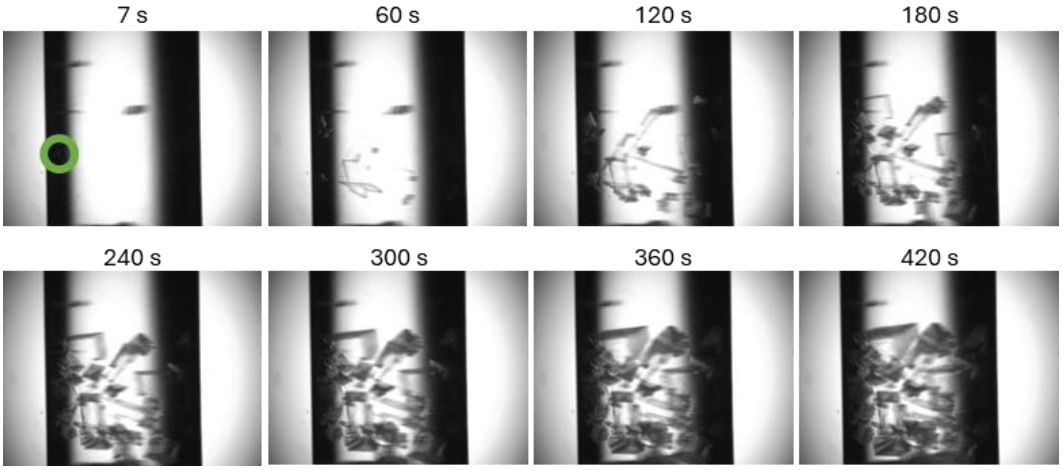

Figure 7.04: Still images from the video capture of KCl_FEP1 conditions following a single 10 ns laser pulse of 8.8 MW/cm^2 peak power density. Annotated circle shows the first visible crystal at 7 s after the laser pulse.

The KCl_FEP1 conditions produced KCl nucleation with high supersaturation, S = 1.10 with a peak power density of 8.8 MW/cm^2. Visible crystals of KCl were grown after 7 s post-laser pulse. The multiple KCl crystals grew to a large size within 60 s, with crystals showing high optical clarity at the 60 s frame. The multiple KCl crystals nucleated implies the peak power density was well above the threshold value, as KCl has been shown to nucleate single crystals with a

single low power laser pulse above the threshold. The remainder of the crystal growth from 120 s – 420 s appears to show secondary nucleation and crystal growth on the crystals formed from the initial NPLIN: the crystals show faceted edge-growth, causing a poorer optical clarity.

KCl condition with supersaturation of S = 1.06 did not produce NPLIN even at high 12.3 MW/cm^2 and 15.9 MW/cm^2 laser powder densities. Considering the laser damage tests resulted in tubing damage with repeated pulses at this laser power, higher laser power to induce KCl nucleation of S = 1.06 is not feasible for the flow experiments which would require thousands of pulses of higher power laser settings. The KCl in FEP experiments show that a higher supersaturation is required to achieve NPLIN in the FEP tubing with a single laser pulse at a peak power density of 8.8 MW/cm^2, a power density potentially feasible for repeated exposures without causing tubing damage.

7.2.4 – Slug triggering adaptation for NPLIN

Another goal for NPLIN in segmented flow was to induce a single crystal of KCl per slug, by exposing a single laser pulse in each slug, potentially for single crystal XRD analysis with the experimental set up shown in Figure 7.07. At low laser powers, a single laser pulse has been shown to produce a single crystal of KCl. To achieve this, it was proposed adapt the slug triggering mechanism, the data acquisition technique for the KRAIC-S, to trigger a laser pulse in the centre of a slug. The slug triggering mechanism for data acquisition uses a Class 2b laser-photodiode pair as a segmented flow monitor, using the photodiode readout plot to trigger the stage movement for data acquisition: the triggering value correspond to the rear edge of the slug where the crystals reside. By modifying the slug triggering script threshold value to correspond to the middle of the slug, it could enable laser triggering at that point, shown in Figure 7.05.

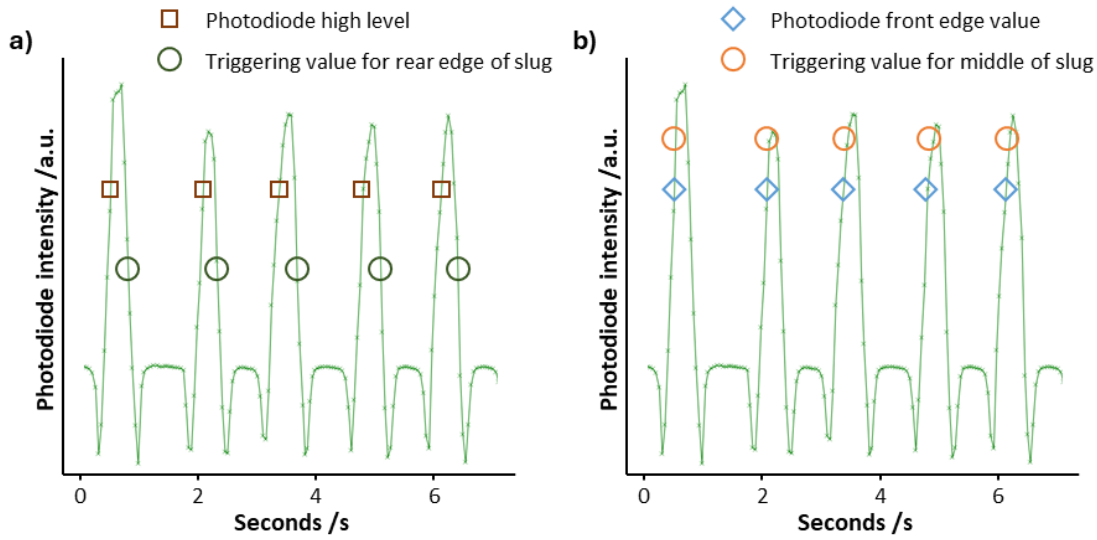

Figure 7.05: Photodiode readout graphs with annotated slug triggering set values for a) in data acquisition mode with high level and triggering value to ensure rear edge of the slug, and b) in laser triggering mode with front edge value and triggering value to ensure laser pulse into middle of solution slug.

For the adaptation of the slug triggering mechanism for laser triggering, a secondary Class 2 635 nm red laser (Thorlabs PL202) with a visible light 350 – 1100 nm responsive photodiode (Thorlabs SM1PD1A) was used for the laser triggering flow sensor. Rather than triggering a stage movement, the laser triggering script was adapted to trigger a laser shutter to open for 100 ms when the segmentation was at the middle of the slug. The repetition rate of the Vibrant laser of 10 Hz (100 ms) ensured only a single pulse would make it through to the slugs within that time frame. This was tested during the feasibility studies of with the Vibrant laser on segmented flow of water with a 3.36 mL/min total flow rate: 1.40, 0.76, and 1.2 mL/min for water, Galden carrier fluid, and air flow rates respectively. A photodiode readout plot during the testing shows the correct triggering corresponding to the centre of a slug, shown below in Figure 7.06a. The shutter opening and corresponding single laser pulse per slug triggering was confirmed with oscilloscope readout of segmented flow, shutter, and Vibrant laser, shown in Figure 7.06b.

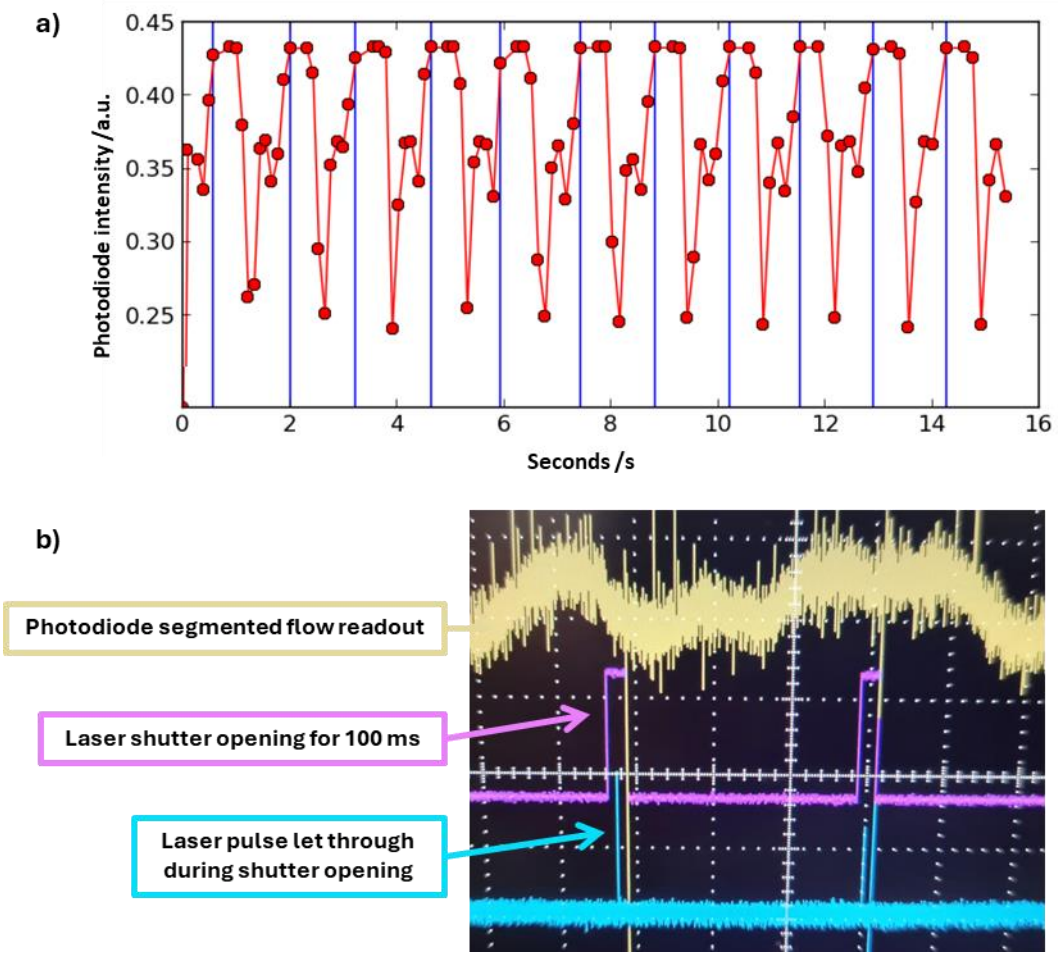

Figure 7.06: a) Photodiode readout plot during segmented flow laser testing feasibility studies. Vertical blue lines show shutter opening triggering at the peak which corresponds to the middle of the slug for a triggering value of 0.43 a.u. photodiode intensity. b) oscilloscope readout for photodiode segmented flow with corresponding laser shutter opening and single laser pulse achieved from the laser slug triggering in the middle of a slug.

7.2.5 – Overall NPLIN feasibility study results

NPLIN has been achieved for KCl at a supersaturation of S = 1.10 at 23 °C in 1.75 mL glass vials for 8.8 – 31.7 MW/cm^2 power density. Monitoring of the crystallisation with a camera showed crystals visible by eye within rapid 7 s timeframe, with initial block KCl crystals grown within the first 60 s. Following 120 s, needle crystals appear to form, potentially caused by secondary nucleation. The Vibrant laser testing with the FEP tubing has shown that tubing damage is dependent on number of laser pulses and peak power density of the laser. Lower peak power densities < 5.1 MW/cm^2 are able to achieve 6,000 laser pulses with minimal tubing damage. The higher laser powers (12.2 and 15.9 MW/cm^2 resulted in tubing damage with <1,000 laser pulses and are therefore unsuitable for NPLIN in segmented flow to minimise the risk of tubing damage and resultant surface property modification effecting segmentation. KCl solution at supersaturation S = 1.10 in prepared FEP tubing section resulted in NPLIN for a laser power of 8.8 MW/cm^2, lower supersaturations of KCl did not result in NPLIN with the 12.3 and 15.9 MW/cm^2 tested. Laser triggering of a single laser pulse per slug was achieved in the feasibility testing through adaptation of the slug triggering mechanism with photodiode threshold control to open a laser shutter.

The feasibility testing defined the range of conditions achievable for NPLIN of KCl in segmented flow by a single laser pulse per slug for the production of a single crystal per slug. The segmented flow rate (3.36 mL/min) resulted in approximately one slug per second, the 6,000 pulse limit for ~5 MW/cm^2 would result in ~100 min of NPLIN of KCl flow before tubing damage; if laser exposure for a tubing section is restricted to 60 min maximum this would limit tubing damage for the conditions required for KCl NPLIN in flow.

7.3 – NPLIN in segmented flow with *in situ* XRD

7.3.1 – Experimental

Following the results of the feasibility studies, NPLIN of KCl in segmented flow for single crystal generation was trialled with the adapted slug triggering mechanism, coupled with *in situ* XRD with beamtime on Beamline I19, experimental hutch 2 (EH2). The X-ray beam size used for these experiments was 120 µm with a wavelength of 0.4859 Å (25 keV). The NPLIN beamtime experiments used the KRAIC-S v3 design, the development of which is discussed in Chapter 6. Three solutions were used during NPLIN beamtime: an aqueous KCl at 37.37 g/100g and two solutions at 38.44 g/100g aiming for S = 1.06 and 1.10 for a room temperature of 23 °C. The KCl purchased for the experiment was Sigma Aldrich ReagentPlus ≥99.0 % and was used without further purification. The inlet from the solution feedstock used a solvent filter to remove larger (>10 µm) particles. The KRAIC-S v3 tubing layout used an increased tubing length prior to the laser pulse point to accommodate the cooling of KCl solution to room temperature to ensure supersaturation for NPLIN. The length of tubing required was calculated based on paracetamol

cooling from previous KRAIC-S v2 experiments, shown in Figure 6.09. The schematic diagram of the KRAIC-S set up for NPLIN beamtime is shown in Figure 7.07. The temperature, flow rate settings, and NPLIN conditions are summarised in Table 7.05. The cooling curve for KCl solution in segmented flow is shown in Figure 7.08 for KCl_flow_S1.04

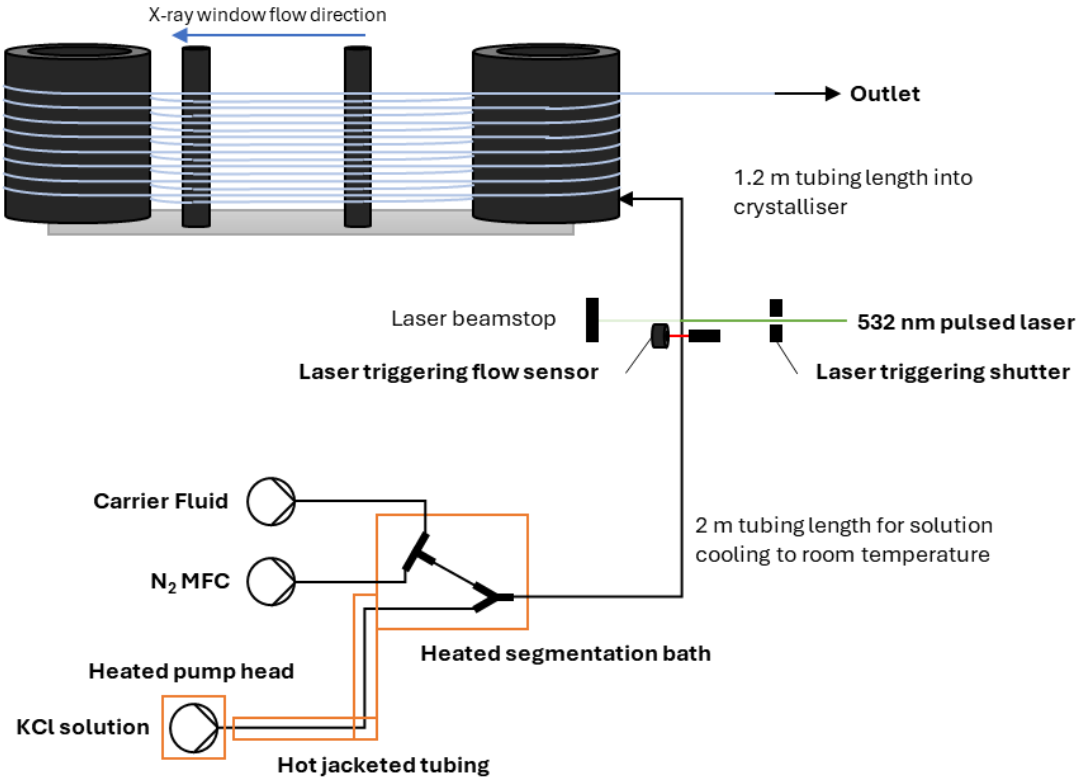

Figure 7.07: Schematic diagram of the KRAIC-S set up with segmentation pieces and laser triggering point, increased tubing lengths prior to the KRAIC-S main body annotated.

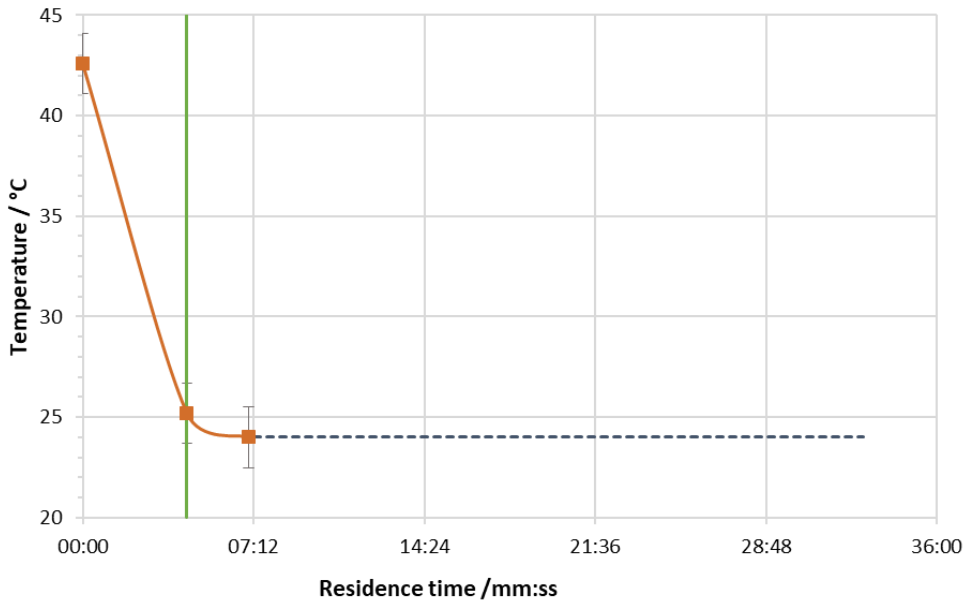

Figure 7.08: Cooling curve of KCl solution in the KRAIC-S measured with a FLIR E5 thermal imaging camera. The vertical green line shows the laser trigger point. Dashed line shows approximate final temperature of solution at 24 °C at all X-ray analysis points.

The room temperature in the hutch was 24 °C, slightly increased on the usual 23 °C due to the extra heating apparatus present, resulting in the higher temperatures at the laser triggering point than anticipated. As shown in Table 7.05, the actual temperature at the laser trigger point was higher than the 23 °C used for supersaturation calculations, resulting in actual supersaturations of KCl solution of S = 1.04 and 1.08 during the two experimental conditions trialled. The KCl_flow_S1.08 conditions were repeated with due to finishing the initial KCl_flow_S1.08_1 solution. Despite the feasibility studies showing no nucleation for KCl at S = 1.06 supersaturation in FEP tubing, lower supersaturation experiments were attempted in segmented flow to see if the crystal growth occurred at longer timescales (> 7 min) than probed in the feasibility study. The KRAIC-S in this layout had 16 analysis window lengths available to use, named X1 to X16, however, only right to left flow direction was set up with the slug triggering data acquisition laser-photodiode pair for simplicity. The overall flow rate of 3.40 mL/min resulted in a residence time of 32:54 min post-segmentation and 28:31 min post-laser pulse point. The segmentation was set up to achieve long solution slugs to assist with slug triggering of a single laser pulse per slug.

Table 7.05: Summary of flow conditions trialled for NPLIN of KCl in segmented flow, with resulting NPLIN conditions, laser settings, and if NPLIN did occur. Overall flow rate remained the same, nitrogen gas flow and carrier fluid flow adjusted to improve segmentation. Heated pump head approximate due to some variation. Increased temperatures for KCl_flow_S1.08 due to higher solution concentration. Calculated supersaturation, S, shown for the actual temperature of solution at the laser trigger point.

		Flow conditions identifier	
		KCl_flow_S1.04	**KCl_flow_S1.08_1, KCl_flow_S1.08_2**
	KCl solution concentration / g/100g	37.37	38.44
Flow rates / mL/min	**Solution**	1.80	1.80
	N2	0.80	1.00
	Carrier fluid	0.80	0.60
	Total flow rate	3.40	
Temperature settings /°C	**Solution hotplate**	45	47
	Segmentation bath hotplate	43	45
	Hot jacketed transfer tubing - water circulator	43	45
	Heated pump head	~ 43	~45
NPLIN conditions	**Laser trigger point temperature /°C**	25.9	25.2
	Supersaturation, S	1.04	1.08
Laser Settings	**Beam size**	7 mm x 5 mm	
	Laser average power /mW	90	
	Gaussian peak power density / MW/cm2	6.6	
	NPLIN?	No	Yes

KCl_flow_S1.04 flow conditions did not result in spontaneous nucleation of KCl with the metastable solution conditions present, as expected. No NPLIN occurred with laser triggering pulses at 6.6 MW/cm^2 power density, concurring with the previous feasibility tests that low supersaturations (S = 1.06) were unable to achieve NPLIN in FEP tubing, even when monitored for longer nucleation and crystallisation times (28:31 min). KCl_flow_S1.04 ran for four residence times with no nucleation or crystallisation achieved.

KCl_flow_S1.08_1 flow conditions ran without laser exposure for 46 min (1.5 residence times) with no spontaneous nucleation and no visible crystal growth, as expected. With the laser triggering at 6.6 MW/cm^2, crystals were spotted at the X2 position at a crystallisation time of 4 min post-laser triggering point. The KCl_flow_S1.08_1 ran for ~ 3.5 residence times, until the first 38.44 g/100g solution ran out. Observations showed a single particle per slug at shorter crystallisation times appearing in the middle of slugs, due to the laser triggering targeting the middle of slugs. As the crystal sizes increased due to increased crystallisation time, the crystals grew larger and dropped to the rear edge of slugs. Slug triggering for data acquisitions were collected at the X3 windows for a post-laser crystallisation time of 5:37 min.

S = 1.08 conditions were repeated with KCl_flow_S1.08_2, similarly running for 46 min with no spontaneous nucleation, then with NPLIN occurring from introduction of 6.6 MW/cm^2 laser pulses. X-ray data was collected at the X9 crystalliser positions for a post-laser crystallisation time of 14:46 min. KCl_flow_S1.08_2 conditions ran for ~ 2 residence times, ending due to a fault with the I19 laser interlock system.

7.3.2 – Results and Discussion

NPLIN was achieved for KCl in segmented flow, achieving a single crystal per slug due to the adaptation of the slug triggering mechanism for laser pulse triggering. With the slow total flow rate and translation speed, slug triggering data acquisitions resulted in data collections of a total of 120 frames of 0.1 s per frame for a single acquisition (~12 s acquisition time). Four data acquisitions containing diffraction were achieved from the X9 collection, with five data acquisitions with diffraction for the X3 position. Due to synchrotron beam-loss during beamtime and issues with the laser interlock system in EH2, no further data could be collected.

Inspection of the collection videos during slug triggering data capture shows single particles were achieved from KCl NPLIN from a single laser pulse, with some videos showing single crystals, other videos showing multi-crystalline single particles. The corresponding X-ray data frames for the single crystal examples clearly shows a strong single crystal lattice visible, whereas the multi-crystalline resulted in diffraction frames with overlapping lattices due to multiple crystals present, shown in Figure 7.09.

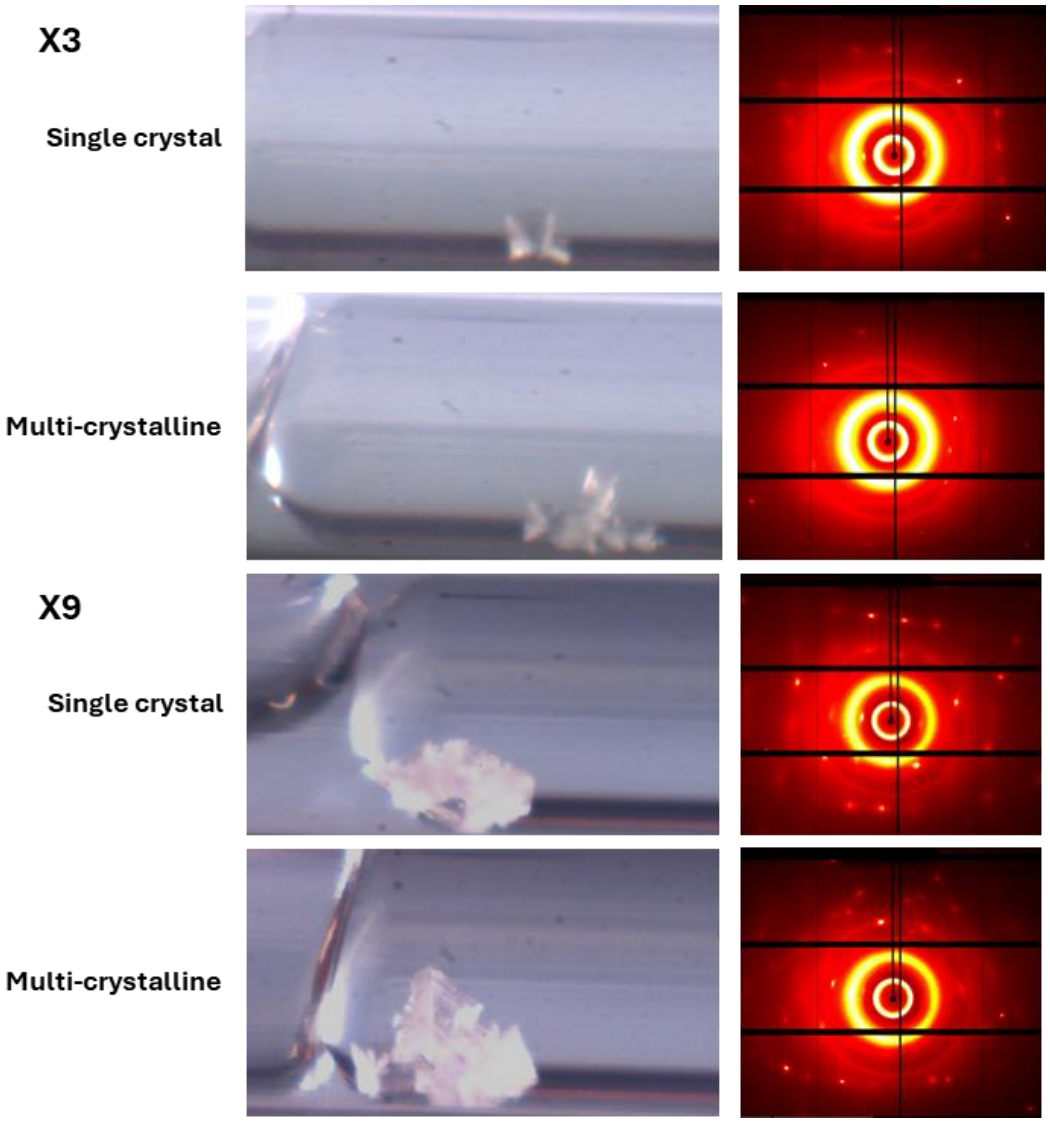

Figure 7.09: Images from on-axis camera view of slug triggering data acquisitions of KCl crystals formed from NPLIN from a single laser pulse per slug in segmented flow. Shown are single and multi-crystalline particles at the X3 and X9 analysis point with a corresponding diffraction frame for each dataset.

Single particles were seen in all 9 diffractions data collections achieved: of the 9 datasets collected, 3 appear to have a multi-crystalline single particle, with the remaining 6 showing single crystals per slug. The KCl diffraction frames show large spot sizes in comparison to the paracetamol system previously studied in the KRAIC-S, compared in Figure 7.10. The spot size for KCl crystals is 3.5 times larger in width than the smallest diffraction spots seen for paracetamol, and 1.4 times larger than the largest paracetamol diffraction spots.

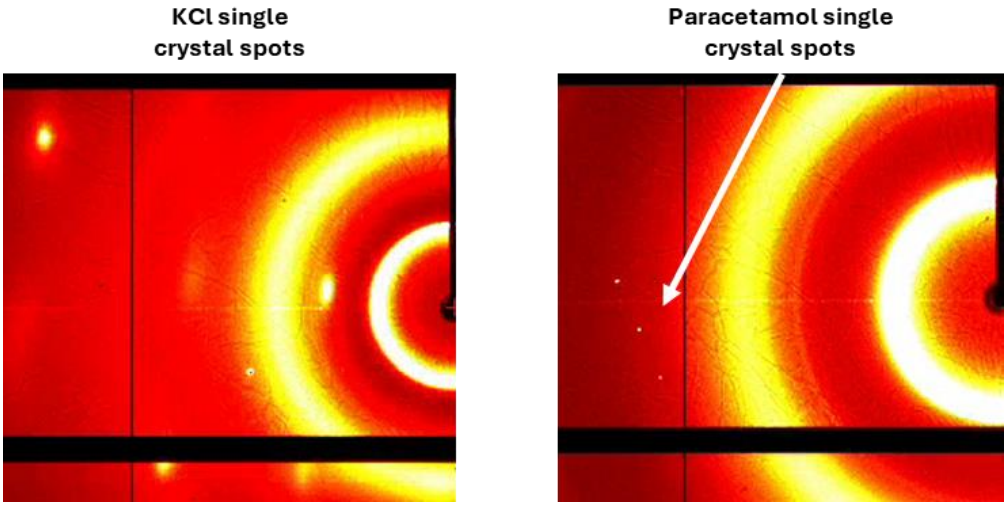

Figure 7.10: Sections of diffraction frames collected for KCl single crystal against paracetamol single crystals in the KRAIC-S. Rings of background scattering seen are from the FEP tubing. N.B. the paracetamol diffraction spots are significantly smaller than the KCl.

Optical microscopy of captured crystals, shown in Figure 7.11, shows high mosaicity of the crystals, clearly showing the crystal edge growth outwards from the initial crystal formed. Crystals are formed from small mosaic blocks of repeating units, when a crystal has a "high mosaicity" the small building blocks are slightly misoriented with respect to each other.[17] The resulting diffraction from a highly mosaic crystal has wider angular range, resulting in widened diffraction spots, like seen in Figure 7.10. The diagram in Figure 7.12, explains the origin of the wider diffraction spots for highly mosaic crystals.

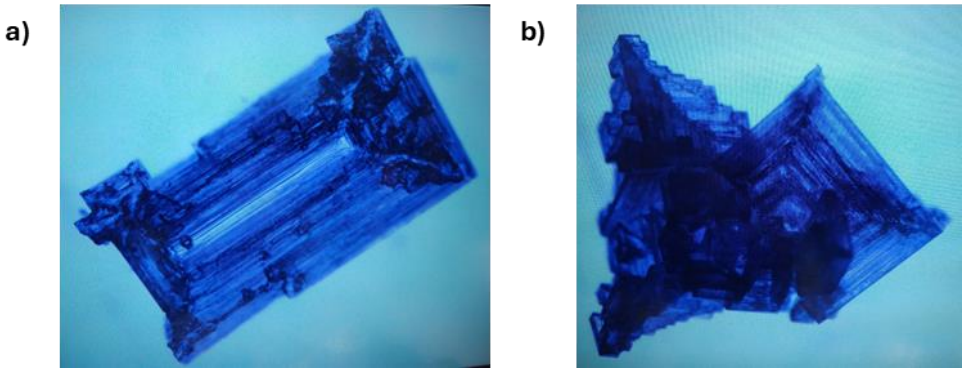

Figure 7.11: Optical microscopy images of KCl crystals produced with NPLIN of supersaturated S = 1.08 KCl solution in segmented flow crystallisation. a) shows a highly mosaic single crystal, b) shows a dendritic crystal growth.

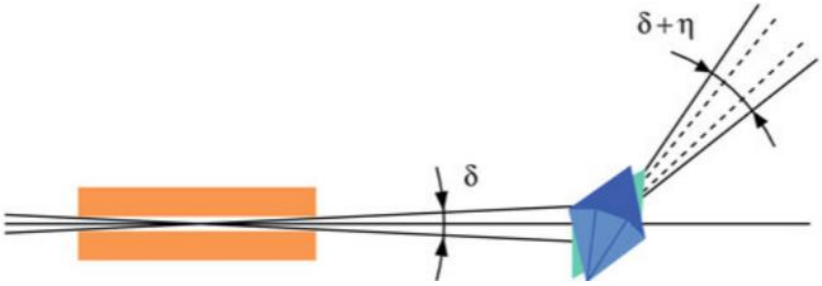

Figure 7.12: Schematic illustration of the beam divergence, δ, and crystal mosaicity, η. Total angular width of the diffraction reflection from a highly mosaic crystal is the sum of these two contributions. Figure taken from [17].

Literature examples of KCl crystals nucleated *via* NPLIN by Korede *et al.* and Hua *et al.* show the formation of cubic/block morphology KCl crystals.[3,12] A paper by Hua *et al.* on the NPLIN of KCl appears to show mosaic KCl crystals but with no discussion concerning the mosaic appearance.[12]

The multi-crystalline single particles have a dendritic crystal growth, potentially formed from a single nucleus from a single laser pulse. The feasibility studies similarly saw a growth phase style mosaic appearance of the KCl crystals after the initial formation of an optically clear crystal in the initial 60 s after the single laser pulse (Figure 7.04). This is potentially the case for the KCl crystals obtained in flow, that they initially formed single crystals with low mosaicity and issues with the growth face caused increasing mosaicity and multi-crystalline style dendritic growth.

A single particle appears to be grown per slug for a single laser pulse, in contrast to the NPLIN feasibility studies in FEP tubing where many crystals grown from one pulse. The supersaturation of the feasibility testing was slightly higher (S = 1.10, compared to S = 1.08) with an 8.8 MW/cm^2 laser power density compared to the 6.6 MW/cm^2 used in segmented flow. The literature states the single crystal NPLIN of KCl occurs at the lower laser powers, accounting for the increased crystallisation in the FEP feasibility tests. The volume in a single slug (~ 55 µL) is lower than the feasibility testing (~ 800 µL), also contributing to the decreased crystallisation.

Data processing was attempted with DIALS using the methodology described in the introduction of Chapter 6.[18] Two datasets of the 9 total passed the indexing stage, resulting in unit cell identification of the KCl crystal form with a=b=c = 6.92 and 6.60 Å, with the 90 °C constrained unit cell angles and $Fm\overline{3}m$ space group. The resulting indexed unit cells are 0.32 - 0.64 Å from the reference crystal axes lengths of KCl with 6.28 Å.[14,15] This is quite a difference from the input reference unit cell likely due to a combination of errors: the 3.2 mm ID of the tubing allows for considerable variation of the sample-to-detector distance by an unknown amount during data collection. Furthermore, the low number of reflections per dataset also contributes to this deviation from the reference. The two datasets failed refinement and integration, similar to the other datasets that failed indexing due to too few reflections per dataset for processing. The high density of KCl crystals (2.00 g/cm^3)[15] combined with the slow flow rate (3.40 mL/min) and resulting lower turbulence in the slugs caused even the small crystals at the X3 analysis window (5:37 min post-laser) to rotate minimally, with too few reflections to process. However, the *in situ* XRD technique for NPLIN in segmented flow has shown capability to identify a crystal system based on the indexed unit cell, opening the door to wider experiments studying the polymorphic behaviours during NPLIN for future experiments.

Subsequent to the KRAIC-S beamtime of KCl NPLIN in segmented flow, Korede *et al.* published a paper on KCl NPLIN in a microfluidic, droplet flow system.[3] The microfluidic system used bi-segmented flow in a hydrophobized glass squared capillary with a solution phase and a silicone oil carrier phase for the NPLIN crystallisation of KCl. KCl NPLIN was investigated with a systematic

study varying key NPLIN properties to see the effects on KCl nucleation. The variables used were:

- Laser wavelength (355, 532, and 1064 nm)
- Peak laser intensity (10 – 100 MW/cm^2)
- Supersaturation ratio (1.05 – 1.10) of solution prepared at 40 °C and cooled to room temperature (25 °C)
- Solution filtration to remove impurities
- Doping with Fe_3O_4 nanoparticles

The Korede *et el.* study found that there was no significant wavelength effect for KCl NPLIN, and that solvent filtration and nanoparticle impurities affected the nucleation probabilities, reinforcing the nanoparticle heating mechanism proposed for NPLN of KCl. The study found that S = 1.05 supersaturation required ≥ 50 MW/cm^2 laser power density, with S = 1.10 producing nucleation at ≥ 10 MW/cm^2. The threshold laser power densities for supersaturated solutions are very different than seen in large volume KCl NPLIN in batch experiments seen in the literature, highlighting the dependence of NPLIN on the sample environment. This could potentially be caused by the low volume present of KCl solution (~1.0 – 1.2 µL) requiring higher supersaturation or higher laser intensity than literature experiments. This was seen for the literature levitated droplets requiring a far higher supersaturation to induce nucleation, and the FEP tubing feasibility study in this work requiring a higher supersaturation to achieve NPLIN in the sample container present.[13] The KRAIC-S with an estimated 55 µL per slug providing a greater volume of solution, increasing the probability of nucleation, requiring a lower power density for NPLIN to occur.

Korede *et al.* note the main drawback of the microfluidic system was the limitation of the system to probe only short nucleation and crystallisation times (70.7 s) due to the 30 cm length of the capillary; longer capillaries suffered from clogging issues due to poor hydrophilization in longer glass quartz lengths. In comparison, the KRAIC-S system ran for hours (~3.5 residence times) for KCl_flow_S1.08_1 for a post-laser residence time of 28:31 min with no blockages occurring during any conditions trialled. The hydrophobic FEP tubing used for the KRAIC-S does not cause and surface issues to cause encrustation and blockages, enabling the study of NPLIN with prolonged crystallisation times in comparison.

7.4 – Conclusions

Non-photochemical laser-induced nucleation of potassium chloride coupled with *in situ* XRD has been achieved in a segmented flow crystalliser, the KRAIC-S v3 on Beamline I19, Diamond Light Source. Initial feasibility studies were conducted with the Opotek Vibrant He 355 II Nd:YAG laser and KCl solutions of supersaturation ratio, S = 1.10 in 1.75 mL glass vials. Single laser pulses of 8.8 – 31.7 MW/cm^2 were found to achieve NPLIN, with visible crystals appearing after 7 – 11 s with video camera monitoring. All three tests showed block morphology KCl growing after 120 s of crystal growth. After 120 s, the 8.8 MW/cm^2 example showed rapid crystallisation of needle-like KCl crystals for the remaining 300 s of monitoring time. However, the 31.7 MW/cm^2 example only produced prominent needle crystals after 420 s. The cause of the two KCl morphologies is unknown, potentially caused by the between laser power density used or secondary nucleation.

Feasibility studies for the flow experiments aimed to identify laser power densities and exposures which caused minimal tubing damage: power densities around 5.0 MW/cm^2 were shown to give minimal tubing damage with 6000 laser pulses on inspection with an optical microscope. Testing to find the laser power threshold for KCl solutions in FEP tubing found that no NPLIN was observed for pre-filled tubing sections with supersaturation, S = 1.06, despite the high laser powers used (12.3 and 15.9 MW/cm^2) for observation times of 7 min. A higher supersaturation of KCl, S = 1.10, produced nucleated multiple KCl crystals from a single 8.8 MW/cm^2 laser pulse. The multiple KCl crystals nucleated implied a lower threshold power density for S = 1.10 KCl in the FEP tubing sample container. The nucleated KCl crystals were observed to initially nucleate with a high optical clarity, then with edge-growth of the crystals showing a poorer optical clarity of the crystals.

To achieve the nucleation of a single KCl crystal per slug in segmented flow, the slug triggering mechanism was adapted to laser shutter control. The slug triggering flow rate sensor enabled the user to set a triggering value corresponding to the centre of slugs, the slug triggering control script then opens the shutter for a period of 100 ms, ensuring only a single laser pulse from the 10 Hz repetition rate laser irradiates the slug.

Following the successful feasibility testing, beamtime on I19 achieved NPLIN in segmented flow, coupled with *in situ* XRD analysis. For a supersaturation of S = 1.04 and single laser pulses per slug of 6.6 MW/cm^2, no crystallisation was observed for a run time of 4 residence times, for a post-laser residence time of 28:31 min. This concludes that lower supersaturations of KCl cannot produce NPLIN in the power density range that the FEP tubing is able to withstand repeated laser pulses. NPLIN of S = 1.08 KCl solution at the same power density of 6.6 MW/cm^2 produced a single particle per slug from the slug triggering laser pulse. The crystals were observed at crystallisation times of 4 min post-laser pulses, with the small crystals residing in the centre of the slug, validating that the laser pulse was triggered in the centre of slugs as per the laser slug triggering input. When the crystals grew larger, they dropped back to the rear of

slugs in flow. Slug triggering X-ray data acquisition was achieved at different X-ray windows with crystallisation times of 5:37 and 14:46 min respectively. Five datasets containing diffraction were collected at the X3 position, with four collections with KCl diffraction at the X9 position. The XRD data collection was limited during beamtime due to beam downtime and a fault in the I19 laser interlock system.

Inspection of the XRD data and corresponding collection videos showed minimal rotation of both the small and large KCl crystals in flow, likely due to the high density of KCl and slow flow rates resulting in low turbulence. As a result, the diffraction datasets could not fully process with a single crystal, serial crystallography style processing methodology. However, two datasets passed the indexing stage of processing, enabling space group and unit cell verification of a, b, c = 6.92 and 6.60 Å, a deviation from the input literature KCl unit cell a, b, c = 6.28 Å. This deviation is likely due to the variation of crystal position in the 3.2 mm ID FEP tubing, causing deviation in the sample-to-detector distance, and the low number of reflections resulting in error in the indexing unit cell. The datasets collected were from single block crystals, or multi-crystalline single particles. Optical microscopy of the collected particles showed the multi-crystalline particles appeared to show a dendritic crystal growth of KCl. The single crystals show high mosaicity with visible edge-growth from the initial crystal, like seen on the video capture from the feasibility testing of KCl in FEP tubing. The diffraction captured also showed high mosaicity with large diffraction spots.

Overall, this work has shown that NPLIN in segmented flow can be achieved with single laser pulses per slug to nucleate from a metastable solution, with no prior spontaneous nucleation. Typical KRAIC experiments show a widening of the metastable zone width from the lack of solid interfaces for primary heterogeneous in segmented flow; low supersaturations struggle to crystallise in KRAIC conditions. Now NPLIN has enabled the nucleation of KCl where no spontaneous nucleation was occurring, this makes attainable the study of crystallisation conditions previously inaccessible in the KRAIC systems. The coupling of the system with *in situ* XRD for phase identification enables a wider range of studies for crystallisation landscapes of polymorphic materials in the unique conditions present. The set-up shows some merit for the repeatable nucleation of single crystals for serial crystallography, however, is currently limited by the slow flow rates and minimal crystal rotation.

7.5 – Future Work

The development of this NPLIN in segmented flow with *in situ* XRD now facilitates the advanced study of polymorphic landscape, investigating supersaturations previously inaccessible in segmented flow. The system has shown the capability for unit cell identification potentially enabling serial crystallography in the future, or conversion of the data to powder XRD patterns for polymorphic identification. The coupling with XRD can also facilitate investigations into the effect of linearly or circularly polarised light on NPLIN

mechanisms. Materials previously studied in KRAIC systems, such as carbamazepine and glycine, demonstrate non-photochemical laser-induced nucleation and the well-documented KRAIC experiments could provide the basis for further NPLIN investigations in segmented flow.[6,8,10]

The highly mosaic KCl crystals grown appeared in both the KCl FEP tubing tests, segmented flow examples, with an example seen in the literature during microfluidic NPLIN of KCl also.[12] Video images from the KCl in glass vials tests did not have a close enough zoom to see if it is present in that sample container also. A study to determine if this is an effect caused by the FEP or simply caused by the rapid crystal growth of KCl is important for any future NPLIN experiments in the KRAIC-S. Determining if the sample container strongly influences the growth and appearance of crystals must be taken into account for future experiments. The glass vial experiments also showed two morphologies of KCl, block and needle. There may be a dependence on laser power on the morphology of formed KCl which could be studied further with a wider range of conditions and a number of repeat experiments.

To improve the laser properties for NPLIN studies, a hydrophobized glass tubing section at the laser pulse point would improve the range of laser power densities in the system, removing the current power limitation from tubing damage. A square profile glass tubing section would minimise interference of the laser beam for more controlled irradiation of slugs. However, an additional tubing section may cause issues with the segmented flow due to FEP-glass connection pieces and poor hydrophobic layer coating causing crystallisation of the material, like seen with the Kapton windows in the KRAIC *in situ* powder XRD systems. The higher power density for NPLIN conditions that a glass tubing section would facilitate would be significantly beneficial for NPLIN in segmented flow studies and should be trialled if it is feasible or causes issue with flow disruption. If it is discovered that the FEP is strongly influencing KCl crystal growth to be highly mosaic, a glass window section may eliminate this effect also.

For KRAIC-S crystallisation, the results of this work and the previous paracetamol results summarised in Chapter 6 both show the need to study systems with more rotation of single crystals and to improve the hit rate of small crystals in the beam. Furthermore, for the study of NPLIN, ideally probing earlier times post-laser would be more informative on the initial stages of crystal growth post-nucleation. However, the main issue with the system is the ability to hit small, rotating crystals. With the slug triggering data acquisition method, the ability to hit the desired region of slugs is repeatable, however, the co-location of small crystals and the X-ray beam is not repeatable due to the large size of slugs in comparison to the crystal sizes desired for study. A further issue with the system is the movement of crystals in-beam, which likely causes the failure of some dataset processing due to the variation of sample-to-detector distance for a single acquisition. The focussing of smaller crystals in beam could be achieved by using smaller ID tubing, which would increase the flow velocity for the equivalent flow rates and improve the co-location of beam and crystal due to the improved matching of beam size (80 – 120 μm) and tubing

diameter. This could improve the quality of X-ray data collected with increased rotation of smaller crystals, improved hit rates, and reduced sample-to-detector variation during data collection. Smaller tubing poses a greater risk for tubing blockage and would require study of the crystal growth of the material to limit the tubing length to prevent crystals growing too large and causing blockages. Furthermore, changing tubing would require modifications to the crystalliser design, with a faster linear motion stage to speed match during slug triggering data acquisitions.

7.6 – References

1. Alexander, A. J. & Camp, P. J. Non-photochemical laser-induced nucleation. *Journal of Chemical Physics* **150**, (2019).

2. Ward, M. R., Jamieson, W. J., Leckey, C. A. & Alexander, A. J. Laser-induced nucleation of carbon dioxide bubbles. *J Chem Phys* **142**, 144501 (2015).

3. Korede, V. *et al.* Design and Validation of a Droplet-based Microfluidic System To Study Non-Photochemical Laser-Induced Nucleation of Potassium Chloride Solutions. *Cryst Growth Des* **23**, 6067–6080 (2023).

4. Garetz, B. A., Aber, J. E., Goddard, N. L., Young, R. G. & Myerson, A. S. Nonphotochemical, Polarization-Dependent, Laser-Induced Nucleation in Supersaturated Aqueous Urea Solutions. *Phys Rev Lett* **77**, 3475–3476 (1996).

5. Alexander, A. J. & Camp, P. J. Single pulse, single crystal laser-induced nucleation of potassium chloride. *Cryst Growth Des* **9**, 958–963 (2009).

6. Ikni, A. *et al.* Experimental demonstration of the carbamazepine crystallization from non-photochemical laser-induced nucleation in acetonitrile and methanol. *Cryst Growth Des* **14**, 3286–3299 (2014).

7. Li, W. *et al.* Non-Photochemical Laser-Induced Nucleation of Sulfathiazole in a Water/Ethanol Mixture. *Cryst Growth Des* **16**, 2514–2526 (2016).

8. Garetz, B. A., Matic, J. & Myerson, A. S. Polarization Switching of Crystal Structure in the Nonphotochemical Light-Induced Nucleation of Supersaturated Aqueous Glycine Solutions. *Phys Rev Lett* **89**, 175501 (2002).

9. Sun, X., Garetz, B. A. & Myerson, A. S. Polarization switching of crystal structure in the nonphotochemical laser-induced nucleation of supersaturated aqueous l-histidine. *Cryst Growth Des* **8**, 1720–1722 (2008).

10. Liu, Y., Van Den Berg, M. H. & Alexander, A. J. Supersaturation dependence of glycine polymorphism using laser-induced nucleation, sonocrystallization and nucleation by mechanical shock. *Physical Chemistry Chemical Physics* **19**, 19386–19392 (2017).

11. Ward, M. R. & Alexander, A. J. Nonphotochemical laser-induced nucleation of potassium halides: Effects of wavelength and temperature. *Cryst Growth Des* **12**, 4554–4561 (2012).

12. Hua, T., Gowayed, O., Grey-Stewart, D., Garetz, B. A. & Hartman, R. L. Microfluidic Laser-Induced Nucleation of Supersaturated Aqueous KCl Solutions. *Cryst Growth Des* **19**, 3491–3497 (2019).

13. Fang, K., Arnold, S. & Garetz, B. A. Nonphotochemical laser-induced nucleation in levitated supersaturated aqueous potassium chloride microdroplets. *Cryst Growth Des* **14**, 2685–2688 (2014).

14. Ahtee, M. Lattice constants of some binary alkali halide solid solutions. *Annales Academiae Scientiarum Fennicae, Series A6: Physica* **313**, 1–11 (1969).

15. Data retrieved from the Materials Project for KCl (mp-23193) from database version v2023.11.1.

16. Aqueous Solubility of Inorganic Compounds at Various Temperatures. in *CRC Handbook of Chemistry and Physics 95th Edition* (eds. Haynes, W. M., Lide, D. R. & Bruno, T. J.) 1070 (CRC Press, 2014).

17. Rajashankar, K. & Dauter, Z. Chapter 17. Data collection for crystallographic structure determination. in *Structural Genomics and Drug Discovery. Methods in Molecular Biology* (ed. Anderson, W. F.) vol. 1140 211–237 (Humana Press Inc., 2014).

18. Winter, G. *et al.* DIALS as a toolkit. *Protein Science* **31**, 232–250 (2022).

Chapter 8 – Conclusions and Future Work

8.1 – Conclusions

The work in this thesis presented the advancement of *in situ* (XRD) analysis techniques during segmented flow through various means; lab-source powder XRD (PXRD) at the Flow-Xl facility, University of Leeds, and synchrotron experiments for higher resolution PXRD at Beamline I11, and single crystal XRD (SCXRD) at Beamline I19 for serial crystallography.

Chapter 5 discussed the commissioning of the KRAIC-T, a temperature cycling segmented flow crystalliser. The KRAIC-T, through the heated aluminium columns and an additional sub-ambient temperature controlled column insert was able to achieve temperature control between 12.2 – 53.6 °C. The sub-ambient temperature cycling demonstrated enhanced control over succinic acid crystallisation, a challenging material for flow processes due to the fast crystal growth rate.

Integration of the KRAIC-T as a sample environment on Beamline I11 used the introduction of an improved data acquisition technique: the slug triggering mechanism. The slug triggering mechanism used laser-photodiode flow monitors to trigger stage movement during data acquisition, increasing data capture time from 100 ms to 2.4 s per single, multi-crystalline slug. When used to study the slurrying crystallisation of the polymorphic system *ortho*-aminobenzoic acid, the increased acquisition times resulted in diffraction frames with enhanced signal-to-noise of PXRD data. The extracted diffraction patterns were used for multi-phase Rietveld refinement for an elevated understanding of the polymorphic balance in the system. The temperature cycling *o*ABA study found the material was undergoing a solvent-mediated phase transition from the metastable Forms III and II to the stable Form I in the starting material flask. The results showed slight fluctuations in polymorphic balance in the crystalliser, potentially as a result of the temperature cycling. The quality of data extracted with the KRAIC-T slug triggered sample environment shows significant improvements over previous results, demonstrating the advancement of the *in situ* PXRD at Beamline I11.

Time-resolved *in situ* powder XRD analysis during crystallisation has been achieved with a lab-source X-ray instrument. Chapter 4 discussed the development of a custom segmented flow system, the KRAIC-Xl, which was used for the study of the anti-solvent crystallisation of aqueous glycine. The study found that relatively high crystal densities from high ethanol anti-solvent volume fractions were required in segmented flow to achieve measurable diffraction, highlighting the difference between lab-source and synchrotron experiments. The lab-source study investigated the crystallisation of the model material glycine, with analysis showing the preferential nucleation of the metastable β-GLY polymorph and rapid transformation to the more stable α-GLY, correlating with literature studies on the model material. The attempted study of L-glutamic acid anti-solvent crystallisation found that the lab-source

system is currently limited to systems where a high crystal slurry density can be achieved, and for crystal systems with minimal overlap of diffraction peaks for the different forms. However, this advancement how provides an alternative to synchrotron studies, enhancing access to the *in situ* study of crystallisation.

Chapter 3 presented the development of several data processing workflows in Python, using specialist Python compatible libraries, now enables the rapid processing of PXRD data for both lab-source and synchrotron PXRD studies of segmented flow crystallisation. A morphological baseline correction processing technique enabled the improved extraction of diffraction signal from the *o*ABA *in situ* PXRD studies on I11. A processing workflow for the lab-source PXRD data was able to correct for instrument errors and extract the maximum diffraction signal from the high background noise data.

Chapter 6 focussed on the upgrades of the KRAIC-S system for serial crystallography on Beamline I19. The improved crystalliser design now enables easy modification of X-ray analysis region to probe different points along the crystallisation process. The design went through two iterations (v2 and v3), with the final robust KRAIC-S v3 allowing for switchable crystalliser bodies to minimise downtime in the event of a blockage during beamtime. The optimised design maximised data collection time from a single crystal, aiming to improve the overall completeness collected for a single dataset. However, a trial study on the *in situ* SCXRD of paracetamol crystallisation focussed on large paracetamol crystals; large crystals were found to display a preferred orientation style effect in flow, and therefore in beam, at the detriment to the completeness of the overall merged dataset. This study defined the previously unknown limitations of the technique, highlighting the need to focus on smaller crystals in future experiments.

The KRAIC-S v3 was used to study the non-photochemical laser induced nucleation (NPLIN) effect on potassium chloride crystallisation, discussed in Chapter 7. To achieve this, the slug triggering mechanism was adapted to enable a single ~10 ns pulse of 6.6 MW/cm^2 laser power per slug to induce a single KCl crystal per slug. The accompanying *in situ* XRD data was able to achieve diffraction from the KCl crystals, however, the dense, highly mosaic crystals did not provide enough high quality data for full data processing. This experimental work provides the framework for NPLIN studies with a highly reproducible crystallisation environment, and the coupling with *in situ* XRD to enable the study of polymorphic systems with the NPLIN effect.

8.2 – Future Work

The developed PXRD processing techniques from Chapter 4 will enable rapid processing during future beamtimes on I11 and at Flow-Xl so users can make informed decisions to maximise experimental output from beamtimes. For example, if the processing shows an interesting polymorphic transition occurring, users could choose to investigate this further during the beamtime, maximising beam usage. The processing technique developed for Beamline I11 has the potential to be included as part of the automatic processing regime conducted in the GDA software can could provide automatically integrated, baseline corrected patterns for users, to increase the efficiency and ease-of-use of the analysis technique. The KRAIC-T has been established as a sample environment for I11 and is now available for the study of crystallisation of concomitant polymorphic systems, and effect of temperature cycling on polymorphic, or crystal form pathways.

The lab-source study of crystallisation with the KRAIC-Xl has achieved the proof-of-principle; future work has scope for the improvement of the technique. Signal-to-noise is a key area that could be improved through the addition of an enhanced data acquisition technique; the slug triggering mechanism used for the synchrotron KRAIC systems. Furthermore, the *in situ* Raman spectroscopy instrument at the Flow-Xl facility could be adapted to the KRAIC-Xl for simultaneous non-invasive Raman and XRD analysis. The addition of temperature control to the KRAIC-Xl would enable a wider range of experimental conditions to be trialled for more comprehensive studies of crystallisation landscape, enhancing the applicability of the system for detailed experimental studies for polymorphic form during crystallisation.

Now that key factors for the serial crystallography technique with the KRAIC-S have been established, future experiments should focus on smaller crystal sizes to achieve a greater crystal rotation. Future experiments should make use of the enhanced KRAIC-S v3 design to effectively target crystals of the right size with the improved data acquisition times to achieve a higher completeness per dataset. Further experiments have already been conducted on the KRAIC-S system, aiming to investigate morphological analysis coupled with *in situ* SCXRD on DL-methionine crystallisation. The DL-methionine crystallisation produced multiple small single crystals per slug, with a greater crystal rotation than seen for paracetamol. The data processing is ongoing to see if single crystal data can be extracted from data collections with multiple crystals in beam. If successful, this would widen the scope of experiments feasible with the technique.

Following the development of the KRAIC-S v3 design, the NPLIN study of KCl provides the groundwork for future NPLIN studies on polymorphic crystal systems to probe conditions not typically accessible in the KRAIC systems. The direct coupling of this technique with *in situ* XRD provides an excellent platform for future research in this area. The results of the KRAIC-S paracetamol and NPLIN KCl studies showed that crystal rotation during data collection, and therefore crystal size is a key factor for the serial crystallography technique.

Smaller crystals should be the focus of any future experimentation. However, this presents issues with co-location of the beam and small crystals in the 3.2 mm tubing width, which also has knock-on effects for sample to detector deviation causing issues with data processing. The DL-methionine study attempts to bypass this issue by having multiple crystals in the slug, but this provides extra challenges for data processing. Another method to improve the data collection from smaller crystals would be through the design of a milli-fluidic size of KRAIC-S with use of smaller ID tubing for the serial crystallography technique; this may potentially improve the co-location of small crystals and the X-ray beam and improve the quality of data collected in terms of completeness and reduction in deviation of the sample to detector distance.

Appendix

Appendix A3 – Chapter 3

A3.1 – Beamline I11 PXRD data processing scripts

Link to the Github public repository for processing workflow scripts referred in Chapter 3 for Beamline I11 PXRD data processing for the KRAIC-T with slug triggering data:

https://github.com/ESGaltry/I11_PXRD_processing_scripts

A3.2 – Flow-Xl PXRD data processing scripts

Link to the Github public repository for script discussed in Chapter 3 for the data processing of Flow-Xl PXRD data collected from the KRAIC-Xl:

https://github.com/ESGaltry/FlowXl_PXRD_processing_script

Appendix A4 – Chapter 4

A4.1 – Calibrant data file comparison

Comparison of I11 CeO_2 calibrant file (a) used for *o*ABA data processing, with thin, distinct powder rings, and (b) the AgBh d80 file collected at Flow-Xl for KRAIC-Xl calibration. KRAIC-Xl calibration file has considerably thicker powder rings and poor distinction of rings 7 – 12 for AgBh calibration.

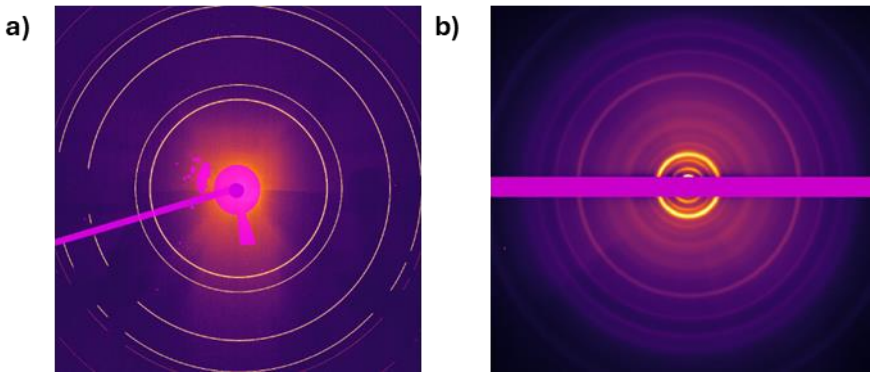

A4.2 – LGA Frame Selector results

The results of the Frame Selector tool in CrysAlisPro for LGA datasets, with notes from the visual inspection of frames.

Dataset Identifier	Number of frames	Used frames	Percentage of "Used frames"	Notes
LGA1_1	7200	10	0.1%	A couple of spots
LGA1_2	4345	12	0.3%	A couple of spots
LGA2_1	7200	7	0.1%	One spot
LGA2_2	2567	0	0.0%	No frames selected
LGA3_1	7200	9	0.1%	A couple of spots
LGA3_2	2674	2	0.1%	A couple of spots
LGA3_3	7200	11	0.2%	A couple of spots
LGA3_4	4967	1	0.0%	One spot
LGA3_5	337	337	100.0%	Encrustation on Kapton window with all frames with diffraction
LGA3_6	3600	10	0.3%	A few spots
LGA3_7	3600	58	1.6%	A few spots
LGA4_1	3600	11	0.3%	One spot
LGA4_2	1344	4	0.3%	One spot
LGA4_3	3600	2	0.1%	One spot

LGA5_1	3600	363	10.1%	On visual inspection, no frames contain diffraction
LGA5_2	3600	280	7.8%	On visual inspection, no frames contain diffraction
LGA5_3	5166	355	6.9%	On visual inspection, no frames contain diffraction
LGA6_1	3600	462	12.8%	On visual inspection, no frames contain diffraction
LGA6_2	3600	134	3.7%	On visual inspection, no frames contain diffraction
LGA6_3	1103	704	63.8%	Some used frames with background scattering only, some with diffraction due to encrustation

Appendix A5 – Chapter 5

A5.1 - Temperature profiles for KRAIC-T commissioning

Temperature profiles collected with A FLIR E5 IR camera for the temperature cycling of heated water at 3 mL/min and 9 mL/min flow rates. “50:30_9_19.4RT” describes temperature cycling between column temperatures of 50 °C and 30 °C with a 9 mL/min water flow rate and a measured room temperature (RT) of 19.4 °C. Temperature measurements have a ± 1.5 °C error calculated by the deviation of temperature readings against a known temperature. Temperature profiles have ± 1.5 °C error bars with annotations indicating Heating Zone (HZ) and X-ray window (X) positions.

A5.1.1 – 50:30 conditions

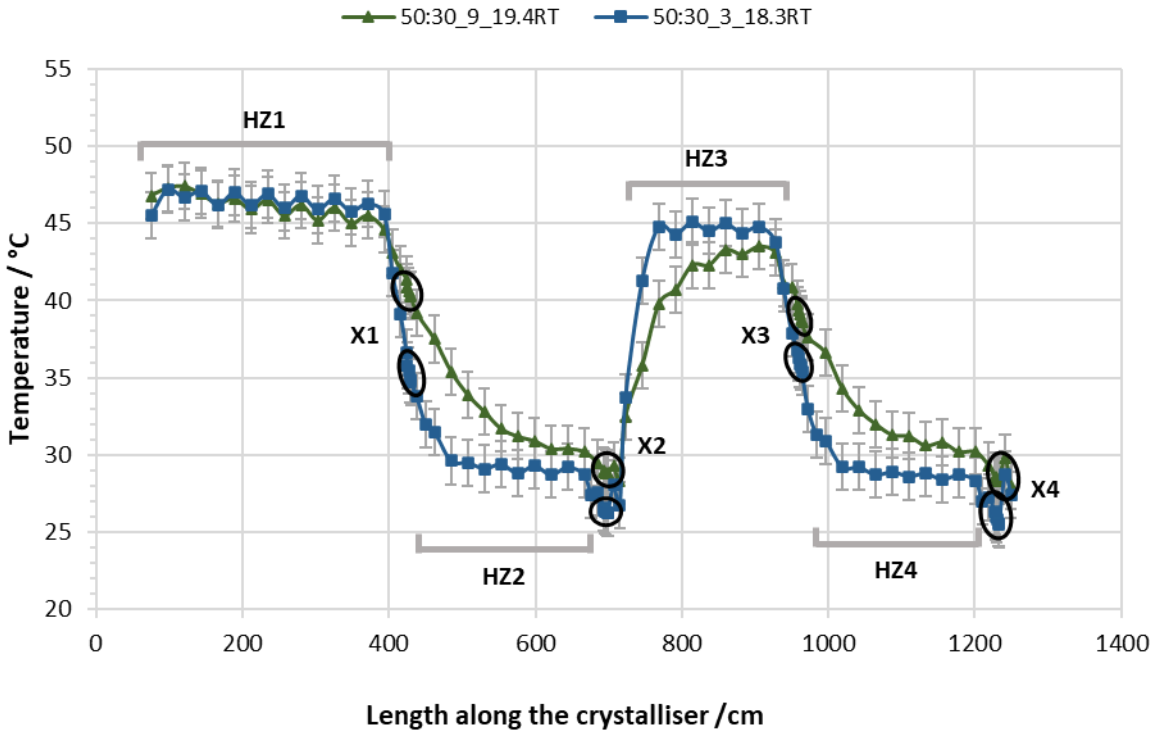

A5.1.2 – 50:40 conditions

50:40_3 measurement compared against 50:40_9 repeated measurements shown previously in Figure 5.08.

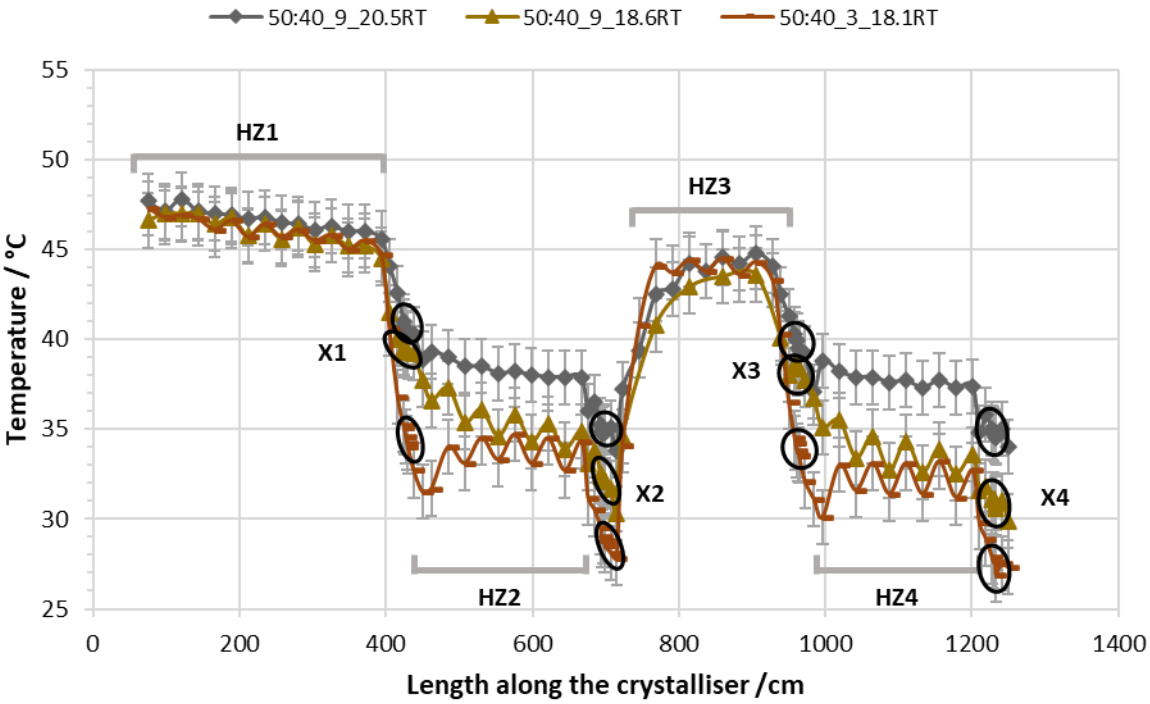

A5.1.3 – 60:30 conditions

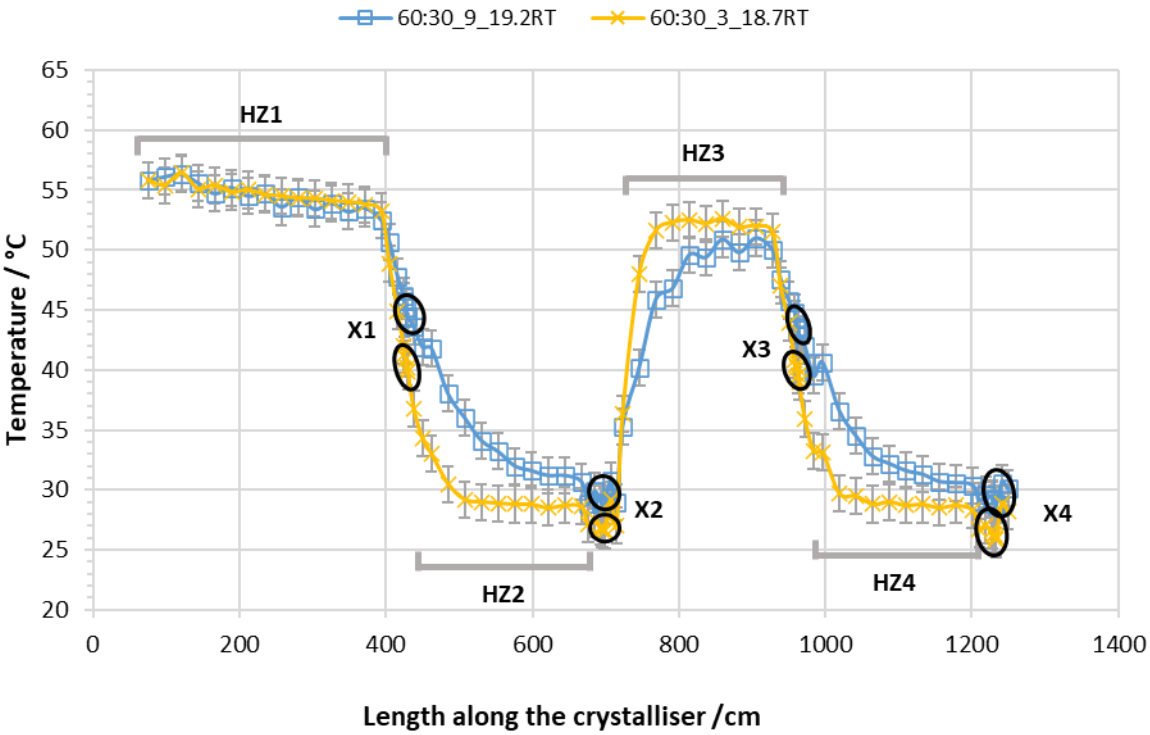

A5.1.4 – 60:40 conditions

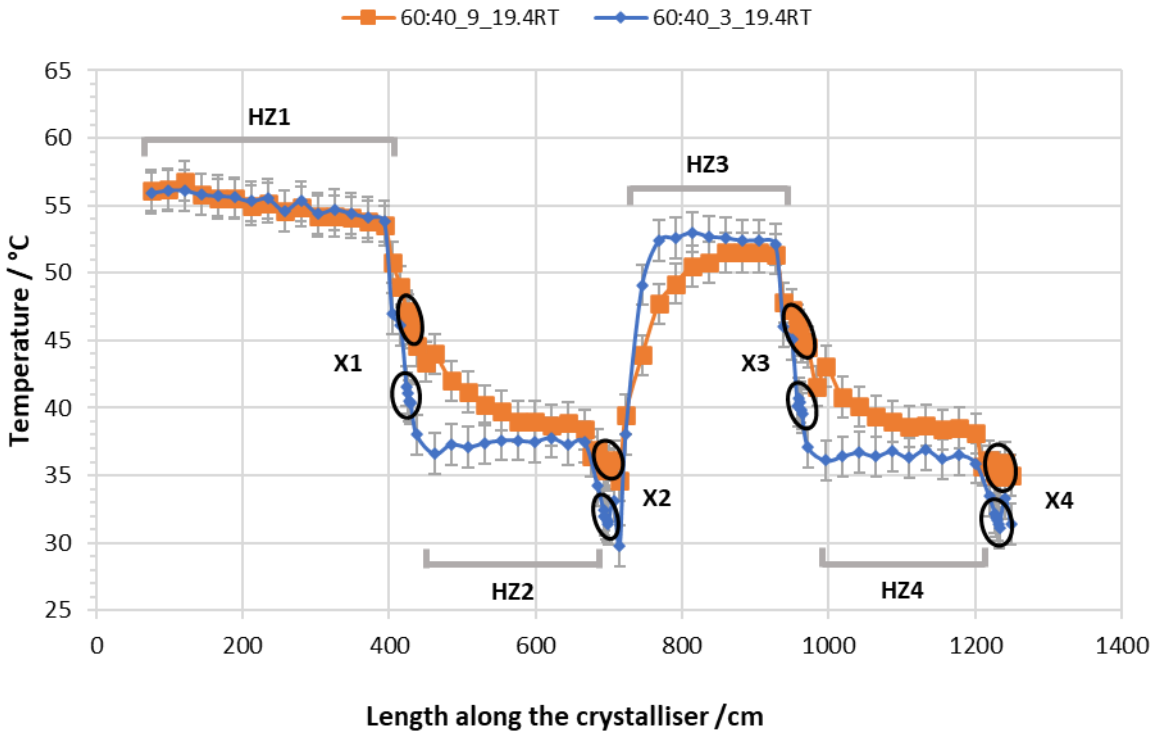

A5.1.5 – 60:50 conditions

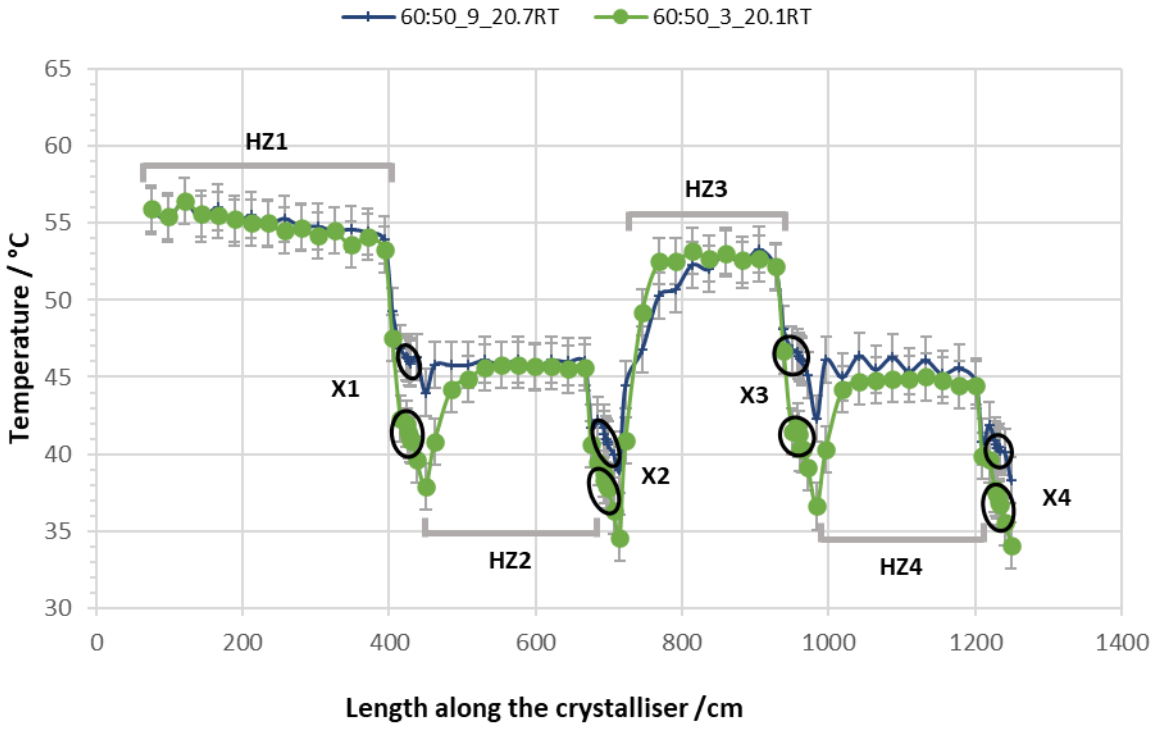

A5.2 – *o*ABA crystallisation conditions

Summary of the range of conditions attempted for *o*ABA and *o*ABA with BA additive crystallisations in the KRAIC-T during beamtime. For *o*ABA stock solution of 22 g/L dissolved at 60 °C. Runs 0.1 – 0.3 using air and carrier fluid flow rates of 1.5 mL/min and 1.2 mL/min respectively, with Runs 0.4 – 0.8 increasing the carrier flow to 1.4 mL/min. *Run 0.8 used HZ1-X1-HZ2 tubing sections only.

		Flow rates / mL/min			
Experiment identifier	**BA loading / g/L | ratio**	**Solution**	**Dilution**	**Total**	**Resultant oABA solution concentration / g/L**
0.1_18.9_*o*ABA_30:55_15	-	3.0	0.5	6.2	18.9
0.2_19.5_*o*ABA_30:55_15	-	3.1	0.4	6.2	19.5
0.3_20.1_*o*ABA_30:55_12.5	-	3.2	0.3	6.2	20.1
0.4_22.0_*o*ABA_30:55_10	-	3.5	0.0	6.4	22.0
0.5_19.5_*o*ABA_BA_30:60_10	8.8 | 0.4	3.1	0.4	6.4	19.5
0.6_19.5_*o*ABA_BA_50:40_12	8.8 | 0.4	3.1	0.4	6.4	19.5
0.7_19.5_*o*ABA_BA_45:35_15	8.8 | 0.4	3.1	0.4	6.4	19.5
0.8_18.9_*o*ABA_BA_45:50_13 *new outlet position	8.8 | 0.4	3.0	0.5	6.4	18.9

	Temperatures / °C		
Experiment identifier	**Cold water circulator - nucleation promoter jacketed tubing**	**C1**	**C2**
0.1_18.9_*o*ABA_30:55_15	15	30	55
0.2_19.5_*o*ABA_30:55_15	15	30	55
0.3_20.1_*o*ABA_30:55_12.5	12.5	30	55
0.4_22.0_*o*ABA_30:55_10	10	30	55
0.5_19.5_*o*ABA_BA_30:60_10	10	30	60
0.6_19.5_*o*ABA_BA_50:40_12	12	50	40
0.7_19.5_*o*ABA_BA_45:35_15	15	45	35
0.8_18.9_*o*ABA_BA_45:50_13 *new outlet position	13	45	50

A5.3 - Rietveld refinement unit cell parameters

Output of Rietveld refinement unit cell parameters for all collection sets. Unit cell angles of 90 ° are not refined as they defined by the crystal lattice structure and therefore have no error calculated.

A5.3.1 – 1_oABA_45:60_1

X1_01				
Phase	***o*ABA_I**		***o*ABA_II**	
a | error /Å	12.90143	0.00398	16.1029	0.01434
b | error /Å	10.82534	0.00711	11.68028	0.00944
c | error /Å	9.36499	0.00934	7.19285	0.01695
α | error /°	90	None	90	None
β | error /°	90	None	90	None
γ | error /°	90	None	90	None
Cell Volume | error /Å^3	1307.93711	1.61295082	1352.87751	3.57856474
Phase	***o*ABA_III**			
a | error /Å	12.26035	0.00651		
b | error /Å	15.42339	0.00498		
c | error /Å	7.58056	0.00418		
α | error /°	90	None		
β | error /°	152.53839	0.01796		
γ | error /°	90	None		
Cell Volume | error /Å^3	661.043779	0.678445396		

X1_02				
Phase	***o*ABA_I**		***o*ABA_II**	
a | error /Å	12.91843	0.00122	16.1111	0.00863
b | error /Å	10.81038	0.00177	11.68216	0.00565
c | error /Å	9.33528	0.0023	7.17787	0.01016
α | error /°	90	None	90	None
β | error /°	90	None	90	None
γ | error /°	90	None	90	None
Cell Volume | error /Å^3	1303.70211	0.404632334	1350.96319	2.14652709
Phase	***o*ABA_III**			
a | error /Å	12.26219	0.00266		
b | error /Å	15.42678	0.00275		
c | error /Å	7.58867	0.00272		
α | error /°	90	None		
β | error /°	152.53046	0.01035		
γ | error /°	90	None		
Cell Volume | error /Å^3	662.172465	0.379187871		

X2_01				
Phase	***o*ABA_I**		***o*ABA_II**	
a | error /Å	12.90316	0.00632	16.11416	0.02375
b | error /Å	10.69564	0.0341	11.68567	0.01505
c | error /Å	9.43954	0.02908	7.25699	0.02672
α | error /°	90	None	90	None
β | error /°	90	None	90	None
γ | error /°	90	None	90	None
Cell Volume | error /Å³	1302.72834	5.81119721	1366.52595	5.69913668
Phase	***o*ABA_III**			
a | error /Å	12.27166	0.00724		
b | error /Å	15.45162	0.0075		
c | error /Å	7.59134	0.0063		
α | error /°	90	None		
β | error /°	152.52187	0.02784		
γ | error /°	90	None		
Cell Volume | error /Å³	664.175441	0.972882513		

X2_02				
Phase	***o*ABA_I**		***o*ABA_II**	
a | error /Å	12.92578	0.00271	16.13602	0.01834
b | error /Å	10.84297	0.00673	11.68108	0.01119
c | error /Å	9.3348	0.00859	7.23704	0.02073
α | error /°	90	None	90	None
β | error /°	90	None	90	None
γ | error /°	90	None	90	None
Cell Volume | error /Å³	1308.30785	1.47797096	1364.08271	4.40260922
Phase	***o*ABA_III**			
a | error /Å	12.27277	0.00471		
b | error /Å	15.4499	0.00416		
c | error /Å	7.59056	0.004		
α | error /°	90	None		
β | error /°	152.53132	0.01551		
γ | error /°	90	None		
Cell Volume | error /Å³	663.882606	0.582104011		

X3_01				
Phase	***o*ABA_I**		***o*ABA_II**	
a | error /Å	12.9148	0.00219	16.11023	0.00858
b | error /Å	10.83198	0.00589	11.69812	0.00551
c | error /Å	9.35031	0.00731	7.2172	0.00954
α | error /°	90	None	90	None
β | error /°	90	None	90	None
γ | error /°	90	None	90	None
Cell Volume | error /Å³	1308.04117	1.26557776	1360.15035	2.04071909
Phase	***o*ABA_III**			
a | error /Å	12.27348	0.00366		
b | error /Å	15.43746	0.00301		
c | error /Å	7.59463	0.00275		
α | error /°	90	None		
β | error /°	152.53307	0.01218		
γ | error /°	90	None		
Cell Volume | error /Å³	663.703332	0.433090592		

A5.3.2 – 2_oABA_45:65_1

X1_01				
Phase	***o*ABA_I**		***o*ABA_II**	
a | error /Å	12.9033	0.00138	16.11374	None
b | error /Å	10.81792	0.0028	11.66835	None
c | error /Å	9.33992	0.00321	7.18365	None
α | error /°	90	None	90	None
β | error /°	90	None	90	None
γ | error /°	90	None	90	None
Cell Volume | error /Å³	1303.731	0.578375	1350.674	None
Phase	***o*ABA_III**			
a | error /Å	12.25366	0.00708		
b | error /Å	15.41545	0.00992		
c | error /Å	7.59351	0.00845		
α | error /°	90	None		
β | error /°	152.5614	0.04318		
γ | error /°	90	None		
Cell Volume | error /Å³	660.9587	1.337332		

X2_01				
Phase	***o*ABA_I**		***o*ABA_II**	
a | error /Å	12.93851	0.00187	16.07687	0.06676
b | error /Å	10.83254	0.00401	11.66667	0.04005
c | error /Å	9.35857	0.0044	7.36716	0.0794
α | error /°	90	None	90	None
β | error /°	90	None	90	None
γ | error /°	90	None	90	None
Cell Volume | error /Å³	1311.667	0.807282	1381.81	16.65072
Phase	***o*ABA_III**			
a | error /Å	12.2924	0.0097		
b | error /Å	15.48138	0.0161		
c | error /Å	7.61856	0.0183		
α | error /°	90	None		
β | error /°	152.8099	0.07222		
γ | error /°	90	None		
Cell Volume | error /Å³	662.4936	2.433757		

X2_02				
Phase	***o*ABA_I**		***o*ABA_II**	
a | error /Å	12.92423	0.00195	16.09909	0.04884
b | error /Å	10.82041	0.00501	11.63893	0.04713
c | error /Å	9.36491	0.00569	7.28663	0.06303
α | error /°	90	None	90	None
β | error /°	90	None	90	None
γ | error /°	90	None	90	None
Cell Volume | error /Å³	1309.639	1.019972	1365.34	13.68187
Phase	***o*ABA_III**			
a | error /Å	12.18947	0.02407		
b | error /Å	15.59097	0.03944		
c | error /Å	7.40132	0.03611		
α | error /°	90	None		
β | error /°	152.8819	0.15427		
γ | error /°	90	None		
Cell Volume | error /Å³	641.1593	5.038049		

X3_01				
Phase	***o*ABA_I**		***o*ABA_II**	
a | error /Å	12.9252	0.00122	16.11854	0.07278
b | error /Å	10.82813	0.00231	11.66131	0.04071
c | error /Å	9.34728	0.00312	7.20433	0.0861
α | error /°	90	None	90	None
β | error /°	90	None	90	None
γ | error /°	90	None	90	None
Cell Volume | error /Å³	1308.205	0.532955	1354.149	17.93355
Phase	***o*ABA_III**			
a | error /Å	12.2849	0.01133		
b | error /Å	15.49671	0.01695		
c | error /Å	7.60486	0.01798		
α | error /°	90	None		
β | error /°	152.8803	0.07677		
γ | error /°	90	None		
Cell Volume | error /Å³	659.9704	2.511453		

A5.3.3 – 3_oABA_45:60_2

X1_01				
Phase	***o*ABA_II**		***o*ABA_III**	
a | error /Å	16.10442	0.00886	12.26253	0.00443
b | error /Å	11.68173	0.00504	15.42315	0.00341
c | error /Å	7.18684	0.00969	7.58321	0.00329
α | error /°	90	None	90	None
β | error /°	90	None	152.52796	0.01272
γ | error /°	90	None	90	None
Cell Volume | error /Å³	1352.04326	2.05431454	661.613831	0.490820043

X1_01				
Phase	***o*ABA_I**		***o*ABA_II**	
a | error /Å	12.85936	0.01238	16.09935	0.00802
b | error /Å	10.65255	0.01292	11.68764	0.00444
c | error /Å	9.54625	0.01447	7.20528	0.01026
α | error /°	90	None	90	None
β | error /°	90	None	90	None
γ | error /°	90	None	90	None
Cell Volume | error /Å³	1307.69348	2.83394093	1355.76957	2.10865212
Phase	***o*ABA_III**			
a | error /Å	12.28011	0.00458		
b | error /Å	15.43268	0.00295		
c | error /Å	7.58619	0.00283		
α | error /°	90	None		
β | error /°	152.5803	0.01325		
γ | error /°	90	None		
Cell Volume | error /Å³	662.066521	0.47435417		

X2_01				
Phase	***o*ABA_II**		***o*ABA_III**	
a | error /Å	16.12873	0.01051	12.26217	0.00442
b | error /Å	11.68735	0.00581	15.43928	0.00387
c | error /Å	7.20614	0.01385	7.58351	0.00367
α | error /°	90	None	90	None
β | error /°	90	None	152.50331	0.01379
γ | error /°	90	None	90	None
Cell Volume | error /Å³	1358.37206	2.83819004	662.860647	0.53044288

X3_01				
Phase	***o*ABA_II**		***o*ABA_III**	
a | error /Å	16.1283	0.00768	12.2837	0.00384
b | error /Å	11.70747	0.004	15.45245	0.00273
c | error /Å	7.20851	0.00959	7.59572	0.00282
α | error /°	90	None	90	None
β | error /°	90	None	152.52823	0.01083
γ | error /°	90	None	90	None
Cell Volume | error /Å³	1361.12191	1.97864026	665.104338	0.420306898

X3_02				
Phase	***o*ABA_II**		***o*ABA_III**	
a | error /Å	16.11843	0.00691	12.27441	0.00347
b | error /Å	11.69633	0.00361	15.43982	0.00247
c | error /Å	7.18712	0.00842	7.5919	0.00259
α | error /°	90	None	90	None
β | error /°	90	None	152.52848	0.00997
γ | error /°	90	None	90	None
Cell Volume | error /Å³	1354.96359	1.74205029	663.718744	0.38345626

A5.3.4 – 4_oABA_45:65_2

X1_01				
Phase	***o*ABA_I**		***o*ABA_II**	
a | error /Å	12.88329	0.00819	16.01368	0.01899
b | error /Å	10.7784	0.00522	11.64441	0.01326
c | error /Å	9.32946	0.01809	7.19412	0.02094
α | error /°	90	None	90	None
β | error /°	90	None	90	None
γ | error /°	90	None	90	None
Cell Volume | error /Å³	1295.50101	2.7175449	1341.4862	4.48382798
Phase	***o*ABA_III**			
a | error /Å	12.21499	0.00737		
b | error /Å	15.37843	0.00755		
c | error /Å	7.54642	0.0067		
α | error /°	90	None		
β | error /°	152.56022	0.02856		
γ | error /°	90	None		
Cell Volume | error /Å³	653.241672	0.993660145		

X2_01				
Phase	***o*ABA_I**		***o*ABA_II**	
a | error /Å	12.84734	0.0054	16.03483	0.01206
b | error /Å	10.80326	0.0163	11.60969	0.00885
c | error /Å	9.22147	0.01573	7.14634	0.01331
α | error /°	90	None	90	None
β | error /°	90	None	90	None
γ | error /°	90	None	90	None
Cell Volume | error /Å³	1279.87656	2.96397704	1330.3576	2.85762763
Phase	***o*ABA_III**			
a | error /Å	12.18037	0.00618		
b | error /Å	15.33794	0.00461		
c | error /Å	7.5421	0.00403		
α | error /°	90	None		
β | error /°	152.50594	0.01998		
γ | error /°	90	None		
Cell Volume | error /Å³	650.486913	0.676776328		

X2_02				
Phase	***o*ABA_I**		***o*ABA_II**	
a | error /Å	12.8443	0.0074	16.01187	0.00933
b | error /Å	10.79121	0.02192	11.61215	0.00634
c | error /Å	9.22585	0.01695	7.16816	0.00987
α | error /°	90	None	90	None
β | error /°	90	None	90	None
γ | error /°	90	None	90	None
Cell Volume | error /Å³	1278.75412	3.57949731	1332.7913	2.1220806
Phase	***o*ABA_III**			
a | error /Å	12.184	0.00472		
b | error /Å	15.34488	0.00403		
c | error /Å	7.53704	0.00374		
α | error /°	90	None		
β | error /°	152.5197	0.01613		
γ | error /°	90	None		
Cell Volume | error /Å³	650.238665	0.565973084		

Appendix A6 – Chapter 6

A6.1 – PCM processing procedure

Data processing used for PCM data based on the original KRAIC-S processing workflow. Processing completed with NoMachine access to Diamond Linux desktop computer (https://www.diamond.ac.uk/Users/Experiment-at-Diamond/IT-User-Guide/Not-at-DLS/Nomachine.html). Processing commands submitted to a Linux command line in a data processing directory.

Importing data

Using a reference detector geometry and detector distance of 139.89 mm

```
module load dials/3.14.1-1

dials.import /your/nexus/file/location/data_collection_name.nxs
reference_geometry=/location/of/reference/geometry/IM.expt
distance=139.89 output.experiments=01_imported.expt
output.log=logs/01_imported.log
```

Generate detector mask

Mask regions of detector with no diffraction, including photodiode detector shadowing and strong FEP rings.

```
dials.generate_mask 01_imported.expt circle=323,217,600
rectangle=972,995,0,1425 rectangle=235,893,1420,1424
resolution_range=5.6,4.9 resolution_range=999,32
output.mask=01_pixels.mask output.log=logs/01_dials.generate_mask.log


dials.apply_mask 01_imported.expt input.mask=01_pixels.mask
output.experiments=02_imported_masks.expt
```

Spot finding

```
dials.find_spots 02_imported_masks.expt
threshold.algorithm=radial_profile radial_profile.n_iqr=11
radial_profile.n_bins=55 radial_profile.blur=wide
output.reflections=03_find_spots.relf output.log=logs/03_find_spots.log
```

Indexing

dials.index 03_find_spots.relf 02_imported_masks.expt
unit_cell=7.08,9.2,11.54,90,97.9,90 space_group=P2/m beam.fix=all
detector.fix=all index_assignment.method=local local.epsilon=0.15
output.reflections=04_index.relf output.experiments=04_index.expt
output.log=logs/04_index.log

dials.report 04_index.relf 04_index.expt output.html=04_dials-report_indexed.html

Refinement

interval_width_degrees increased by increments of 0.01 until refinement succeeds.

dials.refine 04_index.relf 04_index.expt beam.fix=all detector.fix=all
tie_to_group.sigmas=0.1,0.1,0.1,0.0,0.1,0.0
crystal.orientation.smoother.interval_width_degrees=0.5
unit_cell.force_static=1 output.reflections=05_refine.relf
output.experiments=05_refine.expt output.log=logs/05_refine.log

dials.report 05_refine.expt 05_refine.relf
output.html=05_refine_report.html

Integration

dials.integrate 05_refine.expt 05_refine.relf
profile.gaussian_rs.min_spots.per_degree=1
profile.gaussian_rs.min_spots.overall=5 profile.fitting=False
output.reflections=06_integrate.relf
output.experiments=06_integrate.expt output.phil=06_integrate.phil
output.log=logs/06_integrate.log

Scaling

dials.scale 06_integrate.expt 06_integrate.relf
output.reflections=07_scale.relf output.experiments=07_scale.expt
output.html=07_scale.html output.log=logs/07_scale.log

Exporting

dials.two_theta_refine 07_scale.expt 07_scale.relf p4p=08_2t_refine.p4p
output.experiments=08_2t_refine.expt output.log=logs/08_2t_refine.log

dials.export 08_2t_refine.expt 07_scale.relf output.log=logs/09_export.log

mv scaled.mtz 09_export.mtz

xia2.to_shelx 09_export.mtz 011_w10_run5_05 C8H9N1O2